Downloaded from orbit.dtu.dk on: May 04, 2023

DTU Library

Magnetic manipulation and sensing of beads for bioapplications

Henriksen, Anders Dahl

Publication date:
2015

Document Version
Publisher's PDF, also known as Version of record

Link back to DTU Orbit

Citation (APA):
Henriksen, A. D. (2015). *Magnetic manipulation and sensing of beads for bioapplications*. DTU Nanotech.

General rights
Copyright and moral rights for the publications made accessible in the public portal are retained by the authors and/or other copyright owners and it is a condition of accessing publications that users recognise and abide by the legal requirements associated with these rights.

- Users may download and print one copy of any publication from the public portal for the purpose of private study or research.
- You may not further distribute the material or use it for any profit-making activity or commercial gain
- You may freely distribute the URL identifying the publication in the public portal

If you believe that this document breaches copyright please contact us providing details, and we will remove access to the work immediately and investigate your claim.

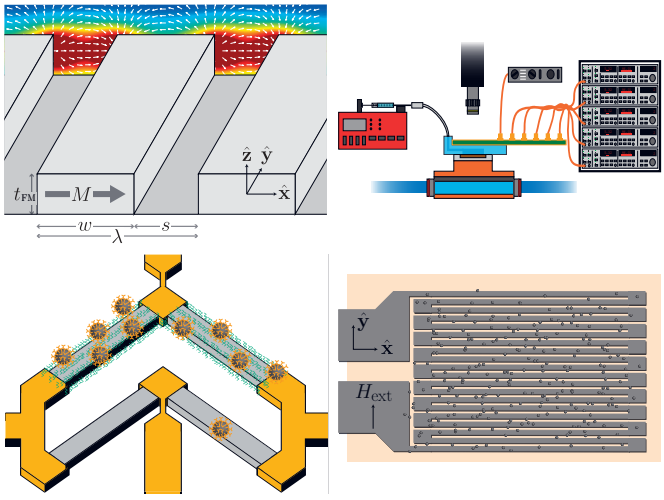

Magnetic manipulation and sensing of beads for bioapplications

Anders Dahl Henriksen
PhD Thesis August 2015

DTU Nanotech
Department of Micro- and Nanotechnology

DTU Nanotech
Department of Micro- and Nanotechnology

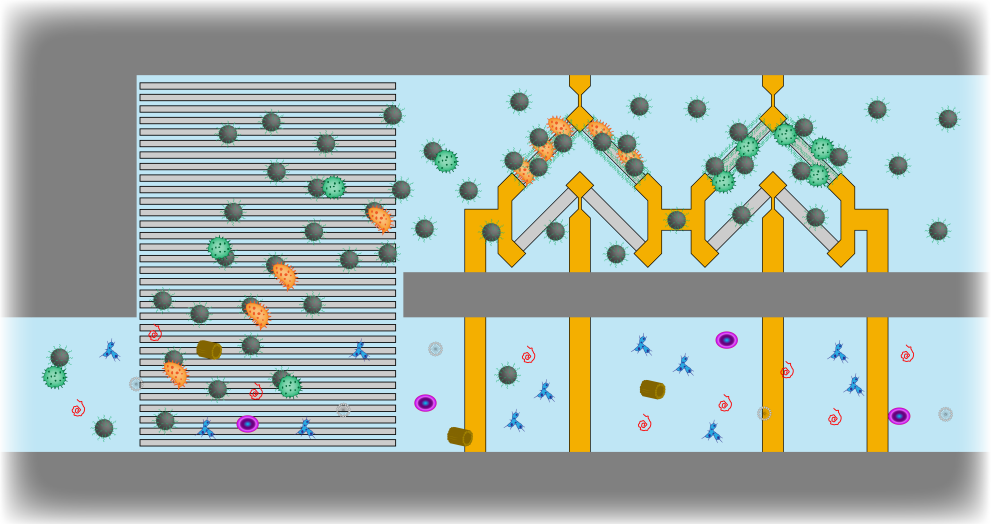

Magnetic manipulation and sensing of beads for bioapplications

Ph.D. project at DTU Nanotech

Anders Dahl Henriksen

Supervisors: Mikkel Fougt Hansen, Associate Professor
Noemi Rozlosnik, Associate Professor

Submission date: August 14, 2015

Abstract

Point-of-care diagnostics is predicted to revolutionize the way of healthcare and advance the field of personalized medicine. Point-of-care diagnostics opens the possibility of doing complex molecular biochemical analysis at the patient's home or at the doctor's office, instead of sending samples to a central laboratory. This will reduce the analysis time leading to earlier detections and easier disease monitoring, both of which are critical parameters for the efficacy of the applied treatment. So far, the commercially successful point-of-care devices have all been single purpose. However, much research have gone into making a customizable and multipurpose sensor platform, which could accelerate the number of practices.

This thesis investigates the role of magnetic beads as candidates for use in these new biosensing devices. Magnetic beads have stable properties and can be easily coated with biological recognition elements like proteins and DNA. Further, as all biological matter is none or weakly magnetic, magnetic beads are well suited for sample extraction and highly sensitive biodetection, where a low background level is needed. This thesis focuses on the use of magnetic beads in both molecular separation based on magnetophoresis and on biodetection based on magnetoresistive sensors.

Part I of this thesis explores magnetophoresis, both experimentally and theoretically. Experimentally, magnetophoresis was done on chips with stripes, two to ten microns in size and made of a permalloy based magnetic stack. The permalloy micro stripes created a spatially varying magnetic field, which in combination with a rotating external field was used to transport magnetic beads from stripe to stripe. Systematic measurements of the magnetophoresis properties on varying stripe geometries were performed. It was found that a symmetric geometry with equal stripe width and spacing was optimal, and that the stripe period should be thrice the bead radius. Magnetophoretic bead velocities of 300 μm/s were measured, and selective separation based on differences in magnetophoretic mobility was hypothesized. However, the fabricated magnetophoresis systems had two major limitations. First, protein-coated magnetic beads had a tendency to stick to the surface, even though multiple surface blockings and modifications were tried. Second, as the systems are fabricated using a single UV lithography step, the stripe width has a minimum feature size of one micron, which limits the movable bead size to approximately one micron.

Parts II and III investigate magnetic bead detection using planar Hall effect bridge (PHEB) sensors. The PHEB sensor also uses a permalloy based magnetic stacks with anisotropic magnetoresistance. By combining four resistors in a Wheatstone bridge, the sensor output is shown to be proportional to low magnetic fields. In this thesis, the PHEB sensors are used for either detection of an external homogeneous magnetic field or for detection of magnetic beads that are magnetized by the sensor self-field. Multiple studies are made to optimize the bead detection using PHEB sensors. First, two new sensor designs are introduced: A parallel PHEB sensor, nominally only sensitive to self-field contributions and optimized for volume based relaxation measurements; a differential PHEB, which does on-chip reference measurements and is optimized for detecting small amounts of surface bound beads. The next study analyzes the thermal properties of the chip and setup. General methods for measuring or calculating the effective heat conductivity are given, along with a discussion on how to optimize this to facilitate the use of higher currents. The thesis then compares ring and diamond shaped PHEB sensors, both designs which have been argued to be superior. Theoretically, the diamond shaped sensors are more sensitive, but experimentally ring sensors are found to be less affected by shape anisotropy. Diamond shaped sensors

are thus only better for magnetic stacks with negligible shape anisotropy. Last, the inclusion of a copper layer in the magnetic stack was investigated. A six angstrom copper layer was found to double the signal from magnetic beads.

After studies of optimizing PHEB sensors, magnetic bead based bio-detection and bio-characterization were performed. PHEB sensors were used to detect magnetic beads tethered to the sensor surface through DNA-DNA interaction. By ramping the temperature on-chip DNA melting curves were measured, and conditions for differentiating mutant type and wild type DNA were identified. This method was also tried for studying of aptamer hybridization to magnetic beads coated with virus protein, a so-called magnetic artificial virus. Two aptamers from the literature were tried, but none of them showed any significant hybridization to the artificial virus.

Last Part IV performed a thorough theoretical analysis on how to measure a surface coverage of magnetic beads that are stochastically bound to the sensor surface and its surroundings. The field, from magnetic beads magnetized by an external field, varies with position and even changes sign. It is derived, how the signal will usually be dominated from magnetic beads outside of the sensor surface, as these are at a lower height relative to the sensor plane, and how magnetic beads on top of the sensor only decreases this signal. After having clarified the origin of the bead signal, a general framework for calculating the expected bead signal and its configurational fluctuations is described. This framework is used for analyzing three state-of-the-art sensors from the literature, and two of them are found to be limited by these statistical fluctuations.

Resumé

Point-of-care diagnostik forventes at revolutionere tilgængeligheden af sundhedsydelser og fremme personlig medicin. Point-of-care diagnostik giver mulighed for kompleks molekylære biokemisk analyse i patientens hjem eller på lægens kontor, i stedet for at sende prøver til et laboratorium. Dette vil reducere analysetiden, førende til tidligere sygdom opdagelser og lettere sygdom overvågning, hvilke begge er kritiske parametre for effektiviteten af den anvendte behandling. Hidtil har de kommercielt succesfulde point-of-care enheder alle været tiltænkt en enkelt analyse. Imidlertid har meget forskning arbejdet på at udvikle en brugerdefinerbar og multifunktionel sensor platform, som kan forøge antallet af analyser.

Denne afhandling undersøger om magnetiske kugler kan bruges i disse nye analyse platforme. Magnetiske kugler har stabile egenskaber og kan let konjugeres med biologiske molekyler som proteiner og DNA. Da alt biologisk materiale er enten ikke eller svagt magnetisk, er magnetiske kugler velegnede til prøveudtagning og til sensitiv biodetektion, hvor der er behov for et lavt baggrundsniveau. Denne afhandling fokuserer på anvendelsen af magnetiske kugler i både molekylær separation baseret på magnetophorese og i biodetektion baseret på magnetoresistive sensorer.

Del I af afhandlingen udforsker magnetophorese, både eksperimentelt og teoretisk. Eksperimentelt blev magnetophorese udført på chips med to til ti mikrometer bredde striber lavet af en permalloy baseret magnetisk stak. Permalloy mikro striberne skabte et rumligt varierende magnetisk felt, hvilket i kombination med en roterende ydre felt blev brugt til at transportere magnetiske kugler fra stribe til stribe. Systematiske målinger af de magnetophoresis egenskaber for varierende stribe geometrier blev udført. Det blev vist at en symmetrisk geometri med lige stor stribe bredde og afstand var optimal, og at stribe perioden bør være tre gange radius af den magnetiske kugle. Magnetophoretiske hastigheder på 300 μm/s blev målt, og en hypotese om selektiv adskillelse, baseret på forskelle i magnetophoretisk mobilitet, blev opstillet. Desværre havde de fabrikerede magnetophorese systemer to store begrænsninger. For det første, protein konjugerede magnetiske kugler var tilbøjelige til at klæbe til overfladen, også selvom flere overflade blokeringer og modifikationer blev forsøgt. For det andet, da striberne er fabrikeret ved UV litografi har striberne en mindste størrelse på en mikrometer, hvilket begrænser systemet til magnetiske kugler af en mikrometer eller større.

Del II og III undersøger detektion af magnetisk kugler ved brug af planar Hall effekt bro (PHEB) sensorer. PHEB sensorerne bruger også en permalloy baseret magnetisk stak der udviser anisotropisk magnetoresitivitet. Ved at kombinere fire modstande i en Wheatstone bro, bliver sensor signalet proportionalt med lave magnetfelter. I denne afhandling er PHEB sensorerne anvendt til enten detektion af et eksternt homogent magnetfelt eller til detektion af magnetiske kugler, der er magnetiseret af sensorens selv-felt. Flere undersøgelser er lavet for at optimere detektion af magnetiske kugler med PHEB sensorer. Først er to nye sensor design introduceret: En parallel PHEB sensor, nominelt kun følsom over for selv felts bidrag og optimeret til volumen baseret relaksometriske målinger; en differentiel PHEB, for reference målinger på sensoren og optimeret til at detektere af små mængder overfladebundne magnetiske kugler. Den næste undersøgelse analyserer de termiske egenskaber af chippen og måleopsætningen. Generelle metoder til måling eller beregning af den effektive varmeledningsevne er givet, sammen med en diskussion om, hvordan man optimerer dette for anvendelsen af stærkere strømme. Afhandlingen sammenligner derefter ring og diamant formede PHEB sensorer, begge designs er blevet argumenteret som overlegne. Teoretisk er diamant formede sensorer mere følsomme, men det vises eksperimentelt at ring formede sensorer er mindre påvirket af form anisotropi. Diamant formede sensorer

er således kun bedre for magnetiske stakke med ubetydelig form anisotropi. Til sidst blev inkluderingen af et kobber lag i den magnetiske stak undersøgt. Det blev vist at et seks ångstrøm kobberlag fordoblede signalet fra magnetiske kugler.

Efter optimeringsstudierne af PHEB sensorer, blev bio-detektion og bio-karakterisering baseret på magnetiske kugler udført. PHEB sensorer blev anvendt til at detektere magnetiske kugler bundet til sensoroverfladen ved hjælp af DNA-DNA binding. Ved gradvist at forøge temperaturen blev DNA smeltekurver målt på chip niveau, og betingelserne for differentiering af original og muteret DNA blev identificeret. Denne metode blev også forsøgt til at studere aptamer hybridisering til magnetiske kugler konjugeret med virus protein, en såkaldt kunstig magnetisk virus. To aptamerer fra litteraturen blev undersøgt, men ingen af dem viste nogen signifikant hybridisering til kunstige virus.

Til sidste præsterer del IV en grundig teoretisk analyse af, hvordan man måler en overflade dækning af magnetiske kugler, der er stokastisk bundet til sensorens overflade og omgivelser. Feltet fra magnetiske kugler, magnetiseret af et eksternt felt, varierer med positionen og skifter endda fortegn. Det er udledt, at sensor signalet normalt vil være domineret af magnetiske kugler uden for sensoroverfladen, da disse er i en lavere højde i forhold til sensorens plan, og at magnetiske kugler på sensoroverladen formindsker dette signal. Efter at have afklaret oprindelsen af signal fra magnetiske kugler, beskrives en generel metode for beregning af det forventede kugle felt og dets konfigurationelle fluktuation. Denne metode bruges til analyse af tre state-of-the-art sensorer fra litteraturen, og to af dem viser sig at være begrænset af disse statistiske fluktuationer.

Preface

This dissertation is written in order to partially fulfill the requirements for obtaining the PhD degree at the Technical University of Denmark (DTU). The work, on which this thesis is based, has been performed at the Department of Micro- and Nanotechnology (DTU Nanotech) in the period from August 2012 to August 2015. The work has been supervised by associate professors Mikkel F. Hansen and Noemi Rozlosnik.

This project was financed by the Department of Micro- and Nanotechnology. I would like to use this opportunity to thank DTU Nanotech for the financial support.

I am especially grateful for the help provided by Giovanni Rizzi and Solène Cherré, who on multiple occasions sat aside their time to help and teach me. Further, the members of the Magnetic Systems group at DTU Nanotech provided many fruitful discussions, ideas on how to advance the project and a good atmosphere at work. Similarly, all members of the PolyMeDiag group at DTU Nanotech at one point helped me when working with viruses and bacteria. I would like to thank Lars E. Larsen and Charlotte K. Hjulsager, both from DTU Vet, for providing and preparing inactivated virus. I thank Henrik Flyvbjerg, Mikkel W. H. Ley and Shan X. Wang for their timely collaboration on the published papers.

Finally, I would like to thank my two supervisors, Noemi Rozlosnik and Mikkel F. Hansen, for their guidance, collaboration and outstanding availability throughout the years.

Anders Dahl Henriksen
Department of Micro- and Nanotechnology
Technical University of Denmark
August 15th, 2015

Contents

1 Introduction & motivation **3**
1.1 Magnetic beads in molecular diagnostics . . . 3
1.2 Magnetic bead detection . . . 4
1.3 Magnetic bead transportation . . . 8
1.4 Motivation and outline . . . 10

I Magnetophoresis **13**

2 Magnetophoresis theory **15**
2.1 Forces on magnetic beads . . . 15
2.2 Magnetic bead motion in a stripe geometry . . . 16
2.3 Geometrical considerations . . . 20

3 Magnetophoresis setup **23**
3.1 Magnetic beads . . . 23
3.2 Fabricated chips . . . 23
3.3 Experimental setup . . . 25
3.4 Beads sticking to the surface . . . 27
3.5 LabView files used . . . 27

4 Magnetophoresis video analysis **29**
4.1 Example of bead actuation data . . . 29
4.2 Bead identification . . . 30
4.3 Velocity determination . . . 30
4.4 Data fitting . . . 31

5 Magnetophoresis results **33**
5.1 Results . . . 33
5.2 Discussion . . . 35
5.3 Conclusion . . . 37

II Planar Hall effect sensors for magnetic bead biodetection **39**

6 Theory **41**
6.1 Anisotropic magnetoresistance . . . 41
6.2 Planar Hall effect bridge sensors . . . 41
6.3 Energies of thin film magnetic materials . . . 43
6.4 External field response . . . 44
6.5 Magnetic field detection . . . 46

6.6 Magnetic bead detection . . . 46
6.7 Summary . . . 49

7 Sensor optimization for bead detection **51**
7.1 Sensor construction elements . . . 51
7.2 Dynamic bead response . . . 52
7.3 New sensor designs . . . 53
7.4 Lock-in measurements . . . 54
7.5 Experimental setup for test of new designs . . . 54
7.6 Results . . . 55
7.7 Conclusion . . . 57

8 Experimental sensor setup **59**
8.1 Sensor geometries . . . 59
8.2 Sensor fabrication . . . 59
8.3 Measurement setup . . . 62
8.4 Lock-in amplification . . . 64
8.5 Measurement procedures . . . 65
8.6 LabView files used . . . 67

9 Sensor heating for bead detection using the sensor self-field **69**
9.1 Theoretical sensor heating . . . 69
9.2 Thermal COMSOL model . . . 70
9.3 Experiments . . . 71
9.4 Results . . . 71
9.5 Discussion . . . 73
9.6 Conclusion . . . 75

10 Comparison of ring and diamond shaped sensor geometries **77**
10.1 Theory . . . 77
10.2 Experiments . . . 78
10.3 Results . . . 78
10.4 Discussion . . . 81
10.5 Conclusion . . . 81

11 Multilayer sensors for magnetic bead detection **83**
11.1 Theory . . . 83
11.2 Experiments . . . 83
11.3 Results . . . 84
11.4 Discussion . . . 86
11.5 Conclusion . . . 87

III Magnetic bead-based characterizations of DNA binding **89**

12 Magnetic bead-based measurements of DNA melting curves **91**
12.1 Theory . . . 91
12.2 Experiments . . . 91
12.3 Results . . . 93
12.4 Conclusion . . . 95

13 Magnetic bead-based characterization of aptamer binding **97**
13.1 Aptamer properties . . . 97
13.2 Experiments . . . 99

13.3 Results . . . 100
13.4 Discussion . . . 102
13.5 Conclusion . . . 105

IV The statistics of measuring a bead surface coverage 107

14 Expected signal and its statistical fluctuation for bead measurements 109
14.1 Theory . . . 109
14.2 The importance of height variations . . . 112
14.3 Configurational statics of magnetic beads . . . 115
14.4 Case studies . . . 116
14.5 Conclusion . . . 119
14.6 Perspective for self-field detection . . . 119

15 Conclusion and outlook 121
15.1 Conclusion . . . 121
15.2 Outlook . . . 122

V Appendix 125

A The magnetic field from periodic and infinite stripe array 127
A.1 Introduction . . . 127
A.2 Derivation approach . . . 127
A.3 General considerations . . . 127
A.4 Geometrical considerations . . . 127
A.5 Conformal mapping . . . 129
A.6 Integration . . . 131
A.7 Formula summary . . . 132

B Stripe system fabrication process flow 133

C Sensor fabrication process flow 137

Bibliography 141

Paper I 149

Paper II 173

Paper III 183

Paper IV 191

Paper V 195

Paper VI 205

Paper VII 217

Paper VIII 225

Paper IX 237

List of Figures

1.1 A magnetic bead, illustration, SEM and hysteresis curve . . . 5
1.2 Four magnetoresistive sensors from the literature . . . 7
1.3 Illustration of the simplest magnetic bead separation . . . 8
1.4 Four magnetic separation techniques from the literature . . . 9

2.1 Illustration of the stripe geometry . . . 17
2.2 Plots of $H_{s,x}, H_{s,z}$ and U_m . . . 17
2.3 Picture series of moving magnetic field maximum and beads . . . 18
2.4 Simulations of the possible bead behaviors . . . 20
2.5 Magnetophoresis phase diagram as function of bead height . . . 21
2.6 Plots of $H_{s,x}, H_{s,z}$ and U_m for different width but same spacing . . . 22
2.7 Driving frequencies and bead velocity as a function of the stripe geometry. . . . 22

3.1 Illustration of a magnetophoresis chip. . . . 24
3.2 VSM data for magnetophoresis stack. . . . 25
3.3 Stripe fabrication process flow . . . 25
3.4 Overview of the magnetophoresis setup . . . 26
3.5 Picture of the magnetophoresis fluid system . . . 26
3.6 Percentage of moving beads over time. . . . 27

4.1 A picture of the video analyzing program . . . 29
4.2 A frame from an analyzed movie. . . . 30
4.3 The decision tree for determining bead velocity . . . 31
4.4 A standard frequency sweep and binomial fit . . . 32

5.1 Frequency sweeps for three similar chips . . . 34
5.2 Magnetophoresis velocities for different geometries . . . 34
5.3 Contour plot of the maximum bead velocity as a function of stripe period and bead height 36
5.4 The optimal and practical stripe period, and the highest bead velocity as a function of bead size. . . . 37
5.5 Picture of beads lining up to reduce drag . . . 37

6.1 Illustration of a magnetoresistive slab of permalloy. . . . 42
6.2 Illustration of a Wheatstone bridge PHEB sensor. . . . 42
6.3 Illustration of a chip hysteresis curve. . . . 44
6.4 Calculated sensor output vs. H_{ext} . . . 45
6.5 The effect of shape anisotropy on the sensor output . . . 47
6.6 Illustration of magnetic bead detection . . . 47
6.7 The sensor volume sensitivity when using the self-field. . . . 48

7.1 Dynamic bead response, χ' and χ'' vs. frequency . . . 53
7.2 Illustrations of the PHEB, dPHEB and pPHEB sensor designs . . . 53

7.3 External field response from the three sensor types. . . . 56
7.4 Magnetic bead response from the three sensor types. . . . 57

8.1 Illustrations of PHEB chips and sensors. . . . 60
8.2 PHEB Sensor fabrication process flow 60
8.3 Schematic representation of the binding chemistry 62
8.4 Overview of the PHEB sensor setup 62
8.5 Pictures of the temperature controlled chip well 63
8.6 Picture of the microfluidic system and PCB 63
8.7 Picture of the Helmholtz coils setup 64
8.8 Illustration of a VSM chip and data 66
8.9 Illustration of a transmission line chip and data 66
8.10 Sensor field sweep and fit 67
8.11 Sensor response to a suspension of magnetic beads 68

9.1 2D COMSOL model of a cross-section of a sensor arm 71
9.2 Change in sensor bridge resistance versus temperature 72
9.3 The sensor temperature increase versus (a) bias current or (b) calculated power 72
9.4 (a) Maximum allowed current for $\Delta T = 1°\mathrm{C}$ and $\Delta T = 5°\mathrm{C}$. (b) The measured and calculated effective heat conductances 73
9.5 The sensor temperature increase for a chip on a Pyrex wafer 74
9.6 The heat networks for a dry and wet system 74

10.1 Illustration of diamond and ring PHEB sensors. . . . 78
10.2 Field sweeps for the four sensor designs and for 6 selected magnetic stacks. . . . 79
10.3 Resistance (top) and sensitivity (bottom) ratios vs. the relative shape anisotropy. . . . 81
10.4 Spatial distributions of the sensor sensitivity and demagnetizing field 82

11.1 VSM measured exchange field for varying permalloy and copper thicknesses. . . . 84
11.2 Signals from a homogeneous bead suspension vs. copper thickness. . . . 85
11.3 Bead signal for current, voltage and power driven sensors. . . . 85
11.4 The low-field normalized sensitivities. . . . 86
11.5 B_{sh} and $B_{\mathrm{sh}}/(B_{\mathrm{ex}} + B_{\mathrm{K}})$ for trilayer sensors. . . . 87

12.1 (a) Illustration of the dPHEB sensor and (b) spotted probes pattern. . . . 92
12.2 Bead hybridization signal for four differently functionalized sensors 93
12.3 Sensor signal during the up and down temperature ramps. . . . 94
12.4 Relative Signal used for measuring DNA melting curves. . . . 95

13.1 Illustration of the aptamer idea. . . . 98
13.2 Example of single stranded DNA folding into a 3D shape. . . . 98
13.3 Hybridization signal between A22 and beads coated with its complementary DNA. . . . 101
13.4 Sandwich assay signal between A22 and inactivated virus. . . . 101
13.5 Hybridization signal between A22 and beads coated with H1N1 protein. . . . 102
13.6 Hybridization signal between RHA0006 and beads coated with H5N1 protein. . . . 103
13.7 AFM signals of artificial virus hybridization to four probes. . . . 104

14.1 Illustration of a single sensor and a sensor array. . . . 110
14.2 Sensor signal as a function ot the bead position. . . . 111
14.3 Sensor signal and fluctuation vs. the biological area. . . . 113
14.4 Sensor signal calculated from plates with different thicknesses. . . . 114
14.5 $\langle \tilde{H}_y \rangle$ for (a) a SpBL and for (b) both a SpBL and a SeBL. . . . 115
14.6 Optimal sensor width vs. the bead height 116
14.7 Normalized signal and surface coverage vs. bead size 117

14.8 Three sensors from the literature 117
14.9 Sensor signal vs. bead position when beads are magnetized by the sensor self-field. 120
14.10 ϕ_{stat} and corresponding number of beads on a PHEB sensor as a function of R, h. 120

A.1 The model used for the theoretical derivation of the stripe field 128
A.2 Illustration of the periodic geometry with surface currents 128
A.3 The single stripe domain with governing Laplace's equation. 129
A.4 The mapping function and resulting upper-half plane domain. 130

List of Tables

5.1 Fitted parameters for the magnetophoresis reliability study 33

7.1 The change in resistance based on the resistor orientation for both the external and the self-field 51
7.2 1^{st} and 2^{nd} harmonic in-phase and out-of-phase signals for the three sensors designs 55

10.1 Extracted parameters for ring and diamond field sweep data 80

14.1 Geometrical parameters for the sensors in Fig. 14.8 118
14.2 Statistical sensor characteristics for the sensors in Fig. 14.8 119

List of symbols

Symbol	Description	Unit
$\mathbf{A}$	Magnetic vector potential	m T
A_y	Magnetic vector potential y-component	m T
A_{stripe}	Magnetic vector potential for Ω	m T
A	Magnetic vector potential for Ω_{ss}	m T
$\tilde{A}$	Magnetic vector potential for Ω_{uh}	m T
A	Sensor area	m^2
A_{BAA}	Biological active area	m^2
A_{bead}	Bead hybridization area estimated from literature	m^2
$\mathbf{B}$	Magnetic field	T
B_{y}	Magnetic field y-component	T
$\mathbf{B}_{\mathrm{ext}}$	External magnetic field	T
B_{ext}	External magnetic field strength	T
$B_{\mathrm{ext},x}$	External magnetic field x-component	T
$B_{\mathrm{ext},z}$	External magnetic field z-component	T
B_{ex}	Exchange field	T
$B_{\mathrm{ex}}^{30\mathrm{nm}}$	Exchange field for stack with $t_{\mathrm{FM}} = 30$ nm, $t_{\mathrm{Cu}} = 0$	T
B_{K}	Anisotropy field	T
B_{sh}	Shape anisotropy field	T
$B_{\mathrm{ex}}^{\mathrm{D}}$, $B_{\mathrm{K}}^{\mathrm{D}}$, $B_{\mathrm{sh}}^{\mathrm{D}}$	Fitted fields for a diamond sensor	T
$\mathbf{B}_{\mathrm{s}}$	Stripe magnetic field	T
B_{s}	Stripe magnetic field strength	T
$B_{\mathrm{s},x}$	Stripe magnetic field x-component	T
$B_{\mathrm{s},z}$	Stripe magnetic field z-component	T
c	Molar concentration	M
DR	Dynamic range in detectable surface coverage	
$\hat{\mathbf{e}}_i$	Unit vector for i-axis	
$E[f]$	Expectation value of f	$[f]$
f	Frequency	s^{-1}
f_{B}	Brownian relaxation frequency	s^{-1}
f_{c}	Critical frequency	s^{-1}
f_{D}	Wall correction factor	
$f_{V=1}$	Fastest phase-locked frequency	s^{-1}
f_σ	standard deviation of the fastest frequencies	s^{-1}
$f(\nu)$	Conformal mapping function	
$f(B_{\mathrm{sh}})$	Sensitivity correction factor for shape anisotropy	
$\mathbf{F}_{\mathrm{m}}$	Magnetic force	N

Symbol	Description	Unit
$\mathbf{F}_\mathrm{d}$	Hydrodynamic drag force	N
G	Total sensor sensitivity	V m A^{-1}
G_eff	Effective heat conductance	W K^{-1}
$G_{\mathrm{SiO_2}}$	Heat conductance of Silicon dioxide layer	W K^{-1}
$G_{\mathrm{Si+SiO_2}}$	Heat conductance of Silicon dioxide layer and wafer	W K^{-1}
$G_\mathrm{eff}^\mathrm{Pyrex,dry}$,$G_\mathrm{eff}^\mathrm{Pyrex,wet}$	Heat conductance of a pyrex wafer setup with and without water in channel	W K^{-1}
h	Bead spacer layer height	m
h_SeBL, h_SpBL	spacer layer on sensor and space outside the sensor	m
$\mathbf{H}$	Auxiliary field	A m^{-1}
H_y	Auxiliary field y-component	A m^{-1}
$\mathbf{H}_\mathrm{De}$	Demagnetization field	A m^{-1}
$\mathbf{H}_0$	Auxiliary field in the absence of the particle	A m^{-1}
$\mathbf{H}_\mathrm{ext}$	External auxiliary field	A m^{-1}
$\hat{\mathbf{H}}_\mathrm{ext}$	Direction of external auxiliary field	
$H_{\mathrm{ext},x}$	External auxiliary field x-component	A m^{-1}
$H_{\mathrm{ext},z}$	External auxiliary field z-component	A m^{-1}
H_ex	Exchange auxiliary field	A m^{-1}
H_K	Anisotropy auxiliary field	A m^{-1}
H_sh	Shape anisotropy auxiliary field	A m^{-1}
H_hom	Homogeneous auxiliary field	A m^{-1}
H_sf	Self-field	A m^{-1}
$H_\mathrm{sf}^\mathrm{stack}$	Self-field from current shunting in stack	A m^{-1}
$H_\mathrm{sf}^\mathrm{beads}$	Self-field from beads	A m^{-1}
$\mathbf{H}_\mathrm{s}$	Stripe auxiliary field	A m^{-1}
$H_{\mathrm{s},x}$	Stripe auxiliary field x-component	A m^{-1}
$H_{\mathrm{s},z}$	Stripe auxiliary field z-component	A m^{-1}
$H_{y,1}$	Field from a single bead	A m^{-1}
$\langle H_y \rangle$	Average field in sensor	A m^{-1}
$\langle H_{y,1} \rangle$	Average field in sensor from 1 bead	A m^{-1}
$\langle \tilde{H}_y \rangle$	$\langle H_y \rangle / M$	A m^{-1}
I	Current	A
I_x	Bias current	A
$I_{x,\mathrm{AC}}$	AC current amplitude	A
$I_{\Delta T}$	Bias current for ΔT heating	A
i	Imaginary unit	
$\mathbf{J}$	Current density	A m^{-2}
K	Anisotropy energy constant	A^2 m^{-2}
$\mathbf{K}$	Bound surface current	A m^{-1}
k_B	Boltzmann constant	J K^{-1}
l	Length	m
m	Magnetic moment	A m^2
M	Magnetization strength	A m^{-1}
$\mathbf{M}$	Magnetization	A m^{-1}
$\mathbf{M}_i$	Magnetization i-component	A m^{-1}
$\hat{\mathbf{M}}$	Direction of magnetization	
M_s	Saturation magnetization	A m^{-1}

Symbol	Description	Unit
$\hat{\mathbf{n}}$	Normal vector	
n	Normal coordinate	m
N	Number of segments for meandering resistor	
$\underline{\underline{N}}$	Demagnetization tensor	
N_i	i-component of diagonal $\underline{\underline{N}}$	
$N(X, Z, X_0, Z_0)$	Neumann function	
$N_{\mathrm{V}<\frac{1}{2}}$	Number of beads with $V < \frac{1}{2}$	
$N_{\mathrm{V}\geq\frac{1}{2}}$	Number of beads with $V \geq \frac{1}{2}$	
P_0	Percentage of moving beads	%
P	Power	W
$P_{\mathrm{heating}}^{\mathrm{DC}}$	Joule heating from DC bias	W
$P_{\mathrm{dissipation}}$	Dissipating heat flow	W
$P_{\mathrm{V}\geq\frac{1}{2}}$	Percentage of beads with $V \geq \frac{1}{2}$	%
$\mathcal{P}_{V=1}$	Probability of bead being phase-locked	
Q	Heat source	W m^{-3}
r	Bead radius	m
r_{AMR}	AMR-ratio	
$\mathbf{r}$	Position vector	m
$\mathbf{r}_0$	Bead position vector	m
R	Resistance	Ω
R_i	Resistance of resistor i	Ω
R_0	Total bridge resistance	Ω
R_{s}	Sheet resistance	Ω
ΔR	Change in resistance	Ω
ΔR_{pp}	Peak-to-peak change in resistance	Ω
$\Delta R_{\mathrm{pp}}^{\mathrm{D}}$,$\Delta R_{\mathrm{pp}}^{\mathrm{R}}$	Peak-to-peak change in resistance for a diamond or ring sensor	Ω
R	Bead radius	m
$\mathcal{R}$	Thermal resistance	K W^{-1}
$\mathcal{R}_{\mathrm{coating}}$	Thermal resistance of Ormocomp coating	K W^{-1}
$\mathcal{R}_{\mathrm{Si}}$	Thermal resistance of wafer	K W^{-1}
$\mathcal{R}_{\mathrm{SiO_2}}$	Thermal resistance of silicon dioxide layer	K W^{-1}
$\mathcal{R}_{\mathrm{top}}$	Thermal resistance of wet fluidsystem	K W^{-1}
s	Stripe spacing	m
$\tilde{s}$	s/λ	
S_0	Low-field sensitivity	V A^{-1} T^{-1}
S_0^{D}, S_0^{R}	Low-field sensitivity for a ring or diamond sensor	V A^{-1} T^{-1}
$\tilde{S}_0$	Low-field sensitivity, when voltage driven	T^{-1}
S_1	Expected field from a bead in the BAA	A m^{-1}
S_N	Expected field from N beads in the BAA	A m^{-1}
S_ϕ	Expected field from surface coverage, ϕ of beads in the BAA	A m^{-1}
$S_{\phi_{\max}}$	Expected field from a bead monolayer	A m^{-1}
SDR	Signal-to-standard deviation ratio	
$SDR_{\phi_{\max}}$	Signal-to-standard deviation ratio from a bead monolayer	

Symbol	Description	Unit
t	Magnetic stack or plate thickness	m
$\tilde{t}$	t/λ	
t_{FM}	Ferromagnetic thickness	m
t_{Cu}	Copper layer thickness	m
$t_{\mathrm{SiO_2}}$	Silicon dioxide thickness	m
t_{wafer}	Wafer thickness	m
t	Time	s
T	Temperature	°C
ΔT	Temperature increase	°C
T_m	Melting temperature	°C
$\mathcal{T}$	Periodic time for ϕ	s
$\tilde{u}$	Normalized energy of the ferromagnetic layer	A/m
$\tilde{u}_{\pm}$	Normalized energy of resistors with $\alpha = \pm\frac{\pi}{4}$	A/m
$\tilde{u}_{\mathrm{sh}}$	Normalized shape anisotropy energy	A/m
U	Energy of the ferromagnetic layer	J
U_{ex}	Unidirectional exchange energy	J
U_{K}	Uniaxial anisotropy energy	J
U_{m}	Magnetic potential energy	J
U_{sh}	Shape anisotropy energy	J
U_{Z}	Zeeman energy	J
$\mathbf{v}$	Bead velocity	m s^{-1}
v_x	Bead velocity x-component	m s^{-1}
$\langle v \rangle$	Average bead velocity	m s^{-1}
V	Normalized average bead velocity	
V_x	Bias voltage	V
$V_{x,\mathrm{RMS}}$	RMS bias voltage amplitude	V
V_y	Bridge output voltage	V
V_y^D, V_y^R	Diamond or ring sensor output voltage	V
V_{pp}	Peak-to-peak amplitude of bridge output voltage	V
V_{n}'	In-phase n^{th} harmonic signal	V
V_{n}''	Out-of-phase n^{th} harmonic signal	V
V_{off}	First harmonic bridge offset	V
V_{PHEB}, V_{pPHEB}, V_{dPHEB}	Output from PHEB, pPHEB or dPHEB sensor	V
ΔV	Signal variation	V
V_{E}	Electrical potential	V
$V_{\mathrm{ref,in-phase}}$	Lock-in in-phase reference signals	V
$V_{\mathrm{ref,out-of-phase}}$	Lock-in out-of-phase reference signals	V
$V_{\mathrm{up}}, V_{\mathrm{down}}$	Output during up and down temperature sweep	V
$V_{\mathrm{down}}^{\mathrm{approx}}$	second order polynomial approximation of V_{down}	V
$V_{\mathrm{init}}^{\mathrm{ref}}$,$V_{\mathrm{up}}^{\mathrm{ref}}$	Output during initial or up temperature sweep for the positive reference sensor	V
ΔV_{ref}	$V_{\mathrm{up}}^{\mathrm{ref}} - V_{\mathrm{init}}^{\mathrm{ref}}$	V
V_{noise}	Sensor noise level	V
$\mathcal{V}$	Volume	m^3
$\mathcal{V}_{\mathrm{FM}}$	Volume of ferromagnetic layer	m^3

Symbol	Description	Unit
$\mathcal{V}_\mathrm{h}$	Hydrodynamic volume	m^3
w	Stripe width	m
$\tilde{w}$	w/λ	
$\tilde{w}_\mathrm{opt}$	Optimal width for highest signal	
w_BAA	Biological active are width	m
x, y, z	Position coordinates	m
x_0, y_0, z_0	Bead position coordinates	m
$x_\mathrm{s}, y_\mathrm{s}, z_\mathrm{s}$	Coordinates for slab geometry	m
X, Z, X_0, Z_0	Mapped position coordinates	
$\hat{\mathbf{x}}, \hat{\mathbf{y}}, \hat{\mathbf{z}}$	Coordinate unit vectors	
$\tilde{y}_0, \tilde{z}_0$	$2y/w, 2z/w$	
z	bead height	m
$\tilde{x}$, $\tilde{y}$, $\tilde{z}$	x/λ, y/λ, z/λ	
z_w	Wall distance	m
z_SeBL, z_SpBL	Height between sensor plane and beads on the sensor and on the space outside the sensor	m
$\tilde{z}_\mathrm{SeBL}$, $\tilde{z}_\mathrm{SpBL}$	z_SeBL/λ, z_SpBL/λ	
$\Delta\tilde{z}$	$\tilde{z}_\mathrm{SpBL} - \tilde{z}_\mathrm{SeBL}$	
$\tilde{z}_0$	$(\tilde{z}_\mathrm{SpBL} + \tilde{z}_\mathrm{SeBL})/2$	
α	Bridge arm angle	rad
α	Temperature coefficient	K^{-1}
β	Bead field proportionality to homogeneous field	
$\tilde{\beta}$	β/χ_0	
$\tilde{\beta}_\mathrm{top}$,$\tilde{\beta}_\mathrm{bottom}$	$\tilde{\beta}$ for top or bottom part of dPHEB sensor	
$\Delta\tilde{\beta}$	$\tilde{\beta}_\mathrm{top} - \tilde{\beta}_\mathrm{bottom}$	
Γ	Ω_up boundary	
γ_0	Proportionality between stack self-field and bias	$\mathrm{A\ m}^{-2}$
γ_1	Proportionality between bead self-field and bias	$\mathrm{A\ m}^{-2}$
$\gamma_{1,\mathrm{top}}$,$\gamma_{1,\mathrm{bottom}}$	γ_1 for top or bottom part of dPHEB sensor	$\mathrm{A\ m}^{-2}$
$\Delta\gamma_1$	$\gamma_{1,\mathrm{top}} - \gamma_{1,\mathrm{bottom}}$	$\mathrm{A\ m}^{-2}$
$\Delta\gamma_1^\mathrm{ref}$	$\Delta\gamma_1$ for the positive reference sensor	$\mathrm{A\ m}^{-2}$
$\tilde{\gamma}_1$	γ_1/χ	$\mathrm{A\ m}^{-2}$
$\tilde{\gamma}_{1,\mathrm{top}}$,$\tilde{\gamma}_{1,\mathrm{bottom}}$	$\tilde{\gamma}_1$ for top or bottom part of dPHEB sensor	$\mathrm{A\ m}^{-2}$
$\Delta\tilde{\gamma}_1$	$\tilde{\gamma}_{1,\mathrm{top}} - \tilde{\gamma}_{1,\mathrm{bottom}}$	$\mathrm{A\ m}^{-2}$
$\delta(x)$	Dirac delta function	
ϵ_0	Permittivity of free space	$\mathrm{F\ m}^{-1}$
η	Viscosity	Pa s
θ	Angle of magnetization	rad
$\theta_\pm$	Angle of magnetization for resistors with $\alpha = \pm\frac{\pi}{4}$	rad
$\theta_\mathrm{H}(x)$	Heaviside step function	
κ_Si	Heat conductivity of silicon	$\mathrm{W\ m}^{-1}\mathrm{K}^{-1}$
$\kappa_{\mathrm{SiO_2}}$	Heat conductivity of silicon dioxide	$\mathrm{W\ m}^{-1}\mathrm{K}^{-1}$
λ	Stripe period	m

Symbol	Description	Unit
λ_{optimal}	Optimal stripe period	m
$\lambda_{\text{practical}}$	Implemented stripe period	m
λ	decay length	m
μ_0	Permeability of vacuum	T m A^{-1}
ν	Complex space variable	
ξ	Magnetophoretic mobility	$m^2Pa^{-1}s^{-1}$
$\xi_{\text{M}-270}$	Magnetophoretic mobility of M-270 beads	$m^2Pa^{-1}s^{-1}$
ρ	Resistivity	Ωm
$\rho_{\parallel}$	Resistivity at parallel current density and magnetization	Ωm
$\rho_{\perp}$	Resistivity at orthogonal current density and magnetization	Ωm
$\Delta\rho$	$\rho_{\parallel} - \rho_{\perp}$	Ωm
σ_{ex}	Interfacial energy per area	J m^{-2}
σ_1	Standard deviation of the field from a bead in the BAA	A m^{-1}
σ_N	Standard deviation of the field from N beads in the BAA	A m^{-1}
σ_ϕ	Standard deviation of the field from surface coverage, ϕ of beads in the BAA	A m^{-1}
$\sigma_{\phi_{\max}}$	Standard deviation of the field from a bead monolayer	A m^{-1}
ϕ	Surface coverage of magnetic beads	
ϕ_1	Surface coverage of a single bead	
$\phi_{\max}$	Surface coverage from a monolayer of magnetic beads	
ϕ_{stat}	Surface coverage for $SDR = 1$	
ϕ_{noise}	Surface coverage for a bead signal equal to the sensor noise	
ϕ_{res}	The surface coverage resolution	
ϕ	Harmonic argument: $x/\lambda - tf$	
φ	phase lag of magnetic susceptibility	rad
φ	Auxiliary angle	rad
χ	Volumetric magnetic susceptibility	
χ'	In-phase component of complex magnetic susceptibility	
χ''	Out-of-phase component of complex magnetic susceptibility	
χ_0	DC magnetic susceptibility	
χ_∞	High frequency magnetic susceptibility	
Ω	Periodic domain	
Ω_{ss}	Simple stripe domain	
Ω_{uh}	Upper half-plane domain	
$\Re$	Real part	
$\Im$	Imaginary part	

List of Abbreviations

Abbreviation	Description
A22	Aptamer against H1N1 surface protein [1]
AC	Alternating (current)
AFM	Atomic force microscopy
AMR	Anisotropic magnetoresistance
APTS	3-Aminopropyltriethoxysilane
BAA	Biological active area
BC	Boundary condition
BSA	Bovine serum albumin albumin
DC	Direct (current)
DNA	Deoxyribonucleic acid
dPHEB	Differential planar Hall effect bridge
ELISA	Enzyme-linked immunosorbent assay
GMR	Giant magneto resistance
MR	Magnetoresistive
MT	Mutant type
NTA	Nitrilotriacetic acid
PBS	Phosphate buffer saline
PCB	Printed circuit board
PDMS	Polydimethylsiloxane
PHE	Planar Hall effect
PHEB	Planar Hall effect bridge
PID	Proportional-integral-derivative
PMMA	Polymethylmethacrylate
POC	Point-of-care
pPHEB	Parallel planar Hall effect bridge
RHA0006	Aptamer against H5N1 surface protein [2]
RT	Room temperature
SB	Selection buffer (50 mM Tris-HCl, pH 7.4, 100 mM NaCl, 5 mM KCl, 1 mM $MgCl_2$)
SeBL	Sensor bead layer
SELEX	Systematic evolution of ligands by exponential enrichment
SEM	Scanning electron microscope
SNP	Single-nucleotide polymorphism
SpBL	Space bead layer
SSC	Saline-sodium citrate
SV	Spin valve
UV	Ultraviolet
VSM	Vibrating sample magnetometer
WT	Wild type

List of Papers

Paper I
A. D. Henriksen, N. Rozlosnik and M. F. Hansen
Geometrical optimization of microstripe arrays for microbead magnetophoresis
Biomicrofluidics (submitted for 2^{nd} review. 1^{st} review suggested acceptance with minor corrections, October 2015)

Paper II
F. W. Østerberg, G. Rizzi, A. D. Henriksen and M. F. Hansen
Planar Hall effect bridge geometries optimized for magnetic bead detection
Journal of Applied Physics **115**, 184505 (2014)

Paper III
A. D. Henriksen, G. Rizzi, F. W. Østerberg and M. F. Hansen
Optimization of magnetoresistive sensor current for on-chip magnetic bead detection using the sensor self-field
Journal of Magnetism and Magnetic Materials **380**, 209−214 (2015)

Paper IV
F. W. Østerberg, A. D. Henriksen, G. Rizzi and M. F. Hansen
Comment on "Planar Hall resistance ring sensor based on NiFe/Cu/IrMn trilayer structure"
Journal of Applied Physics **114**, 106101 (2013)

Paper V
A. D. Henriksen, G. Rizzi and M. F. Hansen
Experimental comparison of ring and diamond shaped planar Hall effect bridge magnetic field sensors
Journal of Applied Physics **118**, 103901 (2015).

Paper VI
A. D. Henriksen, G. Rizzi and M. F. Hansen
Investigation of NiFe/Cu/IrMn trilayer planar Hall effect bridge sensors for magnetic bead detection using the sensor self-field
Journal of Applied Physics (submitted for 1^{st} review, October 2015)

Paper VII
G. Rizzi, F. W. Østerberg, A. D. Henriksen, M. Dufva and M. F. Hansen
On-chip magnetic bead-based DNA melting curve analysis using a magnetoresistive sensor
Journal of Magnetism and Magnetic Materials **380**, 215−220 (2015)

Paper VIII
A. D. Henriksen, S. X. Wang and M. F. Hansen
On the importance of sensor height variation for detection of magnetic labels by magnetoresistive sensors

Scientific Reports **5**, 12282 (2015)

Paper IX
A. D. Henriksen, M. W. H. Ley, H. Flyvbjerg and M. F. Hansen
Configurational statistics of magnetic bead detection with magnetoresistive sensors
PLoS ONE (accepted, October 2015)

1

Introduction & motivation

1.1 Magnetic beads in molecular diagnostics

Development of inexpensive, easy-to-use and compact diagnostic tools will lead to a paradigm shift, with many more diagnoses being performed either by the patient or at the doctor's office, instead of having to send a sample to a central laboratory. Every disease that can be diagnosed closer to the patient and more easily is a step towards personalized medicine. Further, this will improve disease monitoring and earlier detection, which is often crucial for the efficacy of the applied treatment. Point-of-care (POC) devices exemplify the potential of this paradigm shift, with the pregnancy test lateral flow assay [3] and blood glucose meter [4] being the biggest commercial successes. So far, the commercial POC devices have all been single purpose but much research have gone into making an affordable and portable sensor platform that could easily be customized by the user for the required biological assay. Magnetic beads can be used for both target extraction and detection, and are already an important part of molecular diagnostics and could be part of the next generation of diagnostic tools [5] or POC devices [6].

Today magnetic beads are extensively used in magnetic resonance imaging (MRI) to enhance the contrast [7]; in drug delivery, where an external magnet can stop the circulation and localize the drug; in hyperthermia treatments, where an alternating magnetic field can locally heat the magnetic beads [7], and in magnetic labeling and separation, which are the topics of this thesis. The scientific literature contains many articles on magnetic beads and their potential in molecular diagnostics. Excellent reviews of these have been written by Gijs [8], Llandro *et al.* [9] and Mornet *et al.* [10].

1.1.1 Magnetic bead properties

All the mentioned applications of magnetic beads take advantage of the fact that about all biological material is weakly magnetic. For detection, this means zero magnetic background, an advantage compared to the autofluorescence background when detection fluorophores. Similarly, in separation, drug-delivery and hypothermia this allow for spatial manipulation of beads without disturbing or heating the biological material. Further, a suspension of magnetic beads can be dispersed for low diffusion time to the target and then easily collected by a magnet or by centrifugation. Likewise, magnetic beads have high surface area to increase capture efficiency, they are flexible with many sizes and coatings and are commercially available. Moreover, they are stable in biological buffers and in most pH, which are useful properties in POC devices or microsystems [8].

Figure 1.1I shows an illustration of a typical magnetic bead, it consists of multiple iron-oxide cores in a polymer matrix coated with streptavidin, to which biotinylated antibodies against a certain antigen, are coupled. Some of the important bead properties are:

Size. Magnetic beads span a variety of sizes with the smallest being 10 nm and the largest being 100 µm. Figure 1.1II,III show images of 100 nm and 2.8 micron magnetic beads, respectively. Usually, when the magnetic beads are smaller than 50 nm they consist of a single crystal coated by a biochemical active layer, this is called single core magnetic beads. Beads bigger than 50 nm are multi-core where multiple magnetic crystals are bound together in a matrix.

Magnetic cores. The magnetic cores are typically iron oxides like magnetite Fe_3O_4 and maghemite γ-Fe_2O_3 but ferrites, like $CoFe_2O_4$, $MnFe_2O_4$, are also common [11]. Superparamagnetic beads are the most common type, and in this case the magnetic cores are so small that, without an external magnetic field, their magnetic moments fluctuate randomly due to thermal forces, and the beads have no net magnetization. However, in a magnetic field some of the cores align their magnetization to the external field, creating a finite magnetization, as if paramagnetic. This response is stronger and thus termed superparamagnetic [8]. This superparamagnetic response can be measured by hysteresis curves. Hysteresis curves measure the magnetization as a function of the external field to determine the bead properties. Figure 1.1IV shows an example of a hysteresis loop measured on 2.8 µm beads, note that the magnetization is linearly dependent on the external field, when below 10 mT, and with no magnetic remanence or hysteresis, which are all characteristics of superparamagnetic beads.

Biological Matrix. The biological matrix surrounds the magnetic cores. The most common biological matrices are starch or dextran, which serve to make the bead biocompatible, prevent agglomeration and oxidation and decrease hydrophobicity [12].

Functionalization. The biological matrix also allows for easy coating of the beads. Many bead coatings are commercially available including, but not limited to, plain, streptavidin, carboxylic acid, amine, polyethylene glycol (PEG) and nitrilotriacetic acid (NTA). From these coatings, the beads can then be biologically functionalized with either DNA, antibodies, aptamers etc., the wide size range allows magnetic beads to bind to a variety of targets, e.g. proteins, virus and cells [12].

1.2 Magnetic bead detection

Detection of magnetic beads has great potential to improve the resolution of sandwich assay molecular diagnostics, which can lead to earlier detection, e.g. of cancer biomarkers and thus higher survival rates [16]. In the scientific literature many schemes for detection of magnetic beads have been proposed, Tamaha *et al.* [17] and Issadore *et al.* [18] have written great reviews here-of. Today, magnetic bead detection is usually done by either inductive sensors [19, 20], by nuclear magnetic resonance sensors [21, 22, 23] or by magnetoresistive sensors, which is the most popular method.

When using a magnetoresistive sensor, the magnetic beads usually hybridize to the sensor surface, e.g. using a protein sandwich assay or similar biological interactions. The magnetic beads are then magnetized by an excitation field, and the magnetic bead field then perturbs the magnetic field experienced by the magnetoresisitve sensor. By knowing the signal from the excitation field, or using a reference sensor, the bead signal can be calculated, which corresponds to a certain amount of biological target. These magnetoresistive sensors are usually less than a millimeter squared, and can thus be easily integrated in a POC system. Megens *et al.* [24], Freitas *et al.* [25] and Wang *et al.* [26] have all written great reviews on magnetoresistive sensors.

1.2.1 Sensor types

Research in magnetoresistive sensors originated from hard disk drive read heads and have yielded many different sensor technologies. However, today in biodetection the most used sensor types are based on the giant magnetoresistance (GMR) or the anisotropic magnetoresistive (AMR) effects.

AMR sensors usually consist of magnetic Nickel-Iron thin film. The electrical resistance of Nickel-Iron changes with the angle of magnetization. The magnetization is contained to the thin-film plane and usually an anti-ferromagnetic material creates an artificial field, which the magnetization aligns along. However, if an magnetic field is applied in-plane but orthogonal to the anti-ferromagnetic field, the magnetization rotates, which changes the Nickel-Iron resistance. This is discussed in detail

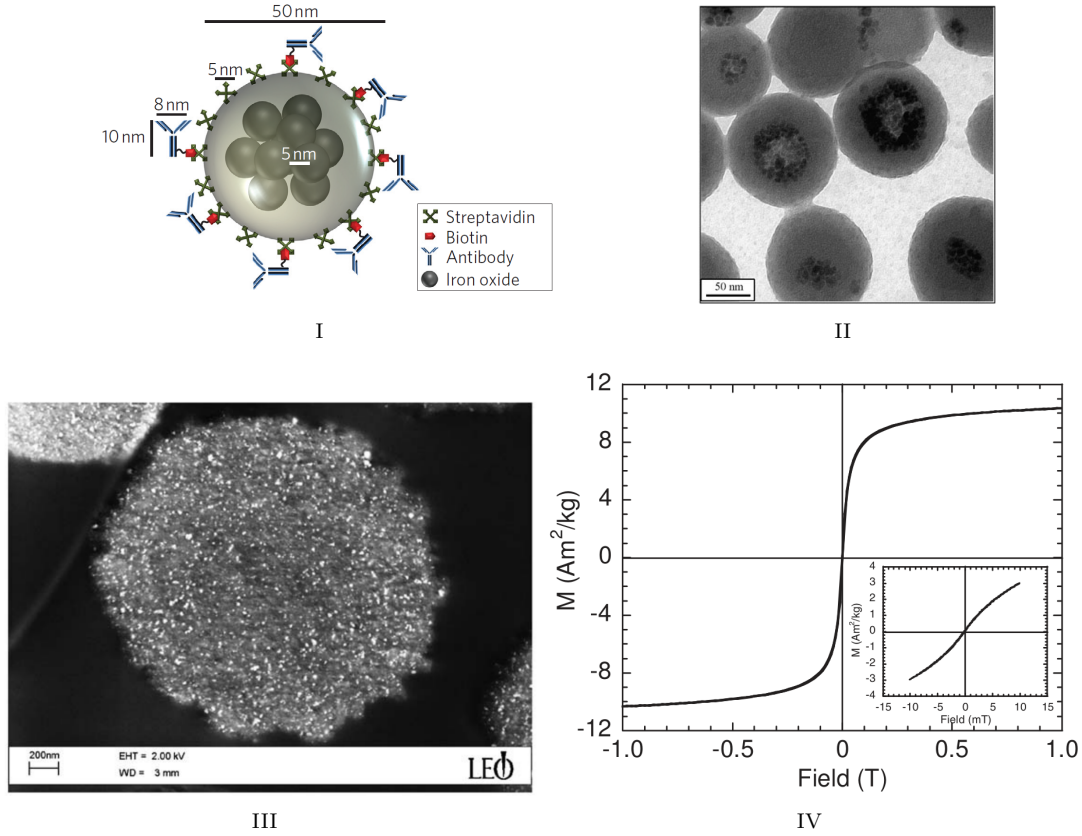

Figure 1.1: I: Illustration of protein-coated magnetic bead. II: TEM (transmission emission microscope) picture of 100 nm beads. III and IV: SEM (scanning electron microscope) and hysteresis curve of Dynabeads® M-280 streptavidin beads, respectively. Figure I is from Gaster *et al.* [13], II: Landfester *et al.* [14] and III and IV: Fonnum *et al.* [15].

in Chapter 6, but in general AMR sensors can be designed to give a response, V_y, proportional to the in-plane orthogonal component of the magnetic field H_y:

$$V_y = I_x S_0 H_y \tag{1.1}$$

where I_x is the sensor current and S_0 is the sensitivity. The development of AMR sensors have been advanced by the research groups of CheolGi [27, 28, 29, 30, 31, 32, 33, 34, 35, 36] and Hansen [37, 38, 39, 40, 41], where this thesis work has been carried out in the latter.

GMR sensors consist of two ferromagnetic materials separated by a non-magnetic metal layer. Due to electron spin scattering, the resistance of this stack changes according to the magnetizations of the ferromagnetic layers: parallel magnetizations give low resistance and antiparallel gives high resistance. For bead detection, GMR is mostly used in a spin-valve (SV) geometry with one layer having a fixed magnetization locked by an antiferromagnetic layer, and the other ferromagnetic layer being free to rotate. Just like the AMR sensor, the SV sensor is made sensitive to one component of the magnetic field and can also be described by Eq. (1.1). The recent development of GMR sensors for biodetection have been driven forward by the research groups of Wang [13, 42, 43, 44], Freitas [45, 46, 47, 48, 49] and Jian-Ping Wang[50, 51, 52], among others. Examples, of sensor designs by four of these major research groups, CheolGi, Hansen, Freitas and Wang are given in Section 1.2.4.

1.2.2 Magnetic Excitation field

As superparamagnetic beads are used for most biodetection experiments, a magnetic field is needed to magnetize the beads as these would otherwise be non-magnetic. This required excitation field can be in the following form

External homogeneous field is the most common excitation field and is usually provided by external electromagnets [6].

Sensor self-field is the excitation field used in this thesis. Here the magnetic beads are magnetized by the self-field from the bias current powering the sensor [41, 53], thus avoiding the need for external electro-magnets.

Field from chip current lines is similar to the sensor self-field, but instead of using the bias current, the sensor chip has thicker wires that can carry a bigger current, and which are only there to produce a magnetic excitation field [54, 55].

1.2.3 Biodetection scheme

Magnetic beads are mostly used in a sandwich assay where their presence, after washing, corresponds to the target being captured. However, in recent years the interest in measurements on beads in suspension has grown. In general, the biodetection scheme can be categorized as either surface or volume based.

Surface-based measurements are the most common bead bioassay technique. Here magnetic beads bind to the sensor surface in a sandwich assay, where the target first binds to a biological probe, tethered to the sensor surface, and then the magnetic beads binds to the target. Or similarly, the magnetic beads are first coated with the target and then bind to the tethered biological probe. This is the same principle as enzyme-linked immunosorbent assay (ELISA) but with a magnetic bead as the label instead of an enzyme. An illustration of this scheme can be seen in Fig. 1.2I,d-h.

Volume-based measurements usually measure the changes in the hydrodynamic volume of magnetic beads when binding to a target molecule, and possibly also clustering. Magnetic beads in a fluid will rotate to align their magnetization to an external magnetic field. For a rotating external magnetic field, there exist a maximum frequency where the bead can follow the rotation of the external field. This critical frequency is called the Brownian relaxation frequency and is limited by the bead drag force. Thus by measured the change in the Brownian relaxation frequency of the magnetic beads, their hydrodynamic volume can be determined, which is an indicator of whether they have bounded to the target in the suspension. Measurements like these are often termed lab on a bead. An illustration of the change in relaxation frequency can be seen in Fig. 1.2III,c.

1.2.4 Magnetoresistive bead detection examples

Below is given four examples of magnetic bead detection, all four magnetoresistive sensors can be seen in Fig. 1.2.

SV by Wang group. Figure 1.2I shows the state-of-the-art magnetoresistive GMR sensor developed by the Wang group [56]. The sensor in Fig. 1.2I is a spin valve (SV) sensor and the beads are magnetized by a homogeneous external field. Fig. 1.2I,a shows a micrograph of the chip with 64 multiplexed SV sensors. Each SV sensor is a meandering resistor of 32 stripes taking up an area of 100 μm × 100 μm. Fig. 1.2I,c shows a SEM picture zoomed in on the sensor stripe with visible magnetic beads. Fig. 1.2I,d-h illustrate the bead based sandwich assay scheme for protein detection. Gaster *et al.* [56] used the sensor to detect the cancer marker carcinoembryonic antigen (CEA), and were able to detect concentration of 5 fM with a dynamic range of 6 orders of magnitude. The measurement were demonstrated in both phosphate buffered saline (PBS), in 0.1% bovine serum albumin (BSA) and directly in mouse serum. These are the most promising results in magnetic biosensing.

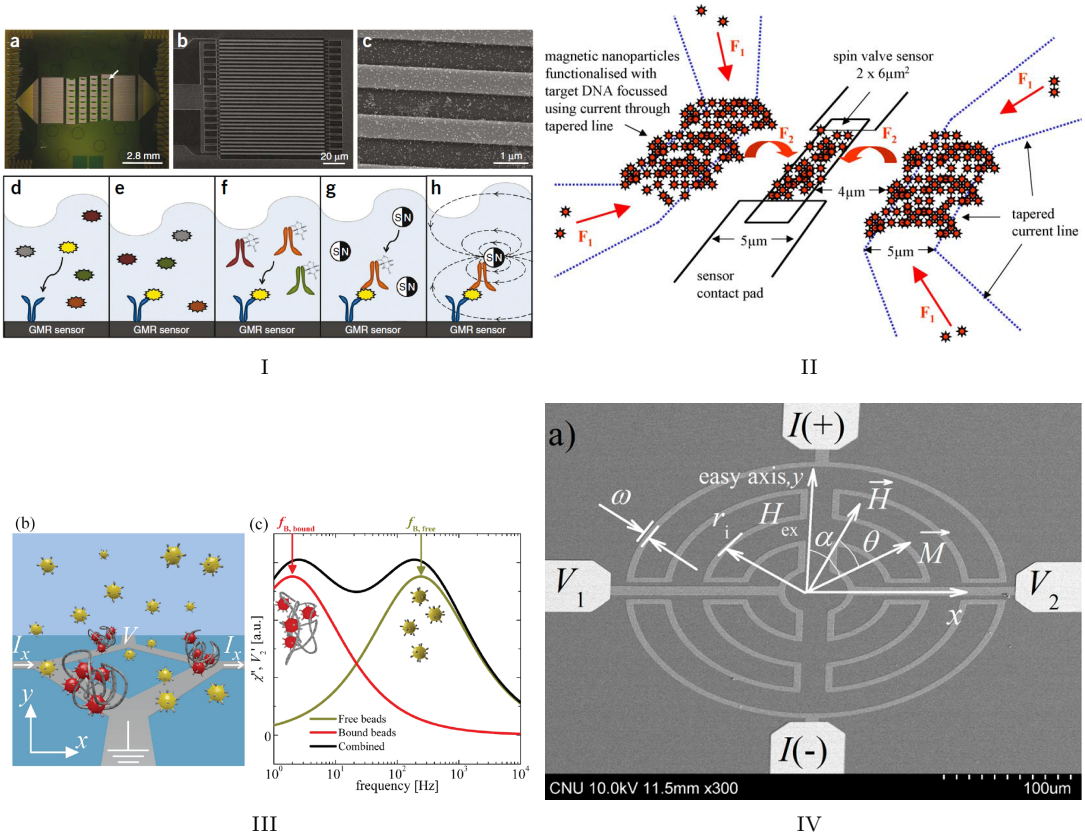

Figure 1.2: Four magnetoresistive sensors from the literature. Figure I, II, III, and IV are from Gaster *et al.* [56], Graham *et al.* [45], Østerberg *et al.* [41] and Hung *et al.* [36], respectively.

SV by Freitas group. Figure 1.2II shows a micro-sized magnetoresistive sensor developed by the Freitas group [45]. Like the Wang group, the sensor illustrated in Fig. 1.2II is a SV sensor and the beads are magnetized by a homogeneous external field. However, the sensor by Gaster *et al.* [56] had an area of 100 µm × 100 µm, while the sensor by Graham *et al.* [45] is only 2 µm × 6 µm. To decrease diffusion times, the sensor was surrounded by current lines that could attract the in-suspension magnetic beads and focus them closer to the sensor surface. The sensor was used to detect magnetic beads coated with DNA, which hybridized to complementary surface-bound DNA probes. Graham *et al.* [45] were able to measure DNA concentrations of 10 pM to 200 pM, which were calculated to be 50 to 100 sensor-bound magnetic beads. Further, Graham *et al.* hypothesized that single bead detection is within reach. This is further discussed in Chapter 14.

AMR sensor by Hansen group. Figure 1.2III shows a planar Hall effect bridge sensor based on the AMR and developed by the Hansen group [41]. The sensor uses a Wheatstone bridge geometry of area 200 µm × 200 µm and the beads are magnetized by the magnetic field from the current powering the sensor. Further, the sensors by Østerberg *et al.* [41] were used for volume-based measurements, where DNA coils, formed by rolling circle amplification, hybridized with magnetic beads functionalized with the DNA complementary to the amplified pattern. Depending on the amount of starting biological material, varying amounts of DNA coils were made and varying amounts of beads were trapped in the coils. The magnetic beads captured by the DNA coils (colored red in Fig. 1.2III) had a larger hydrodynamic volume, i.e., a lower Brownian relaxation frequency, cf. Fig. 1.2III,c. By measuring the shift from high to low Brownian relaxation frequency, Østerberg *et al.* [41] were able to perform on-chip detection of the two pathogens Bacillus globigii

and Vibrio cholerae, with limits of detection down to 500 Bacillus globigii spores and 2 pM of Vibrio cholerae, which are comparable to results obtained in a macro-scale AC susceptometer.

AMR sensor by CheolGi group. Figure 1.2IV shows a meandering ring planar Hall effect bridge sensor developed by the CheolGi group [36]. The sensor is approximately the same size as that used by Østerberg *et al.* [41]. The beads are magnetized by a homogeneous external field and the sensor is optimized to detect the lowest possible magnetic moment from a 1 µL droplet placed on top on its surface. This sensor, by Hung *et al.* [36], is able to detect 10^7-fold dilution of the stock concentration of fluidMAG-streptavidin nanoparticles, i.e. ≈ 1800, magnetic beads with a diameter of 100 nm. This detection of a magnetic moment of $4 \cdot 10^{-13}$ emu is below the detection limit of Superconducting Quantum Interference Device (SQUID) systems, which are the gold standard.

1.3 Magnetic bead transportation

Transportation of magnetic beads has a crucial role in lab-on-a-chip manipulation or diagnostics, as it is useful for sample enrichment/clean-up, and separation [57]. Classical separation techniques like liquid chromatography, electrophoresis [58] or centrifugation [59] are widely used. However, to achieve higher selectivity the target can be labeled and then sorted. These labeling separation techniques allow for separation of rare cells like circulating tumor cells [60, 61]. Magnetic separation utilizes that biological material is not affected by a magnetic field. Further, magnetic beads have stable magnetic properties and are not affected by standard buffers and not subject to photo-bleaching effects. Last, the magnetic field is not screened by aqueous solutions. While all magnetic separation techniques utilize these properties, the exact bead separation can be done in many ways. Section 1.3.1 describes some of these techniques.

1.3.1 Magnetic separation techniques

When using magnetic separation, the biological sample is mixed with a suspension of magnetic beads. The biological target is here captured on the functionalized magnetic beads using biological specific bindings (cf. Section 1.1.1). The magnetic beads and the bound target then needs to be extracted from the complex suspensions. This can be done either by diverging the path of magnetic beads in a liquid flow [62, 63, 64] or by completely trapping the magnetic beads [54, 65, 66]. Figure 1.3 shows the simplest possible extraction technique of using a magnet on the beaker/tube side to temporary traps the magnetic beads, while Fig. 1.4 shows more advanced techniques with increasing complexity and higher throughput potential.

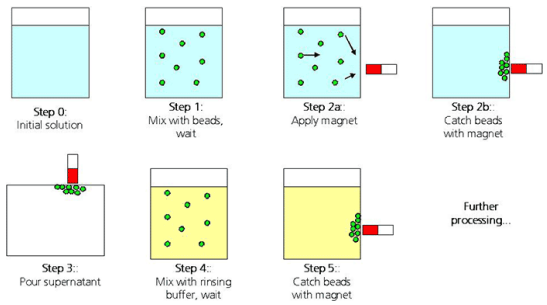

Figure 1.3: Illustration of the standardized and simplest magnetic bead separation.

Magnetic Capture. As the magnetic force scales with bead volume, the simple magnet-on-tube separation of Fig. 1.3 has a lower bead-diameter limit of $100 \sim 250$ nm. For smaller beads, the thermal/diffusion force keeps the bead in the suspension. To increase the magnetic force and bead trapping efficiency, a magnetic separation column can be used. Figure 1.4I illustrates a magnetic separation column where a ferromagnetic and porus steel-mesh is magnetized by permanent magnets to generate

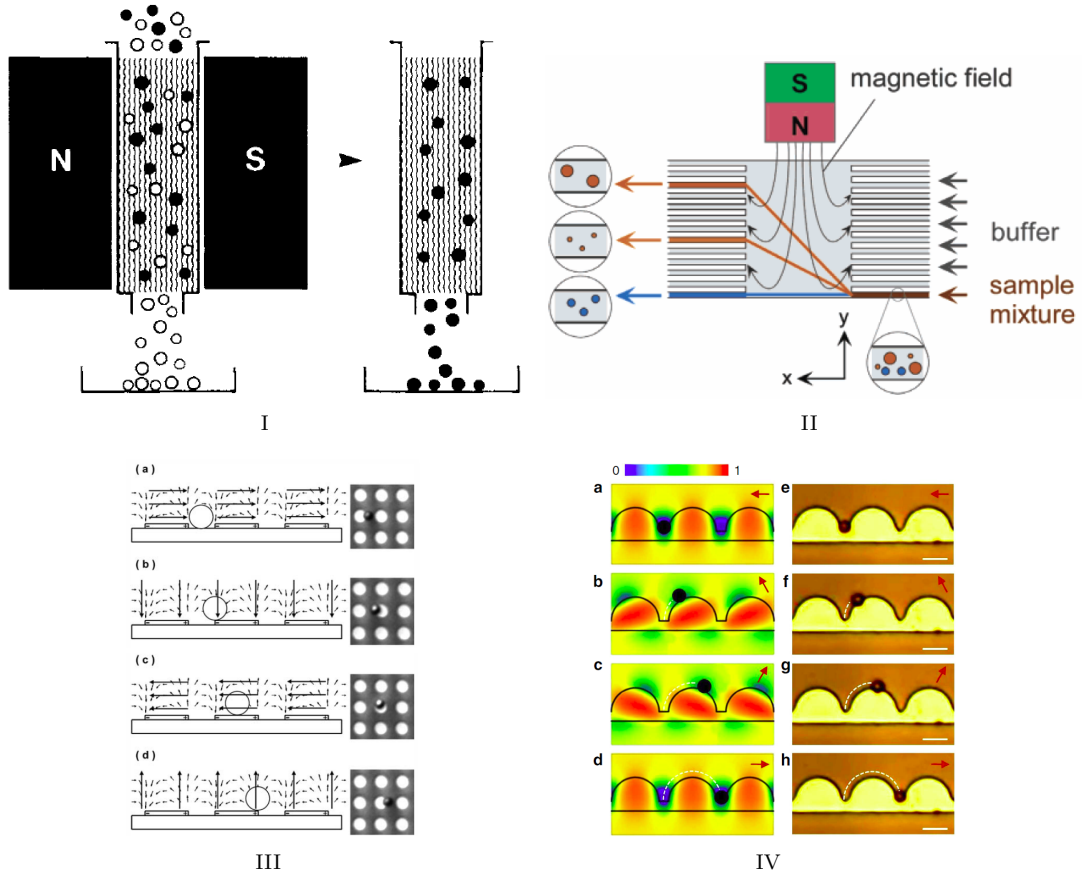

Figure 1.4: Four magnetic separation techniques from the literature. I: Trapping the magnetic beads in a magnetized steel mesh. II: Diverging the flow of magnetic beads. III and IV: Using hard and soft magnetic materials along with an external field to move the beads. Figure I, II, III and IV are from Miltenyi *et al.* [65], Pamme *et al.* [64], Gao *et al.* [67] and Lim *et al.* [68], respectively.

higher magnetic gradient and thus a higher bead trapping force. A similar technique, of using micro-sized stripes of magnetic material (e.g. nickel) has been used for on-chip trapping of magnetic beads from a flow, when an external magnet is adjacent to the magnetic material [69]. The group of Soh [70, 71, 72] has published excellent papers on this technique.

In-flow divergence. Instead of completely trapping the beads, it can be advantageous to divert the beads from one stream to another [62, 63, 64]. Utilizing predictable laminar flow and magnetic forces, this allows for single bead analysis, a concept similar to flow cytometry. Similarly, if more than one target need to be extracted from the biological sample, it is possible to use magnetic beads of different sizes and transporting them separately [64, 73]. Potentially one could separate beads bound to the biological target from both the sample and from unbound beads. Figure 1.4II illustrates how the combined fluid and magnetic force can be used to separate beads of different sizes. Using this technique Adams *et al.* [73] achieved 500 fold enrichment of two cells at 10^9 cells/hour by coupling to two differently sized magnetic beads.

Dynamic magnetic transportation using hard magnets. Instead of using magnetic forces to separate the magnetic beads from the rest of a mobile fluid flow, magnetic forces can also be used for actuating the magnetic beads from the stationary fluid. Similarly to Fig. 1.4II, this allows selective separation, but with the potential for a much higher separation resolution, and with no lower limit of the

usable bead concentration. In these techniques, a flow is often not required but instead a varying external magnetic field is needed, usually provided by two sets of electromagnets. The group of Yellen [67, 74, 75, 76] has pioneered this field of magnetophoresis, using the principle in Fig. 1.4III, where magnetic beads are transported above periodic patches of similar sized magnetic material by rotating an external field. This method has the advantageous of both a high magnetic gradient (i.e. magnetic force) for fast bead movement and a low minimum bead size. The technique enables selective separation based on the magnetic or drag properties, e.g. bead size, target binding. In this technique, a hard magnetic material is used which keeps its magnetization direction independently of the applied magnetic field.

Dynamic magnetic transportation using soft magnets. This technique uses a soft magnetic material where the magnetization changes with the applied magnetic field. An example used for bead transportation is seen in Fig. 1.4IV. Here the magnetization of the material, and thus the point of maximum field strength, rotates with an external magnetic field, thereby dragging the bead along the structure. This technique [68, 77] is well suited for very low amount of beads, where precise control is needed. A variation of this is to use a magnetic material with multiple magnetic domains and then move the domain wall, where the beads are placed, by using an external field [78, 79].

1.4 Motivation and outline

1.4.1 Earlier work

This thesis is split into four parts. I: Magnetophoresis; II: Planar Hall effect sensors for magnetic bead biodetection; III: Magnetic bead-based characterizations of DNA binding; and IV: The statistics of measuring a bead surface coverage.

Part I Magnetophoresis was inspired by the work of Yellen *et al.* [74, 75] and Soh *et al.* [70, 71, 72, 80, 81] who both constructed state-of-the-art magnetophoresis systems for magnetic bead separation. Yellen focused on the fundamental understanding while Soh focused on their applications for diagnostics. Further, Part I builds on the master thesis of Henriksen [82], which describes the magnetophoresis properties of stripe systems.

Part II Planar Hall effect sensors for magnetic bead biodetection builds on the earlier work concerning planar Hall effect sensors in the Magnetic Systems group [37, 38, 40, 83], and especially on the recent work of Rizzi [84, 85] and Østerberg [41, 86, 87], who worked with surface based and volume based bead detection, respectively. Further, Rizzi and Østerberg collaborated on much of the sensor work in this thesis and have co-authorship on multiple papers.

Part III Magnetic bead-based characterizations of DNA binding was also inspired by the work of Rizzi [53, 84] describing how planar Hall effect sensors could be used for DNA detection. Further, Gold *et al.* [5] inspired the use of DNA methods for measuring proteins and pathogens through aptamers [88, 89, 90]. The choice of aptamers was based on articles by Shiratori *et al.* [2], Sung *et al.* [1] and Kiilerich-Pedersen [91].

Part IV The statistics of measuring a bead surface coverage was inspired by the work of Damsgaard *et al.* [92] who first showed that a monolayer of beads gives zero magnetic field. This was contrary to the working results by research groups lead by Freitas [45, 48] and Wang [13, 56], who both have a working sensor platform but with varying dynamic ranges.

1.4.2 Motivation

This thesis has three aims:

Aim 1 A general goal of improving the fundamental understanding of how to best use magnetic beads for labeling and detection.

Aim 2 A practical goal of optimizing the existing sensor system, and investigating its fundamental properties, to improve its application as a bead-based biodetection system and test its limitations.

Aim 3 A forward-looking goal of adapting the system to biodetection of proteins and pathogens using aptamers in combination with magnetic beads, for a new level of bio applications and possibilities.

1.4.3 Outline

The thesis is split into four main parts each with its own chapters, below these chapters and parts are described.

Part I, Magnetophoresis investigates magnetophoresis for manipulation of magnetic beads as part of *Aim 1*. Part I contains chapter 2-5.

Chapter 2 describes the magnetophoresis theory. The two main forces, the magnetic force and fluid drag force, acting on magnetic beads are described. It is discussed how a periodic geometry of magnetic stripes along with an external magnetic field gives rise to a constant magnetic force. Further, it is discussed how to optimize the stripe geometry.

Chapter 3 describes the home-built setup used for magnetophoresis measurements. The setup consists of a simple fluid system, two sets of Helmholtz coils and a microscope with attached camera for video capturing. The chapter further goes into the magnetophoresis chip fabrication along with the magnetic beads used.

Chapter 4 describes the analysis procedure for the captured magnetophoresis videos. This chapter describes both the video analysis, i.e. how the beads are identified, how their velocities are determined, and the data analysis of the measured bead velocities.

Chapter 5 describes the result of Paper I. This chapter contains the experimental results from measuring magnetophoresis, and the influence of the geometry of the magnetic stripe, along with a discussion of how to optimize the stripe geometry.

Part II, Planar Hall effect sensors for magnetic bead biodetection investigates planar Hall effect sensors for detecting magnetic beads for later use in biodetection. This is part of *Aim 1* & *2*, and Part II contains chapter 6-11.

Chapter 6 describes the theory of planar Hall effect (PHE) sensors. PHE sensors are based on a magnetic stack, with the main part being a thin film layer of permalloy, which shows the anisotropic magnetoresistance. This chapter describes how the magnetic stack works and how the magnetic field dependent stack resistance can be used for detection of either an external magnetic or magnetic beads.

Chapter 7 describes the result of Paper II. This chapter goes into three different sensor designs (PHEB, pPHEB, dPHEB) and how each is best suited for a particular application. With the PHEB as the do-it-all, the pPHEB being only sensitive to the bead field, and the dPHEB being able to do differential measurements.

Chapter 8 describes the experimental setup used for PHE measurements. This chapter goes into the fabricated PHE sensor chips and the surrounding setup including the fluid system, temperature control, and lock-in amplifiers. Further, the procedures for both sensor characterization and bead measurements are described.

Chapter 9 describes the result of Paper III. This chapter describes a general applicable procedure for both theoretically estimating and practically measuring the thermal properties of the sensor chip and setup.

Chapter 10 describes the result of Paper IV and V. This chapter goes into a detailed experimental comparison of bridge and ring shaped PHEB sensors, as both has been argued to be the superior design in the literature.

Chapter 11 describes the result of Paper VI. This chapter investigates if the magnetic stack can be optimized by including an intermediate copper layer between the ferromagnetic and antiferromagnetic layer.

Part III, Magnetic bead-based characterizations of DNA binding uses the bead detection through planar Hall effect sensors for characterizing biodetection through both DNA and aptamers. This is part of *Aim 3* and Part III contains chapter 12-13.

Chapter 12 describes the result of Paper VII. This chapter describes how DNA melting curves were measured on a dPHEB chip by ramping the temperature up and down, and how everything but the biological temperature dependence can be corrected for.

Chapter 13 describes biodetection using aptamers in place of DNA. This opens the potential for studying the aptamer binding to protein and virus, among other, but preliminary testing was unsuccessful.

Part IV, The statistics of measuring a bead surface coverage investigates why randomly placed bead gives a non-zero sensor signal and how to calculate it. This is part of *Aim 1* and Part IV contains chapter 14.

Chapter 14 describes the result of Paper VIII and IX. This chapter states the fundamental problem that the bead signal vary and changes sign with bead position. The chapter goes through how to calculate the bead signal and determine if its fluctuation, due to the stochastic bead hybridization process, is important. It is found that having a height difference between the bead on top of the sensor and outside is the most important parameter for a high signal, Further, having a large sensor area reduces the statistical fluctuations. This knowledge is used to analyze cases from the literature.

Part I

Magnetophoresis

2

Magnetophoresis theory

This chapter explains the theory to understand translational bead forces and movements for use in magnetophoresis. The used magnetophoresis system consists of stripes of a hard magnetic material. Superparamagnetic beads are naturally attracted to the edges of the stripes, as these are the points of highest magnetic field strength. By applying a rotating external field, the point of maximum field strength can be moved across the stripe geometry, and the beads can be transported from one edge to the next, thus moving the beads one period of the geometry per rotation of the external field.

While the field of magnetophoresis is too big to cover thoroughly, the key concepts of forces on magnetic beads, phase-locked motion and the effect of the stripe geometry, and how to achieve bead separation is explained. For a more detailed analysis confer to Henriksen [82].

2.1 Forces on magnetic beads

In Section 2.1 the magnetic forces relevant for magnetic separation and magnetophoresis is defined. For micron sized beads, gravitational forces will quickly pull the beads to the chip surface where transportation happens, and where the gravitational force is assumed to be outbalanced by the surface normal force. When the gravitational force is outbalanced, the magnetophoresis bead movement is dominated by two forces, the magnetic force and the hydrodynamic drag force.

2.1.1 Superparamagnetism

For the magnetophoretic experiments, Dynabeads® M-270 micron sized magnetic beads (Life Technologies, CA, USA) were used for easy optical detection and quantification. The Dynabeads® M-270 are physically similar to the M-280 but with a carboxylic acid coating instead of streptavidin. As seen in Fig. 1.1 the beads are superparamagnetic and their magnetization $\mathbf{M}$ is proportional to the experienced magnetic field $\mathbf{H}$ as

$$\mathbf{M} = \chi \mathbf{H} \tag{2.1}$$

where χ is the volume magnetic susceptibility. This proportionality is true when the external field is below 10 mT as seen in Fig. 1.1.

2.1.2 Magnetic force

The magnetic force ($\mathbf{F}_\mathrm{m}$) on a magnetized body is given by [93]

$$\mathbf{F}_\mathrm{m} = \int_{\mathcal{V}} \mu_0 (\mathbf{M} \cdot \nabla) \mathbf{H}_0 \, \mathrm{d}^3\mathbf{r} \tag{2.2}$$

where $\mathcal{V}$ is the volume of the body, μ_0 is the permeability of free space, $\mathbf{M}$ is the magnetization and $\mathbf{H}_0$ is the auxiliary field in the absence of the body. When the integrand is nearly constant over the volume of the body, the force can be simplified to

$$\mathbf{F}_\mathrm{m} \simeq \mu_0 \mathcal{V} \chi (\mathbf{H}_0 \cdot \nabla) \mathbf{H}_0 = \frac{\mathcal{V} \mu_0 \chi}{2} \nabla (\mathbf{H}_0^2) \tag{2.3}$$

where a non-magnetic medium (e.g. water) has been assumed. Instead of the magnetic force, it can be easier to visualize the corresponding energy landscape. The magnetic force, Eq. (2.3), can be converted to the magnetic potential energy of the bead

$$U_{\mathrm{m}} = \frac{-\mathcal{V}\mu_0\chi}{2}\mathbf{H}_0^2. \tag{2.4}$$

For higher values of the magnetic field strength, the potential energy is lower, and thus a magnetic bead is attracted to the point of maximum field strength.

2.1.3 Hydrodynamic drag

A colloidal particle moving relative to the carrier liquid is subject to a drag force $\mathbf{F}_{\mathrm{d}}$. In the low Reynold regime, found in lab-on-a-chip systems, this drag force is very well approximated by the Strokes drag given by [94]

$$\mathbf{F}_{\mathrm{d}} = -6\pi\eta r\mathbf{v}f_{\mathrm{D}} \tag{2.5}$$

where η is the liquid viscosity, r is the particle radius, $\mathbf{v}$ is the particle velocity relative to the liquid and $1 \leq f_{\mathrm{D}} \leq \frac{256}{83}$ is a correction coefficient if the particle is in the vicinity of a wall, given by [8, 95]

$$f_{\mathrm{D}} = \left(1 - \frac{9}{16}\left(\frac{r}{r+z_{\mathrm{w}}}\right) + \frac{1}{8}\left(\frac{r}{r+z_{\mathrm{w}}}\right)^3 - \frac{45}{256}\left(\frac{r}{r+z_{\mathrm{w}}}\right)^4 - \frac{1}{16}\left(\frac{r}{r+z_{\mathrm{w}}}\right)^5\right)^{-1} \tag{2.6}$$

where z_{w} is the distance for particle-perimeter to the wall.

In the micro-regime, the inertia of the particle is often negligible [75] and the bead velocity in a static liquid is thus given by

$$\mathbf{v} = \frac{\mu_0\chi r^2}{9\eta f_{\mathrm{D}}}\nabla(\mathbf{H}_0^2) = \mu_0\xi\nabla(\mathbf{H}_0^2) \tag{2.7}$$

where ξ in Eq. (2.7) is the magnetophoretic mobility defined by

$$\xi \equiv \frac{\chi r^2}{9\eta f_{\mathrm{D}}}. \tag{2.8}$$

The magnetophoretic mobility describes how fast the magnetically actuated bead moves through the liquid in response to a magnetic field gradient. For magnetic separation, bead can be separated based on their difference in magnetophoretic mobilities.

2.2 Magnetic bead motion in a stripe geometry

Section 2.2 explains how the spatially varying magnetic field from an array of stripe magnetic material, combined with an external rotating field, can be used for bead actuation. The rotational frequency of the external field determines the kind of motion the magnetic bead undergoes. For low frequencies, the bead is phase-locked, moving one geometrical period per rotation. For higher frequencies, the average bead velocity becomes intermediate, and then stationary for even higher frequencies.

2.2.1 Stripe geometry

High-resolution magnetophoresis is best performed in a periodic geometry as this give rise to a periodic field, which can keep a strong magnetic gradient for infinite distances. A chip with periodic stripes of magnetic material generated the stripe field used in the experiments. An illustration of this periodic stripe system can be seen in Fig. 2.1. The periodic magnetic stacks are modeled as homogeneously magnetized stripes with magnetization $\mathbf{M} = M\hat{\mathbf{x}}$, width w, spacing s, period $\lambda = w+s$ and ferromagnetic thickness t_{FM}. Each stripe is infinite in the y-direction and the array is assumed to have an infinite amount of stripes. The resulting stripe field $\mathbf{H}_s$, is zero in the y-direction and periodic in the x-direction.

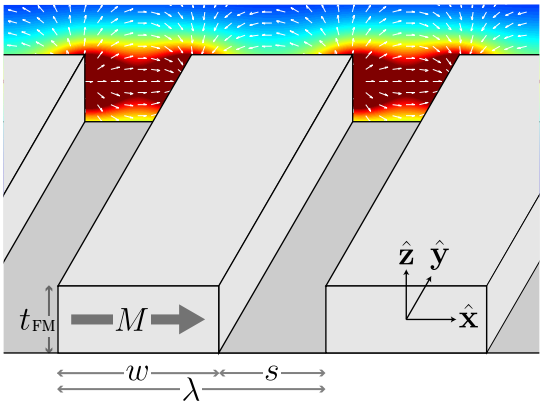

Figure 2.1: Illustration of the periodic stripe geometry, parameters and coordinate system. The background is an example of the calculated magnetic stripe field $\mathbf{H}_s$. Red colors indicate a high field magnitude. Figure is adapted from Paper I.

The coordinate origin is situated at the centroid of a stripe with the coordinate axis along the principal axes of the stripe.

The magnetic field from the stripe geometry can be found using the Ampère-Maxwell law for the magnetic potential, this is explained in Appendix A. The background of Fig. 2.1 shows an example of the stripe field. The stripe field resembles that from a bar magnet; the field points towards the poles (faces of the magnetic stack) and is stronger closer to the poles. Thus when no external field is present the magnetic beads are attracted to the poles. This is illustrated in Fig. 2.2 where the stripe field components $H_{\mathrm{s},x}, H_{\mathrm{s},z}$ are plotted along with the magnetic potential energy U_{m}.

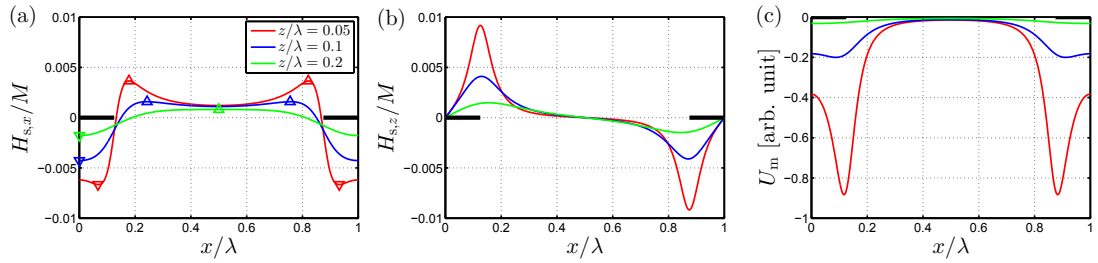

Figure 2.2: (a) x and (b) z component of the magnetic stripe field for different height to period ratios. (c) The magnetic potential energy for a stripe geometry like in Fig. 2.1. The black bars indicate the periodic magnetic stripes and the triangle indicate the field maxima for $|H_{\mathrm{s},x}|$. Used parameters: $w = 2.5$ µm, $s = 7.5$ µm, $t_{\mathrm{FM}}/\lambda = 0.003$. Figure is adapted from Paper I.

For beads high above the stripe-plane, the distances from the bead center to neighboring poles is of comparable length, and the field highly overlaps with significant contributions from many poles. This creates a weak but sinusoidal varying magnetic field with $H_{\mathrm{s},x}$ being strong between the poles and $H_{\mathrm{s},z}$ being strong above the poles. Conversely, when a bead is close to the stripe plane, the distance to one pole can be much smaller that the distance to the rest of the poles. In this case, the field experienced by the bead is stronger but very inhomogeneous, with rapidly changing fields close to the poles. These effects can be seen in Fig. 2.2 and give rise to $\mathbf{H}_{\mathrm{s}}$ having three distinct shapes (i.e. modes of $H_{\mathrm{s},x}$) depending on the bead height. This is important for optimization of the field sequence [82].

To move the magnetic beads from the poles, an external magnetic field can alter the energy landscape to shift the energy minima and field maxima to different parts of the chip. Generally, the potential energy decreases (increases) where the stripe field and external field are parallel (antiparallel). For

example, if the external field, H_{ext}, is oriented along the x-direction, the potential energy between the stripes decreases as the stripe field here is also along the x-direction. Figure 2.3 illustrates how this can be used to sweep the point of maximum field strength from the north pole to the chip middle, then to south pole and ending back at the north pole thus transporting the magnetic beads one stripe period.

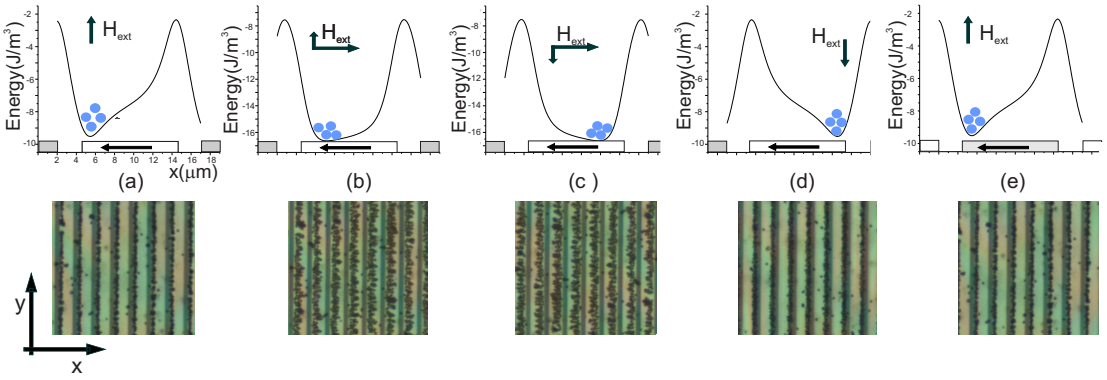

Figure 2.3: Illustrations and pictures of magnetic beads moving by applying a rotating sequence of external fields. Top row: The magnetic energy landscape for a sequence of four different external fields, note how the energy minimum gradually changes position. Bottom row: Picture series of magnetic beads moving across the chip with the changing external field. The figure is from [96].

2.2.2 Sinusoidal approximation

The superposition of the spatially varying stripe field and temporally varying external field creates a magnetic wave for bead propagation. Expanding Eq. (2.7) with these fields yields

$$v_x = \mu_0 \xi \frac{\partial}{\partial x}\Big((H_{\text{ext},x} + H_{\text{s},x})^2 + (H_{\text{ext},z} + H_{\text{s},z})^2 \Big). \tag{2.9}$$

For beads high above the stripe plane and for a symmetric geometry ($w = s$), the stripe field consists of contributions from many poles and is approximately sinusoidally varying. This is used as an illustrative case, as the bead motion can be analytically solved when

$$\begin{aligned} \mathbf{H}_{\text{s}} &= \left(-H_{\text{s}} \cos\left(2\pi x/\lambda\right), H_{\text{s}} \sin\left(2\pi x/\lambda\right)\right) \\ \mathbf{H}_{\text{ext}} &= \left(H_{\text{ext}} \cos\left(2\pi t f\right), -H_{\text{ext}} \sin\left(2\pi t f\right)\right) \end{aligned} \tag{2.10}$$

where t is the time, and f is the rotational frequency of the external field. Note, that the external field rotates counterclockwise for a positive velocity when $\mathbf{M} \propto \hat{\mathbf{x}}$. Inserting Eq. (2.10) in Eq. (2.9) yields

$$\begin{aligned} v_x &= \left(4\pi\mu_0 \xi H_{\text{s}} H_{\text{ext}}/\lambda\right)\left(\sin\left(2\pi x/\lambda\right)\cos\left(2\pi t f\right) - \cos\left(2\pi x/\lambda\right)\sin\left(2\pi t f\right)\right) \\ &= \left(4\pi\mu_0 \xi H_{\text{s}} H_{\text{ext}}/\lambda\right)\sin\left(2\pi\left(x/\lambda - t f\right)\right). \end{aligned} \tag{2.11}$$

Thus, the magnetic beads are propagated by a traveling magnetic wave. Eq. (2.11) can be simplified by using a variable substitution for the argument $\phi = (x/\lambda - tf)$, such that

$$\frac{\mathrm{d}\phi}{\mathrm{d}t} = v_x/\lambda - f = f_c \sin\left(2\pi\phi\right) - f, \tag{2.12}$$

where the critical frequency has been defined as

$$f_c = 4\pi\mu_0 \xi H_{\text{s}} H_{\text{ext}}/\lambda^2. \tag{2.13}$$

For $f \leq f_c$, Eq. (2.12) has the simple steady-state solution

$$\phi = \arcsin(f/f_c)/(2\pi) \Rightarrow v_x = \lambda f \tag{2.14}$$

However for $f > f_c$ Eq. (2.12) needs to be integrated, which gives

$$\phi(t) = \frac{1}{\pi} \arctan\left(\frac{f_c}{f} - \sqrt{1 - \frac{f_c^2}{f^2}} \tan\left(\pi t f \sqrt{1 - \frac{f_c^2}{f^2}}\right)\right). \tag{2.15}$$

Eq. (2.15) shows that $\phi(t)$ is decreasing and periodic in time with period $\mathcal{T} = (f^2 - f_c^2)^{-1/2}$.

From the above analysis, two different velocities regimes were found. When the frequency of the external field is less than the bead critical frequency, $f < f_c$, the bead velocity is phase-locked to the propagating magnetic wave. The bead is not located at the energy minimum as this point has zero magnetic force but is instead being dragged behind and towards the point of minimum energy. Yellen *et al.* [74] termed this motion as phase-locked as the bead follows the magnetic wave but with a constant phase lag. As the driving frequency and speed increases, the bead lag increases until at the critical frequency the bead lags a quarter period (or 90°) behind and is constantly at the point of maximum magnetic force. If the driving frequency is increased beyond the critical frequency, the bead can no longer stay phase-locked. Instead, it slips out of the potential well from one energy minimum and is absorbed in the next, which drags it along for a time $\mathcal{T}$. This motion is described as phase slipping, and while the bead is not moving with the velocity of the magnetic wave, it is still being carried forward at a lower velocity. Phase-slipping gives rise to a complicated bead motion where the bead moves back and forth, but the average velocities are

$$\langle v \rangle = \begin{cases} \lambda f & f \leq f_c \\ \lambda\left(f - \sqrt{f^2 - f_c^2}\right) & f > f_c \end{cases}. \tag{2.16}$$

The sinusoidal approximation of Eq. (2.10) exemplifies how magnetic bead transportation happens. However, as can be seen in Fig. 2.2, when the magnetic bead is closer to stripes the bead is attracted to stripe poles where natural energy minima exist. For beads at a low height, two distinct motions can happen when phase slipping occurs.

- If phase slipping occurs late enough past the first energy minimum, the bead is attracted towards the next energy minimum and can catch up to the magnetic wave. In this case, the beads moves fast when approaching the poles and slow when leaving the poles. This velocity varies but the average velocity is phase-locked: $\langle v \rangle = \lambda f$.
- If phase slipping occurs when the magnetic bead has not left the potential well the bead is dragged back into the energy minimum from which it originated. While the bead may still move back and forth, the net velocity is zero: $\langle v \rangle = 0$.

While not predicted by the sinusoidal approximation, beads with zero net velocity are generally observed in the performed experiments and simulations. This motion is described as stationary. A simulation of all three behaviors can be seen Fig. 2.4. The geometry in Fig. 2.4 has a stripe field of $B_s = 2.5$ mT, and along with the other used parameters this corresponds to a theoretical critical frequency of $f_c = 7.5$ Hz, based on the sinusoidal approximation of Eq. (2.13). As the stripe field is not perfectly sinusoidally varying, the simulated critical frequency is $f_c = 5.7$ Hz. For real stripe geometries, the sinusoidal approximation is best used to get a rough estimate of the critical frequency.

Last, as the direction or magnitude of the bead velocity varies during any kind of transportation, and as the velocity is limited to that of the magnetic wave, the averaged normalized velocity will be used

$$V = \frac{\langle v \rangle}{\lambda f}, \tag{2.17}$$

with $V = 1$ corresponding to phase-locked motion, $0 < V < 1$ is phase-slipping and $V = 0$ means the bead is stationary.

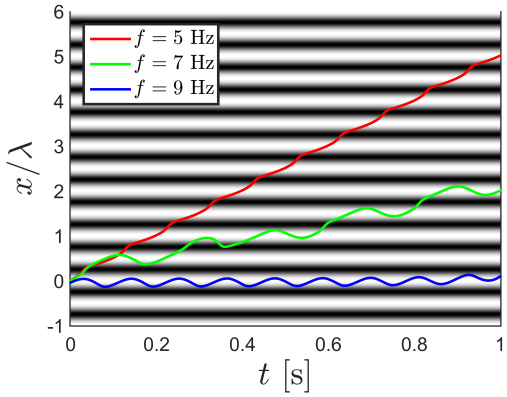

Figure 2.4: Simulations of the possible bead behaviors, phase-locked (red), phase-slipping (green) and stationary (blue) respectively as the frequency increases. Used parameters: $w = s = 5$ µm, $z = 1.5$ µm, $t_{\mathrm{FM}} = 30$ nm, $\mu_0 M = 1$ T, $B_{\mathrm{ext}} = 3$ mT and $\xi = 10\ \frac{(\mu\mathrm{m})^2}{\mathrm{Pas}}$. The background image displays the magnetic energy U_{m}, dark colors corresponds to a lower energy.

2.3 Geometrical considerations

In this section, different stripe geometries are compared for magnetophoresis. A much more detailed analysis can be found in Henriksen [82]. It is shown that bead transportation in an asymmetric geometry ($w \neq s$) has the same critical frequency as a symmetric geometry with the largest pole distance, i.e. $f_c(w = 5\ \mu\mathrm{m}, s = 8\ \mu\mathrm{m}) = f_c(w = 8\ \mu\mathrm{m}, s = 8\ \mu\mathrm{m})$, which will be needed to understand Chapter 5.

2.3.1 Velocity visualization by phase diagram

To visualize how the dynamics of the system changes when a parameter is changed, phase diagrams can be used. Figure 2.5 shows an example of a relevant phase diagram with five geometry-frequency regions, where different normalized velocity are found, as a function of the bead height. For example, if the combination of the bead height and the driving frequency of the external field corresponds to a point in the red region, the bead motion is phase-locked to the external field. If the frequency is increased in such a way that the corresponding point in the phase diagram changes color, the bead changes to the velocity interval defined in the phase-diagram legend. For a thorough analysis of how the phase diagrams are calculated see Henriksen [82]. In short, for calculating the expected bead velocity in a given system, the stripe field was first calculated (cf. Appendix A) and then used in the equation of motion, Eq. (2.7), along with a rotating external field. The equation of motion was then integrated until a periodic bead motion was observed. To obtain the maximum velocity, the phase-locked frequency was determined by bisection.

The phase diagram in Fig. 2.5 shows how bead transportation varies as the bead height changes. The red region of Fig. 2.5 corresponds to the region of phase-locked bead motion. For a given height, a frequency exists where the bead motion stops being phase-locked, this maximum frequency is termed $f_{V=1}$. Instead of plotting the whole phase diagram, sometimes only the line $f_{V=1}$ is plotted, as this allows for more plots in one figure.

For low frequencies, in Fig. 2.5, the velocities are generally phase-locked, while for high frequencies and at a low height, beads are stationary, due to the strong trapping potential in the wells. For a high height and high frequencies, beads are phase slipping but with $V < \frac{1}{4}$. Figure 2.5 shows that an optimal height exist at $\frac{z}{\lambda} = 0.13$ which has the highest critical frequency. For lower heights, the potential traps slow down bead transportation as the bead velocity is decreased when leaving the potential well. For higher bead heights, the potential traps are not a problem anymore but the decreasing stripe field decreases the critical frequency.

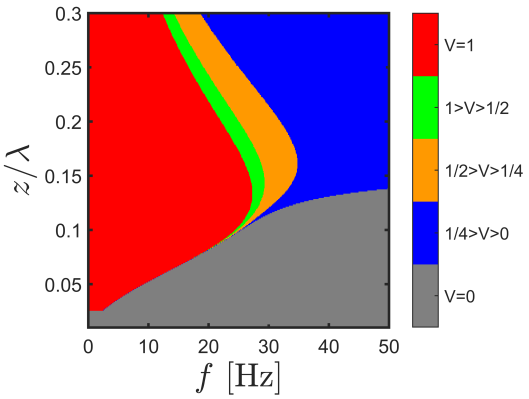

Figure 2.5: Normalized velocity phase diagram as function of bead height. Each color corresponds to a velocity range. Used parameters: $w = s = 5$ µm, $z = 1.5$ µm, $t_{\mathrm{FM}} = 15$ nm, $\mu_0 M = 1$ T, $B_{\mathrm{ext}} = 5$ mT and $\xi = 54\ \frac{(\mu\mathrm{m})^2}{\mathrm{Pas}}$, which correspond to M-270 beads.

2.3.2 Visualizing separation from phase diagram

If the magnetophoreses system is used for separation of beads with different magnetophoretic mobilities, e.g. due to an attached biological target. The driving force scales with the magnetophoretic mobility ξ, and if bead A has twice the magnetophoretic mobility of bead B, then it will have twice the critical frequency, which can be used for separation of beads with different mobilities. The phase diagram can be used to decide on a good geometrical period, λ. In the phase digram of bead A, Fig. 2.5, this corresponds to bead B being at the same height as bead A but at twice the frequency. Thus, a geometry where the bead motion go directly from phase-locked (red region of Fig. 2.5) to stationary (i.e. in the gray region of Fig. 2.5) when increasing the driving frequency is good for separating beads with different mobilities. If separating beads at different heights, one still tune λ to have one bead phase-locked and the other bead stationary. In general, geometries with $z < 0.1\lambda$ are good for separation as they go directly from phase-locked to stationary when decreasing the height or decreasing the mobility (corresponding to an increase in f).

2.3.3 Stripe geometry variations

The critical frequency and thus achievable speed for magnetophoresis is usually limited by the stretch with the lowest magnetic force. In Fig. 2.2 the stretch, with lowest magnetophoretic velocity, is around $0.1 \leq \frac{x}{\lambda} \leq 0.6$, as there is either a strong trapping force or the gradient of the stripe field is low. The hardest stretch is where the bead leaves a pole, especially if there is a large distance to the next pole. In terms of magnetophoresis speeds, this makes it unfavorable to have an asymmetric geometry where $w \neq s$. Figure 2.6 shows a comparison of fields from asymmetric and symmetric geometries.

All geometries in Fig. 2.6 have the same spacing $s = 8$ µm and the different widths indicated in the legend. The longer spacing contribute the hard stretch for bead transportation. Decreasing the stripe width and keeping a constant spacing, only changes the stripe field over the stripe area and leaves the hard stretch mostly unchanged. This can be seen in Fig. 2.6 where the stripe field and potential trap, in the spacing, are both constant as a function of width. As the largest distance $\max(w, s)$ is the hardest stretch, the largest velocity can be obtained by a symmetric geometry where the spacing and stripe width are equal. This can also be seen in the critical frequencies, for the three geometries in Fig. 2.6. These are found to be identical $f_{V=1}(w = 8\ \mu\mathrm{m}, s = 8\ \mu\mathrm{m}) = f_{V=1}(w = 5\ \mu\mathrm{m}, s = 8\ \mu\mathrm{m}) = 5.7$ Hz and lower for $f_{V=1}(w = 2\ \mu\mathrm{m}, s = 8\ \mu\mathrm{m}) = 4.7$ Hz (all $f_{V=1}$ values are calculated for M-270 beads and $B_{\mathrm{ext}} = 5$ mT) as this geometry has a lower gradient of $H_{\mathrm{s},z}$ in the spacing region. A plot of the critical frequencies as the stripe geometry is varied can be seen in Fig. 2.7a.

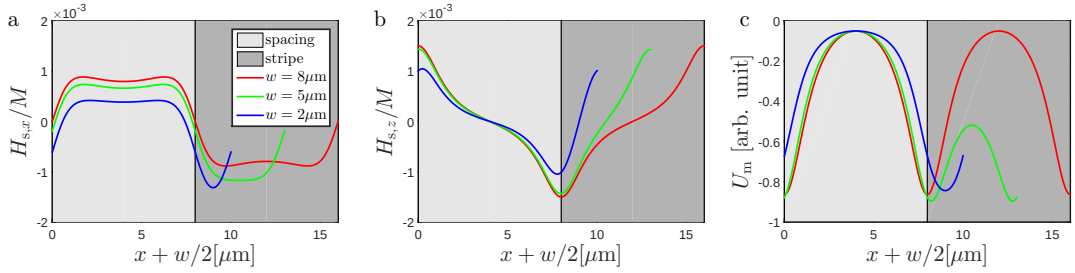

Figure 2.6: (a) x-component, (b) z-component of the magnetic stripe field and (c) the magnetic potential energy, for geometries with different widths but same spacing . The light gray area "spacing" refers to the area in-between the stripes. Note, that all $H_{s,x}, H_{s,z}, U_m$ are nearly constant in the spacing as a function of w. Used parameters: $z = 1.5$ µm, $s = 8$ µm, $t_{FM} = 15$ mm.

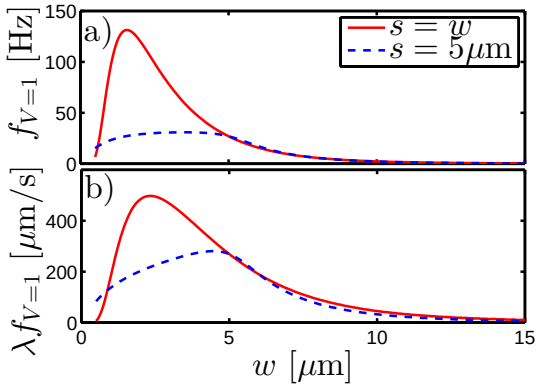

Figure 2.7: The possible driving frequencies (a) and bead velocity (b) as a function of the stripe width for an asymmetric and a symmetric geometry. Used parameters: $z = 1.5$ µm, $t_{FM} = 15$ nm, $\mu_0 M = 1$ T, $B_{ext} = 5$ mT and $\xi = 54$ $\frac{(\mu m)^2}{Pas}$, corresponding to M-270 beads.

Figure 2.7 compares the simulated critical frequency and maximum velocity between asymmetric and symmetric geometries. Figure 2.7a shows how the asymmetric geometry, with e.g. $w = 10$ µm and $s = 5$ µm, has the same critical frequency as the symmetrical geometry with $w = s = 10$ µm, and thus naturally a lower highest velocity $\lambda f_{V=1}$ due to the lower λ. If high separations speeds are desired, a symmetric geometry should be used.

Further, Fig. 2.7 shows how very high critical frequencies and speeds can be obtained from a symmetric geometry with a small width $w \approx 2$ µm. However, an increase of the speed could also be achieved by increasing t_{FM}. However, the depth of the potential trap goes with the square of t_{FM}, and if t_{FM} is increased too much, the beads will be permanently stuck at the edges. Chapter 5 will expand on this, but in general, the design process should answer the following question:

- Which types of beads will be separated and how much will a biological target change the drag force. The bead radius is usually the dominating contribution to the bead height z.
- How strong an external field can be made. The strength of the external field determines the maximum t_{FM}, as the external field needs to overcome the potential trapping.
- Consider if the setup (i.e. coils and power supplies) has a maximum driving frequency.
- Choose the width and spacing either for high critical speed, cf. Chapter 5, or such that $\frac{z}{\lambda}$ is low enough that the beads are either stationary or phase-locked.

3

Magnetophoresis setup

This chapter goes through the experimental setup used for the magnetophoresis experiments in Chapter 5. An overview of the stripe fabrication procedure is given where only a single mask and lithography step is used. Further, the Helmholtz coil setup used electromagnetic actuation is introduced along with the video capturing procedure for documentation. Last, bead sticking is discussed.

3.1 Magnetic beads

For the experiments in Chapter 5, Dynabeads® M-270 Carboxylic Acid beads were used. M-270 beads have a nominal diameter of $2r = 2.8$ µm and their susceptibility has been measured by Fonnum *et al.* [15]. Combining these results the magnetophoretic mobility of the M-270 beads was calculated to be $54\ \frac{(\mu m)^2}{Pas}$ for $\eta = 1.002$ mPas, $\rho = 1.4$ g/cm^3, and $\chi = 0.76$ and $f_D(z_w = 0)$ using Eq. (2.8).

M-270 beads were chosen for the experiments, as they are already well established for isolation and handling in molecular diagnostics, are visible through optical microscopy and allow for fabrication of magnetic stripes of comparable size. Further, the carboxylic acid coating provided the least problems with of bead sticking, cf. Section 3.4. Before use, the beads were diluted 100 times (to $2 \cdot 10^7$ beads/mL) in Milli-Q and mixed using a Vortex mixer.

3.2 Fabricated chips

3.2.1 Fabrication procedure

The magnetophoresis chips had a physical size of 6 mm × 6 mm and consisted mostly of stripes of magnetic stacks width widths and spacings varying between $2 - 10$ µm, a chip example can be seen in Fig. 3.1.

Two wafers, with approximately 180 chips like Fig. 3.1, were fabricated in the Danchip clean room. A schematic overview of the fabrication process flow can be seen in Fig. 3.3. Generally, this is the simplest of clean-room fabrication with only a single mask and lithography step. A detailed fabrication guide can be seen in Appendix B and can be summed up as

- Photoresist is spun on an oxidized wafer and patterned by the stripe mask. No aligning was needed.
- The photoresist is reversal baked and developed.
- The magnetic stack consisting of Ta (3)/$Ni_{80}Fe_{20}$ (5)/$Mn_{80}Ir_{20}$ (10)/$Ni_{80}Fe_{20}$ (10)/$Mn_{80}Ir_{20}$ (10)/ Ta (3) (thickness in nm) is deposited in a constant field of 20 mT and defined by liftoff.
- A protective coating of SiO_2 (100 nm) is sputter deposited.
- The wafer is diced.

All sputtering was done in the Kurt J. Lesker CSM-18 magnetron sputter system and each layer of the magnetic stack had the following purposes

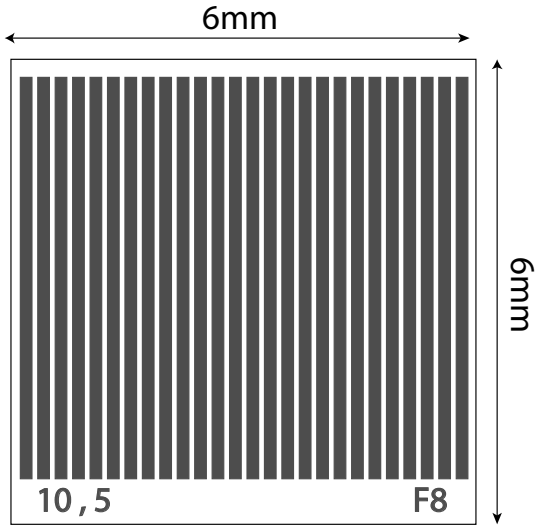

Figure 3.1: Illustration of a magnetophoresis chip. The dark gray color indicate where the magnetic stack is present. The numbers in the lower left corner are w, s in microns, and lower right indicate chip placement on the wafer. The stripes have been amplified in size to be visible.

Tantalum. Reduces lattice mismatching and improve adhesion.

Nickel-iron. A ferromagnetic material that generates the stripe field.

Manganese-iridium. An antiferromagnetic material that helps to keep a constant magnetization in the nickel-iron layer.

By surrounding the central nickel-iron thin film on both sides with manganese-iridium, a double exchange bias effect is created which helps to align the magnetization even for small stripes where demagnetization effects try to rotate the magnetization, cf. Section 6.3. To measure the effect of the double exchange bias VSM measurements were made on four chips, cf. Section 8.5.1. Figure 3.2 shows the result of these VSM measurements. The VSM chip show a nice hysteresis curve with a constant magnetization for an external below 10 mT. However, for stripe chips of decreasing widths, shape anisotropy has an increasing role and the magnetization gradually changes instead of a sharp flipping, cf. Section 6.4.4. For an external field strength of 5 mT and a magnetic stack with $t_{\mathrm{FM}} \geq 10 + 5$ nm a double exchange bias is needed for the stripes to have an approximately constant magnetization.

3.2.2 Chip designs

For measuring the importance of the stripe geometry, 13 chips with different stripe width and spacing were fabricated. The chips could be categorized into the three geometries groups

Symmetric: $w = s = 5, 6, 8, 10$ μm.

Constant spacing: $s = 5$ μm, $w = 2, 4, 5, 6, 8, 10$ μm.

Constant period: $w + s = 10$ μm, $w = 2, 4, 5, 6, 8, 10$ μm.

Note, that the geometry $w = s = 5$ was in all three groups.

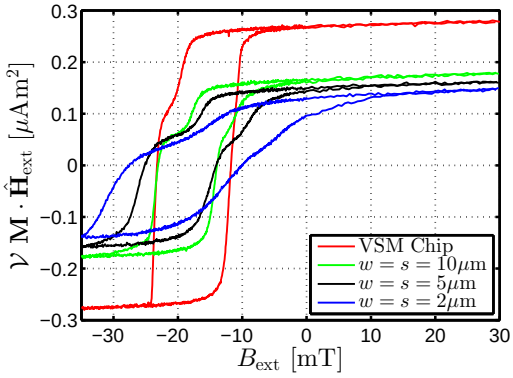

Figure 3.2: VSM measurements on three symmetric geometries and a VSM chip with dimensions 5×5 mm^2.

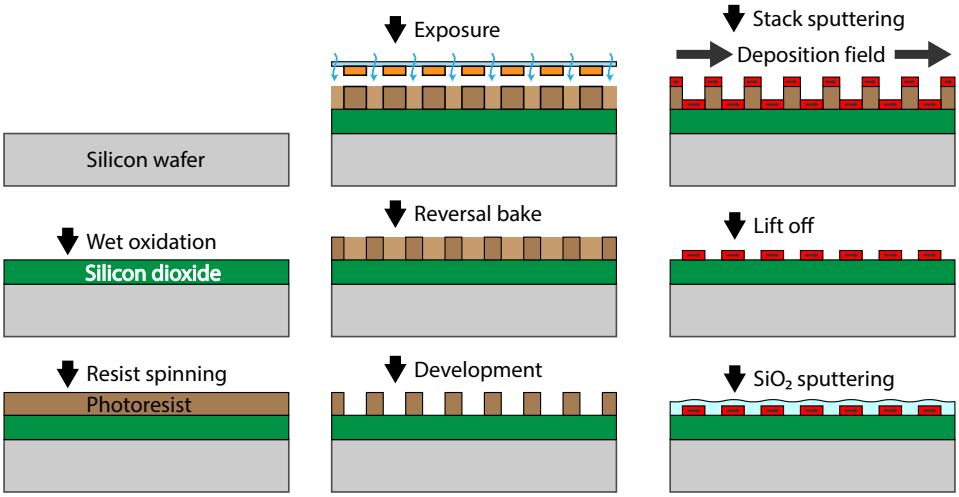

Figure 3.3: Illustration of the stripe fabrication process flow. After the nine displayed steps, the wafer is diced into single chips. The figure is not to scale.

3.3 Experimental setup

For the magnetophoresis experiments, a simple setup was used. The setup consisted of a square fluid channel milled in polymethylmetacrylate (PMMA) with a polydimethylsiloxane (PDMS) gasket, two set of homebuilt Helmholtz coils, a microscope for video capture and a computer for control and synchronization. An illustrative overview of the setup can be seen in Fig. 3.4, and all the parts are described in the following sections.

3.3.1 Electromagnetic actuation

Bead actuation was done using two home-built Helmholtz coils of radii 3.5 cm and 11.5 cm and with 130 and 979 number of windings. The coils were both placed around the chip holder to provide external fields in the $\hat{\mathbf{x}}$ and $\hat{\mathbf{z}}$-directions. The coils were driven by two KEPCO (Kepco Inc., NY, USA) bipolar operational power supplies, a 200 watt BOP 20-10M and a 400 watt BOP 50-8M, which were current-controlled by the PC. The PC ran LabView and provided control voltages through a NI PCI-6723 card (National Instruments, Austin, Texas, U.S.) with 13 bit resolution. When current driven

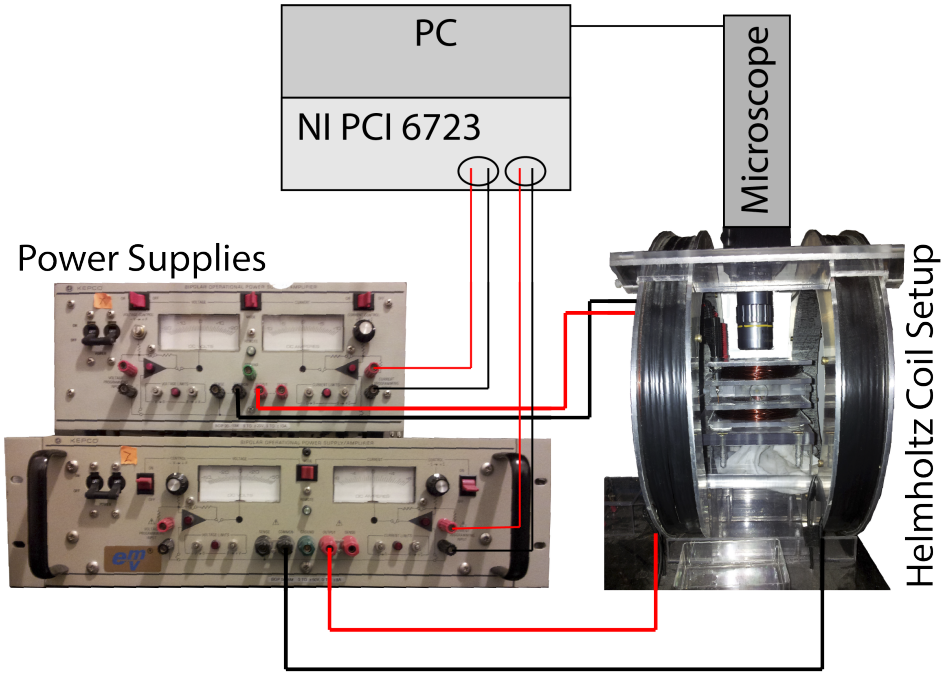

Figure 3.4: Overview of the magnetophoresis setup. Figure is adapted from Paper I.

by a control voltage the BOP 20-10M and 50-8M had conversion factors of 2.036 $\frac{\mathrm{A}}{\mathrm{V}}$ and 0.8064 $\frac{\mathrm{A}}{\mathrm{V}}$, respectively. Similarly, the bigger and smaller Helmholtz coils had conversion factors of $\frac{B_{\mathrm{ext},x}}{I} = 7.55\ \frac{\mathrm{mT}}{\mathrm{A}}$ and $\frac{B_{\mathrm{ext},z}}{I} = 3.34\ \frac{\mathrm{mT}}{\mathrm{A}}$, respectively, and negligible hysteresis. Throughout all the experiments, a rotating external field with a magnitude of 5 mT was used.

3.3.2 Chip holder

A very basic chip holder was milled from PMMA and can be seen in Fig. 3.5. The fluid system was defined in the bottom part, with a chip well and with an inlet and outlet, the fluid system had a depth of 1 mm and volume of 50 µL. The top part worked as a frame such that a microscope glass cover could be inserted and work as the top, thus giving optimal conditions for the microscope. The whole fluid system was sealed by a PDMS gasket.

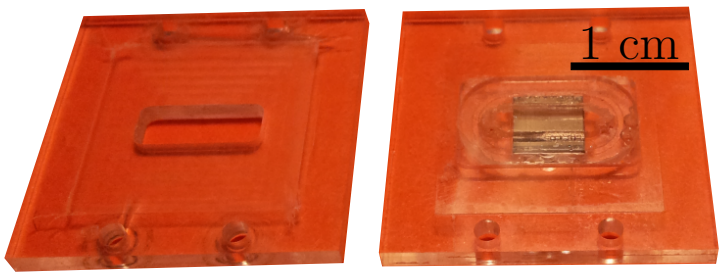

Figure 3.5: Picture of the top (left) and bottom (right) part of the magnetophoresis fluid system with chip and gasket. The top is designed to hold a thin microscope slide for optimal picture quality, and the inlet and outlet are attached to the bottom part. The fluid system was photographed against a red background to enhance the contrast of the PMMA.

3.3.3 Image acquisition

A Unibrain Fire-I 785c CCD camera captured an image after each rotation of the external field and compiled them into a still picture video. The shutter timing was controlled by a hardware trigger link to the NI PCI-6723 card, and a shutter speed of 4 ms was needed for the beads to have sharp edges. With such fast shutter speeds, the comparatively low light intensity was compensated for by using a high gain and exposure. Last H.264 compensation was used to keep the file size at a minimum while not limiting the image quality. During measurements, the setup was fixed to an optical table on a vibration damping table to obtain stable videos with no shaking from the outside environment.

3.4 Beads sticking to the surface

For all experiments, some of the beads stuck to the surface after sedimentation. For plain or carboxylic acid coated beads, usually 90 % of the beads were able to be actuated. However, when using protein-coated beads, e.g. streptavidin coated, up to half the beads were usually stuck. An example of this can be seen in Fig. 3.6 where the percentage of moving beads (P_0) are plotted as a function of time. As seen in Fig. 3.6 only 65 % of the beads were initially moving, and this percentage decreased approximately 2 percentage-point every 5 minutes.

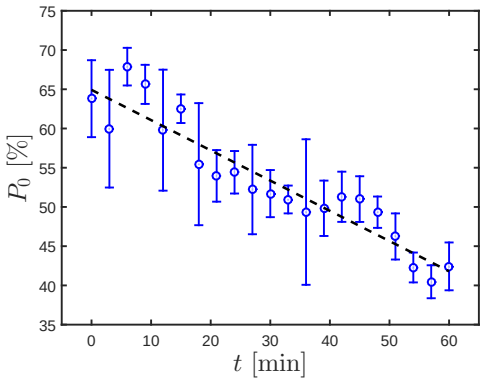

Figure 3.6: Percentage of moving beads over time. The black line is a linear fit of $P_0 = 65\% - 0.4\%/\text{min} \cdot t$.

To reduce the fraction of beads sticking to the chip surface, a variety of surface modifications and blockings schemes were tried.

Surface modifications. With the help of local experts, the chip surfaces were modified to have a layer of PEG (polyethylene glycol), PMMA and Teflon (based on Fluorinert FC-40).

Surface blocking schemes. The following blocking solutions were tried, and for each solution the chip was fully submerged in it between 30 min and 2 hours. The tried solutions were BSA-Tween (bovine serum albumin) (1 % BSA and 0.05% Tween-20); Casein (0.1 %); Pluronic F127 (0.1 %); Superblock (1%). All percentages are v/v.

All combinations of surface modification and blocking schemes were tried, but none of them worked reliably.

3.5 LabView files used

If needed in the future the following LabView files were mostly used:

- ADH_KEPCO_SimpleControl.vi
- ADH_PCI-6723_Waveform_KEPCO.vi
- ADH_CompressionCapture3.vi

4

Magnetophoresis video analysis

In Chapter 4 the automated video analysis procedure is explained; a picture of the home-built analysis program can be seen in Fig. 4.1. For the experimental part, a picture was taken after each rotation of the external driving field and these pictures were compiled into a still picture video. A separate video was made for each measured driving frequency and these videos were then analyzed to find the number of beads moving at this driving frequency. To ease the understanding, Chapter 4 starts with the example of a video frame, and then the bead identification and velocity determinations procedures are explained. Lastly, the statistics and data fitting of the whole frequency sweep are discussed. The video analysis program, but not the fitting procedure, was developed in Henriksen [82], and more details can be found here.

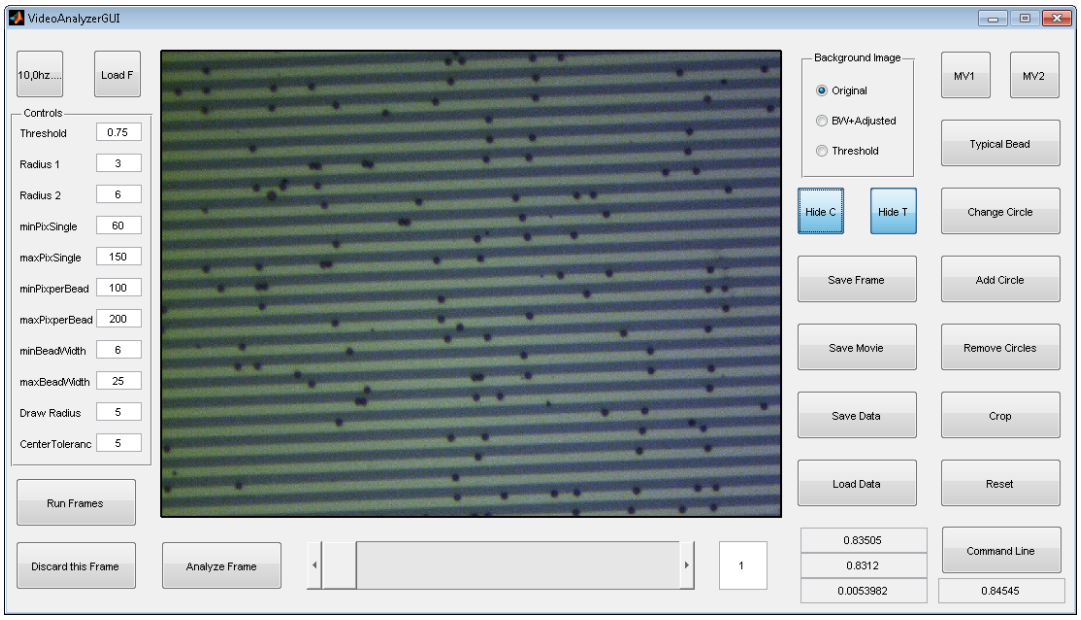

Figure 4.1: A picture of the homebuilt video analysis program.

4.1 Example of bead actuation data

An example of an analyzed frame from a video of bead motion can be seen in Fig. 4.2. Usually, 11 frames were recorded, but as bead motion were determined as the change in bead positions between frames, the first frame could not be part of the analysis. For frames 2-11 each identified bead was analyzed to be either phase-locked, stationary or in an undetermined state, which corresponds to green, red and blue circles in Fig. 4.2.

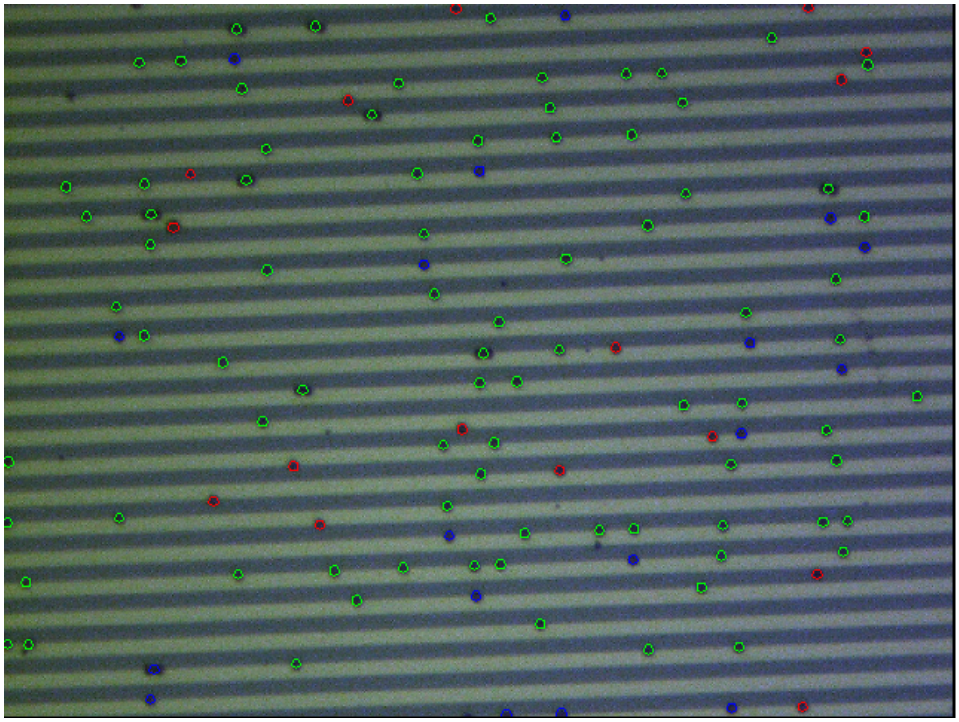

Figure 4.2: Frame from an analyzed movie of bead motion. Green and red circles indicate that the program has analyzed the bead to be phase-locked and stationary, respectively. Blue circles indicate the program is unsure. The frame is from the reliability experiment, i.e. $w = s = 6$ µm.

4.2 Bead identification

Bead identification is done by converting the picture to gray-scale and analyzing whether the area around each pixel is darker than the intensity of a bigger area. If the average intensity of the close-vicinity of the pixel is darker by some threshold than the intensity of a larger-vicinity, that pixel is assumed to be part of a bead. Doing this for all pixels gives a binary picture of pixels in beads. The binary picture is analyzed in-terms of clusters, with too small clusters being discarded as noise and big clusters being broken up into multiple beads, which are typically aligned along the stripe edges.

In addition to identifying the bead positions in each frame, the algorithm also determines the stripe period and angle. This is done by fitting a stepwise light-dark pattern along an arbitrary direction of the gray picture, and rotating its direction to minimize the period of the stepwise changes in dark and light intensity.

4.3 Velocity determination

After identifying the beads in each frame of the video, the algorithm determines whether each bead has undergone phase-locked motion, is stationary or something in-between. This velocity determination is done by calculating the anticipated bead positions, from the bead positions in the last frame and the geometrical period, and comparing to the new bead positions. If a bead is in an unexpected position and a bead was at the same position last frame, it is assumed to be the same bead, which has not moved (stationary). If the bead is in an expected position and no beads is behind it, the bead is assumed to have moved (phase-locked). If the position where the bead came from is occupied, then the algorithm determines if the occupying bead was expected to be there, until a conclusion can be reached, see the decision tree of Fig. 4.3. From these rules, all beads can be determined to be either stationary,

phase-locked, or in-between/unknown as illustrated by red, green and blue circles in Fig. 4.2. In practice, most beads were observed to be either phase-locked or stationary, and the few phase-slipping beads were not counted by the algorithm. When all the bead movements have been tracked, the calculated average velocity of each bead, that has been tracked through more than 3 frames, are logged for further analysis like Eq. (4.1)

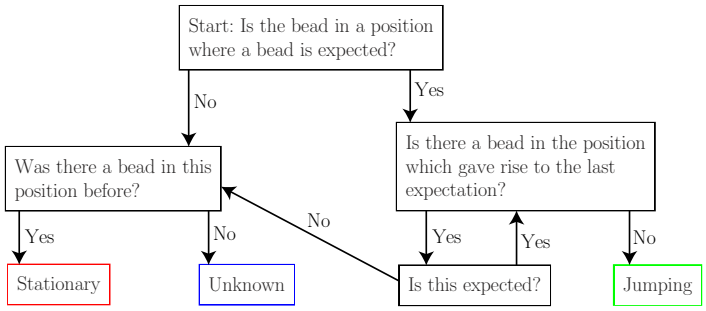

Figure 4.3: The decision tree for determining whether each bead is phase-locked, stationary or something in between. Picture is from Henriksen [82].

4.4 Data fitting

After calculating the velocity of each trackable bead, the move percentage was calculated as

$$P_{\mathrm{V}\geq\frac{1}{2}} = \frac{N_{\mathrm{V}\geq\frac{1}{2}}}{N_{\mathrm{V}<\frac{1}{2}} + N_{\mathrm{V}\geq\frac{1}{2}}} \times 100\% \tag{4.1}$$

where $N_{\mathrm{V}\geq\frac{1}{2}}$ is the number of beads with normalized velocity above one-half and $N_{\mathrm{V}<\frac{1}{2}}$ is the number of the beads with velocity below one-half. In practice, $N_{\mathrm{V}\geq\frac{1}{2}}$ is very closed to the number of phase-locked beads, and $N_{\mathrm{V}<\frac{1}{2}}$ is close to the number of stationary beads. $P_{\mathrm{V}\geq\frac{1}{2}}$ gives a quantitative measure of the relative number of moving beads, even though unknown beads are omitted from the counts. The result of this automated analysis is similar to the result of a human analysis [82]. Generally, for a slowly rotating field, most of the beads are moving while some of the beads are naturally stuck ($P_{\mathrm{V}\geq\frac{1}{2}} \approx 90\%$). Similarly, for a fast rotational field, faster than the critical frequency of the beads, no beads can follow and in practice all beads becomes stationary.

Even for the same batch of magnetic beads, small differences will be found in the bead diameters and magnetic content. These will be evident in differences in the transportation properties of the beads. It is thus assumed that the magnetophoretic mobility will be normal distributed as a micron-size bead contains many magnetic nano-particles. The magnetophoretic mobility for a bead, ξ, is proportional to its critical frequency, and thus a normal distribution of the magnetophoretic mobilities results in a normal distribution of critical frequencies. The probability of a given bead being phase-locked, i.e. the probability that a given bead has a critical frequency higher than the driving frequency, is the area of the normal distribution of beads with higher critical frequencies than the applied rotational frequency:

$$\mathcal{P}_{V=1} = \int_f^\infty \frac{1}{\sqrt{2\pi}f_\sigma} \exp\left(-\frac{(f'-f_{V=1})^2}{2f_\sigma^2}\right) \mathrm{d}f' = \frac{1}{2}\mathrm{erfc}\left(\frac{f_{V=1}-f}{\sqrt{2}f_\sigma}\right) \tag{4.2}$$

where f is the rotational-frequency of the external field, and $f_{V=1}$ and f_σ are the mean and the standard deviation of the critical frequencies for phase-locked motion.

Knowing the probability that each bead follows the rotational field, and the number of beads in each video, the number of moving beads should follow a binomial distribution. As the rotational frequency increases, the binomial distribution shifts from favoring phase-locked beads to favoring stationary beads.

Chapter 5 measures the frequency where this change happens as a function of the stripe geometry. To measure the critical frequency for a given geometry, frequency sweeps were used. In a frequency sweep, like Fig. 4.4, the driving frequency was increased from a value much lower than the critical frequency to a value much higher, and for each frequency the move percentage $P_{\mathrm{V}\geq\frac{1}{2}}$ was measured. As mentioned, usually 10 % of the beads tended to be stuck on the chip and would not move at any frequency. To adjust for this constant error, a new fitting parameter, P_0 is included in Eq. (4.2) to reduce the maximum move percentage

$$\mathcal{P}_{V=1}(f|f_{V=1}, f_\sigma, P_0) = \frac{P_0}{2}\mathrm{erfc}\left(\frac{f_{V=1}-f}{\sqrt{2}f_\sigma}\right). \tag{4.3}$$

Combining the measured decreasing move percentage, Eq. (4.1), with the probability function, Eq. (4.3), enabled fitting the $f_{V=1}$ and f_σ parameters using maximum likelihood estimation. Note, that the fitted $f_{V=1}$ value is the estimator of the mean critical frequency of beads for that geometry. Lastly, an example of the frequency sweep along with the fitted binomial distribution with probability given by Eq. (4.3) can be seen Fig. 4.4. The error bars on $P_{\mathrm{V}\geq\frac{1}{2}}$ arise from variation throughout the 10 frames of each video, but they were not used for the fitting.

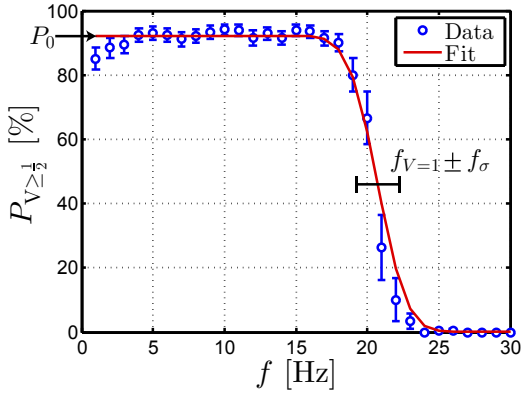

Figure 4.4: A standard frequency sweep and fit of binomial distribution with the indicated parameter. Figure is adapted from Paper I.

5

Magnetophoresis results

This chapter presents the results of an experimental investigation of the dependence of magnetophoresis on the stripe geometry. This builds on the earlier magnetophoresis proof-of-concept by Donolato *et al.* [96]. It is explained how some geometries are better suited for the transportation of magnetic beads and that an asymmetric geometry is not needed.

First, the reliability and chip-to-chip variations of the magnetophoresis properties were measured and only low variations were found in the measured critical frequencies. Then, frequency sweeps series of magnetophoresis measurements were performed on thirteen stripe geometries with varying stripe width and spacing. It was found that magnetophoresis is easier in a symmetric geometry with a small width comparable to the bead size. This chapter summarizes the results of Paper I.

5.1 Results

This section goes through measurements of the magnetophoresis properties. The measurements were performed using the setup described in Section 3.3 and by performing frequency sweeps measurement series like described in Section 4.4. Two experimental studies are presented: First, a reliability study that examines the experimental variations in the frequency sweep measurement procedure. Second, the main study of varying the stripe geometry parameters and how these affect the critical frequency of M-270 beads.

5.1.1 Reliability assessment

Three magnetophoresis measurements for increasing frequency of the rotating external field, i.e. frequency sweep, can be seen in Fig. 5.1. The data is plotted as the percentage of beads moving with normalized velocity $V \geq \frac{1}{2}$, $P_{V\geq\frac{1}{2}}$, versus the driving frequency. For low frequencies, 90 % of the beads usually move, and 10 % are stuck due to unspecific binding. As the driving frequency increases, $P_{V\geq\frac{1}{2}}$ stays around 90 % until the critical frequency is approached, at which point the move percentage decreases rapidly to 0 %.

To test variations between chips, three chips with the same geometry ($w = s = 6$ µm) was measured and Fig. 5.1 shows the result. Each curve in Fig. 5.1 is fitted as described in Section 4.4 and the result can be seen in Table 5.1. From Fig. 5.1 and Table 5.1 it is found that the measured frequency sweeps are reproducible, even between different chips, and frequency sweeps are a reliable way to measure the critical frequency. However, while measurements are similar the critical frequency varies 8 % between chips.

Table 5.1: Fitted parameters from the frequency sweeps in Fig. 5.1. The table is adapted from Paper I.

	$f_{V=1}$ [Hz]	f_σ [Hz]	P_0 [%]
Chip 1	20.5(1)	1.5(1)	93(1)
Chip 2	20.7(3)	1.6(2)	92(1)
Chip 3	22.1(1)	1.2(1)	94(1)

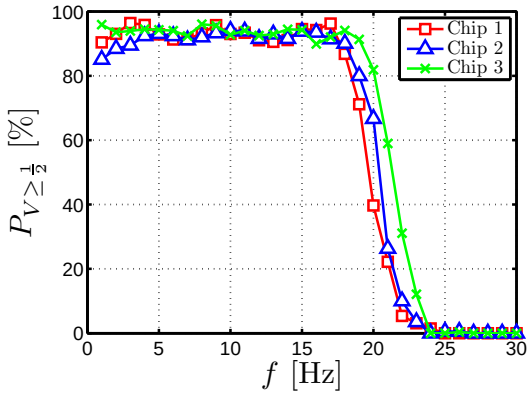

Figure 5.1: Frequency sweeps to asses reproducibility of magnetophoresis on three similar chips.

5.1.2 Geometrical dependence

The critical frequencies, determined from frequency sweeps like Fig. 5.1, were measured for the thirteen different fabricated geometries and are plotted in Fig. 5.2. Three different groups can be seen in Fig. 5.2 symmetric geometries, constant spacing and constant period.

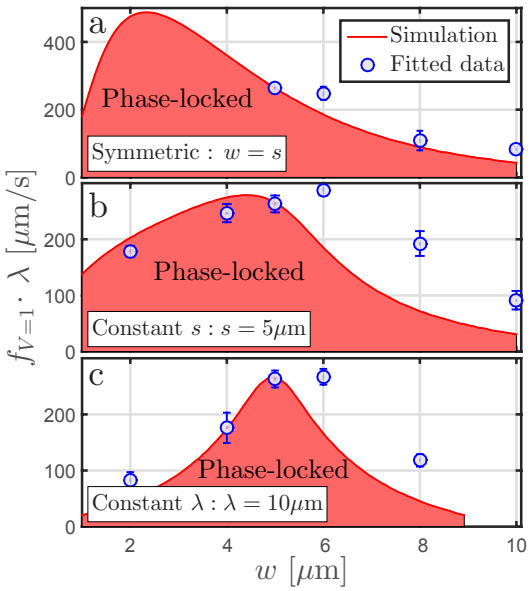

Figure 5.2: Phase-locked velocity, $f_{V=1} \cdot \lambda$, vs. stripe width. The blue circles are measured velocities, and the red area is simulated using $\xi_{\mathrm{M}-270}$. The error bars correspond to $\pm f_\sigma \cdot \lambda$. Figure is adapted from Paper I.

Symmetric geometries. Figure 5.2a shows the calculated critical frequency (cf. Section 2.3.1), as well as the measured for a symmetric stripe geometry ($w = s$) with varying period. Note, that no fitted parameter is used to obtain the theoretical data. An overall agreement is seen between the theory and measurements and both agree that a small geometrical period, comparable to the bead size, is better for transportation. In the earlier work by Donolato *et al.* [96] it was hypothesized that magnetophoresis will not work in a symmetric geometry. Figure 5.2a shows this is not the

case, and in general, symmetric geometries have the most sinusoidally varying stripe field, which is optimal for magnetophoresis with a rotating field.

Constant spacing. In Fig. 5.2b the measured and calculated magnetophoresis properties for geometries with a constant spacing $s = 5$ µm and varying widths are plotted. Experimentally, the best geometry is found to be $w = 6$ µm, $s = 5$ µm, while for the simulations the best geometry is $w = 4.5$ µm, $s = 5$ µm. In general, the measured velocities follow the predicted pattern but is higher than predicted for larger widths. Possible sources of error are discussed in Section 5.2. Both experiments and theory agrees that the geometry should be close to symmetric. For larger widths $w > 5$ µm it is more difficult for the beads to cross the width of the stripe than the space between the stripes. As explained in Section 2.3.3, a $w = 10$ µm, $s = 5$ µm geometry has the same critical frequency as a $w = 10$ µm, $s = 10$ µm geometry, which is not optimal for transportation. Contrary to Fig. 5.2a, decreasing the width below $w \leq 5$ µm is not good for transportation when the spacing is constant. In this case, the maximum velocity slowly decreases as the critical frequency is constant (limited by the spacing-region) and the geometrical period deceases.

Constant period. Last, Fig. 5.2c shows the data for geometries with a constant period $\lambda = 10$ µm. As in Fig. 5.2b the measured transportation properties are above the predictions for high widths, but generally follows the calculated trend. It is clear from Fig. 5.2c that higher velocities are found is a symmetric geometry, as the largest region otherwise limits the critical frequency as discussed in Section 2.3.3.

5.2 Discussion

5.2.1 Optimal period and bead height

Magnetophoretic transportation was found possible in all the fabricated geometries using M-270 beads. However, the maximum velocities vary. Figure 5.2 shows that the highest magnetophoretic separation velocity can be obtained for a symmetric geometry with $\lambda \approx 5$ µm, which for M-270 beads provide stripe-fields with both high amplitudes and sinusoidal variations. If the setup had another bead height (e.g. another bead type or spacer), another period would be optimal.

In practice, the external field strength will be limited by the experimental setup, and the bead type (i.e. radius and magnetophoretic mobility) will be limited by the application (e.g. diffusion time, sedimentation, binding capacity). Assuming these parameters to be constant, the parameters that can be varied are the stripe parameters w, s, t_{FM} and a spacer of height h can be used to increase the bead heights beyond the lower limit of one bead radius, $z = r + h$.

The stripe field is proportional to the ferromagnetic thickness, t_{FM}, and a stronger stripe field gives faster transportation but can lead to beads being trapped at the stripe edges. In theory, t_{FM} should be maximized to give the strongest stripe field that the external field can still overcome, at the given bead height. This can be calculated from Appendix A. However, in practice a somewhat lower stripe field and ferromagnetic thickness can be desirable to prevent bead trapping at the edges.

For a symmetric geometry, the period, λ, and possible spacer layer, h, can be decided from Fig. 5.3. Figure 5.3 shows a contour plot of the maximum velocity as function of the period and bead height. Note, that Fig. 5.3 is calculated for a low thickness of $t_{\mathrm{FM}} = 1$ nm to prevent bead trapping at the edges. In Fig. 5.3 three regions can be seen, separated by the dashed lines given by $\frac{\partial \lambda f_{V=1}}{\partial z}|_{\lambda} = 0$ and $\frac{\partial \lambda f_{V=1}}{\partial \lambda}|_{z} = 0$.

I In the top region, $z > 0.32\lambda$, the bead period is too small, which reduces the amplitude of the stripe field. The bead velocity can thus be increased by increasing λ, i.e. by moving to the right in Fig. 5.3, until $z = 0.32\lambda$.

II In the middle region, the bead velocity can be increased by decreasing either z or λ while still keeping $0.32 > \frac{z}{\lambda} > 0.13$.

III In the bottom region, $z < 0.13\lambda$, the beads are too close to the stripes, which gives a very localized stripe field. Here, the bead velocity can be increased by increasing the bead height by having a thicker spacer layer, this corresponds to move upwards in Fig. 5.3. Thus by increasing λ or adding a spacer, i.e. increasing z, an optimized the stripe geometry corresponds to a point in the middle region, $0.32 > \frac{z}{\lambda} > 0.13$.

This combined with using a symmetric geometry $w = s$ and calculating the stripe field through Appendix A to determine the optimal stripe thickness gives a complete approach for optimizing the stripe geometry.

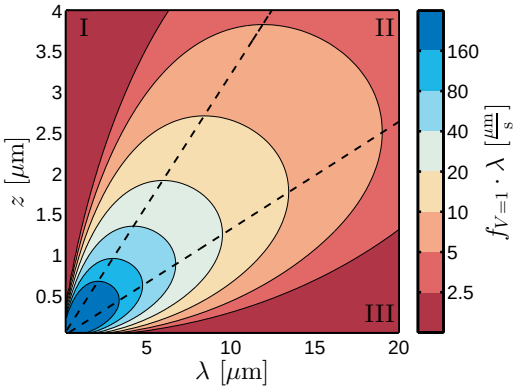

Figure 5.3: Contour plot of the maximum bead velocity as a function of stripe period, λ, and bead height z. The dashed lines correspond to $\frac{z}{\lambda} = 0.1317$ and $\frac{z}{\lambda} = 0.3217$. The data was calculated for $B_{\text{ext}} = 5$ mT, $t_{\text{FM}} = 1$ nm, $w = s = \lambda/2$ and $\xi = \xi_{\text{M-270}}$. The figure is adapted from Paper I.

5.2.2 Bead size limit

Figure 5.3 shows that for small beads, i.e. lower z values, optimally, a small geometrical period should be used. However, the width of the fabricated stripes have a lowest limit defined by the fabrication process, e.g. photolithography diffraction limitations. Figure 5.4 shows the possible bead velocity as function of bead size and when the stripe period has a lower limit of $\lambda = 2$ µm. Note, that for the velocities in Fig. 5.4, the magnetophoretic mobility was assumed to vary as $\xi = \xi_{\text{M-270}} \frac{r^2}{(1.4\mu\text{m})^2} = 54 \frac{(\mu\text{m})^2}{\text{Pas}} \cdot \frac{r^2}{(1.4\mu\text{m})^2}$, cf. Eq. (2.8). Interestingly, as long as $\lambda_{\text{optimal}} > 2$ µm, corresponding to $r > 640$ nm, the possible bead velocity is stable at 490 µm/s. However, when $\lambda_{\text{optimal}} < 2$ µm, the bead velocity decreases, and at $r = 200$ nm the bead velocity is 10 % of the maximum velocity. Thus, the fabrication process, and its feature limitations, limits the bead sizes that can be transported and separated. For systems based on UV-lithography, with a minimum period of 4 µm, it will not be possible to transport bead much smaller than $r = 0.32 \cdot 4\mu\text{m} = 1.3\mu\text{m}$.

5.2.3 Sources of error

The measured maximum velocities in Fig. 5.2 agreed quantitatively with the model but not perfectly. Three factors responsible for these discrepancies were identified.

- The UV-lithography process was imperfect, over-exposing the stripes and thus decreasing the width below the nominal widths. Measuring the stripe width from the magnetophoresis videos showed the actual width to be, on average, 0.24 µm smaller than the nominal width. This helps explain why the measured velocities in Fig. 5.2c are faster for $w > 5$ µm than for $w < 5$ µm.

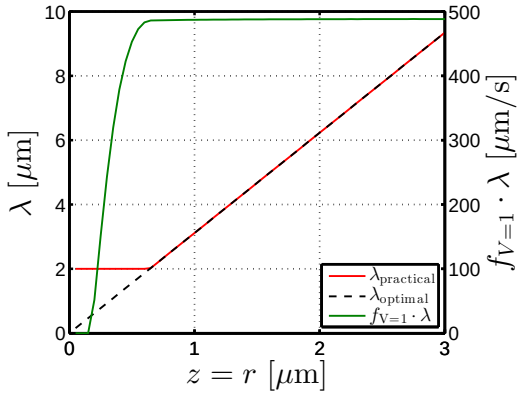

Figure 5.4: The optimal stripe period, λ_{optimal}, and the implemented period when a practical lower limit of 2 µm has been chosen based on UV-lithography limitations, $\lambda_{\text{practical}}$. The right axis shows the highest bead velocity as a function of bead size when $\lambda = \lambda_{\text{practical}}$. Further, as the bead size changes the magnetophoretic mobility is assumed to change as $\xi = \xi_{\text{M-270}} \frac{r^2}{(1.4\mu\text{m})^2} = 54 \frac{(\mu\text{m})^2}{\text{Pas}} \cdot \frac{r^2}{(1.4\mu\text{m})^2}$. The data was calculated for $B_{\text{ext}} = 5$ mT, $w = s = \frac{\lambda}{2}$, $t_{\text{FM}} = 15$ nm. The figure is adapted from Paper I.

- Magnetic stripes with small widths, $w < 5\mu$m, have inhomogeneous magnetization due to shape anisotropy, cf. Section 6.4.4, This effectively decreases their magnetic-moment thus decreasing the possible velocities for these chips. This could explain the why the measured velocity in Fig. 5.2b decreases below the theory when $w < 5\mu$m.
- Moving magnetic beads tended to line-up behind each other. An example of this can be seen in Fig. 5.5. The chains of magnetic beads, indicated by orange lines in Fig. 5.5, had an overall smaller drag force, which helped to achieve higher critical velocities than modeled. This effect could decrease separation efficiency.

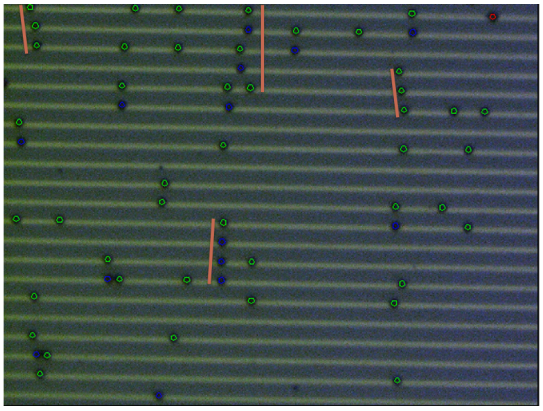

Figure 5.5: Picture of beads lining up behind each other to reduce drag. The longer bead lines have been indicated by the orange stripes.

5.3 Conclusion

Magnetophoresis of micron-sized beads in a stripe geometry has been analyzed. It was shown, both experimentally and theoretically, that a symmetric stripe geometry is always preferable and that the

thickness of the magnetic material should be matched to the bead size and external field. Further, the stripe period and bead height should be adjusted to be in the range $0.32 > \frac{z}{\lambda} > 0.13$. For micro- or nano-sized magnetic beads, the optimal period will often be impossible to fabricate with UV-lithography and will have uneven magnetizations due to shape anisotropy. Thus, one should consider how small magnetic stripes that are feasible in practice, and use this as the minimum feature size, which also limits the minimum bead size.

In theory, stripe systems are well suited for magnetophoresis, as they are easy to fabricate, and the many geometrical parameters can be tuned for high magnetophoretic bead velocities approaching 1 mm/s. However, in practice these magnetophoretic systems have two major disadvantages. First, implementation is hard, as beads coated with proteins have a tendency to stick to the surface, thus becoming impossible to transport. Second, for separating beads significantly smaller than one micron, a stripe system with widths smaller than two microns is needed, which is usually not possible to fabricate with UV-lithography. Moreover, for beads of one-micron size or larger, the conventional separation technique (a tube with a magnet on its side) is usually sufficient.

Part II

Planar Hall effect sensors for magnetic bead biodetection

6

Theory

Chapter 6 explains the overall theory of planar Hall effect bridge (PHEB) sensors, which is the sensor type used in the experimental work. First, the anisotropic magnetoresistance is introduced. Then the focus shifts to planar Hall effect bridge sensors, including a discussion of the magnetic energies from the magnetic stack. It is explained how the sensor can be applied for both magnetic field and magnetic-bead detection.

6.1 Anisotropic magnetoresistance

The planar Hall effect bridge (PHEB) sensors used in the experimental work are based on permalloy ($Ni_{80}Ir_{80}$), which shows anisotropic magnetoresistance (AMR). For magnetic stacks exhibiting AMR, the resistivity is higher when the current is parallel to the magnetization, $\rho_\parallel$, and lower when the magnetization and current are perpendicular, $\rho_\perp$. The difference in resistivity, $\Delta\rho = \rho_\parallel - \rho_\perp$, is quantified through the AMR-ratio of the stack

$$r_{\mathrm{AMR}} = \frac{\rho_\parallel - \rho_\perp}{\rho_\parallel/2 + \rho_\perp/2}, \tag{6.1}$$

which for permalloy thin films of above 20 nm thickness is around 2 % [29, 97]. For a slab (i.e. rectangular prism) of a permalloy based magnetic stack, like Fig. 6.1, placed in the (x, y)-plane, with an angle α to the x-axis and with magnetization M rotated θ, the resistance is [98]

$$R(\theta, \alpha) = \frac{l}{wt}\left(\cos^2\alpha(\rho_\parallel - \Delta\rho\sin^2\theta) + \frac{\Delta\rho}{2}\sin(2\alpha)\sin(2\theta) + \sin^2\alpha(\rho_\parallel - \Delta\rho\cos^2\theta)\right) \tag{6.2}$$

where l, w, t is the slab's length, width and thickness, respectively. The case of $\alpha = \pm\frac{\pi}{4}$ is of special interest in sensor design, in this case, the resistance simplifies to

$$R\left(\theta, \alpha = \pm\frac{\pi}{4}\right) = \frac{l}{wt}\left(\frac{\rho_\parallel + \rho_\perp}{2} \pm \frac{\Delta\rho}{2}\sin(2\theta)\right). \tag{6.3}$$

When $\theta = 0$ in Eq. (6.3), resistors with both $\alpha = \pm\frac{\pi}{4}$ has the average resistance of

$$R_0 = \frac{l(\rho_\parallel + \rho_\perp)}{2wt}. \tag{6.4}$$

6.2 Planar Hall effect bridge sensors

When measuring changes in resistance, the Wheatstone bridge design allows for measuring the resistance change without measuring the offset. Similarly, it is optimal for measuring only the θ-dependent part of Eq. (6.3), which is possible by aligning the bridge resistors in a diamond shape, like in Fig. 6.2a. This design is termed a planar Hall effect bridge (PHEB) sensor [40]. This names comes from the prior sensor

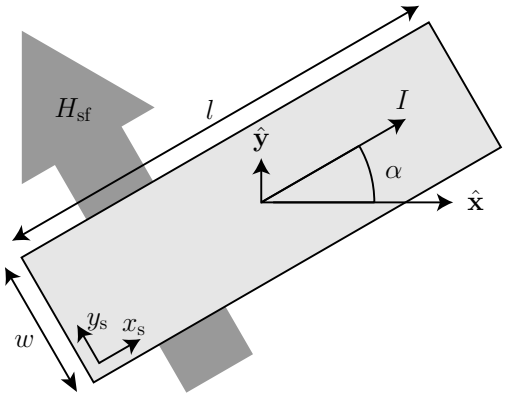

Figure 6.1: Illustration of a magnetoresistive slab, along with dimensions, coordinate system, direction of self-field and coordinate system of the principal axes used for shape anisotropy calculations.

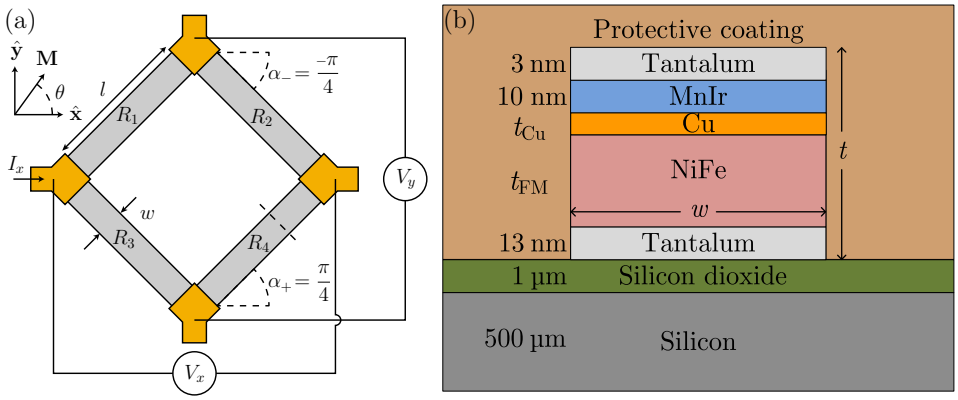

Figure 6.2: (a) Illustration of a Wheatstone bridge PHEB sensor. (b) Sensor cross-section at the dashed line in (a), illustrating a typical magnetic stack used in this thesis. The figure is not to scale. Figure is adapted from Paper VI.

design, the planar Hall effect (PHE) cross sensors, which also didn't use the ordinary Hall effect, but used the same geometry as ordinary Hall sensors.

For a general Wheatstone bridge, with resistors R_1, R_2, R_3 and R_4 arranged like in Fig. 6.2a the bridge output is given by

$$V_y = I_x \frac{R_1 R_4 - R_2 R_3}{R_1 + R_2 + R_3 + R_4} = V_x \left(\frac{R_1}{R_1 + R_2} - \frac{R_3}{R_3 + R_4} \right) \tag{6.5}$$

where I_x, V_x is the bias current and voltage, respectively. Note, that the sign of V_y sometimes changes depending on the direction of the voltage measurement. For a balanced bridge where $R_1 + R_2 = R_3 + R_4$, Eq. (6.5) simplifies to

$$V_y = I_x(R_1 - R_3). \tag{6.6}$$

Using the resistance from Eq. (6.3) the output becomes

$$V_y = \frac{I_x \Delta\rho}{2} \frac{l}{wt} \sin(2\theta) = \frac{V_x r_{\mathrm{AMR}}}{2} \sin(2\theta) \tag{6.7}$$

where it has been used that the bridge has constant resistance (i.e. independent of θ) of R_0, cf. Eq. (6.4).

Equation 6.7 shows that the bridge output is proportional to $\sin(2\theta)$. In zero external field the magnetization is aligned by the exchange field along the x-direction, i.e. $\theta = 0$, cf. Section 6.3.3. For $\theta = 0$ the sensor output is zero as all resistors have a resistivity of $\rho = (\rho_{\parallel} + \rho_{\perp})/2$ as displayed in Fig. 6.4. An external field can rotate the magnetization, $\theta > 0$, and while θ is small, the bridge output is proportional to the θ. When θ reaches $\frac{\pi}{4}$ the bridge is maximally unbalanced as R_1 and R_3 have resistivity $\rho_{\parallel}$ and R_2 and R_4 have resistivity $\rho_{\perp}$ and, as seen in Fig. 6.4 the output peaks with value

$$V_y(\theta = \tfrac{\pi}{4}) = \frac{I_x \Delta\rho}{2} \frac{l}{wt} = V_{\text{pp}}/2 \tag{6.8}$$

where V_{pp} is the peak-to-peak value. If the external field increases further, θ increases towards $\frac{\pi}{2}$ and the bridge becomes more balanced again and the output diminishes towards zero.

6.3 Energies of thin film magnetic materials

Section 6.3 explains the magnetic energies of a magnetic thin film when subject to an external field. Through energy minimization the magnetization angle, θ, is related to the strength of the external field, H_{ext}. Finally, the effect of shape anisotropy is discussed.

A cross-section of the magnetic stack used, can be seen in Fig. 6.2b, and it consist of a ferromagnetic layer adjacent to an antiferromagnetic layer. This stack is analyzed in terms of a single domain model, where the thin film ferromagnetic layer is assumed to be a single magnetic domain with a homogeneous magnetization. Further, the magnetization is assumed to be restricted to the (x, y)-plane by shape anisotropy.

6.3.1 Zeeman energy

The Zeeman energy U_{Z} from a magnetic moment, $\mathbf{M}\mathcal{V}_{\text{FM}}$, in an external field H_{ext} is

$$U_{\text{Z}} = -\mu_0 \mathcal{V}_{\text{FM}} \mathbf{M} \cdot \mathbf{H}_{\text{ext}} \tag{6.9}$$

where $\mathcal{V}_{\text{FM}}$ is the volume of the ferromagnetic layer and μ_0 is the vacuum permeability and $\mathbf{M}$ is the magnetization, usually at the saturated value $\mathbf{M} = M_s \hat{\mathbf{M}}$. The external field thus pulls the magnetization toward its direction.

6.3.2 Uniaxial anisotropy energy

When the ferromagnetic material is deposited in an applied field, the resulting crystal structure gives the magnetic moment a preferred axis. The uniaxial anisotropy energy, U_{K}, describes the tendency of the magnetic moment to align with this easy-axis and is given by

$$U_{\text{K}} = -K \mathcal{V}_{\text{FM}} \left(\hat{\mathbf{M}} \cdot \hat{\mathbf{e}}_{\text{easy}} \right)^2 \tag{6.10}$$

where K is an anisotropy constant and $\hat{\mathbf{e}}_{\text{easy}}$ is the unit vector for the easy-axis direction. The uniaxial anisotropy energy thus pulls the magnetization towards the easy axis. However, as the uniaxial anisotropy energy has energy minima in two directions, it causes hysteresis in permalloy, when the magnetization varies along the easy axis.

6.3.3 Exchange energy

For a ferromagnetic layer adjacent to an anti-ferromagnetic layer, spin-exchange interaction creates a preferred orientation of the ferromagnetic layer. This unidirectional anisotropy exchange energy U_{ex} is experimentally found to be

$$U_{\text{ex}} = -\sigma_{\text{ex}} \mathcal{V}_{\text{FM}} t_{\text{FM}}^{-1} \left(\hat{\mathbf{M}} \cdot \hat{\mathbf{e}}_{\text{easy}} \right), \tag{6.11}$$

σ_{ex} is the interfacial energy per area and $\mathcal{V}_{FM} t_{FM}^{-1}$ is the interface area. Assuming that the antiferromagnetic and ferromagnetic layers are deposited during the same applied field, the easy direction of Eq. (6.11), $\hat{\mathbf{e}}_{easy}$, is the same as in Eq. (6.10). The exchange energy pulls the magnetization towards the single preferred direction.

6.4 External field response

The following section relates θ to the external field. It is assumed that the easy direction is perfectly aligned with the x-direction, $\hat{\mathbf{e}}_{easy} = \hat{\mathbf{x}}$, and that the external field is either perfectly aligned with the $\hat{\mathbf{x}}$ or $\hat{\mathbf{y}}$ directions. For a discussion of misalignments see Henriksen [98].

6.4.1 Total energy

Collecting the described energy contributions gives a normalized energy density of

$$\tilde{u} = \frac{U}{\mu_0 M_s \mathcal{V}_{FM}} = -\hat{\mathbf{M}} \cdot \mathbf{H}_{ext} - \frac{1}{2} H_K \left(\hat{\mathbf{M}} \cdot \hat{\mathbf{x}} \right)^2 - H_{ex} \hat{\mathbf{M}} \cdot \hat{\mathbf{x}} \tag{6.12}$$

where M_s is the saturation magnetization, and the anisotropy and exchange fields are given as $H_K = \frac{2K}{\mu_0 M_s}$ and $H_{ex} = \frac{\sigma}{t \mu_0 M_s}$, respectively.

6.4.2 Easy axis response

When the external field is applied along the easy direction, i.e. $\hat{\mathbf{x}}$-direction, the magnetization will also be confined to either $\hat{\mathbf{M}} = -\hat{\mathbf{x}}$ or $\hat{\mathbf{M}} = \hat{\mathbf{x}}$. Generally, the exchange energy is stronger than the uniaxial energy, so in zero external field the magnetization is aligned along the exchange direction. If a strong enough external field is applied against the exchange direction, then the magnetization will flip when $H_{ext} \leq -(H_{ex} + H_K)$. After the magnetization has flipped, the uniaxial energy works against the exchange energy, and if the external field is reduced the magnetization will flip back to the original position when $H_{ext} \geq -H_{ex} + H_K$. Overall this gives a hysteresis curve, as illustrated in Fig. 6.3, with a square box of width $2H_K$ and center at $-H_{ex}$. These curves are measured in Vibrating Sample Measurements (VSM) to determine the material parameters H_{ex}, H_K, as discussed in Section 8.5.1.

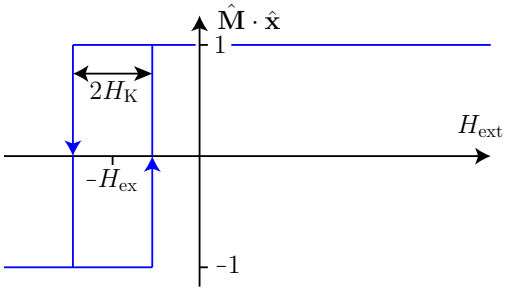

Figure 6.3: Illustration of the hysteresis curve when measuring the easy axis response.

6.4.3 Hard axis response

When the external field is applied in the $\hat{\mathbf{y}}$-direction it rotates the magnetization from the easy direction towards the $\hat{\mathbf{y}}$-direction and Eq. (6.12) can be rewritten as

$$\tilde{u} = -H_{ext} \sin\theta - \frac{1}{2} H_K \cos^2\theta - H_{ex} \cos\theta. \tag{6.13}$$

When H_{ext} is small compared to $H_{\text{K}} + H_{\text{ex}}$, θ is small and Eq. (6.13) can be linearly approximated and solved

$$\theta \approx \frac{H_{\text{ext}}}{H_{\text{K}} + H_{\text{ex}}}. \qquad \text{Low–field approximation.} \tag{6.14}$$

In the low-field approximation of Eq. (6.14), θ is proportional to the external field and the sensor output approximates to

$$V_y \approx \frac{I_x l \Delta\rho}{wt} \frac{H_{\text{ext}}}{H_{\text{K}} + H_{\text{ex}}} = I_x S_0 H_{\text{ext}} \tag{6.15}$$

where S_0 is the important low-field sensitivity

$$S_0 = \frac{l\Delta\rho}{wt} \frac{1}{H_{\text{K}} + H_{\text{ex}}}. \tag{6.16}$$

The whole simulated sensor output is plotted in Fig. 6.4. For stronger external fields the sensor outputs becomes non-linear. The peak output, i.e. $\theta = \pm\frac{\pi}{4}$, is achieved for $H_{\text{ext}} = \pm(H_{\text{ex}} + H_{\text{K}}/\sqrt{2})$. For even stronger external fields the sensor output diminishes as the magnetization angle increases towards $\theta = \pm\frac{\pi}{2}$.

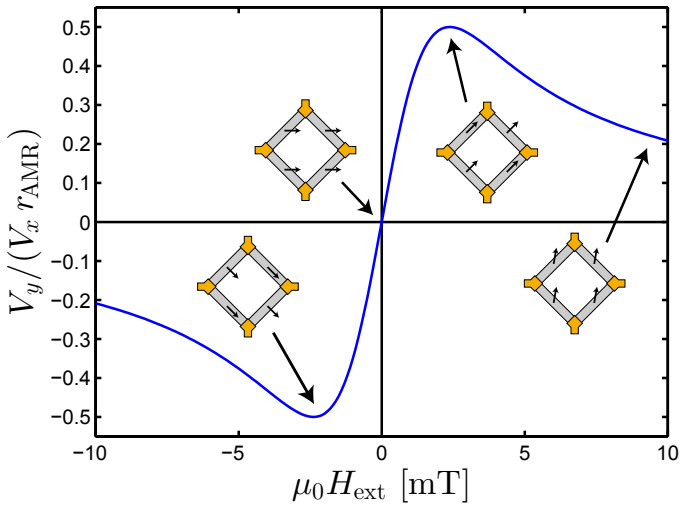

Figure 6.4: Calculated sensor output as function of the applied external field. Parameters used were $\mu_0 H_{\text{ex}} = 2.1$ mT and $\mu_0 H_{\text{K}} = 0.4$ mT.

6.4.4 Shape anisotropy

Besides the Zeeman, uniaxial anisotropy and exchange energies a slab of magnetic thin film is also subject to shape anisotropy. Figure 6.1 shows an elongated slab of magnetic material and its rotated coordinate system of the principal axes.

If the slab is magnetized along the y_{s} direction, a more energy requiring field is created outside the slab than if the magnetization is along x_{s}. Thus, the magnetic energy can be reduced by rotating the magnetization parallel to the longest side. Mathematically, the shape anisotropy is described by a demagnetization tensor, $\underline{\underline{N}}$, and a demagnetization field, $\mathbf{H}_{\text{De}}$, related as [99]

$$\mathbf{H}_{\text{De}} = -\underline{\underline{N}} \cdot \mathbf{M} \tag{6.17}$$

For a symmetrical system with principal axes along the coordinate axes, as in Fig. 6.1, the demagnetization tensor becomes diagonalized, with trace 1, and the energy can be calculated as [100]

$$\begin{aligned} U_{\mathrm{sh}} &= -\mu_0 \mathcal{V}_{\mathrm{FM}} \int_0^H \mathbf{M}\, \mathrm{d}\mathbf{H} = \mu_0 \mathcal{V}_{\mathrm{FM}} \sum_{i=x_{\mathrm{s}},y_{\mathrm{s}},z} \left(\int_0^{M_i} M_i N_i \mathrm{d}M_i \right) \\ \tilde{u}_{\mathrm{sh}} &= \frac{1}{2} M \sum_{i=x_{\mathrm{s}},y_{\mathrm{s}},z} N_i \left(\hat{\mathbf{M}} \cdot \hat{\mathbf{e}}_i \right)^2 . \end{aligned} \tag{6.18}$$

For a slab of dimensions $t \ll w < l$, N_z has a high value just below 1. This factor prevents the magnetization from pointing in the z-direction and limits $\mathbf{M}$ to the (x, y)-plane. Using $\mathbf{M} \cdot \hat{\mathbf{z}} = 0$ and remembering that the y_{s}-direction is perpendicular to the current direction, the energy can be simplified as

$$\tilde{u}_{\mathrm{sh}} = -\frac{1}{2} H_{\mathrm{sh}} \cos^2(\alpha - \theta) \tag{6.19}$$

with $H_{\mathrm{sh}} = M_{\mathrm{s}} (N_{y_{\mathrm{s}}} - N_{x_{\mathrm{s}}})$, which is positive when $l > w$. Note, that the $\tilde{u}_{\mathrm{sh}}$ depends on α, and for significant shape anisotropy, the assumption of the whole sensor having the same magnetization direction for all resistors is incorrect. Instead the resistors R_1 and R_3 with $\alpha = \frac{\pi}{4}$ have one magnetization direction, θ_+ while R_2 and R_4 with $\alpha = \frac{-\pi}{4}$ have another, θ_-, which are given by minimization of the energies

$$\tilde{u}_{\pm} = -H_{\mathrm{ext}} \sin\theta_{\pm} - \tfrac{1}{2} H_{\mathrm{K}} \cos^2\theta_{\pm} - H_{\mathrm{ex}} \cos\theta_{\pm} - \tfrac{1}{2} H_{\mathrm{sh}} \cos^2(\theta_{\pm} \mp \pi/4) \tag{6.20}$$

and the sensor output becomes

$$V_y = \frac{I_x \Delta\rho}{2} \frac{l}{wt} \frac{\sin(2\theta_+) + \sin(2\theta_-)}{2}. \tag{6.21}$$

Even in the low-field regime, a simple analytical solution does not exist when shape anisotropy is included, and instead Eq. (6.20) and Eq. (6.21) have to be solved numerically. In general θ_+ (θ_-) has a positive (negative) offset for zero external field and will be less sensitive to an external field. While the θ_+, θ_--offsets cancel out to first order, the sensor sensitivity is still reduced by the shape anisotropy. Figure 6.5 shows plots of the normalized sensor output for different values of the shape anisotropy field. The plots were calculated by minimizing Eq. (6.20) to find θ_+ and θ_- and inserting them into Eq. (6.21). For increasing values of $H_{\mathrm{sh}} \leq H_{\mathrm{ex}}$, the low-field sensitivity decreases, and the linear low-field-region becomes more "S "-shaped, but both the positions of the peaks and the peak-to-peak signal, V_{pp}, remain constant. Values of $H_{\mathrm{sh}} > H_{\mathrm{ex}}$ result in a decrease of V_{pp} and the sensor response can also become hysteretic. Overall, as the shape anisotropy increases the sensor becomes less sensitive, and in practice the sensor becomes unusable if $H_{\mathrm{sh}} > H_{\mathrm{ex}}$.

6.5 Magnetic field detection

As seen from Eq. (6.15), for small, usually < 1 mT, magnetic fields the sensor output increases proportionally to y-component of the experienced magnetic field and PHEB sensors are well suited for magnetic fields in the micro- and nano-tesla range. However, due to imperfect fabrication of the sensor, leading to variations in the bridge resistors, a small resistance offset can be present, and the sensitivity can vary between wafers. Therefore, the sensor should be characterized before use. This is discussed in Section 8.5.3.

6.6 Magnetic bead detection

When detecting the presence of magnetic beads two approaches can be used. The two methods are illustrated in Fig. 6.6. Either the beads can be magnetized by an external homogeneous field or by the inhomogeneous field due to the current in the sensor; the last is termed the sensor self-field method.

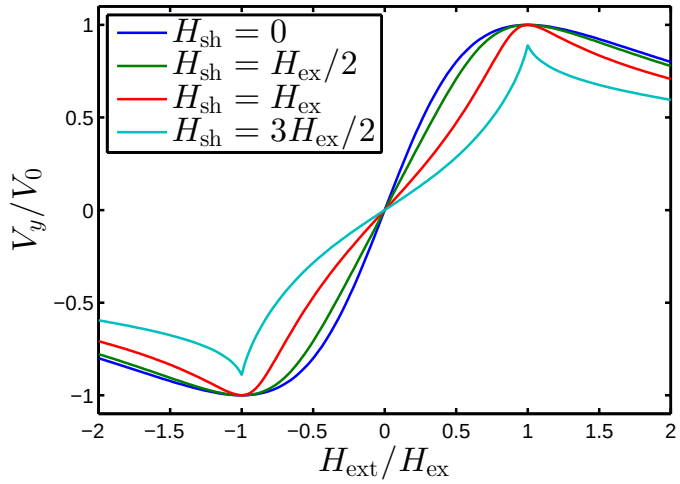

Figure 6.5: The response of a PHEB sensor vs. magnetic field, calculated from Eq. (6.20) and Eq. (6.21)) for increasing shape anisotropy field, H_{sh}. The calculations were performed for $H_K = 0$. The signal is normalized to that obtained for zero shape anisotropy, V_0. The Figure is adapted from Paper V.

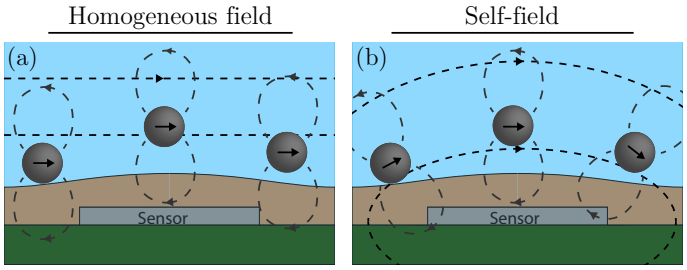

Figure 6.6: Illustration of the two magnetic bead detection schemes. (a) Beads magnetized by a homogeneous field. (b) Beads magnetized by the self-field.

6.6.1 Beads magnetized by a homogeneous field

Magnetic beads, magnetized by an external magnetic field, each produces a dipole field, which is superimposed on the original magnetic field, see Fig. 6.6a. Assuming the sensor is experiencing a homogeneous field, H_{hom}, when no beads are present, then the addition of magnetic beads modifies the experienced field to

$$H_{ext} = (1 + \beta)H_{hom} \tag{6.22}$$

where β is a constant to account for the bead field. β is zero if no beads are present and depends on the bead distribution and type. A more detailed discussion of the bead field is given in Part IV. By either doing measurements before and after injecting the bead suspension, or by a having a reference sensor, the bead contribution β can be measured. This can be linked to, e.g., the biological attachment of magnetic beads to the sensor surface.

6.6.2 Beads magnetized by the self-field

Due to the rotating nature of the dipole field, beads magnetized by a homogeneous field give different signal contributions depending on their position in regards to the sensor. Part IV will expand on this.

Figure 6.6a illustrates the problem, the two beads outside the sensor contribute with a positive field while the bead on top of the sensor contributes with a negative field. This is a general trend, and in the case of a perfect monolayer of beads, their added field cancels out. To prevent this, the sensor self-field, illustrated in Fig. 6.6b, can be used to magnetize the beads instead of an external homogeneous field. The self-field rotates around the sensor, thus the dipole moments of the beads vary with position. However, this spatial variation ensures that all beads contribute with a net positive field in the sensor [101].

While all beads provide a positive field contribution, when using the self-field, their field magnitudes vary with position. Generally, the beads closer to the sensor both experience a stronger self-field and their own field decays less. This yields a strong position dependence when using the self-field. This was investigated in detail by Hansen *et al.* [101] and their results can be found in Fig. 6.7, where the volume sensitivity is plotted as contours of the cumulative signal contribution. The calculation is made for a sensor subject to a homogeneous bead distribution taking up the half-plane above the sensor. 50 % of the signal arises from beads in a box with the same width as the sensor and a height of $z \approx w/4$. However, even though beads close to the sensor surface contribute a large part of the signal, beads magnetization by the self-field have successfully been used for both surface-based [53] and volume-base bead detection [41, 87].

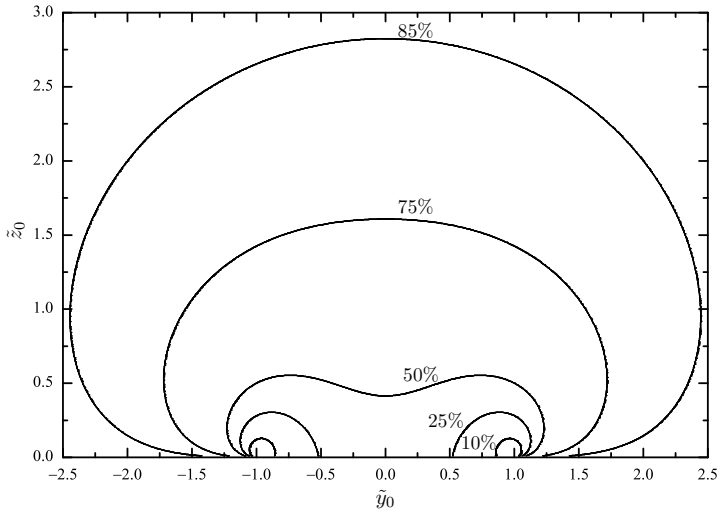

Figure 6.7: Sensor volume sensitivity when using the self-field plotted as contours of the cumulative signal. Calculations are done for a homogeneous bead distribution in the upper half-plane. The dimensions are normalized by half the sensor width $(\tilde{y}_0, \tilde{z}_0) = (\frac{2y}{w}, \frac{2z}{w})$. Figure is from Hansen *et al.* [101].

In general, two self-field contributions affect the sensor resistors, a field from the beads and a field from the other stack layers.

Stack contribution. As the sensor consists of more layers than the magnetoresistive permalloy layer, the current is partially shunted through these other layers. For an arbitrary resistor, as shown in Fig. 6.1, the shunted current creates a magnetic field in the permalloy layer given by

$$H_{\mathrm{sf}}^{\mathrm{stack}} = \gamma_0 I \tag{6.23}$$

where γ_0 is a constant depending on the sensor stack composition. Based on the directions in Fig. 6.1, γ_0 is positive (negative) if the majority of the shunted current is running above (below) the permalloy layer.

Bead contribution. Similar to the stack contribution of Eq. (6.23), the bead contribution is proportional to the resistor current and can be described as

$$H_{\mathrm{sf}}^{\mathrm{beads}} = \gamma_1 I \tag{6.24}$$

where γ_1 is a positive constant depending on the amount and distribution of beads over the resistor. A more detail analysis of γ_1 can be found in Hansen *et al.* [101].

Sensor output. The self-field contributions of Eq. (6.23) and Eq. (6.24) was described on a resistor level. For calculating the sensor output, one needs to remember that only half of the sensor current runs through a given resistor and that the self-field is along y_{s}, cf. Fig. 6.1, which for all bridge resistors is 45° offset from the y-direction. Taking these into account and using Eq. (6.15) the sensor output becomes

$$V_y = \frac{S_0(\gamma_0 + \gamma_1) I_x^2}{2\sqrt{2}}. \tag{6.25}$$

6.7 Summary

In this chapter, the theoretical response for planar Hall effect bridge (PHEB) sensors was derived. The PHEB consisted of magnetoresistive thin film resistors aligned in a Wheatstone bridge geometry. The PHEB sensor output, for low external fields, is given by Eq. (6.15)

$$V_y = I_x S_0 H_{\mathrm{ext}} \quad \text{where} \quad S_0 = \frac{l\Delta\rho}{wt}\frac{1}{H_{\mathrm{K}} + H_{\mathrm{ex}}}. \tag{6.26}$$

Section 6.4.4 discussed how shape anisotropy offsets the magnetization direction differently in the different sensor arms, which decrease the sensor sensitivity, and must not exceed the exchange field, if the sensor should be hysteresis free.

Finally, it was discussed how the PHEB sensor can be used to measure an external magnetic field and beads magnetized here-by. However, for this approach the signal contributions, from beads on top of, cancel out the contributions from beads outside, and in the case of perfect monolayer the sensor experiences no bead field. Instead, the simple solution of magnetizing the magnetic bead by the sensor self-field, from the bias current, can be used. This self-field gives an offset value from the current shunting through the none permalloy layers.

7

Sensor optimization for bead detection

Chapter 7 introduces and characterizes novel designs of PHEB sensors that are optimized for magnetic bead detection. First, the response to an external and the self-field is calculated for different sensor construction element, i.e., resistors with different orientations. This is used to design sensors that are only sensitive to the magnetic field from beads being magnetized by the sensor self-field. These sensor designs are fabricated and characterized as function of the external field, and by measurements of the dynamic response from a suspension of magnetic beads. Overall, Chapter 7 summarizes the result of Paper II.

7.1 Sensor construction elements

All the proposed sensors are made of the same magnetoresistive slabs, as in Fig. 6.1, but angled differently. By combining the previously derived results, Eqs. (6.3,6.14), the slab resistance can be rewritten as

$$R(\alpha) = R_0 + \sin(2\alpha) S_0 H_y \tag{7.1}$$

where R_0 is the average resistance defined in Eq. (6.4). As discussed in Section 6.6, the sensors can be subject to an external field and a self-field given by

$$H_y = H_{\text{ext}} + H_{\text{sf}} \cos\alpha \tag{7.2}$$

and the sensor response becomes

$$R(\alpha) = R_0 + \underbrace{\sin(2\alpha) S_0 H_{\text{ext}}}_{\text{External field}} + \underbrace{\sin(2\alpha) S_0 H_{\text{sf}} \cos\alpha}_{\text{Self-field}} . \tag{7.3}$$

Note, that the external field and self-field contributions of Eq. (7.3) have different α-dependences. The sign of the external field and self-field contributions can be seen in Table 7.1. Table 7.1 shows that the external field and self-field can be chosen independently by using the appropriate orientation. Combining Table 7.1 with Eq. (6.6) the Wheatstone bridge sensor geometry can be tailored to only be sensitive to the external magnetic field, only the bead self-field or a combination thereof.

Table 7.1: The sign of change in resistance based on the orientation, α and the external field and self-field contributions in Eq. (7.3).

Direction	↗	↖	↙	↘
α	$\frac{\pi}{4}$	$\frac{3\pi}{4}$	$\frac{-3\pi}{4}$	$\frac{-\pi}{4}$
External field	+	−	+	−
Self-field	+	+	−	−

7.2 Dynamic bead response

Throughout this thesis, the bead field is assumed to be instantaneous to the magnetizing field. However, just like in magnetophoresis, if the field is switching too fast, the bead response, i.e. the bead field, will lag behind the excitation field. While this dynamic bead response is not the focus of this thesis, it is used to characterize the sensors and their bead response in this chapter. While a full derivation of the dynamic bead response will not be given here, the result will be summarized to make the response curve understandable. Further information is found in Østerberg *et al.* [41, 86, 87].

Generally, the dynamic bead response is calculated using a complex bead susceptibility

$$\chi = \chi' - \mathrm{i}\chi'' = |\chi|\cos\varphi - \mathrm{i}|\chi|\sin\varphi \tag{7.4}$$

where χ' and χ'' are the in-phase and out-of-phase magnetic susceptibility, respectively. Both χ' and χ'' depend on the switching speed of the magnetic field, i.e. the frequency for a AC-field, which is shown in the second part of Eq. (7.4) where χ is written in terms of its magnitude $|\chi|$ and the phase-lag behind the excitation field φ. Further, the two constants β and γ_1 describing the field contributions from magnetic bead depends on the complex susceptibility of the magnetic beads, which is written explicitly by substituting

$$\begin{aligned} \beta &= \tilde{\beta}\chi_0 \\ \gamma_1 &= \tilde{\gamma}_1\chi \end{aligned} \tag{7.5}$$

where χ_0 is the DC susceptibility.

Two relaxation mechanisms enable the bead to follow the switching magnetic field. The whole bead can physically rotation to align with the magnetic field, this is called Brownian relaxation [102], or only the moment of the magnetic cores can rotate to align, this is called Néel relaxation [103]. The mean time for Néel relaxation increases exponentially with the volume of the magnetic core. For the relaxation measurement, thermally blocked 80 nm magnetic beads were used. In this case, the Néel relaxation time is on the order of seconds [86], which is assumed much longer than the Brownian relaxation time. Thus, Brownian relaxation is the dominating relaxation mechanism, and its timescale is characterized by the Brownian relaxation frequency f_B given by

$$f_\mathrm{B} = \frac{k_\mathrm{B}T}{6\pi\eta\mathcal{V}_\mathrm{h}} \tag{7.6}$$

where T is the absolute temperature, k_B is the Boltzmann constant, η is the dynamic viscosity of the liquid and $\mathcal{V}_\mathrm{h}$ is the hydrodynamic volume of the relaxing entity. Thus by measuring f_B, the hydrodynamic volume can be calculated, and any change herein changes f_B. By monitoring f_B, changes in hydrodynamic volume from, hybridization of biomolecule target or from target induced bead agglomerations, can be measured. This enables precise measurement on the whole sample volume and so-called lab-on-a-bead diagnostics.

The Brownian relaxation frequency is measured from the magnetic susceptibility. The relationship between χ and f_B was first described by Debye [104] for dielectric materials and is given by

$$\chi(f) = \chi' - \mathrm{i}\chi'' = \frac{\chi_0 - \chi_\infty}{1 + \mathrm{i}f/f_\mathrm{B}} + \chi_\infty \tag{7.7}$$

where χ_0 and χ_∞ are the DC and high-frequency susceptibilities, and f is the frequency of the AC field. The change in χ' and χ'' vs. the frequency can be seen in Fig. 7.1. For low frequencies, $f < f_\mathrm{B}$, the magnetic beads rotate in-phase with the magnetic field and the susceptibility is the DC value $\chi = \chi_0$. As the frequency approaches f_B the magnetic moment starts to lag behind and χ' starts decreasing and χ'' increases towards its maximum value $\chi''(f = f_\mathrm{B}) = \frac{\chi_0 - \chi_\infty}{2}$. For even higher frequencies, $f \gg f_\mathrm{B}$, the bead cannot follow the magnetic field and the susceptibility has decreased to $\chi = \chi_\infty$.

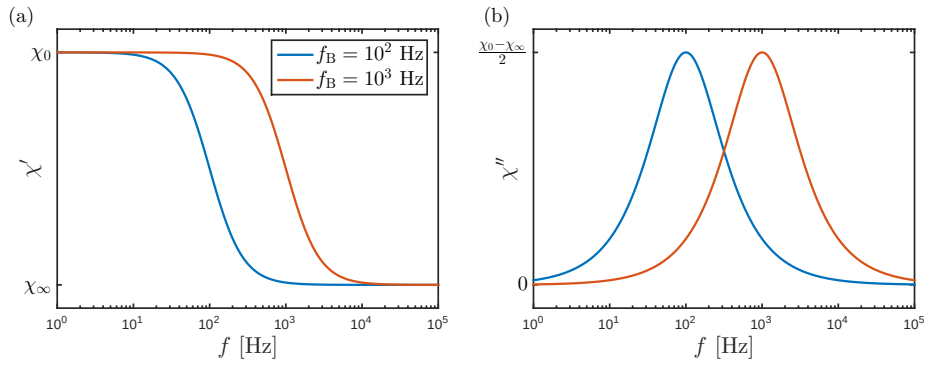

Figure 7.1: Dynamic bead response, χ' and χ'' vs. the driving frequency of the magnetic field.

7.3 New sensor designs

Paper II introduces two new sensor designs: The parallel PHEB (pPHEB) and the differential PHEB (dPHEB). Both, along with the original PHEB, are illustrated in the top row of Fig. 7.2. Further, the bottom row of Fig. 7.2 shows the three designs when meandering resistors are used to increase the sensor length without increasing the area too much. For all designs, the current is passed through the sensor in the x-direction and the bridge output voltage is measured along the y-direction. All the designs are a balanced Wheatstone bridge, and the sensor output can be calculated as $V_y = \frac{1}{2} I_x (R_1 - R_3)$.

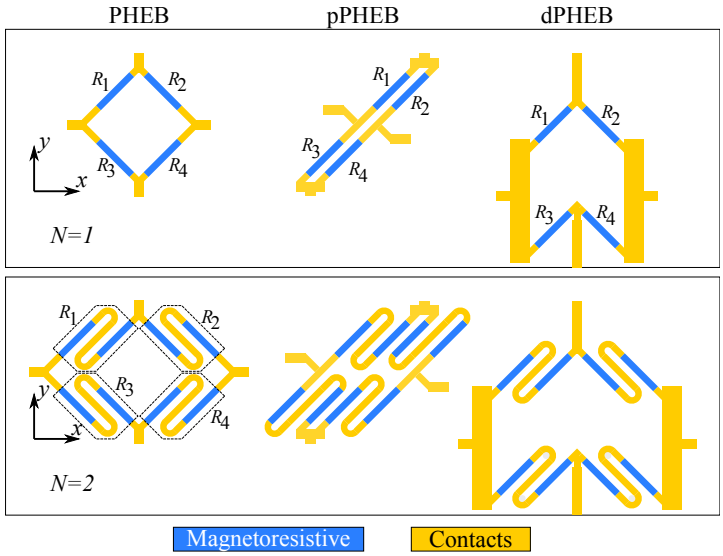

Figure 7.2: Illustrations of the three sensor types (PHEB, pPHEB, dPHEB) and their counterparts ($N = 2$) with meandering resistors. N is the number of segments for each resistor, blue is magnetic stack and yellow is contact stack. Figure is adapted from Paper II.

7.3.1 PHEB design

The PHEB design is the standard sensor, that was introduced by Henriksen *et al.* [40], where the first meander design was also introduced. For the meander design, all resistors in R_1 and R_4 has $\alpha = \frac{\pi}{4}$ and similarly for R_2 and R_3, $\alpha = \frac{-\pi}{4}$. Assuming all resistors experience the same external and self-field, the

sensor signal is given by

$$V_{\mathrm{PHEB}} = NS_0 \left(H_{\mathrm{ext}}(1+\tilde{\beta}\chi_0)I_x + \frac{\gamma_0 + \tilde{\gamma}_1\chi}{2\sqrt{2}} I_x^2 \right). \tag{7.8}$$

Eq. (7.8) shows that the PHEB design is sensitive to both the external field (including bead contributions) and the self-field.

7.3.2 pPHEB design

The first new design is the pPHEB (parallel PHEB) sensor geometry, which is designed to be nominally insensitive to the external magnetic fields while being maximally sensitive to magnetic beads magnetized by the sensor self-field. This is done by having $\alpha = \frac{\pi}{4}$ for R_1 and R_4 and $\alpha = \frac{-3\pi}{4}$ for R_2 and R_3, which makes the self-field contributions additive while the external field contributions cancel out. The sensor signal is given by

$$V_{\mathrm{pPHEB}} = NS_0 \frac{\gamma_0 + \tilde{\gamma}_1\chi}{2\sqrt{2}} I_x^2 \tag{7.9}$$

where the signal due to the external field is eliminated.

7.3.3 dPHEB design

The second new design is a differential design, the dPHEB (differential PHEB), which is sensitive to the difference in magnetic fields between the top and bottom of the sensor and where the influence of external variables has been minimized. This enables analyte detection with an on-sensor subtraction of the background signal due to unspecifically bound beads and temperature effects. For equal conditions between top and bottom, the sensor is designed to eliminate all field sensitivity by having $\alpha = \frac{\pi}{4}$ for R_1 and R_3 and $\alpha = \frac{-\pi}{4}$ for R_2 and R_4, which gives

$$V_{\mathrm{dPHEB}} = NS_0 \left(\frac{1}{2} H_{\mathrm{ext}} \Delta\tilde{\beta}\chi_0 I_x + \frac{\Delta\tilde{\gamma}_1\chi}{4\sqrt{2}} I_x^2 \right). \tag{7.10}$$

where Δ denotes the difference between the top and bottom branches, such that $\Delta\tilde{\beta} = \tilde{\beta}_{\mathrm{top}} - \tilde{\beta}_{\mathrm{bottom}}$ and $\Delta\tilde{\gamma}_1 = \tilde{\gamma}_{1,\mathrm{top}} - \tilde{\gamma}_{1,\mathrm{bottom}}$. For the dPHEB design, the sensor output is zero unless there is a difference between the top and bottom branches

7.4 Lock-in measurements

The sensors are biased by an AC current and the sensor outputs are measured using lock-in technique. A discussion of lock-in technique and how the signals are calculated is given in Section 8.4. Note, that the dual-channel lock-in amplifiers measure $V_n = V_n' + \mathrm{i}V_n''$, i.e. both the in-phase and out-of-phase of the nth harmonic signal. The calculated in-phase and out-of-phase 1$^{\mathrm{st}}$ and 2$^{\mathrm{nd}}$ harmonic signals are summarized in Table 7.2. Note, that the in-phase 2$^{\mathrm{nd}}$ harmonic sensor signal V_2' is proportional to the out-of-phase magnetic susceptibility χ'', and that the out-of-phase 2$^{\mathrm{nd}}$ harmonic sensor signal V_2'' is linearly related to the in-phase magnetic susceptibility χ'.

7.5 Experimental setup for test of new designs

To characterize the new designs, sensors were tested in terms of their response to a varying external field and the dynamic response of the bead signal vs. frequency of the self-field.

Table 7.2: 1st and 2nd harmonic in-phase and out-of-phase signals calculated for the three sensors designs. The table should be read horizontally such that the prefactor has to be multiplied with each of the sensor signals in each row. The table is adapted from Paper II.

	Prefactor	PHEB	pPHEB	dPHEB
V_1'	$\frac{1}{\sqrt{2}}NS_0I_{\mathrm{AC}}$	$H_y(1+\tilde{\beta}\chi_0)$	0	$\frac{1}{2}\Delta\tilde{\beta}H_y\chi_0$
V_1''	$\frac{1}{\sqrt{2}}NS_0I_{\mathrm{AC}}$	0	0	0
V_2'	$-\frac{1}{8}NS_0I_{\mathrm{AC}}^2$	$\tilde{\gamma}_1\chi''$	$\tilde{\gamma}_1\chi''$	$\frac{1}{2}\Delta\tilde{\gamma}_1\chi''$
V_2''	$-\frac{1}{8}NS_0I_{\mathrm{AC}}^2$	$\gamma_0+\tilde{\gamma}_1\chi'$	$\gamma_0+\tilde{\gamma}_1\chi'$	$\frac{1}{2}\Delta\tilde{\gamma}_1\chi'$

7.5.1 Fabricated sensors

PHEB, pPHEB and dPHEB sensors with $N = 1, 2$ and 3 were fabricated in-according with Section 8.2. The sensors had dimensions of $l \times w = 250$ µm$\times 25$ µm and a magnetic stack of Ta(3 nm)/$Ni_{80}Fe_{20}$(30 nm)/ $Mn_{80}Ir_{20}$(20 nm)/Ta(3 nm), which was further protected by a 1 µm thick layer of Ormocomp, to prevent pin holes and electrolysis.

7.5.2 Fluid system

For measuring the Brownian relaxation frequency a shallow microfluidic channel with dimensions length × width × height = 5 mm × 1 mm × 0.1 mm was used. And the dPHEB sensors were designed such that the bottom row is placed outside the microfluidic channel where $\tilde{\gamma}_{1,\mathrm{bottom}} = 0$.

7.5.3 External field measurements

For the external field measurements, the setup described in Section 8.3 was used. When measuring the 1st harmonic in-phase response, V_1', a sensor AC current of amplitude $I_{x,\mathrm{AC}} = 1$ mA and frequency $f = 67$ Hz was used. However, when measuring the 2nd harmonic in-phase response, V_2'', the sensor current was increased to $I_{x,\mathrm{AC}} = 20$ mA.

7.5.4 Dynamic bead measurements

Before performing the dynamic bead measurements, a reference measurements with Milli-Q water in the fluidic channel was made for correcting the influence of the measurement setup. Then a 1 mg/mL suspension of plain 80 nm BNF-starch beads (Micromod, Germany) was injected into the fluidic channel and left stagnant for ~ 30 min.

The 2nd harmonic sensor response was measured by decreasing the external field frequency from 10.9 kHz to 1.9 Hz in 25 logarithmically equidistant steps. Between each data point, a reference point was recorded at 482 Hz to facilitate monitoring of the time dependence of the signal.

7.6 Results

7.6.1 External field characterization

To test the predicted sensor responses of Table 7.2, the sensor response vs. magnetic field was measured for all sensor types. Fig. 7.3a and Fig. 7.3b shows the measured V_1' and V_2'', respectively, for all three sensors when applying a varying external magnetic field. Note, that the signal from dPHEB and pPHEB are both multiplied by 100 to be visible on the same scale. Similarly V_2'' for the dPHEB sensor is multiplied by 50.

PHEB response. As expected the PHEB sensor output is proportional to the applied external field for small fields (less than 2 mT), and only little hysteresis and offset is seen. As seen in Fig. 7.3b when the slope of V_1' decreases with the applied magnetic field, so does the V_2'' signal due to constant γ_0 and changing S_0.

pPHEB response. The measured V_1' for the pPHEB sensor is about 500 times smaller than the signal from the PHEB, and thus the signal from the applied field is very efficiently canceled out. However, the 2$^{\text{nd}}$ harmonic out-of-phase signal changes significantly with the applied magnetic field and increases from 40 µV at zero field to 51 µV at 1 mT.

dPHEB response. The dPHEB 1st harmonic response resembles that of the PHEB but with a 50 times smaller sensitivity. Likewise, the 2$^{\text{nd}}$ harmonic signal is also 50 times less sensitive to the external field. This design thus effectively cancels the influence of the external field for dynamic bead measurements.

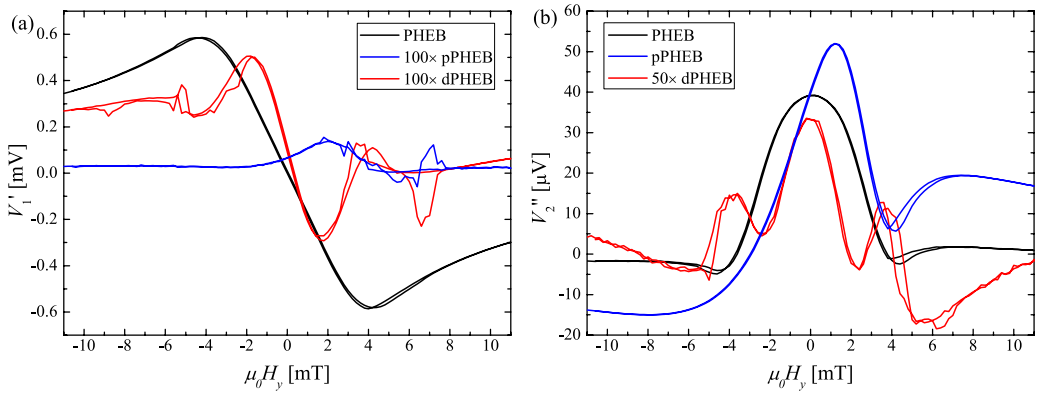

Figure 7.3: External field response from the three sensor types with $N = 1$. (a) V_1', (b) V_2''. Note, that some of the signals have been multiplied by 50 or 100. Similar results were obtained for $N = 2$ and $N = 3$ but with twice and thrice the amplitude. The figure was adapted from Paper II.

7.6.2 Dynamic bead measurements

In Fig. 7.4 the in-phase and out-of-phase second harmonic dynamic bead signals are plotted. The signal is normalized with N, and all sensors show the expected behavior. V_2'' decreases around the Brownian relaxation frequency and the phase-lag, V_2', is at its maximum value here. The signal amplitude is proportional to N and as expected dPHEB sensors yields half the signal of the PHEB or pPHEB sensor. As all nine spectra have the same shape, all the designs are viable for bead measurements.

7.6.3 Discussion

In general, the fabricated sensors perform as predicted, all signal amplitudes scaled with N, and only the PHEB sensed the external field while measuring V_1'. The small dPHEB V_1' signal is likely due to small imbalance of the design. When measuring V_2'' without an external field, the PHEB and pPHEB showed the same magnitude of response, due to γ_0, while the response of the dPHEB was 50 times smaller. For varying external field the PHEB sensor has a flat V_2'' response to the external field, and a small applied field will not interfere with bead measurements. However, for the pPHEB sensor, V_2'' was sensitive to external field. This behavior is attributed to the lower symmetry of the design.

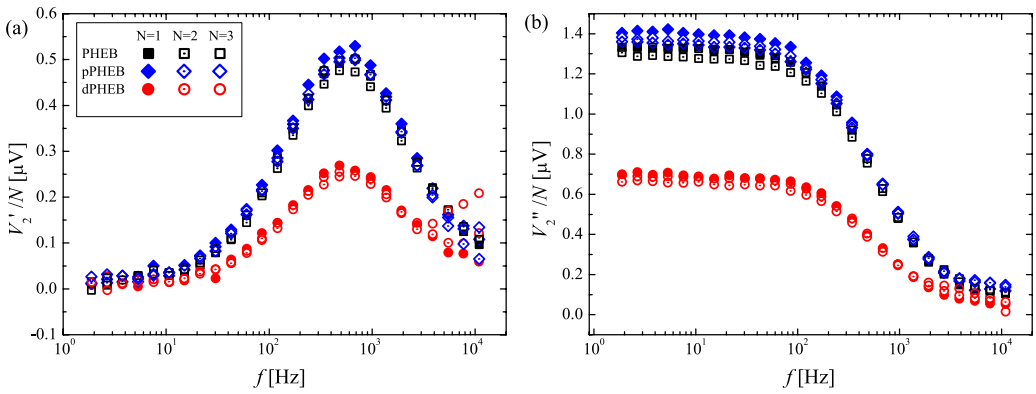

Figure 7.4: 2^{nd} harmonic bead measurements from nine different sensors. (a) In-phase corresponding to χ''. (b) Out-of-phase corresponding to χ'. Note, that all measurements have been normalized with N. The signal level measured in the absence of magnetic beads was subtracted from all spectra. The figure was adapted from Paper II.

7.6.4 Sensor applications roundup

Each sensor design has its pros and cons and is thus suited for different applications.

PHEB sensor. The standard PHEB sensor can be used for both external and self-field detection. It is the only sensor that is sensitive to the external field, which has the advantage that the PHEB sensor can be used to characterize the low-field sensitivity S_0. The PHEB sensor is general applicable as most measurement can be done with it, but self-field bead detection should be carried out in near-zero magnetic conditions.

pPHEB sensor. The pPHEB sensor is more compact than the PHEB sensor, which allows for a denser array in the channel, and the close resistors are less affected by temperature or a magnetic gradient. It could be imagined that the self-field from the close resistors would partially cancel out, but Fig. 7.4 shows that this is not the case. Further, as the sensors have the lowest 1^{st} harmonic output, the lock-in amplifiers will be able to better resolve the 2^{nd} harmonic signal. Overall the pPHEB design is better suited for dynamic bead measurements without an external field, for example measuring V_2'' to get the Brownian relaxation frequency from a bead suspension.

dPHEB sensor. For the dPHEB sensor both the self-field offset and the external field sensitivity was reduced 50 times. Thus, the dPHEB sensor is optimal for application where small changes in V_2'' has to be measured, for example, weak bead fields when detecting surface bound magnetic beads as in Chapter 12.

7.7 Conclusion

Paper II showed a theoretical analysis of the construction elements for Wheatstone bridge magnetic sensors and introduced two new sensor design the dPHEB and pPHEB. These two new sensors designs, along with the original PHEB sensor, were fabricated and characterized by their response to an external magnetic field and by their dynamic response from beads magnetized by the sensor self-field. The pPHEB sensor uses an asymmetric bridge design to only be sensitive to the self-field contribution. As expected the pPHEB efficiently canceled the signal from a low external field and provided a more compact design, which is suitable for dynamic magnetic measurements of the Brownian relaxation frequency. The dPHEB design is symmetric but performs differential measurements between the top and bottom part. This eliminates the self-field offset from current shunting in the magnetic stack, and the dPHEB is

thus an optimal choice for measuring small second harmonic fields like that from surface-based bead hybridization.

8

Experimental sensor setup

Chapter 8 goes through the experimental setup used for upcoming measurements. The experimental setup is based around Planar Hall Effect Bridge (PHEB) sensors. First, the cleanroom procedure for fabricated the sensor chips is explained. Secondly, the experimental setup and its subparts are reviewed, and finally, the different measurements procedures are explained. The measurements procedures usually fall into one of the two categories, PHEB sensor characterization or magnetic bead measurements. If not noted otherwise, all chemicals in this chapter were bought from Sigma-Aldrich Denmark ApS (Brøndby, Denmark).

8.1 Sensor geometries

Two examples of the fabricated sensor chips can be seen in Fig. 8.1. Figure 8.1a shows a dPHEB sensor chip for bead measurements, with five dPHEB sensors all located inside the fluid channel, see Fig. 8.6a, and one PHEB sensor for characterization of the chip sensitivity, see Section 8.5.3. Likewise, Fig. 8.1c shows a PHEB sensor chip, used for testing sensor geometries, with six different sensors. All chips had a physical size of 7.5 mm $\times$ 4.5 mm and six sensors with contacts at the same location. Figure 8.1b and Fig. 8.1d shows a close-up of a single dPHEB and PHEB sensor, respectively. A typical sensor had resistors of dimension $l \times w = 250$ µm $\times$ 25 µm, and round corners to avoid high potential gradients. Further, most sensors were surrounded by the magnetic stack, as in Fig. 8.1b, only offset by a 3 µm gap, to reduce shape anisotropy.

8.2 Sensor fabrication

The following section describes the fabrication procedure for PHEB sensors. A detailed description can be found in Appendix C and an illustration of the process flow can be seen in Fig. 8.2. The PHEB sensors were fabricated in the Danchip clean room and used three photolithography masks: One for the magnetic stack, one for the contact stack and one for the protective coating.

A detailed fabrication guide can be seen in Appendix C. An overview is illustrated in Fig. 8.2 and can be summed up as

- P-type silicon wafers, with a thermally grown oxide layer of 1 µm is used.
- Photoresist is spun and patterned by the magnetic-stack mask. The photoresist is reversal baked and developed.
- The magnetic stack, consisting of e.g. Ta (13 nm)/$Ni_{80}Fe_{20}$ (30 nm)/$Mn_{80}Ir_{20}$ (10 nm)/Ta (3 nm), is deposited in a constant field of 20 mT and defined by liftoff.
- Photoresist is spun and patterned by the contact-stack mask. The photoresist is reversal baked and developed.
- The contact stack, consisting of Ti (10 nm) / Pt (100 nm) / Au (100 nm) / Ti (10 nm), is deposited and defined by liftoff.

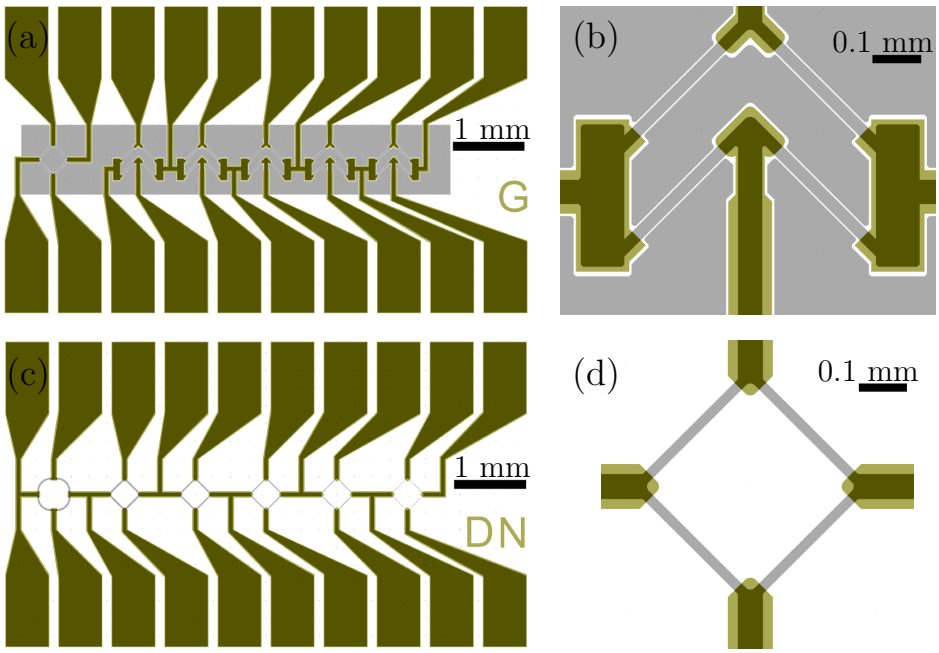

Figure 8.1: (a),(c) Illustrations of two examples of PHEB chips and (b),(d) a sensor from each chip. The gray color indicate where only the magnetic stack is present, light green indicate only contact stack and dark green is both magnetic and contact stack.

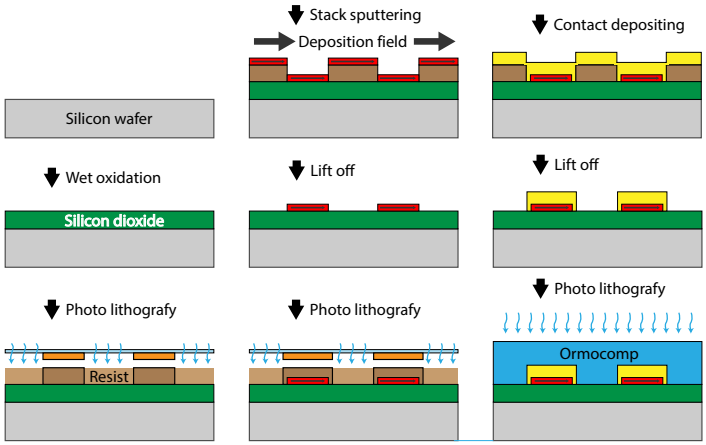

Figure 8.2: Illustration of the sensor fabrication process flow. After the nine displayed steps, the wafer is diced into single chips. The figure is not to scale. Note, that some of the photolithography substeps have been omitted but can be found in Fig. 3.3.

- A hybrid organic-inorganic polymer passivation layer, Ormocomp®, is spun to a thickness of 1 µm. The Ormocomp® is then patterned by the protective-coating mask, baked, developed and finally hard-baked.
- The wafer is diced.

The following sections describe these fabrication steps in further detail.

8.2.1 Magnetic stack deposition

The magnetic stack was deposited in the Kurt J. Lesker CSM-18 magnetron sputter system in an applied field of 20 mT. For some of the work in Part II a copper layer was added to the stack. Figure 6.2b illustrates the magnetic stack, and the purpose of the different layers are:

Tantalum. Reduces lattice mismatching and improve adhesion to both silicon-oxide and contact-stack.

Nickel-iron. The ferromagnetic material which is magnetoresistive.

Copper. An intermediate copper layer for weakening the exchange coupling between the ferromagnetic and antiferromagnetic material.

Manganese-iridium. Antiferromagnetic material that through exchange coupling defines the easy direction in the nickel-iron layer, cf. Section 6.3.

8.2.2 Contact stack deposition

The electrical contact stack was deposited by e-beam evaporation and always had a composition of Ti (10 nm) / Pt (100 nm) / Au (100 nm) / Ti (10 nm). Before deposition, the wafer should undergo a sputter cleaning process to reduce contact resistance between the magnetic and contact stack.

8.2.3 Protective coating

To prevent electrolysis due to the bias voltage, the sensors were passivated with Ormocomp® (Micro resist technology GmbH, Berlin, Germany). Ormocomp® is a hybrid organic-inorganic polymer curable in ultraviolet (UV) light, and like other photoresist it can be spun on the wafer. A 1 µm thick Ormocomp® layer was spun on each wafer, then defined by UV lithography, to not cover the sensor contact pads, and developed. Last, the Ormocomp® was hard-baked for 3 hours at 150° C to evaporate its solvent.

8.2.4 Sensor functionalization

Some of the PHEB sensors were used for biological sensing, with aptamers or DNA functionalized on the surface, cf. Chapter 12. This section describes the process of functionalizing the sensor with DNA probes. The DNA probes were purchased from DNA Technology A/S (Risskov, Denmark). Using 3-Aminopropyltriethoxysilane (APTS) and Glutaraldehyde, the DNA-probes were covalently bound to the Ormocomp surface. Figure 8.3 shows an overview of the surface functionalization procedure along with the chemical structure of the ingredients. The practical procedure for each chip was

1. Surface activation by immersing in 45 % H_2O_2 for 10 min.
2. Rinse in Milli-Q and dry in N_2 stream. Wash in acetone for 2 min.
3. Immerse the chip in 10 % v/v solution of 3-Aminopropyltriethoxysilane (APTS) in acetone for 30 min.
4. Wash in acetone and dry in N_2 stream.
5. Immerse the chip in 5% v/v solution of glutaraldehyde in Milli-Q water for 30 min.
6. Wash in Milli-Q and dry in N_2 stream.

From here on, the sensor surface needed to be selectively exposed to the DNA probes. To only functionalize the top half of a dPHEB sensor, the DNA probes were spotting using a Nanoplotter with NanoTip (GeSim GmbH, Grosserkmannsdorf, Germany) at room temperature and at a controlled humidity of 65 %. Amino labeled DNA probes were diluted to 20 µM in 3× saline-sodium citrate (SSC) and tiny droplets hereof, approximately 100 micron in size, were used to selectively cover the sensor arms. The amino label then reacted with the glutaraldehyde while the droplets evaporated.

Finally, just before use, the sensor surface was blocked by immersing it in 1 mg/mL of bovine serum albumin (BSA) in phosphate buffered saline (PBS) for 20 min, and finished off by a last rinse in Milli-Q and drying in N_2 stream.

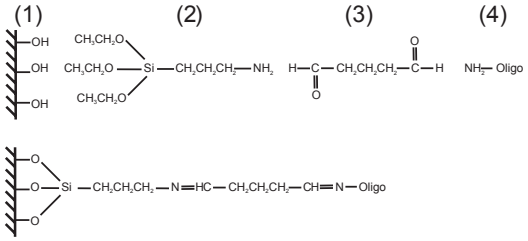

Figure 8.3: Schematic representation of the binding chemistry, including the four main components: (1) Surface activated chip, (2) APTS for silanization, (3) glutaraldehyde and (4) amino labeled oligonucleotide. The figure is from Rizzi [84].

8.3 Measurement setup

For the bead detection experiments, a setup developed by Rizzi was used [84]. An overview of the PHEB sensor setup can be seen in Fig. 8.4. The setup consists of a fluid system on top of the chip and with a syringe pump for fluid injection; a metal chip holder with a Peltier element connected to a programmable temperature controller; a microscope for optical inspection; and a printed circuit board (PCB), which provides electrical contact between the PHEB sensor chip and the data-logging lock-in amplifiers. Each part is described in the follow sections. Some measurements were unique to the analysis of each paper, and is described in the corresponding chapters.

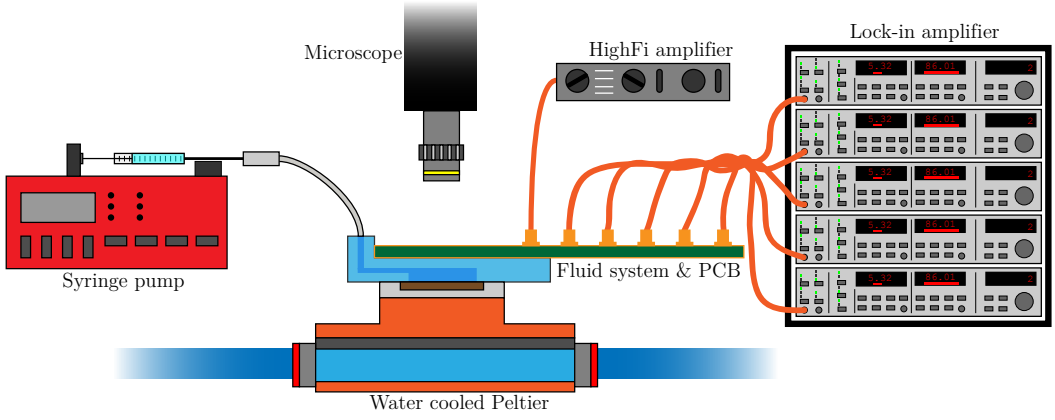

Figure 8.4: Overview of the typical PHEB sensor setup.

8.3.1 Temperature control

For controlling the temperature, e.g. keeping a constant temperature or ramping the temperature, the experimental setup used a programmable temperature controller and a Peltier element. Pictures of the temperature controlled chip well can be seen in Fig. 8.5. Figure 8.5a shows the Peltier element, that through PID control can heat or cool the connected copper stub. For improved stability and efficiency, the bottom part was kept at room temperature using a commercial CPU liquid cooler. As seen in

Fig. 8.5b, the temperature of the chip well was measured inside the copper stub and feedback to a LFI-3751 temperature controller (Wavelength Electronics Inc., MT, USA), which was controlled by LabView. The chip was placed in the aluminum well, and a very small amount of heat sink grease (Circuit Works® CT40-5) was used to ensure optimal thermal contact.

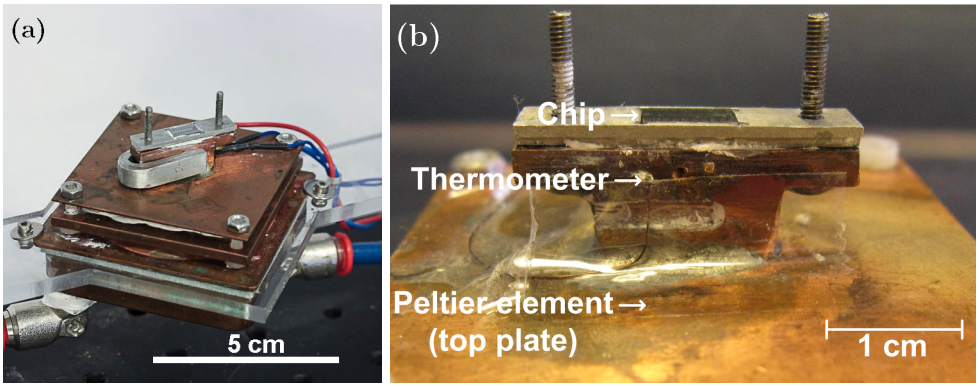

Figure 8.5: (a) Overview picture of the temperature controlled chip well. The picture is from Rizzi [84]. (b) Close-up of chip well subparts. Picture is from Paper III.

8.3.2 Fluid system and electrical contacts

The sensor chip was placed in an aluminum well, and a milled top, made from poly(methyl methacrylate) (PMMA), was placed on top to define the microfluidic system. A picture of the PMMA top can be seen in Fig. 8.6 along with the printed circuit board (PCB) and syringe pump. The fluid system was made from multiple layers of PMMA bonded together, and a rubber gasket made of polydimethylsiloxane (PDMS) defined the main chamber above the chip and ensured leak-proof operation. Two channels connected the inlet and outlet to the main chamber, which had dimensions of length × width × depth = 5 mm × 1 mm × 1 mm. The whole system, including connecting tubing, had a volume of ∼ 50 µL while the main chamber had a volume of 5 µL.

A PCB connected the power supply and lock-in amplifiers to the sensor chip. The PMMA top also provided contact between the sensor chip and the PCB by having spring loaded pins (POGO-PIN-5.94-1, Emulation Technology Inc., Camarillo, CA, USA) that are placed on top of the contact pads of the sensors. Different PCBs were used depending on whether the sensors were current or voltage driven.

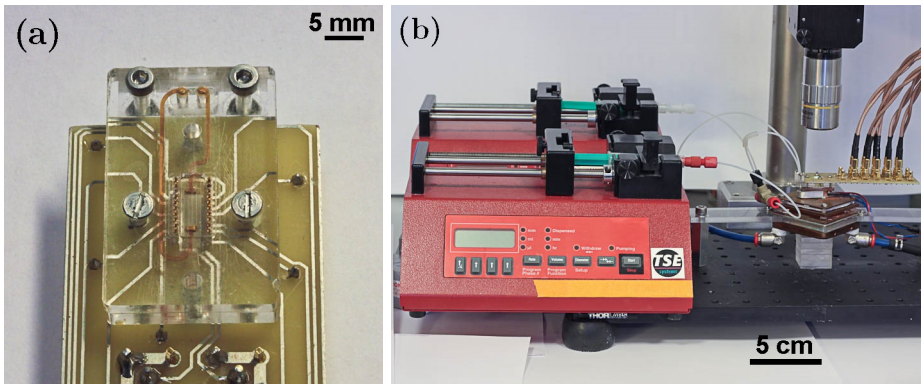

Figure 8.6: (a) Picture of the milled PMMA microfluidic system and PCB. (b) Picture of the syringe pump and connection to the microfluidic system. Both pictures are from Rizzi [84].

8.3.3 Sensor biasing

The measurement setup allowed for the sensors to be either voltage or current driven. When current-drive a Keithley 6221 Current Source (Keithley Instruments, USA) provided the AC current to the sensor and a trigger signal to the lock-in amplifiers. When voltage driven, one lock-in amplifier, Stanford Research Systems SR830 (Stanford Research Systems Inc., Sunnyvale, CA, USA), provided the bias voltage. However the SR830 could not provide the needed power and a hi-fi amplifier, Audiolab 8000A, amplified the bias signal to provide the needed power. The SR830 provided the trigger link to other lock-ins. In both cases, the AC bias had a frequency of 167 Hz, a frequency with low $1/f$-noise, high sampling rate and high susceptibility.

8.3.4 Helmholtz coil for external field

For characterizing the magnetic sensors, a set of Helmholtz coils could be attached to the setup. Figure 8.7 shows the Helmholtz coils, positioned around the chip holder. The Helmholtz coils had a radius of 6 cm, 400 number of windings, had negligible hysteresis and provided a field of $B_{\text{ext}} = 6.08\frac{\text{mT}}{\text{A}}I$. The coils were driven by either a KEPCO (KEPCO Inc., NY, USA) bipolar operational power supply, BOP 20-5D or for small fields a Keithley 2400 Sourcemeter. When using the KEPCO power supply a National Instrument USB 6211 data acquisition card provided the control voltage and the KEPCO provided a current of $I = 0.5\frac{\text{A}}{\text{V}}V$.

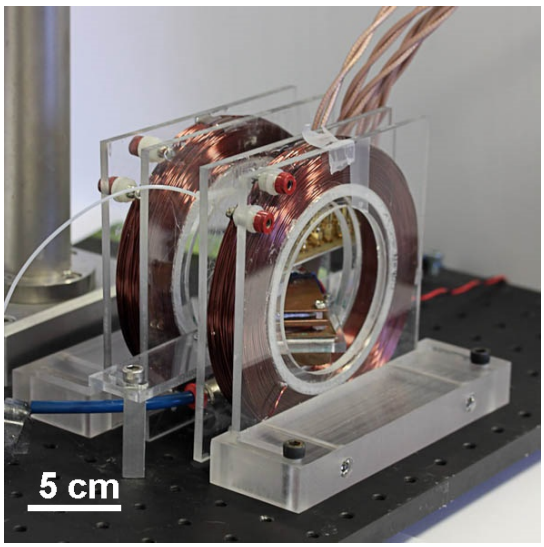

Figure 8.7: Picture of the Helmholtz coils around the chip holder. The picture is from Rizzi [84].

8.4 Lock-in amplification

To reduce noise, lock-in amplifiers are used for measuring the sensor signal. The AC sensor signals are first preamplified 100× by a Stanford Research Systems SR552, which also removed the DC signal by AC coupling. The preamplified AC signal is then measured by a Stanford Research Systems SR830 Digital Lock-in amplifier. The SR830 digitizes the input signal, then multiplies it with a reference signal, averages and scales it [105]. As the SR830 is a dual channel lock-in, the signal is multiplied by the two reference signals:

$$\begin{aligned} V_{\text{ref,in-phase}}(t) &= \sqrt{2}\sin(n2\pi ft + \varphi) \\ V_{\text{ref,out-of-phase}}(t) &= \sqrt{2}\sin(n2\pi ft + \varphi + \frac{\pi}{2}) \end{aligned} \tag{8.1}$$

where n is the n^{th} harmonic of the detection and φ is variable phase change with a default value of zero. For shortening the notation, n^{th} harmonic in-phase and out-of-phase signals are termed $V_n^{'}$ and $V_n^{''}$ respectively. Mathematically these are calculated as

$$\begin{aligned} V_n^{'} &= 100 \times \frac{\sqrt{2}}{2\pi} \int_0^{2\pi} V_y(t) \sin(n2\pi ft + \varphi)\ \mathrm{d}(2\pi ft) \\ V_n^{''} &= 100 \times \frac{\sqrt{2}}{2\pi} \int_0^{2\pi} V_y(t) \sin(n2\pi ft + \varphi + \tfrac{\pi}{2})\ \mathrm{d}(2\pi ft). \end{aligned} \tag{8.2}$$

when the sensor is biased by a AC current $I_x = I_{x,\text{AC}} \sin(2\pi ft)$. This enabled measuring the DC and AC field.

DC field measurement. For DC field measurements of $H_{\text{ext,DC}}$, the 1st harmonic in-phase response is

$$V_1^{'} = 100 \times \frac{I_{x,\text{AC}}}{\sqrt{2}} \left(S_0 H_{\text{ext,DC}} + R_{\text{offset}}\right) \tag{8.3}$$

where R_{offset} is any resistance offset due to imperfect fabrication. Note, that the logged voltage output is scaled with $100/\sqrt{2}$, which should be corrected for.

AC field measurement When measuring an AC field from the bias current, the 2nd harmonic out-of-phase response is

$$V_2^{''} = -100 \times \frac{I_{x,\text{AC}}^2}{2\sqrt{2}} S_0 \gamma \tag{8.4}$$

which should be corrected for when determining γ.

8.5 Measurement procedures

The following section describes some of the reoccurring measurements procedures. When new sensors have been fabricated, the wafer is usually characterized by measuring the magnetic thin-film properties using Vibrating Sample Magnetometer (VSM) and through four-point measurements on a transmission line structure. When the wafer has been characterized, the chips are used for either field measurements or bead measurements.

8.5.1 VSM

By vibrating the magnetic sample up and down in a DC magnetic field, an AC field from the vibrating sample is superimposed on the DC field, which can be detected by pick-up coils and lock-in amplifiers. By slowly varying the DC field, the magnetic thin film response to an external field can be measured. This measurement is usually done along the easy-axis or hard-axis of the material. As discussed in Section 6.4, when the magnetic thin film experiences a varying magnetic field along the easy axis, its magnetization will flip when the external field becomes stronger than the exchange field and anisotropy field. In general, this technique maps out the hysteresis curve, from which H_{ex} and H_{K} can be extracted.

In practice, each fabricated wafer had five VSM chips, like the one illustrated in Fig. 8.8a, and the VSM measurements were performed in a LakeShore model 7407. An example of an easy-axis hysteresis loop can be seen in Fig. 8.8b, and from this, the exchange and anisotropy fields can be read as the midpoint and half width of the hysteresis loop, respectively. Further, if the magnetic volume of the sample is known, the magnetic saturation, M_{s}, can be extracted from the magnetization magnitude.

8.5.2 Transmission line measurement

When measuring the AMR-ratio, $\Delta\rho/(\rho_{\parallel}/2 + \rho_{\perp}/2)$, a special chip was made for easy four-point measurements. An illustration of the chip can be seen in Fig. 8.9a, the chip has a long resistor along

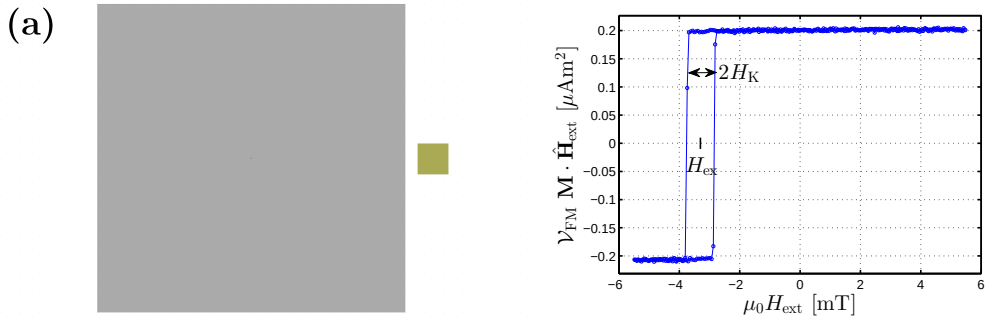

Figure 8.8: (a) Illustration of a VSM chip. Grey color is the 3 mm × 3 mm square pad of magnetic thin film. Light green is contact stack for orientation the chip in the VSM. (b) An example of typical VSM data when measuring the easy-axis hysteresis curve. The measured sensor had $t_{FM} = 30$ nm.

the x-direction. For measuring $\rho_{\parallel}$, the chip is placed in a strong magnetic field of 40 mT, generated by a permanent magnet magnetic frame, that saturates the magnetization to the x-direction, and the resistance is measured. By using the different contacts, this can be done for a couple of different lengths to determine if there is any contact resistance. Likewise for measuring $\rho_{\perp}$, the magnetization is saturated along the y-direction and again the resistance is measured.

Figure 8.9b shows an example of typical transmission line data. The resistance is perfectly linear, within the measurement precision, when varying the length, and $\rho_{\parallel}$ and $\rho_{\perp}$ can be obtained by fitting as the slopes.

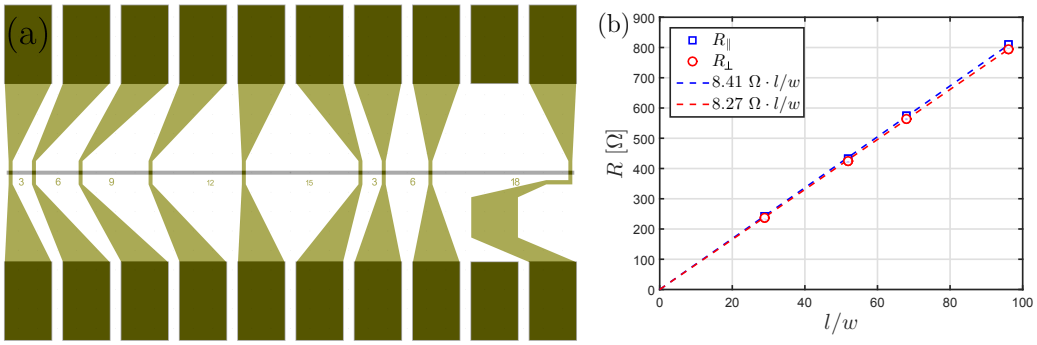

Figure 8.9: (a) Illustration of a transmission line chip, the gray is magnetic stack with width $w = 50$ µm. light green is the magnetic stack. (b) An example of typical transmission line data. The measured stack had an AMR-ratio of $r_{AMR} = 1.8$ %.

8.5.3 Magnetic field sweep

The Helmholtz coil setup in Fig. 8.7 was used for measuring the sensor response to an external field. The external field was aligned along the sensor y-direction, i.e. the hard-axis, and was swept back and forth as -11 mT $\rightarrow$ 11 mT $\rightarrow -11$ mT, this rotates the magnetization angle, and an example of the sensor output can be seen in Fig. 8.10. Generally, a low sensor current, e.g. $I_{x,AC} = 1$ mA, is sufficient for field sweeps, which reduces sensor heating and self-field contributions. The response in Fig. 8.10 is then fitted to the single domain model like

$$\tilde{u}_{\pm} = -H_{ext}\sin\theta_{\pm} - \tfrac{1}{2}H_K\cos^2\theta_{\pm} - H_{ex}\cos\theta_{\pm} - \tfrac{1}{2}H_{sh}\cos^2(\theta_{\pm} \mp \pi/4) \tag{8.5}$$

which for each data point, i.e. value of H_{ext}, is minimized for $\alpha = \pm\frac{\pi}{4}$, and used to calculate the expected output as

$$V_y = \frac{I_x R_0 r_{\text{AMR}}}{2} \frac{\sin(2\theta_+) + \sin(2\theta_-)}{2} + V_{\text{off}} \tag{8.6}$$

where V_{off} is a signal offset value. From the single domain model of Eq. (8.5) and Eq. (8.6) the values of $H_{\text{K}}, H_{\text{ex}}, H_{\text{sh}}, r_{\text{AMR}}, V_{\text{off}}$ can be extracted as fitting parameters. Further, the low-field sensitivity, S_0, is measured as the slope of the fitting function at low fields ($\mu_0 H_{\text{ext}} < 0.1$ mT), as the fitting function reliably matches the data and is free of noise.

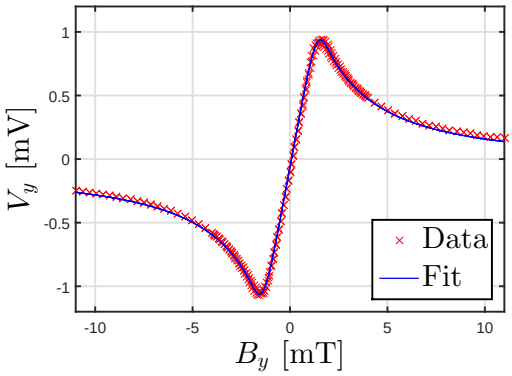

Figure 8.10: An example of a sensor field sweep and fit. The AC-bias current amplitude was $I_{x,\text{AC}} = 1$ mA. Preamplification has been corrected for.

8.5.4 Bead Measurement

When a magnetic bead suspension is injected into the microfluidic system, it will flow on top of the last five magnetic sensors of the chip. These sensors can then measure the magnetic field from the beads being magnetized by the sensor bias current. Figure 8.11 shows an example of a PHEB sensor response when Milli-Q water is exchanged with a bead suspension. The change to a magnetic suspension is easily detected and can be washed away again. Note, that the field offset, from current shunting, is bigger than the field from the bead suspension, 17 µV and 7 µV, respectively. An AC bias current of 20 mA and a bead suspension of concentration 10 mg/mL, were used. Both of these are around the maximum value, and thus the current shunting offset is important if a differential measurement is not used. Lastly, after injection, the beads signal can be seen to slowly increase. This is due to bead sedimentation, which can be corrected for by having a reference sensor or avoided if small beads (diameter ≤ 50 nm) are used.

Generally, for measurements on bead suspensions, the data analysis consist of correcting for preamplification and lock-in amplification. After this, three values are usually read off the time-series measurement: The initial signal due to current shunting, the signal after bead injection, $V_2''(t = 0)$, and the signal some time later, e.g. 30 minutes, due to beads binding to the sensor surface probes, $V_2''(t = 30\text{ min})$. The signal due to bead binding is given by the difference between the last two

$$\Delta V_2'' = V_2''(t = 30\text{ min}) - V_2''(t = 0) \tag{8.7}$$

8.6 LabView files used

If needed in the future the following LabView files were mostly used:

- `Global_PID-control.vi`

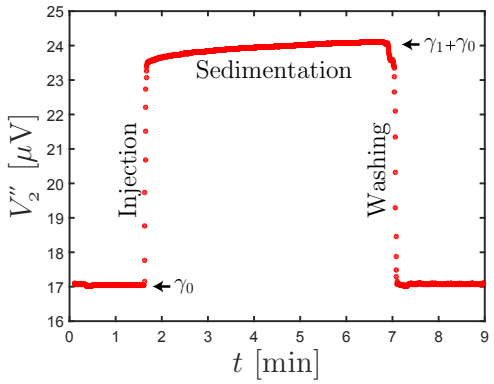

Figure 8.11: An example of the 2nd harmonic out-of-phase PHEB sensor response to a suspension of magnetic beads. The bead suspension was injected and washed at 1.5 and 7 min, respectively. γ_0 indicate the signal from current shunting through the non-permalloy layers, and γ_1 indicate the signal due to the bead suspension. An AC bias current of $I_{x,\mathrm{AC}} = 20$ mA was used and the bead suspension consisted of 80 nm beads at a concentration of 10 mg/mL. The signal has been corrected for amplification by preamplifier and lock-in amplifier.

- `GIORI_TEMPController.vi`
- `TempSweep.vi`
- `fieldsweepv3.11_NlockIns_NOSETTINGS.vi`
- `SignalVsTimeNOSETTINGS_NLockIns.vi`

9

Sensor heating for bead detection using the sensor self-field

Chapter 9 investigates PHEB sensor heating from using a strong bias current to magnetize a bead suspension. Rizzi *et al.* [85] have earlier measured how the low-field sensitivity increases with increasing temperature. This effect could be reduced by including an annealing step in the fabrication but the sensor still remains sensitive to the temperature. In Chapter 9 it is analyzed and measured how the sensor bias current alone can increase the sensor temperature. This is especially important to consider when doing a temperature dependent biological assay on the chip surface. Further, for self-field detection the signal scales with the square of the bias current. Often, the sensor noise originates from the readout electronics, and the signal-to-noise ratio can be increased by maximizing the bias-current for a given sensor self-heating.

Most importantly, Chapter 9 outlines a general approach for estimating the expected heating from any current and any magnetoresistive sensor geometry. By first measuring the dependence of the sensor resistance on the temperature, i.e. the temperature coefficient, the sensor resistance can subsequently be used as a thermometer. Then, the heat conductivity of the system can be extracted by measuring the sensor temperature increase, calculated from the resistance increase of the sensor, as a function of the bias current. Experimentally, 3 wafers with different magnetic stacks were fabricated and their temperature coefficient was measured. Further, for each wafer, the heat conductance of different PHEB sensor geometries were measured, by measuring the resistance increase for increasing bias current.

Theoretically, two analytical and one COMSOL model was developed. The simplest analytical model assumed heat transfer to be limited by the electrically insulating silicon-oxide layer. The expanded analytical model also included the thermal resistance of the silicon wafer. Both the expanded model and the COMSOL simulation fitted the measured heat conductances and can be used if measurements are not possible. Last, it is showed, that for the used setup, the above framework and results are accurate even when liquid is present on top of the chip, and that the protective coating, i.e. Ormocomp layer, does not shield the biology from the sensor heating. This chapter summarizes the result of Paper III.

9.1 Theoretical sensor heating

For all temperatures used in biological assays, the resistance of either a single permalloy resistor or a PHEB sensor is found to increase linearly with temperature, T, as

$$R(T) = R_0(1 + \alpha(T - T_0)) \tag{9.1}$$

where R_0 is the resistance at $T = T_0$ and α is the temperature coefficient.

The driving current or voltage heats the sensor. This Joule heating is given by

$$P^{DC}_{\text{heating}} = R(I_x)I_x^2 \tag{9.2}$$

where the bridge resistance dependence of the bias current has been explicitly written. Note, that, I_x in Eq. (9.2) is the RMS or DC value. When the sensor is hotter than its surroundings, heat is transported from the sensor. This dissipating heat flow is given by

$$P_{\text{dissipation}} = G_{\text{eff}}\Delta T \tag{9.3}$$

where G_{eff} is the effective thermal conductance. In equilibrium, the dissipated power must equal the Joule heating, and by combining Eqs. (9.1,9.2,9.3) the equilibrium resistance and temperature difference are given by

$$R(I_x) = \frac{R_0}{1 - \alpha R_0 I_x^2 / G_{\text{eff}}} \tag{9.4}$$

$$\Delta T = \frac{1}{\frac{G_{\text{eff}}}{R_0 I_x^2} - \alpha}. \tag{9.5}$$

The materials of the magnetic sensor, see the sensor cross-section in Fig. 6.2b, can generally be categorized into either good or bad thermal conductors. The metals and alloys of the magnetic stack and the silicon substrate are generally good heat conductors while the silicon dioxide and protective coated are generally bad heat conductors. Note, that the sensor stack is surrounded by bad thermal conductors. However, as silicon is a good thermal conductor, the heat is expected to primarily flow through the thin silicon dioxide underneath the sensor, to get to the big silicon substrate. Because the thickness of the SiO_2 layer is much smaller than the sensor width, the heat-flow is expected to be approximately vertical through the SiO_2 under the sensor. In this case, the heat conductance is given by

$$G_{\text{SiO}_2} = \kappa_{\text{SiO}_2}(4wl)/t_{\text{SiO}_2}. \tag{9.6}$$

where κ_{SiO_2} is the SiO_2 thermal conductivity (bulk value: $\kappa_{\text{SiO}_2} = 1.4$ W/(m °C)) and t_{SiO_2} is its thickness. The simple model of Eq. (9.6) can be expanded to also include the heat resistance of the silicon substrate. As the width of the resistor elements is small compared to the wafer thickness, the resistor is approximated by a point surface on the wafer cross-section, from where the heat flows radially away into the substrate. This radial heat flow can be approximated as heat conductance through a cylinder shell running along the resistor with inner radius $r_{\text{inner}} = \frac{w}{2}$ and outer radius $r_{\text{outer}} = t_{\text{wafer}}$, see Fig. 9.1 for an illustration. Including this approximation, the combined heat conductance is

$$G^{-1}_{\text{Si+SiO}_2} = \frac{t_{\text{SiO}_2}}{\kappa_{\text{SiO}_2}(4wl)} + \frac{\ln(2t_{\text{wafer}}/w)}{\kappa_{\text{Si}}\pi 4l}, \tag{9.7}$$

where κ_{Si} is the thermal conductivity of silicon (bulk value: $\kappa_{\text{Si}} = 149$ W/(m °C)).

If a known limit for the acceptable sensor self-heating is defined, for example by the bioassay requirements, Eqs. (9.2) and (9.3) can be rearranged to find the maximum current

$$I_{\Delta T} = \sqrt{\frac{G_{\text{eff}}\Delta T}{R}} \approx w\sqrt{\frac{\kappa_{\text{SiO}_2}\Delta T}{t_{\text{SiO}_2} R_s}} \tag{9.8}$$

where R_s is the sheet resistance of the sensor and the simplest model of Eq. (9.6) has been used in the last approximation. Note, in Eq. (9.8) that the maximum current is independent of the sensor length and approximately proportional to w.

9.2 Thermal COMSOL model

A 2D COMSOL model was made for comparison of the simple heat networks of Eqs. (9.6,9.7) to the full geometry. The model (Fig. 9.1) consists of a nickel domain (pink domain in Fig. 9.1; $w \times 55$ nm), which emulates a sensor with $t_{\text{FM}} = 30$ nm, on a silicon-dioxide domain (green domain; 2000 µm × 1 µm) on top of a silicon domain (gray domain; 2000 µm × 500 µm). The bottom boundary of the silicon domain was set to 25°C (red boundary in Fig. 9.1) while all other boundaries were set to insulating (blue boundary), $\mathbf{n} \cdot \nabla T = 0$, with $\mathbf{n}$ being the normal vector. The top boundary was assumed insulating as the measurements were done with air, a very poor thermal conductor, in the channel. However, measurements with water in the channel are discussed in Section 9.5. The nickel domain was changed to a uniform heat source, $Q = 2.5 \cdot 10^{14}$ W/m^3. All material parameters were taken from the COMSOL material library. The width of the nickel domain was varied from 5 µm to 25 µm and the steady-state mean nickel temperature was recorded for each configuration, which was used to calculate the heat conductance of the system.

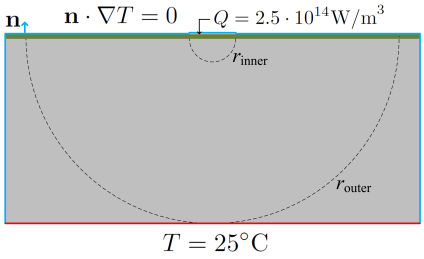

Figure 9.1: 2D COMSOL model of a cross-section of a sensor arm. The sensor arm cross-section is modeled as a uniform heat source. The figure is adapted from Paper III

9.3 Experiments

Measurements were done on three wafers with the stack seen in Fig. 6.2b but with no copper layer and with permalloy thicknesses of $t_{\mathrm{FM}} = 10, 20$ and 30 nm. For each wafer a chip with five different PHEB sensors was used for all measurements. The sensors had a fixed length of $l = 250$ µm and different widths of $w = 5, 10, 15, 20$ and 25 µm, respectively. The sensors were current driven, as discussed in Section 8.3, but with a DC current and both the ordinary sensor output, V_y, and voltage drop measured along the x-direction, V_x, were measured simultaneously. For this to be possible, each sensor was measured on individually by two lock-in amplifiers.

Last, to investigate if the sensor current can be used for purposefully heating the sensors, e.g. for DNA melting experiments; measurements were done on a fourth wafer made of Pyrex Borosilicate glass. The wafer had the same stack with $t_{\mathrm{FM}} = 30$ nm and a PHEB sensor of dimensions $l \times w = 250$ µm $\times$ 25 µm was used.

9.4 Results

9.4.1 Bridge resistance vs. temperature

Paper III outlines the general applicable approach of using the sensor resistance, $R(T)$, as a thermometer for the chip. The sensors resistance is calculated from V_x as $R(T) = V_x/I_x$. Before using the resistance as a thermometer, the temperature coefficient, α, was first measured for each chip. By using the temperature controller (cf. Section 8.3.1) to adjust the chip temperature, the bridge resistance was measured for $T = 20, 25, 30, 40$ and 50°C. Fig. 9.2 shows the increasing bridge resistance vs. temperature for the five chips with $t_{\mathrm{FM}} = 30$ nm and fits of Eq. (9.1) to this data. As a linear relationship is observed between the resistance and temperature, the fitted α perfectly models these reference curves. The fitted α values for all three wafers can be seen in the inset of Fig. 9.2. Only small variations on α is seen for different chips on the same wafer, but α is seen to depend on the magnetic stack composition with an increasing temperature coefficient for increasing permalloy thicknesses.

9.4.2 Sensor self-heating by the bias current

To obtain the effective heat conductivity, the bridge resistance, for increasing bias current I_x, was measured. The resistance was calculated to a temperature increase using $\Delta T = \frac{1}{\alpha}\frac{\Delta R}{R_0}$ with α measured in Fig. 9.2. Figure 9.3a plots the calculated temperature vs. the bias current for the five sensors on the wafer with $t_{\mathrm{FM}} = 30$ nm. An increasing bias current, increases the Joule heating and thus resistance. Likewise, each measurement of resistance increases were fitted to Eq. (9.4) with R_0 and G_{eff} as free fitting parameters. The corresponding curve for $\Delta T(I_x)$, cf. Eq. (9.5), are seen as black lines in Fig. 9.3a. Excellent agreements between the theory and data are observed for all stacks and sensors. Figure 9.3b shows the same temperature increase versus the heating power $P = R(I_x)I_x^2$. The temperature increase

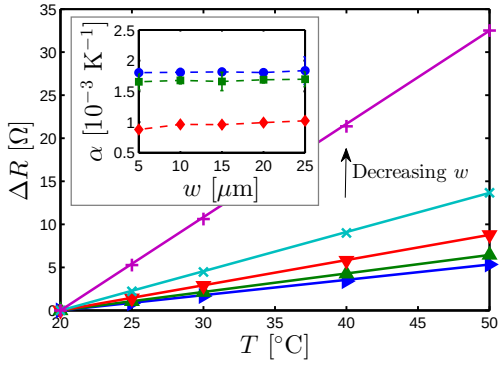

Figure 9.2: Measured PHEB resistance for temperatures between 20 and 50°C. The solid lines are fits of Eq. (9.1). The data is from the wafer with $t_{\mathrm{FM}} = 30$ nm. The inset shows the fitted temperature coefficients, α, for all wafers and sensor widths; blue circles, green squares and red diamonds correspond to $t_{\mathrm{FM}} = 30, 20$ and 10 nm, respectively. The figure is adapted from Paper III.

are seen to be proportional to the power with slopes given by the effective heat-conductance of the system.

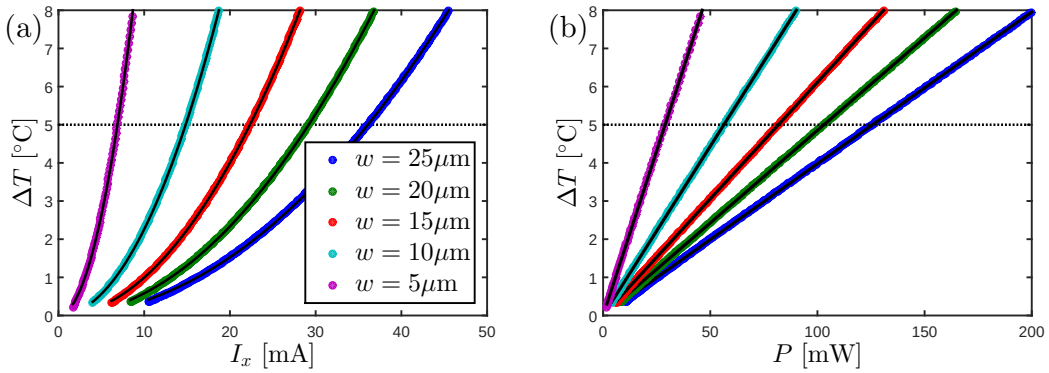

Figure 9.3: The sensor temperature increase versus (a) the sensor current or (b) calculated power. The black lines are plots of Eq. (9.5) with the values of R_0 and G_{eff} obtained from fits of Eq. (9.4) to $R(I_x)$ vs. I_x data. The data is from the wafer with $t_{\mathrm{FM}} = 30$ nm. The horizontal lines indicates a maximum allowed temperature increase of 5°C. Figure (a) is adapted from Paper III.

From measurements like Fig. 9.3a, or from the fitted heat conductance, the maximum sensor current, $I_{\Delta T}$, cf. Eq. (9.8), can be found. In Fig. 9.3 an arbitrarily chosen maximum temperature increase of $\Delta T = 5$°C is shown as a dashed line. The corresponding maximum currents are seen in Fig. 9.4a for $\Delta T = 1$°C and $\Delta T = 5$°C, respectively. As expected by the approximation of Eq. (9.8), the values of $I_{\Delta T}$ are observed to increase approximately linearly with the sensor width, and with a slope that increases with the permalloy thickness. For the standard sensor geometry [53, 87] of $t_{\mathrm{FM}} = 30$ nm and $w = 25$ µm one finds RMS amplitudes of $I_{\Delta T=1^\circ\mathrm{C}} \approx 16$ mA and $I_{\Delta T=5^\circ\mathrm{C}} \approx 36$ mA.

Fig. 9.4b shows the fitted values of G_{eff}, from fits like in Fig. 9.3, as function of the sensor area $4lw$ for all sensor stacks. Further, the predictions of the two simple analytical models (Eqs. (9.6) and (9.7)) and the COMSOL model (cf. Section 9.2) are shown. The measured G_{eff} increases with the sensor area and only small variation are found for varying stack compositions. Fig. 9.4b shows that the simple model of heat transportation, only limited by the silicon dioxide (cf. Eq. (9.6)), overestimates the heat

conductance compared to the experimental results. This overestimation increases with the sensor width and assumes a value of about 30% for $w = 25$ µm. In such cases the thermal resistance of the silicon wafer cannot be ignored, and instead the two-layer model (Eq. (9.7)) or a COMSOL model can be used, which both have a relative error less than 10%.

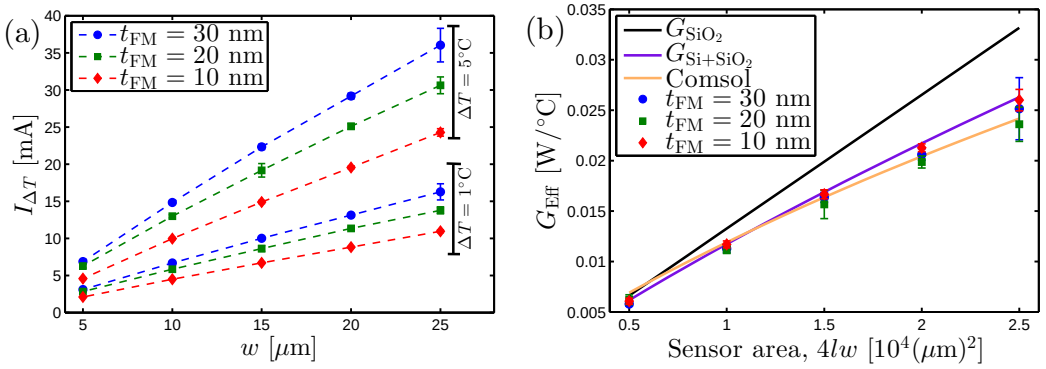

Figure 9.4: (a) Values of the maximum allowed current $I_{\Delta T}$ that keeps the sensor self-heating below $\Delta T = 1$°C and $\Delta T = 5$°C. The dashed lines are guides to the eye. (b) The effective heat conductance G_{eff}, from fits like Fig. 9.3, as well as the theoretical predictions of Eqs.(9.6) and (9.7) and the COMSOL model for $t_{\text{FM}} = 30$ nm. Figures are adapted from Paper III.

9.4.3 Pyrex wafer self-heating

The general procedure used above to measure the effective heat conductances in Fig. 9.4b was also used on a PHEB sensor on a Pyrex substrate. Pyrex is bad thermal conductor which severely hinders heat transportation compared to silicon. The purpose of using a Pyrex substrate was to investigate if the sensor could be heated enough to measure DNA melting curves without the use of an external temperature controller. The sensor resistance was first measured to be $R = 80.3\ \Omega$ and $88.97\ \Omega$ at 20.7°C and 70.2°C, respectively, which equal a temperature coefficient of $\alpha = 2.2 \cdot 10^{-3}\ \text{K}^{-1}$. These measurements were done in an oven, with a homogeneous temperature, to make sure there was no temperature gradient between thermometer and chip. Then the sensor resistance was measured for increasing bias current, and converted to a temperature increase, using α. Figure 9.5 shows the temperature increase vs. the sensor bias current. Compared to Fig. 9.3a, the sensor on the Pyrex substrate is seen to heat-up an order of magnitude more, but the measurement also extends to higher currents. As seen from Fig. 9.5, the system had a heat conductance of $G_{\text{eff}}^{\text{Pyrex,dry}} = 1.06$ mW/°C and $G_{\text{eff}}^{\text{Pyrex,wet}} = 1.31$ mW/°C when dry and filled with Milli-Q, respectively. These heat conductances are approximately 20 times smaller than for the $w = 25$ µm sensors on a silicon wafer. Accordingly, the sensor current can approximately heat the sensor to the temperatures required for DNA melting curves measurements. A temperature increase of $\Delta T = 50$°C is suitable for DNA melting, this plotted as a dashed line in Fig. 9.5. For heating the sensor to $\Delta T = 50$°C, a sensor current of $I_x = 27$ mA is needed for the wet fluidic system.

9.5 Discussion

9.5.1 Effect of liquid in the fluid system

All measurements leading to the heat conductances of Fig. 9.4b was done in dry microfluidic system. However as water is a better thermal conductor than air, a filled fluidsystem voids the assumption of an isolating boundary on top of the chip, and this increases the effective heat conductances as in Fig. 9.5. Figure 9.6 shows the heat networks for the dry system, where heat transportation through the chip top

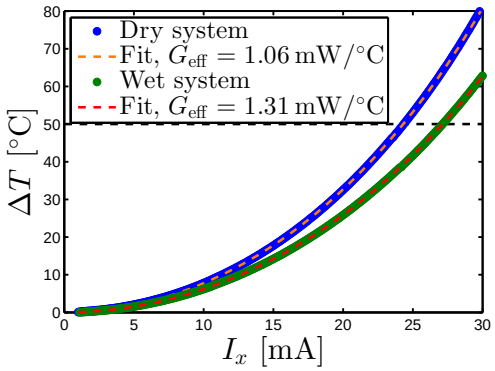

Figure 9.5: The sensor temperature increase versus the sensor current for a sensor on a Pyrex substrate. Measurements in a dry and Milli-Q filled (wet) fluid system are presented. The dashed lines are plots of Eq. (9.5) with the values of R_0 and G_{eff} obtained from fits of Eq. (9.4) to $R(I_x)$ vs. I_x data. The horizontal line indicate a temperature increase of 50°C.

is neglected, and for the wet system, where the pathway is not neglected. For the wet system heat can flow through the protective sensor coating and water filled top to the surroundings. In Fig. 9.6, the temperature between the sensor and the top surface of its protective coating, δT, is defined. Defining the heat conductance of the new heat pathway as $\Delta G_{\text{eff}} = (\mathcal{R}_{\text{coating}} + \mathcal{R}_{\text{top}})^{-1}$, where $\mathcal{R}$ is used for heat-resistance, the temperature drop, δT, is given by

$$\frac{\delta T}{\Delta T} = \frac{\mathcal{R}_{\text{coating}}}{\mathcal{R}_{\text{coating}} + \mathcal{R}_{\text{top}}} = \mathcal{R}_{\text{coating}} \Delta G_{\text{eff}}. \tag{9.9}$$

Just as in Fig. 9.5, measurements of ΔT vs. I_x were carried out with and without Milli-Q in the fluidic system. For the sensor on a silicon substrate an increase of the thermal conductance of $\Delta G_{\text{eff}} = 60$ mW/°C was observed. This increase is an order of magnitude smaller than the thermal conductance of the smallest sensor with $w = 5$ µm, and thus only little heat is transported through the top when using a silicon substrate. Assuming that the thermal conductivity of the $t_{\text{coating}} = 1$ µm thick Ormocomp coating equals that of SiO_2 the thermal conductance of the coating is $\mathcal{R}_{\text{coating}} = t_{\text{coating}}/(4lw\kappa_{SiO_2})$ and the temperature drop is $\delta T/\Delta T \approx 9\%$. Thus, the top of the surface is approximately at the same temperature as the sensor and the sensor self-heating is important to consider when doing surface based sensing based on biological interaction.

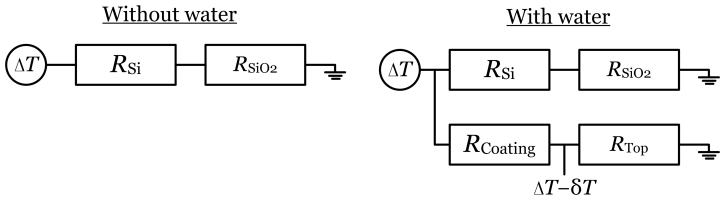

Figure 9.6: The heat networks considering only heat transport through the underlying silicon wafer (i.e. Without water) and when the pathway through protective coating and water filled topped is included (i.e. With water). ΔT is the temperature increase compared the surroundings. δT is the temperature drop from the sensor to the top of the sensor protective coating. The figure is adapted for Paper III.

9.5.2 Consequences for applications

When the sensor is used for detection magnetic beads magnetized by the self-field the sensor output is $V_y = S_0 \gamma I_x^2$. Combining the sensor output with the estimated maximum current, Eq. (9.8), the self-field signal is

$$V_y \approx \gamma w l \frac{\kappa_{\mathrm{SiO_2}} \Delta T}{t_{\mathrm{SiO_2}}} \frac{S_0}{R_0}. \tag{9.10}$$

For a given magnetic stack the value S_0/R_0 is independent of the geometry. From Eq. (9.10) the sensor signal can be increased by increasing l as this increases the sensor resistance but not heating. However, the maximum sensor bias voltage is limited by the integrity of the sensor coating, which thus limits l. If the sensor is limited by electrolysis from the bias voltages, the sensor length should be decreased (and current increased) until heating is limiting the sensor. This ensures maximum signal as the self-field bead signal scales with the Joule heating and not the bias voltage. From Eq. (9.10) the senor signal can be increased by increasing w, however this generally reduces γ and is not recommended, but is a topic for further studies. Finally, the sensor heating can be reduced by $t_{\mathrm{SiO_2}}$. Note, that as $t_{\mathrm{SiO_2}}$ decreases, the simple approximation of Eq. (9.8) and thus Eq. (9.10) are incorrect. By using the expanded model of Eq. (9.7) a power increase by a factor of 3.5 was calculated by reducing $t_{\mathrm{SiO_2}}$ from 1 µm to 0.1 µm for $w = 25$ µm.

9.6 Conclusion

Paper III outline a general approach for measuring the self-heating of magnetoresistive sensors, and optimizing the sensor current while limiting the sensor self-heating. This is important as the signal, from beads magnetized by the sensor self-field, scales with the square of the sensor current. A systematic characterization of the Joule heating was carried out for varying geometries and stack compositions. It was found that the 1 µm thick insulating silicon dioxide layer was the limiting factor of the dominating heat pathway, and two simple analytical thermal models were made. Experimentally, the sensor heating was determined from the sensor resistance increase, and by measuring the temperature coefficient, and sensor resistance as function of the bias current, the effective heat conductance was extracted. It was shown that a 25 μm wide sensor with a RMS bias current of 30 mA induced a temperature increase of 5°C and 80°C when the sensor is fabricated on an oxidized-silicon substrate and a pyrex substrate, respectively.

10

Comparison of ring and diamond shaped sensor geometries

Chapter 10 compares four different PHEB sensor designs, with the focus on experimental comparison between ring and diamond shaped PHEB sensors. This comparison has become especially interesting, as both ring shaped sensors with curved resistors [31, 33, 35, 36, 106] and diamond shaped sensors with straight resistors [40, 107] have been argued to be the superior design and are used in scientific research. For investigating which design is optimal, a systematic study, both theoretically and experimentally, was performed. This included fabrication of magnetic stacks with t_{FM} =10, 20 and 30 nm and t_{Cu} =0, 0.3 and 0.6 nm. Theoretically diamond shaped sensors are predicted to be 41% more sensitive than corresponding ring shaped sensors, to verify this both ring and diamond shaped sensor were characterized by sweeping the external field and fitting the sensor response to a single domain model. Surprisingly, the improvement in field sensitivity for the diamond sensor was never 41 % but varied between 0-35% with the highest improvements for magnetic stacks with a strong exchange field. However, the total resistance change was generally 41 % or more improved. Thus, the ring shaped sensors must be less affected by shape anisotropy, which was supported by the fitted B_{sh} parameters. To expand the study on shape anisotropy, Chapter 10 also characterized sensors that were surrounded by magnetic stack. As expected these were less affected by shape anisotropy, which enabled the use of magnetic stacks with weaker exchange bias as discussed in Chapter 11. This chapter summarizes the result of Paper IV and V.

10.1 Theory

This study focused on four different PHEB geometries, all illustrated in Fig. 10.1. The sensors in Fig. 10.1 either have a ring (curved resistors) or diamond (straight resistors) geometry and are either bare (top row of Fig. 10.1) or surround by magnetic stack (bottom row of Fig. 10.1). The diamond resistors had dimensions of $l \times w = 250$ µm $\times$ 25 µm and to have the electrical contacts at the same locations the ring sensor had a radius of $r = l/\sqrt{2}$.

The sensor response is fitted to the single domain model including shape anisotropy, Eq. (6.20),

$$\tilde{u}_{\pm} = -H_{\mathrm{ext}} \sin\theta_{\pm} - \tfrac{1}{2} H_{\mathrm{K}} \cos^2\theta_{\pm} - H_{\mathrm{ex}} \cos\theta_{\pm} - \tfrac{1}{2} H_{\mathrm{sh}} \cos^2(\theta_{\pm} \mp \pi/4) \tag{10.1}$$

where the magnetization direction for resistor R_1 and R_3 (cf. Fig. 6.2a), θ_+ is different from the magnetization direction for resistor R_2 and R_4, θ_-. The expression for the shape anisotropy energy was calculated for a rectangular resistor slab, cf. Section 6.4.4, and is not viable for the ring-shaped sensor. However, a similar energy contribution is assumed to exist and Eq. (6.20) is also used to fit the response of the ring sensors. For the curved resistors of the ring sensors the resistance and output V_y^{R} is found by integration an infinitesimal resistor piece, cf. Paper IV

$$\mathrm{d}R = \frac{1}{wt}\rho(\theta,\alpha)\mathrm{d}l = \frac{r}{wt}\rho(\theta,\pi/2-\varphi)\mathrm{d}\varphi \tag{10.2}$$

$$R_1 = \int_0^{\pi/2} \frac{r}{wt}\rho(\theta_+,\pi/2-\varphi)\mathrm{d}\varphi = \frac{r}{2tw}\left[\frac{\pi(\rho_{\parallel}+\rho_{\perp})}{2} + \Delta\rho\sin(2\theta_+)\right] \tag{10.3}$$

$$V_y^{\mathrm{R}} = \frac{r}{4wt} I_x \Delta\rho[\sin(2\theta_+) + \sin(2\theta_-)] \tag{10.4}$$

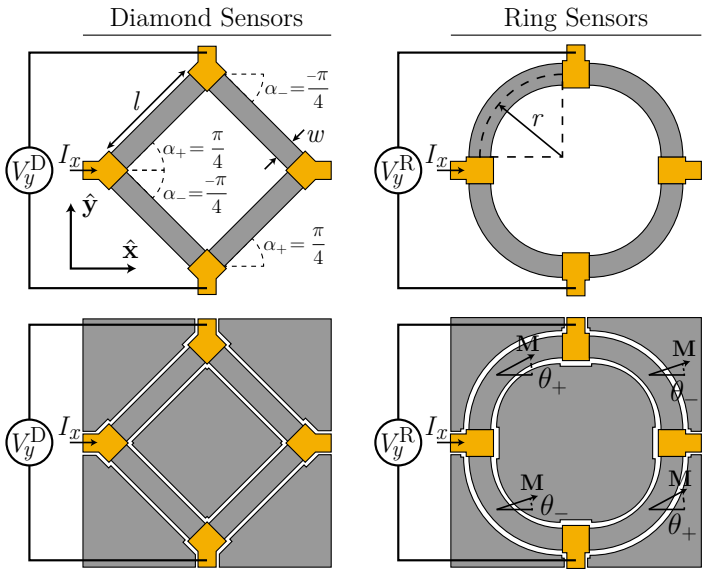

Figure 10.1: Illustration of diamond (left column) and ring (right column) PHEB sensors. For both geometries, a bare (top row) and a surrounded (bottom row) variant was fabricated. Dark gray and orange indicate magnetic stack and contact stack, respectively. The figure is adapted from Paper V.

where φ is the auxiliary angle. The diamond sensor output is given by Eq. (6.21)

$$V_y^{\mathrm{D}} = \frac{l}{4wt} I_x \Delta\rho[\sin(2\theta_+) + \sin(2\theta_-)]. \tag{10.5}$$

Comparing Eq. (10.4) and Eq. (10.5) the output from the diamond sensor is $\sqrt{2} \approx 41\%$ higher than that of the equivalent ring sensor. Further, the resistance, R_0, of the ring sensor is a factor of $\frac{\pi}{2\sqrt{2}} \approx 1.11$ higher than that of the diamond sensor.

10.2 Experiments

Nine different magnetic stacks were used for the experiments, all with the structure (cf. Fig. 6.2b) Ta(13 nm)/$Ni_{80}Fe_{20}$(t_{FM})/Cu(t_{Cu})/$Mn_{80}Ir_{20}$(10 nm)/Ta(3 nm) with all combinations of $t_{\mathrm{FM}} = 10, 20$ or 30 nm and $t_{\mathrm{Cu}} = 0, 0.3$ or 0.6 nm. All four geometries of Fig. 10.1 were fabricated on the nine wafers and were characterized by field sweeps as described in Section 8.5.3. The field sweeps were fitted using Eq. (10.1) and Eqs. (10.4,10.5), the fitting parameters were peak-to-peak resistance change ΔR_{pp}, a sensor offset and the fields B_{ex}, B_{K}, and B_{sh}. However, it was found that B_{K} only varied slightly between the different sensors, and thus B_{K} was fixed to its average value $B_K = 0.72$ mT. Further, the low-field sensitives, $S_0^{\mathrm{D}}, S_0^{\mathrm{R}}$, was extracted from the fits and the sensor resistance R_0 was measured independently.

10.3 Results

10.3.1 Field sweeps for different sensors and stacks

Figure 10.2 shows the sensor responses from six selected magnetic stacks and for all four sensor geometries. The output is given in terms of ΔR, as any offset has been subtracted and the sensor output has been normalized with the current. Some general observations are

- For increasing t_{FM} or t_{Cu}, the exchange field B_{ex} decreases as expected, and a smaller external field is needed for the sensor to reach its peak signal. This is discussed further in Chapter 11.
- For $t_{\mathrm{FM}} = 10\,\mathrm{nm}$, the diamond sensors (red lines) have a higher change in resistance and low-field sensitivity, $\Delta R_{\mathrm{pp}}, S_0$ than the corresponding ring sensors (blue lines), as theoretically expected.
- If the ferromagnetic thickness increases to $t_{\mathrm{FM}} = 30$ nm the output of the bare sensors shows the S-shape characteristic for a significant shape anisotropy, cf. Fig. 6.5. Further, the ring and diamond sensors have comparable low-field sensitivities, but the diamond sensors maintain a higher total change in resistance, ΔR_{pp}. This decrease of only the sensitivity is caused by increasing shape anisotropy, thus the diamond sensors are more affected by shape anisotropy than the ring sensor.
- For sensors with a low exchange field, the low-field sensitivity is increased by the presence of the surrounding stack. Further, in the extreme case of $t_{\mathrm{FM}} = 30\,\mathrm{nm}$ and $t_{\mathrm{Cu}} = 0.6\,\mathrm{nm}$ only the sensors with surrounding stack are functional, as for this weak exchange field, the shape anisotropy of the bare sensor renders them unusable.

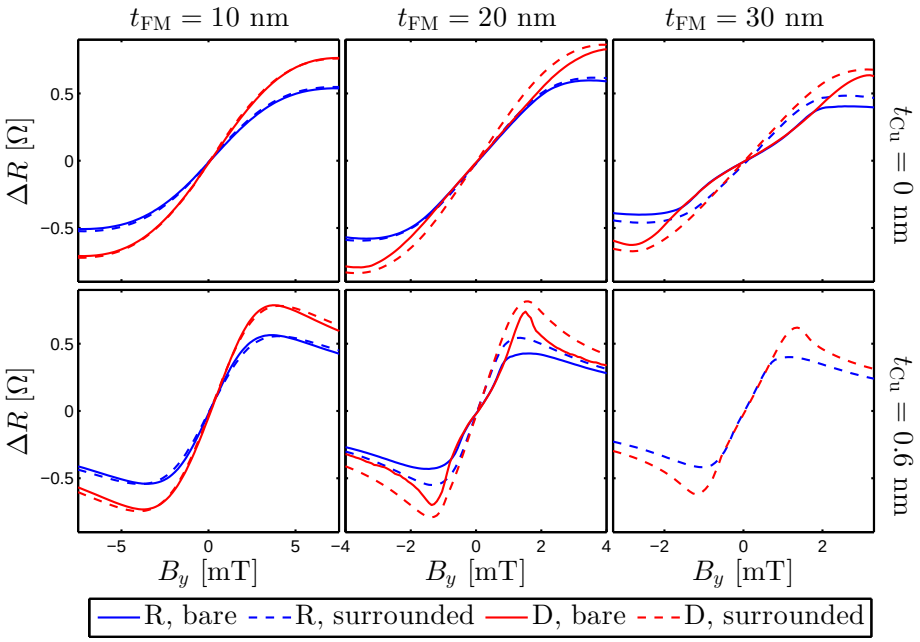

Figure 10.2: Field sweeps for the indicated values of t_{FM} and t_{Cu} for ring (R, blue) and diamond (D, red) sensors that are either bare (solid lines) or surrounded by the magnetic stack (dashed lines). Note, the different scales on the B_y axes. Figure is adapted from Paper V.

10.3.2 Parameters extracted from the field sweeps

The measured resistance change, ΔR_{pp}, and fitted parameters from field sweeps, like in Fig. 10.2, are given in Table 10.1.

The fitted parameters of Table 10.1 contains some expected and some new results.

As expected R_0 does not depend on the presence of the surrounding stack, decreases with increasing t_{FM} or t_{Cu} and are 9(1) % higher for diamond sensors than for ring sensors, close to the theoretical increase of 11 %. ΔR_{pp} are independent of the presence of the surrounding stack and are generally 40 % higher for diamond sensors. ΔR_{pp} is highest for $t_{\mathrm{FM}} = 20$ nm and should increase with decreasing t_{FM},

Table 10.1: Extracted values for field sweep data like in Fig. 10.2. The values to the left and right of the slashes are from bare and surrounded sensors, respectively. The table is adapted from Paper V.

	Ring				
t_{Cu}	$R_0[\Omega]$	$\Delta R_{\mathrm{pp}}[\Omega]$	B_{ex} [mT]	B_{sh} [mT]	$10 \times S_0^{\mathrm{R}}$ [Ω/mT]
$t_{\mathrm{FM}} = 10$ **nm**					
0 Å	245/254	1.0/1.1	6.7/6.6	0.6/0.0	1.2/1.3
3 Å	235/241	1.1/1.1	3.1/3.5	0.5/0.4	2.6/2.3
6 Å	234/230	1.1/1.1	1.8/1.7	0.2/0.0	4.0/4.6
$t_{\mathrm{FM}} = 20$ **nm**					
0 Å	139/141	1.2/1.2	3.0/3.1	1.1/0.6	2.6/2.8
3 Å	133/133	1.0/1.2	1.5/1.6	0.7/0.3	3.9/4.7
6 Å	133/131	0.9/1.1	1.1/0.9	0.4/0.3	4.2/6.6
$t_{\mathrm{FM}} = 30$ **nm**					
0 Å	105/108	0.8/1.0	2.1/2.1	1.7/0.5	1.8/2.9
3 Å	98/99	0.5/0.9	1.2/0.9	0.8/0.4	2.0/4.8
6 Å	94/96	-/0.8	-/0.6	-/0.3	-/5.8
	Diamond				
t_{Cu}	$R_0[\Omega]$	$\Delta R_{\mathrm{pp}}[\Omega]$	B_{ex} [mT]	B_{sh} [mT]	$10 \times S_0^{\mathrm{D}}$ [Ω/mT]
$t_{\mathrm{FM}} = 10$ **nm**					
0 Å	224/230	1.5/1.5	6.9/6.9	1.2/0.6	1.7/1.7
3 Å	214/220	1.5/1.5	3.2/3.5	1.1/0.9	3.2/3.1
6 Å	212/209	1.5/1.6	1.8/1.8	0.8/0.3	4.9/5.7
$t_{\mathrm{FM}} = 20$ **nm**					
0 Å	127/130	1.6/1.7	3.2/3.2	2.5/1.5	2.8/3.5
3 Å	121/121	1.6/1.7	1.7/1.6	1.8/1.1	3.7/5.4
6 Å	122/120	1.5/1.6	1.0/1.0	1.4/0.8	4.0/7.2
$t_{\mathrm{FM}} = 30$ **nm**					
0 Å	97/100	1.3/1.4	2.4/2.3	2.8/1.7	1.9/3.2
3 Å	90/92	1.0/1.2	0.9/1.0	1.8/1.0	1.8/4.9
6 Å	86/88	-/1.3	-/0.8	-/0.9	-/5.6

but for $t_{\mathrm{FM}} \leq 15$ nm the AMR ratio decreases [29]. B_{ex} is independent of geometry and of the presence of surrounding stack, and its dependence on the magnetic stack is described in Chapter 11.

Some new results are: B_{sh} are considerably smaller for sensors surrounded by stack. Further, B_{sh} is also substantially, i.e. a factor of two, smaller for ring sensors than for diamond senors. B_{sh} increases with increasing t_{FM}, this is due to N_{z_s} (cf. Section 6.4.4) decreasing, which increases N_{x_s}, N_{y_s} [100]. However, B_{sh} is surprisingly found to decrease with increasing t_{Cu}, this is discussed in Chapter 11. S_0 increases with t_{FM} or t_{Cu} due to weaker exchange field. Comparing S_0 for different geometries, the increase of using a diamond sensor is dependent on the stack composition and is generally higher by 20-40%, 10-25% and 0-10 % for $t_{\mathrm{FM}} = 10, 20$ and 30 nm, respectively. For both ring and diamond sensors, the highest sensitivities are obtained for a surrounded sensor with $t_{\mathrm{FM}} = 20$ nm and $t_{\mathrm{Cu}} = 0.6$ nm.

10.3.3 Comparison of ring and diamond sensors

The increased sensitivity of using a diamond sensor compared to a ring sensor is never the expected 41 % and for some stacks the improvements are negligible. From Fig. 10.2 it seems that shape anisotropy is important and Fig. 10.3 shows the ratios $\Delta R_{\mathrm{pp}}^{\mathrm{D}}/\Delta R_{\mathrm{pp}}^{\mathrm{R}}$ and $S_0^{\mathrm{D}}/S_0^{\mathrm{R}}$ as a function of the relative importance of the shape anisotropy for the diamond sensors, $B_{\mathrm{sh}}^{\mathrm{D}}/(B_{\mathrm{ex}}^{\mathrm{D}} + B_{\mathrm{K}}^{\mathrm{D}})$, obtained from Table 10.1. For $\Delta R_{\mathrm{pp}}^{\mathrm{D}}/\Delta R_{\mathrm{pp}}^{\mathrm{R}}$ the ratio is generally the expected ratio of $\sqrt{2}$ higher for diamond sensors but increases further for high values of $B_{\mathrm{sh}}/(B_{\mathrm{ex}} + B_{\mathrm{K}})$. Likewise, $S_0^{\mathrm{D}}/S_0^{\mathrm{R}} \approx 1.3$ for low shape anisotropy but decreases

monotonically towards 1 when $B_{\mathrm{sh}}^{\mathrm{D}}/(B_{\mathrm{ex}}^{\mathrm{D}} + B_{\mathrm{K}}^{\mathrm{D}})$ increases towards 0.6.

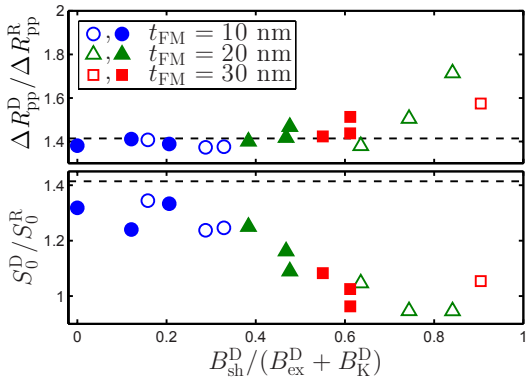

Figure 10.3: Resistance (top) and sensitivity (bottom) ratios vs. the relative shape anisotropy. t_{FM} is indicated by the color and both bare (open symbols) and surrounded sensors (filled symbols) are present. The dashed lines are the theoretical improvements of $\sqrt{2}$. The figure is adapted from Paper V.

10.4 Discussion

Table 10.1 shows that diamond sensors are more affected by shape anisotropy (i.e. higher B_{sh}) and therefore only 30% more sensitive than ring sensors, for stacks with low shape anisotropy. Further, the ring and diamond sensitivities are similar if the magnetic stack have high relative shape anisotropy. This section hypothesizes why ring sensors are less affected by shape anisotropy.

Figure 10.4 shows a map of both the absolute sensitivity of the sensor resistance to a change in θ, which is proportional to $|\sin(2\alpha)|$, and of the demagnetization field, calculated as the magnetic energy density when the sensor is magnetized along the x-direction. The diamond sensor (left column of Fig. 10.4) is maximally sensitive to a change in θ, and the demagnetization field is of medium magnitude, both throughout the whole sensor. Contrary, the ring sensor is most sensitive in the middle of each resistor, while the demagnetization field is strongest in the part of each resistor closest to the current contacts. These insensitive parts of the ring sensor gives the theoretical improvement of $\sqrt{2}$. However, the ring demagnetization field is strongest in an insensitive area, and it is hypothesized that the magnetization relaxes in this area, i.e. breaks from the single domain and orient some part to minimize the demagnetization field energy. This relaxation won't affect the sensor output in the same way, as if the diamond sensor relaxes, which will happen in a sensitive area.

10.5 Conclusion

Ring and diamond shaped PHEB sensors were systematic experimentally compared with a focus on the low-field sensitivity and total change in resistance. Theoretically, the diamond sensors have 41 % higher sensitivity and total change in resistance compared to ring shaped sensors. To verify this nine wafers with magnetic stacks with permalloy and copper thicknesses of $t_{\mathrm{FM}} = 10, 20$ and 30 nm and $t_{\mathrm{Cu}} = 0, 0.3$ and 0.6 nm were fabricated. Each wafer had four sensors, ring or diamond geometries and bare or surrounded by magnetic stack. Each sensor was characterized by a field sweep and fitting of this response to a single domain model and measuring the low-field sensitivity and total change in resistance. The total change in resistance was found to agree with the theory, but the low-field sensitivity only increased 0-35 % for diamond sensors compared to ring sensors. This is explained by the ring sensors being less affected by shape anisotropy, and accordingly the sensitivity improvement of the diamond geometry is only observed for magnetic stacks with low shape anisotropy. Last, surrounding the sensor

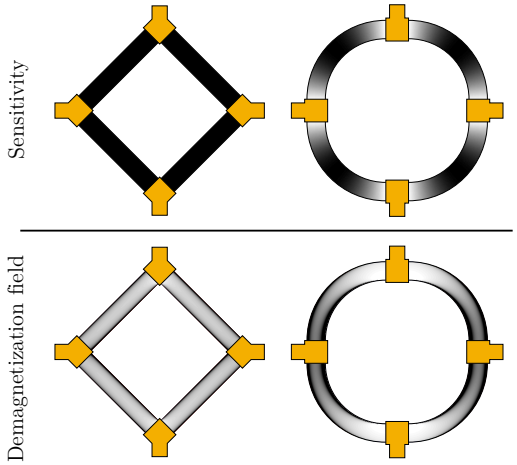

Figure 10.4: (Top) Spatial distributions of the sensor sensitivity, i.e. $|\partial R(\alpha, \theta)/\partial\theta|$. (Bottom) Spatial distributions of the demagnetizing field when the sensors are magnetized along the x-direction. Black indicates high sensitivity and demagnetization field while white is zero. The same scales are used for the diamond and ring sensors. The figure is adapted from Paper V.

with the magnetic stack successfully reduced the shape anisotropy field experienced by the sensor and increased the sensitivity.

11

Multilayer sensors for magnetic bead detection

Chapter 11 investigates if a trilayer magnetic stack is more sensitive for measurements of magnetic beads than a bilayer stack. In the trilayer stack, a copper layer has been included to reduce the exchange field. This works stems from the discovery by Gökemeijer *et al.* [108], that a noble metal spacer layer in an exchange biased permalloy stack weakens the exchange coupling, and from the work of Hung *et al.* [27, 28, 29, 30, 34, 36] that increased the field sensitivity of PHE cross sensors 7 times by incorporating 2 Å thick copper spacer layer in the magnetic stack. To investigate if similar improvements can be obtained for self-field bead detection, a systematic analysis of the best multilayer stack is performed along with a discussion of the practical limitations. Experimentally, magnetic stacks with $Ni_{80}Fe_{20}(t_{FM})/Cu(t_{Cu})/Mn_{80}Ir_{20}(10\,nm)$ with t_{FM} =10, 20 and 30 nm and $0 \leq t_{Cu} \leq 0.6$ nm were characterized by VSM measurements, by sweeping an external field and by measuring the response from a suspension of magnetic beads. The measured exchange field was inversely proportional to the permalloy thickness and decayed exponentially with increasing copper thickness. This reduction of the exchange field resulted in a higher field and bead sensitivities. By switching from the standard magnetic stack of t_{FM} = 30 nm,t_{Cu} = 0 Å to a magnetic stack with a copper layer, i.e. t_{FM} = 30 nm,t_{Cu} = 6 Å, the bead signal is improved by $\sim$ 90 %, assuming the sensor bias is limited by Joule heating. This chapter summarizes the result of Paper VI.

11.1 Theory

For a current driven PHEB sensor the output for small external field can be described as $V_y = I_x S_0 B_y$ with the sensitivity given by $S_0 = R_0 r_{AMR} f(B_{sh})/(B_{ex} + B_K)$ where $f(B_{sh})$ is a correction factor for shape anisotropy reduction of the sensitivity (cf. Section 6.4.4). Similarly, for a voltage driven sensor one can define $V_y = V_x \tilde{S_0} B_y$ with

$$\tilde{S_0} = S_0/R_0 = r_{AMR} \frac{1}{B_{ex} + B_K} f(B_{sh}). \tag{11.1}$$

$\tilde{S_0}$ then combines the influence of the AMR-ratio, bias fields and shape anisotropy.

11.2 Experiments

12 different magnetic stacks were used for the experiments, all with the structure (cf. Fig. 6.2b) $Ta(13\,nm)/Ni_{80}Fe_{20}(t_{FM})/Cu(t_{Cu})/Mn_{80}Ir_{20}(10\,nm)/Ta(3\,nm)$ with $t_{FM} = 10, 20$ or 30 nm and $t_{Cu} = 0, 1.5, 3, 4.5$ or 6 Å. The PHEB sensors had an area of $l \times w = 250\,\mu m \times 20\,\mu m$ and their field sweep and bead responses (cf. Section 8.5.4) were characterized. The field sweeps were fitted using the single domain model of Eq. (6.20) and Eq. (6.21) as in Section 10.2. The bead response, $\Delta V_2''$, was measured by injection a suspension of plain (i.e. uncoated) 80 nm BRF-Starch beads from Invitrogen (Auckland, New Zealand) diluted to 10 mg/mL in Milli-Q water, and the signal was calculated as the difference 5 minutes after and just before bead injection

$$\Delta V_2'' = V_2''(t = 5\text{ min}) - V_2''(t = 0_-). \tag{11.2}$$

Last, VSM were made according to Section 8.5.1.

11.3 Results

11.3.1 VSM measurements

Figure 11.1 shows the exchange field, from VSM measurements, for all fabricated wafers, i.e. three different permalloy thicknesses and 3-6 copper thicknesses. The exchange field decreases with increasing t_{FM} or t_{Cu}. This is expected, as the exchange field is an interface effect, and thus the volume average energy is inversely proportional to t_{FM}. Further, Gökemeijer *et al.* found that the spin coupling between an antiferromagnetic layer and a ferromagnetic layer could persist if a spacer layer (e.g. copper) was introduced in-between, but the exchange field decreases exponentially (copper decay length $\lambda = 4.1\,\text{Å}$) with the spacer thickness. Combining these effects yields

$$B_{\mathrm{ex}} = B_{\mathrm{ex}}^{30\,\mathrm{nm}} \frac{30\,\mathrm{nm}}{t_{\mathrm{FM}}} \exp\left(\frac{-t_{\mathrm{Cu}}}{\lambda}\right) \tag{11.3}$$

where $B_{\mathrm{ex}}^{30\,\mathrm{nm}}$ is the exchange field for $t_{\mathrm{FM}} = 30\,\mathrm{nm}$, $t_{\mathrm{Cu}} = 0\,\text{Å}$, and λ is the decay length. Fig. 11.1 shows a fit of Eq. 11.3 to the VSM data, and for the parameters $\lambda = 4.3 \pm 0.2\,\text{Å}$, $B_{\mathrm{ex}}^{30\,\mathrm{nm}} = 2.1 \pm 0.1\,\mathrm{mT}$ good agreement is observed.

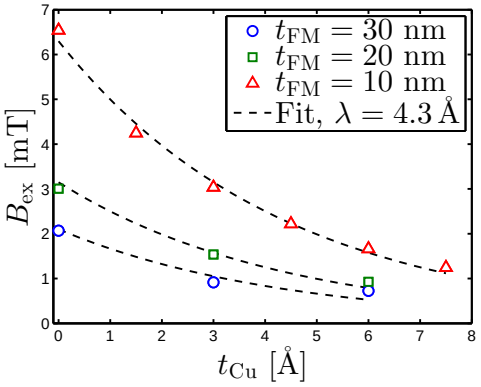

Figure 11.1: Exchange field, measured by VSM, for varying permalloy and copper thicknesses. The dashed lines are a single fit of Eq. (11.3). The figure is adapted from Paper VI.

11.3.2 Bead suspension responses

Figure 11.2 shows three examples of bead detection using sensors with $t_{\mathrm{FM}} = 30$ nm and varying copper thicknesses. For increasing copper thickness, the offset increases due to more current being shunted through the non-permalloy layers. Fortunately, the bead signal also increased by 45 % for $t_{\mathrm{Cu}} = 6$ Å compared to the output without a copper layer.

Figure 11.3a shows the bead signal magnitude, from measurements like in Fig. 11.2, but for all stacks. Similarly, Fig. 11.3b and Fig. 11.3c shows the recalculated response if a bias voltage of $V_x = 3\,\mathrm{V}$ or bias power of $P = 0.02$ W had been used, respectively. The conversion was done by an independent measurement of the sensor resistance, similar to the data in Table 10.1. In Fig. 11.3, $t_{\mathrm{Cu}} > 5\,\text{Å}$ is advantageous for bead detection as the bead signal increase with increasing copper thicknesses. However, for current driven sensors, the magnetic stacks with $t_{\mathrm{FM}} = 10\,\mathrm{nm}$ and high resistances had a high bead signal, while also being some of the worst if they had been voltage driven. Thus, a resistance independent measure of the stack optimality is needed, based on the practical limitations. This is discussed in Section 11.4.1.

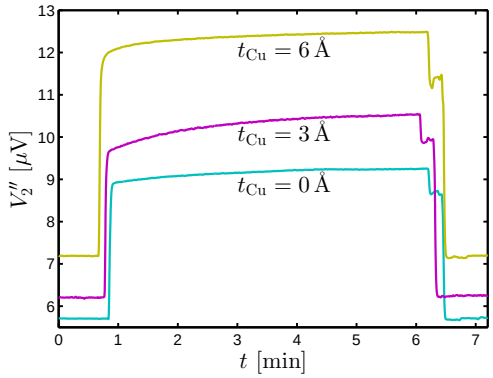

Figure 11.2: Measurements on a homogeneous bead suspension for sensors with increasing t_{Cu}. The beads were injected around $t \approx 1$ min and washed away at $t \approx 6$ min. All sensors had a stack with $t_{FM} = 30$ nm. The figure is adapted from Paper VI.

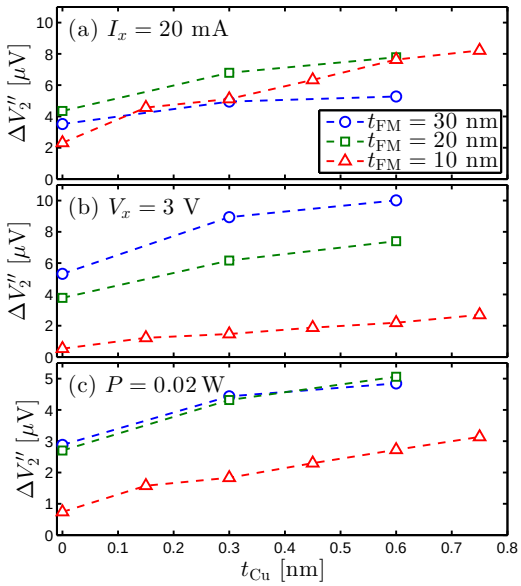

Figure 11.3: (a) The measured bead signal for sensors with varying t_{FM} and t_{Cu} while biased by an AC-current of 20 mA. (b) Calculated bead signal if the sensors had been biased by an AC voltage of 3 V. (c) Calculated bead signal if the sensor had been limited to a heating of $P = 0.02$ W, corresponding to $\Delta T = 1°$C. The dashed lines are only present to guide the eye. The figure is adapted from Paper VI.

11.3.3 Magnetic stack properties

Figure 11.4 shows the normalized field sensitivity, $\tilde{S}_0$, for all stacks, obtained from field sweeps and measurements of the sensor resistance. $\tilde{S}_0 = r_{AMR} f(B_{sh})/(B_{ex} + B_K)$ combines stack parameters like pinning fields, AMR-ratio and shape anisotropy and is a good measure for stack optimality. In general, $\tilde{S}_0$ increases with increasing t_{Cu} due to decreasing B_{ex}. However, decreasing t_{FM} below 30 nm affects the sensor in three ways:

- r_{AMR} decreases [28], which is bad. AMR-ratios of 1.7%, 1.5%, 0.8% were measured for $t_{FM} = 30$ nm, 20 nm, 10 nm, respectively, and with negligeble influence of the copper thickness.

- B_{sh} decreases [109], which is good and due to the demagnetization field in the z-direction increasing.
- B_{ex} increases, see Fig. 11.1, which is bad.

For the magnetic stacks with different t_{FM} and highest t_{Cu}, the normalized sensitivity of the $t_{\mathrm{FM}} \geq 20$ nm stacks are approximately equal and 65 % higher than the stack with $t_{\mathrm{FM}} = 10$ nm, as the lower shape anisotropy of the stacks with $t_{\mathrm{FM}} = 10$ nm cannot compensate the influence of the lower AMR-ratio.

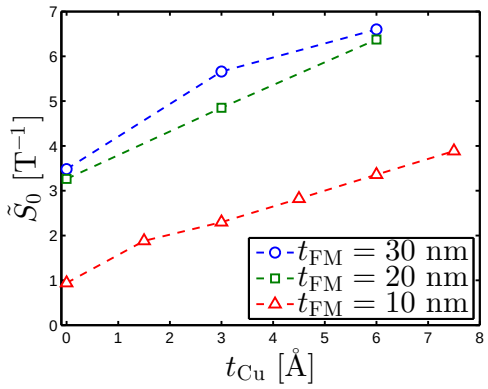

Figure 11.4: The measured low-field normalized sensitivities vs. the copper thickness. The lines are only present to guide the eyes. The figure is adapted from Paper VI.

11.4 Discussion

11.4.1 Heat-limited sensor bias

The theoretical bead signal for a given Joule heating can be simply expressed by combining the equation for sensor output, self-field, and Joule heating,

$$V_y = 2\gamma \tilde{S}_0 P. \tag{11.4}$$

From Eq. (11.4) it can be seen how the bead signal is proportional to the Joule Power P. In practice, the sensor bias is either limited by the voltage difference, due to electrolysis breakdown of the protective coating, or due to Joule heating, which is often limited by the bio-assay on the sensor surface (cf. Chapter 9). If electrolysis limits the sensor bias, the resistance should be decreased (e.g. shorter l). By decreasing R_0 and adjusting the bias voltage or current to give the same heating as prior to decreasing R_0, the bead signal is unaffected but the bias voltage is reduced. Using this approach the sensor can be made limited by Joule heating, at which point the bead signal is at its maximum value. For a given heating and given experimental condition, the bead signal scales with the normalized sensitivity, $\tilde{S}_0$, which is the best measure of the optimality of the magnetic stack. Figure 11.3c shows the data from Fig. 11.2 that has been normalized, according to a heating of $P = 0.02$ W, corresponding to $\Delta T = 1^\circ$ C. By comparing Fig. 11.3c and Fig. 11.4, we find that the bead signal scales with $\tilde{S}_0$ in accordance with Eq. (11.4). Thus, the sensor stacks with $t_{\mathrm{FM}} \geq 20$ nm and $t_{\mathrm{Cu}} = 6$ Å are approximately equally good and 90 % more sensitive than their sensor counterparts without copper.

11.4.2 Shape anisotropy of multilayer sensors

If shape anisotropy becomes stronger than the pinning fields $B_{\mathrm{sh}} > (B_{\mathrm{ex}} + B_{\mathrm{K}})$, the sensor output will have hysteresis even at low fields, and the sensor is unusable. Figure 11.5a shows the shape anisotropy for the magnetic stacks, measured from fits of the sensor field sweeps. Surprisingly the fitted shape

anisotropy in Fig. 11.5a decreases with increasing t_{Cu}. This can be explained by the single domain approximation breaking down, and that the sensor magnetization rotates near the edges of each resistor to reduce the magnetic pole density $\mathbf{M} \cdot \hat{\mathbf{n}}$ here. The weaker the exchange field is, the more the magnetization at the edges can rotate thus reducing the shape anisotropy energy, and for sensors with $w = 20$ µm this relaxation will have negligible effect on the sensor output. Fig. 11.5b shows the ratio of shape anisotropy to pinning fields, similarly to Fig. 11.5a, $\frac{B_{\mathrm{sh}}}{B_{\mathrm{ex}}+B_{\mathrm{K}}}$ increases slower than expected. Fig. 11.5b shows that sensors with $t_{\mathrm{FM}} = 30\,\mathrm{nm}$ have the highest ratio of $\frac{B_{\mathrm{sh}}}{B_{\mathrm{ex}}+B_{\mathrm{K}}} \approx 0.7$. It is thus not recommended to increase t_{Cu} further than 6 Å, for $t_{\mathrm{FM}} = 30$ nm, but it could be done for $t_{\mathrm{FM}} \leq 20$ nm.

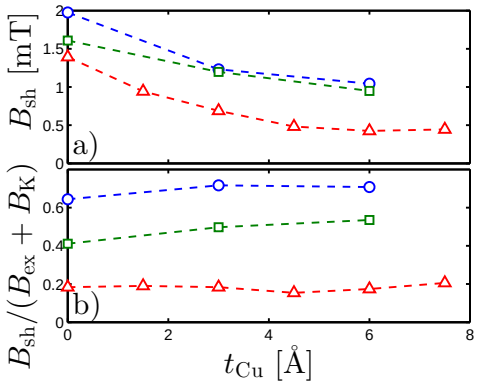

Figure 11.5: Extracted (a) B_{sh} and (b) $B_{\mathrm{sh}}/(B_{\mathrm{ex}}+B_{\mathrm{K}})$ from field sweeps and fitting (cf. Section 10.3). The lines are only present to guide the eyes, and red, green, blue corresponds to $t_{\mathrm{FM}} = 10, 20, 30\,\mathrm{nm}$, respectively. The figure is adapted from Paper VI.

11.5 Conclusion

12 magnetic stacks were characterized by VSM, and by measuring their responses to an external field and to a homogeneous bead suspension. Introducing a copper layer between the permalloy and antiferromagnetic layer reduced the exchange bias and generally resulted in an increased sensitivity as long as $B_{\mathrm{sh}} < B_{\mathrm{ex}} + B_{\mathrm{K}}$. When decreasing the permalloy thickness below 30 nm the shape anisotropy decreases but so does the AMR ratio. For measuring beads magnetized by the sensor self-field and with the bias voltage limited by Joule heating, sensors with $(t_{\mathrm{FM}}, t_{\mathrm{Cu}}) = (20; 30\,\mathrm{nm}, 6\,\mathrm{Å})$ were optimal and these had a low exchange field, while having both acceptable shape anisotropy and AMR-ratio. These sensors had 90 % increased sensitivity compared their non-copper alternative.

Part III

Magnetic bead-based characterizations of DNA binding

12

Magnetic bead-based measurements of DNA melting curves

Chapter 12 investigates measurements of magnetic bead hybridized to the sensor surface through DNA-DNA binding. This works builds on the work of Rizzi *et al.* [53, 84], where Single Nucleotide Polymorphism (SNP) was detected by immobilizing mutant type (MT) and wild type (WT) DNA on dPHEB sensors, letting complementary DNA coated beads hybridize, and then wash away the weakest bound beads. Expanding on this work, a temperature ramping instead of single wash condition is used in Chapter 12. Further, the streptavidin-biotin bead hybridization is seen to be constant even for temperatures of 70° C. The streptavidin-biotin positive reference signal is used to normalize out the sensor temperature dependence during temperature ramping. This allows for real-time measurements of DNA melting curves in a chip-based system, combining the advantageous of multiple DNA probes without the limitations of a single wash condition. This chapter summarizes the result of Paper VII.

12.1 Theory

Chapter 7 showed that dPHEB sensors are well suited for detecting low amounts of magnetic beads bound to the sensor surface and magnetized through the sensor self-field. For measurements of DNA melting curves, dPHEB sensors, like the one in Fig. 12.1a, were used. In Section 7.3.3 the output, Eq. (7.10), of the dPHEB sensor, was shown to be

$$V_{\mathrm{dPHEB}} = \frac{S_0 \Delta\gamma_1}{4\sqrt{2}} I_x^2 \tag{12.1}$$

which for a voltage driven sensor, measured by lock-in technique can be described as

$$V_2'' = \frac{S_0(T) V_{x,\mathrm{RMS}}^2}{8R(T)^2} \left(\gamma_{1,\mathrm{top}}(T) - \gamma_{1,\mathrm{bottom}}(T)\right) + V_{\mathrm{off}}(T) \tag{12.2}$$

where $V_{x,\mathrm{RMS}}$ is the root mean square value of the AC voltage amplitude, $V_{\mathrm{off}}(T)$ is a possible offset due to any sensor imbalance, $\gamma_{1,\mathrm{top}}$ ($\gamma_{1,\mathrm{bottom}}$) is the γ_1 signal from magnetic beads on the top (bottom) half of the sensor. In Eq. (12.2) all the temperature dependences have been explicitly written. Note that, both the low-field sensitivity, the sensor resistance and the sensor offset are all temperature dependent. The top and bottom parts of the sensor can be functionalized with different probes, and it is of interest to measure $\gamma_{1,\mathrm{top}}(T)$ and $\gamma_{1,\mathrm{bottom}}(T)$ as these describe the DNA-DNA temperature stability, while all other temperature dependent signal contributions should be normalized out.

12.2 Experiments

12.2.1 Sensor and probe coating

dPHEB sensors with resistor dimensions $l \times w = 250$ µm $\times$ 25 µm and with magnetic stack Ta(5)/ $Ni_{80}Fe_{20}(30)/Mn_{80}Ir_{20}(10)$/Ta(5) (thicknesses in nm) were fabricated as described in Chapter 8.

DNA capture probes, purchased from DNA technology A/S, (Denmark) were spotted on the silanized sensor surface as described in Section 8.2.4. The used DNA probes were designed by Petersen *et al.*

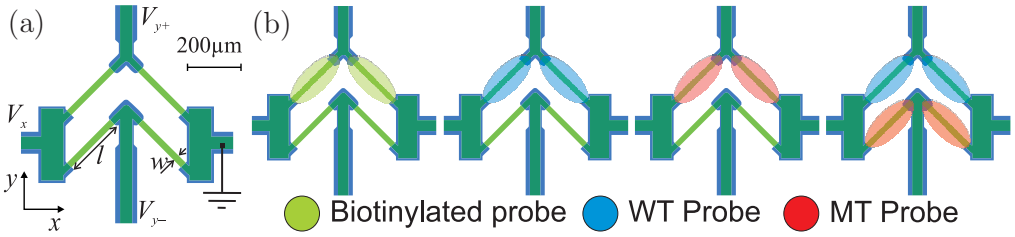

Figure 12.1: (a) Illustration of the dPHEB sensor along with parameters, voltages and coordinate system. (b) Spotted probes pattern. The biotinylated probe is the positive reference, while the melting temperature of the MT and WT probe is of interest. The figure is adapted from Paper VII.

[81] for SNP genotyping of the human beta globin gene at the codons 8/9 mutation site, and the probe sequence can be found in Rizzi *et al.* [53]. The spotted probe pattern on four dPHEB sensors can be seen in Fig. 12.1b. The wild type (WT) and mutant type (MT) probes differ by a single base insertion. Further, a biotinylated capture probe was used as a positive reference where streptavidin magnetic beads could directly bind to the sensor surface.

12.2.2 Experimental procedure

The experimental procedure had three steps, a initial measurement, followed by the hybridization step and finally the temperature ramping.

Initial measurement. First, the temperature dependence of the second harmonic out-of-phase signal offset was measured, $V_{\text{init}}^{\text{ref}}(T)$, which will be important for temperature correction of the positive reference. Prior to DNA binding the sensor was exposed to 0.05×Saline-Sodium Citrate buffer (SSC) ($c(\text{Na}^+) = 10\,\text{mM}$) and V_2'' was measured while the temperature was linearly varied from 20°C to 70°C and back to 20°C at 0.1°C/s.

DNA and bead hybridization. 50 nm Miltenyi streptavidin MicroBeads (Miltenyi Biotec Norden AM, Sweden) were mixed in 1:1 v:v ratio with biotinylated WT DNA target, to a final DNA concentration of 5 nM in 2×SSC ($c(\text{Na}^+) = 400\,\text{mM}$). This sample was injected in the fluidsystem and there incubated at 37°C for 30 min. These low-stringency conditions enabled formations of mismatched hybrids between WT target and MT probes.

Wash and temperature ramping. After a 30 min hybridization period the temperature was lowered to 20°C. Further, unbound DNA and unbound magnetic beads were washed with 0.05×SSC ($c(\text{Na}^+) = 10\,\text{mM}$) for 80 s at a flow rate of 30 µL/min. In the 0.05×SSC buffer the temperature was then ramped from 20°C to 70°C at 0.1°C/s for denaturing the DNA probes while the sensor output was measured ($V_{\text{up}}(T)$). Simarly the sensor output was measured while ramping back 20°C at 0.1°C/s, ($V_{\text{down}}(T)$).

12.2.3 Data treatment

To obtain the DNA temperature dependence, of $\gamma_{1,\text{top}}$ and $\gamma_{1,\text{bottom}}$ in Eq. (12.2) the temperature dependences of both the offset ($V_{\text{off}}(T)$) and scaling ($S_0(T)/R(T)^2$) need to be corrected for. For the positive reference with biotinylated DNA probes, the sensor offset is corrected for by subtracting the signal during the first reference measurement.

$$\Delta V^{\text{ref}}(T) = V_{\text{up}}^{\text{ref}}(T) - V_{\text{init}}^{\text{ref}}(T) \tag{12.3}$$

where $V_{\text{up}}^{\text{ref}}$ and $V_{\text{init}}^{\text{ref}}(T)$ are the measured reference biotinylated signal during the temperature up ramp and during the initial measurement. Due to the strong biotin-streptavidin bond the beads

stayed tethered even at high temperatures and $\Delta\gamma_1^{\text{ref}}$ is independent of the temperature. For all temperatures, the reference signal is then proportional to the sensitivity and its temperature dependence $\Delta V_{\text{ref}}(T) \propto S_0(T)/R(T)^2$. For the WT and MT DNA sensors, the signal during temperature down ramping was used for offset subtraction

$$\Delta V(T) = V_{\text{up}}(T) - V_{\text{down}}^{\text{approx}}(T) \tag{12.4}$$

where V_{down} is the measured signal during the temperature down ramp. However, to prevent a doubling of the noise $V_{\text{down}}(T)$ is approximated by a second order polynomial, $V_{\text{down}}^{\text{approx}}(T)$. $\Delta V(T)$ should be independent of the sensor offset, $V_{\text{off}}(T)$ and by normalizing with the reference signal, $\Delta V_{\text{ref}}(T)$, the temperature dependence of the scaling factor $S_0(T)/R(T)^2$ is also normalized out as

$$\textit{Relative Signal} = \frac{\Delta V(T)}{\Delta V^{\text{ref}}(T)} = \frac{\Delta\gamma_1(T)}{\Delta\gamma_1^{\text{ref}}}. \tag{12.5}$$

This signal only has a temperature dependence from the DNA-DNA hybridization.

12.3 Results

12.3.1 Hybridization

Figure 12.2 shows the signal $\Delta V_2''(t) = V_2''(t) - V_2''(0_-)$ for the WT target - magnetic bead mixture hybridization to the four functionalized sensors in Fig. 12.1b. The time of sample injecting was defined as $t = 0$. The positive reference is seen to increase rapidly in the beginning, due to the strong biotin-streptavidin bond, and then saturated after 15 min when the biotinylated probes have all hybridized. For all WT and MT functionalized sensors, the signal increased steadily, with decreasing rate. The WT probes hybridized the fastest, but the signal for both the MT and WT-MT sensors also showed significant signal. Thus, the target coated beads prefer hybridization to the WT probe but also hybridize to the MT probes.

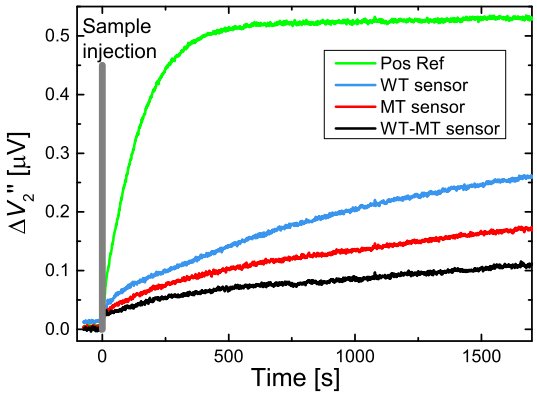

Figure 12.2: Bead hybridization signal for the four differently functionalized sensors in Fig. 12.1b. Figure is adapted from Paper VII.

12.3.2 Melting curve

Figure 12.3 shows the measured melting curves, i.e. the raw signal from the four sensors (cf. Fig. 12.1b) after bead hybridization but during the temperature ramping from 20°C to 70°C and back. While Fig. 12.3a,c and d show the up and down ramp as separate graphs, this is not the case for Fig. 12.3b.

Figure 12.3b show the signal for the positive reference, i.e. biotinylated, sensor during temperature ramping. Two curves are present, 'No Beads' is the initial measurement in 0.05× SSC before beads, and

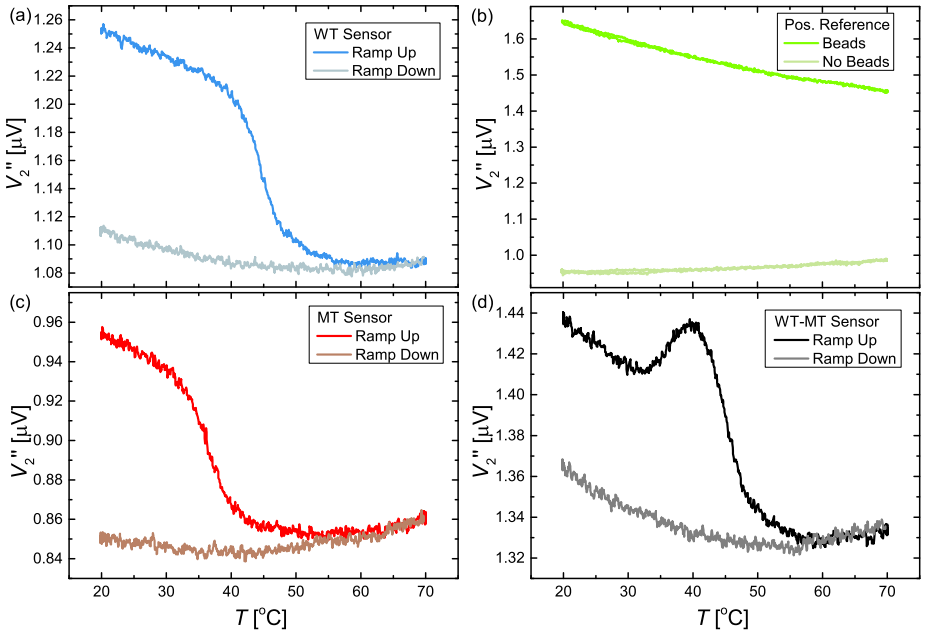

Figure 12.3: The sensor signal during the up and down temperature ramps. The legend titles indicate the sensor functionalization (cf. Fig. 12.1b). For (a,b,c,d) the signal was measured during the temperature ramping, but (b) (the reference sensor) also contains the data from the initial measurement before beads. Contrary to (a,c,d), the data for (b) overlapped during both the up and down temperature ramps and is plotted with only one color. Figure is adapted from Paper VII.

the curve is both the up and down ramp. Similarly, 'Beads' is the temperature ramp measurements after hybridization and wash, again both the up and down curve is present. For both 'No Beads' and 'Beads' the up and down ramps overlap, and it can be concluded that no irreversible changes take places in the sensor output, and that the biotin-streptavidin bond is stable, such that no beads are lost during temperature ramping. Thus, $\Delta V_{\text{ref}}(T)$ is proportional to $S_0(T)/R(T)^2$.

Figure 12.3a,c and d show the signals from WT, MT and WT-MT sensors, respectively, with one curve for the temperature up-ramp and one for the temperature down-ramp. For all sensors, the down-ramp signal varied slightly with temperature but was generally at a constant lower level. Similarly, the up-ramp signal decreased with increasing temperature and had one big drop-off at $T \approx 30 - 50°\text{C}$, where DNA hybrids are denatured and thus the magnetic beads are re-dispersed in the fluid. Note, that the WT-MT sensor also had a smaller signal increase at $T \approx 35°\text{C}$, where the MT denatured and $\gamma_{1,\text{bottom}}$ decreased. The signal drop-offs (and increase for WT-MT) is thus consistent with the melting of DNA hybrids and the corresponding detachment of beads from the sensor surface.

From the data in Fig. 12.3 the relative signal can be calculated in accordance with Eq. (12.5). Figure 12.4 shows this relative signal. Compared to Fig. 12.3, the bead signal is now constant for $T < 30°\text{C}$, the amplitudes are in descending order: WT, MT, WT-MT, as expected, but most importantly the melting temperatures are more clear from the data, and error function fits give $T_m = 35(1)°\text{C}$ and $T_m = 43(1)°\text{C}$ for the MT and WT sensor, respectively. Note, that the melting temperature uncertainties of 1°C are the standard deviation from triplicate experiments. As expect the MT had a lower melting temperature to the target than the perfectly matched WT, and temperatures between $35 - 43°\text{C}$ can thus be used for genotyping the SNP. Similarly, the WT-MT sensor shows a signal increase at $T \simeq 35°\text{C}$ due to MT probes detaching from the target coated beads. This signal peak was followed by a signal loss at $T \simeq 43°\text{C}$ where the WT probes also detached.

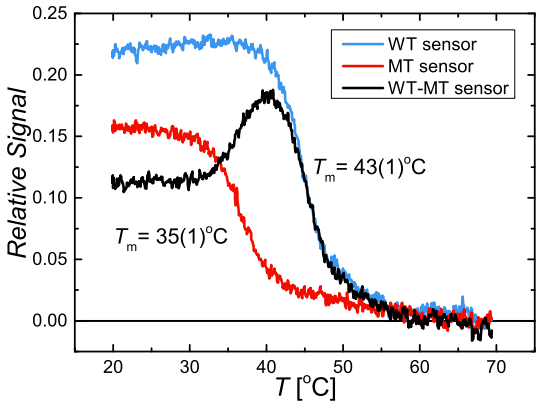

Figure 12.4: The calculated Relative Signal used for measuring DNA melting curves. The relative signal was calculated using Eq. (12.5) from the data in Fig. 12.3. The three sensors were measured simultaneously and the melting temperatures T_m were obtained from error function fits on triplicate experiments. Numbers in parentheses give the standard deviations. Figure is adapted from Paper VII.

12.4 Conclusion

Real-time measurements of DNA melting curves were performed in a chip-based system. By measuring the bead signal while ramping the temperature up and down past the DNA melting point, the bead signal dropped as DNA melted and the beads detached from the surface. It was shown how a stable positive reference, made from the strong biotin-streptavidin bond, can be used to normalize out the sensor temperature dependence. Further, by using two probes on one dPHEB sensor, a single sensor can genotype a SNP, which increases the number of possible mutation investigations on the same chip. This technology allows for measurements on many probes without the limitations of using a single washing condition (i.e. temperature), thus combining the power of melting analysis and the throughput of multiplexed assays.

13

Magnetic bead-based characterization of aptamer binding

The technique used to characterize DNA-DNA interaction (cf. Chapter 12) was also used for aptamers and their binding to influenza virus. The idea is illustrated in Fig. 13.1 and went like: By immobilizing aptamers, against the virus, on the dPHEB chip and coating magnetic beads with the same aptamers, the virus could be detected through a sandwich assay. From real-time measurements of the binding between aptamers and the virus target the association and dissociation constant could be calculated. Then by varying the buffer conditions, while monitoring the magnetic signal, the aptamer-virus affinity dependence on buffer conditions could be determined. This is useful for determining if the aptamer-virus bond is stable when the temperature, salt concentration or pH is varied, and thus under which conditions the aptamers can be used as the biological recognition element in an assay.

A full aptamer-virus sandwich assay was developed and tested using inactivated virus provided by DTU VET. A new concept of creating an *artificial virus*, was also tried. The artificial viruses consisted of magnetic beads coated with the virus surface protein, which the aptamers could bind to. Compared to a sandwich assay, the immobilized aptamers hybridized directly to the artificial magnetic virus label, which gives a more direct measurement method. However, for both methods the hybridization signals were nonexistent or below the noise limit. In pursuit of working conditions, different buffer conditions, different magnetic beads, different proteins and different aptamers were tried. However, none worked as expected, even though the aptamers successfully hybridized to beads coated with complementary DNA.

13.1 Aptamer properties

13.1.1 Aptamer basics

Aptamers are short single stranded oligonucleotide with an antibody like affinity toward a biological target. The aptamer DNA or RNA sequence is usually less than 100 nucleotides long. Because of the attraction between nucleotide pairs, aptamer molecules have a three dimensional shape which spatial form depends on the nucleotide sequence. The most common example is the aptamer against thrombin protein, which can be seen in Fig. 13.2 where a single stranded DNA sequence have folded into G-tetrads due to hydrogen bonding (dashed lines). The diverse three dimensional shapes allow aptamers to bind to a variety of targets with high affinity and specificity [110, 111].

13.1.2 SELEX technique

The all important aptamer sequence is evolved using the SELEX technique (Systematic Evolution of Ligands by Exponential Enrichment). SELEX as in in-vitro process which combines PCR amplification with a screening process to evolve an initially random pool of e.g. DNA, into a pool of DNA with high affinity for the screening target [111, 112]. After the final DNA pool has been sequenced, the aptamer biological recognition element can be easily in-vitro produced, which is comparably easier than the in-vivo production of antibodies. After the development of SELEX in 1990, aptamers have been seeing use in pharmaceutical basic research, drug development, diagnosis, and therapy [111]. Aptamers has been successfully evolved against a long list of targets including: Ions, small molecules, nucleotides, cofactors,

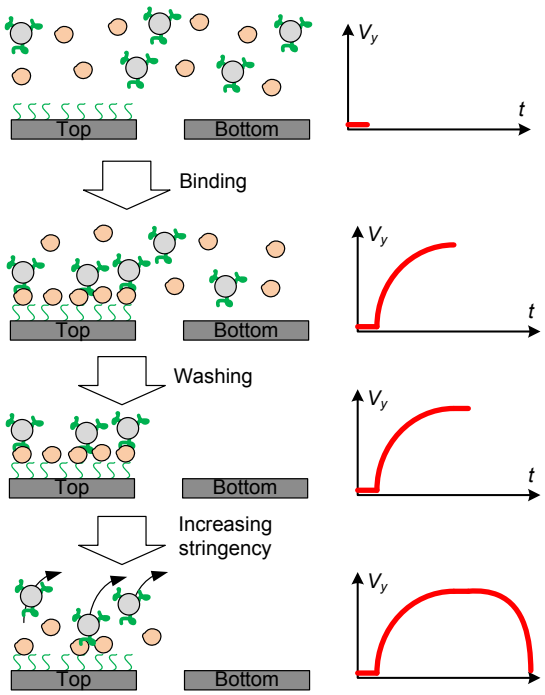

Figure 13.1: Illustration of the aptamer idea. The top of dPHEB sensor and the magnetic beads are coated with aptamers. Viruses and magnetic beads bind in a sandwich assay which increases the sensor output. Through the sensor output, the sandwich assay can be monitored while the stringency, e.g. temperature or salt concentration, is increased. At one point, the increased stringency breaks the aptamer bound, the magnetic beads are released, and the aptamer limitation is identified.

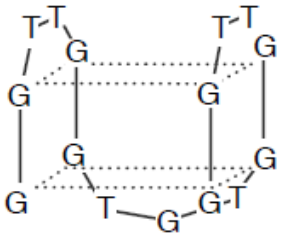

Figure 13.2: Example of a single stranded DNA folding into a 3D shape. Figure is from James [110].

amino acids, carbohydrates, antibiotics, proteins, peptides and complex structures like leukemia cells. Aptamers can bind to a lot of different targets, many of them outside the field of antibody interaction. The most important might be proteins, including cellsurface receptors, which are excellent aptamer targets with their large multifunctional surfaces [89].

13.1.3 Comparison to antibodies

While both antibodies and aptamers can bind with high affinity and specificity to their target they each hold some advantages compared to each other [89]. Protein antibodies are larger in size than compared to the nucleotide aptamers. This large size gives antibodies a longer half-life when circulating inside the bloodstream were as naked aptamers will be filtered by the kidneys or are easily degraded, if not chemically modified. The smaller size of the aptamers means they can be more densely packed and

easier penetrate biological barriers and tissue [90]. Aptamers are in-vitro chemically produced in fast, scalable and contamination free process, antibodies are in-vivo biologically produced by animals which takes fostering time. Likewise aptamers can be reversibly denatured and have a long shelf-life.

While aptamers have advantages compared to antibodies, antibodies have the been used for so long that their behaviors are well characterized and a whole industry is developed for their production. Likewise, selection of the best antibody is often given by e.g. disease pathways while new aptamers have to be screened without any prior knowledge provided. This is both an advantage and a disadvantage as aptamers for new targets can be found without any knowledge about their biological interaction. In this thesis, aptamers are interesting as they allow DNA technology to work with a larger variety of targets.

13.2 Experiments

As multiple experiments were performed, different procedures were used, which are described below.

13.2.1 Setup

All magnetic measurements were done using the setup described in Chapter 8. dPHEB magnetic sensors with resistor dimensions $l \times w = 250\ \mu\text{m} \times 25\ \mu\text{m}$ and with magnetic stack Ta(5)/$Ni_{80}Fe_{20}$(30)/$Mn_{80}Ir_{20}$(10)/Ta(5) (thicknesses in nm) were used. The sensors were voltage driven and lock-in technique was used (cf. Eq. (12.2)). Further the dPHEB chip usually had a negative reference sensor (blank sensor or with an unspecific aptamer), a positive reference sensor (biotinylated DNA probes that bind to the streptavidin beads), and multiple sensors with aptamers immobilized.

13.2.2 Aptamer immobilization

Aptamers and the biotinylated positive reference probe, purchased from DNA technology A/S (Denmark), were spotted on the top half of the dPHEB sensor surface as described in Section 8.2.4. Two aptamers, A22 and RHA06, were used; both sequences were extracted using the SELEX method.

A22 was extracted by Sung *et al.* [1] in 2004, with affinity to H1N1 virus of strain A/PR/8/34, and had the following sequence:
5'-`AATTAACCCTCACTAAAGGGCTGAGTCTCAAAACCGCAATACACTGGTTGTATGGTCGAATAAGTTAA`-3'

RHA0006 was extracted by Shiratori *et al.* in 2014 and had many times higher binding affinity than A22 [2]. RHA0006 was extracted against H5N1 virus of strain A/Anhui/1/2005 but showed significant binding to all subtypes of influenza A viruses. RHA0006 had the following sequence:
5'-`GGGTTTGGGTTGGGTTGGGTTTTTGGGTTTGGGTTGGGTTGGGAAAAA`-3'

Before using the aptamers, they were first denatured at 75° C for 3 min.

13.2.3 Buffers

Both A22 and RHA0006 used the same selection buffer (SB: 50 mM Tris-HCl, pH 7.4, 100 mM NaCl, 5 mM KCl, 1 mM $MgCl_2$) and hybridized at stagnant conditions. Some experiments were also carried out in PBS or SSC buffer.

13.2.4 Protocol for complementary DNA beads

50 nm Miltenyi streptavidin MicroBeads (Miltenyi Biotec Norden AM, Sweden) or 100 nm Micromod (Rostock, Germany) streptavidin beads were mixed with biotinylated DNA, with a sequence complementary to A22. Both bead types and DNA had a final concentration of 1 nM (assuming a Miltenyi stock concentration of 2 nM). The suspension was then incubated for 10 min at room temperature (RT), before injection in the fluid system and measured for 30 min.

13.2.5 Protocol for inactivated virus

For the sandwich assay with real virus, DTU Vet provided the H1N1 virus of strain A/SW/Denmark/19126/93 grown in eggs and inactivated by β-propiolactone. The virus concentration was unknown, but high enough to color the suspension light yellow. For the experiments, 50 nm Miltenyi streptavidin MicroBeads were mixed with biotinylated A22 aptamer, for a final concentration of 2 nM beads and 4 nM biotinylated-A22. The magnetic beads and biotinylated-A22 was then incubated 30 min at RT. First, the beads were prepared and the chip with A22 spotted was mounted. Secondly, the virus was diluted 100× in SB and injected into the fluidic system. Here, it incubated for 30 min at 37° C. Finally, the A22 coated magnetic beads were injected in the fluid system and the hybridization was measured for 30 min at 37° C.

13.2.6 Protocol for artificial virus

The artificial virus consisted of: (1) streptavidin coated magnetic beads, (2) a linker molecule with biotin and NTA (Nitrilotriacetic acid) and (3) virus surface proteins with a His-tag (Polyhistidine-tag), which in combination with Nickel-ions bounded to NTA.

Beads. The magnetic beads were usually 50 nm Miltenyi streptavidin MicroBeads, but 80 nm and 100 nm Micromod (Rostock, Germany) streptavidin beads were also used. In the washing step, the 50 nm Miltenyi beads were washed using a Miltenyi MACS® Cell Separation Columns (Miltenyi Biotec Norden AM, Sweden), while the bigger Micromod beads where washed in an Eppendorf tube using a permanent magnet.

Linker. Biotin-X-NTA (N_ϵ-(N-(+)-biotinyl-6-aminohexanoyl)-N_α,N_α-bis(carboxymethyl)-L-lysine tripotassium salt) was bought from Sigma-Aldrich (Saint Louis, MO, USA).

Proteins. Two proteins were tested, both with His-tag: (1) Influenza A H1N1 (A/Puerto Rico/8/34) Hemagglutinin, HA, Protein. (2) Influenza A H5N1 (A/Anhui/1/2005) Hemagglutinin, HA1 Subunit, Protein. Both were bought from Sino Biological Inc. (Beijing, PR China).

The magnetic beads were coated and measured through the following procedure:

1. Mix 10 µL stock magnetic beads with 30 µL (1 ng/µL) biotin-X-NTA solution and 4 µL $NiCl_2$ (10 µM), and incubate with mixing for 30 min at RT. For all bead types, this gives 10 biotin-X-NTA and Nickel-ions per streptavidin molecule and should saturate the beads.
2. Wash the beads. Then add 2 µg protein and incubate overnight at 5° C. This corresponds to approximately one protein per biotin-X-NTA, and each bead should thus have multiple proteins attached.
3. Wash the beads again but this time in SB for a final volume of 100 µL. This finalizes the coating procedure. After this, the beads were injected in the fluid system and hybridization was measured for 30 min or longer.

13.3 Results

The results from the aptamer assays are presented below. While many more measurements were performed, these represent the general trend and most trustworthy data obtained.

13.3.1 Aptamer binding to complementary DNA

Figure 13.3 shows the hybridization signals for beads with complementary DNA. The chip had four sensors with A22 aptamers or biotinylated probes immobilized and one sensor which is blank. In Fig. 13.3a 50 nm beads have been used, and as expected the blank sensor shows no signal over time. Likewise, the biotinylated sensor shows the highest signal, and the three sensors with A22 probes show a

smaller but still significant signal. Of the four significant signals, three of them rises with the same time constant, while one takes more time to saturate. In Fig. 13.3b 100 nm beads have been used, and now all sensors show a significant signal, even the blank. However, the blank signal is 30 % lower than the other signals, indicating that the beads sediment to all sensors but stay on the coated sensors instead of diffusing away.

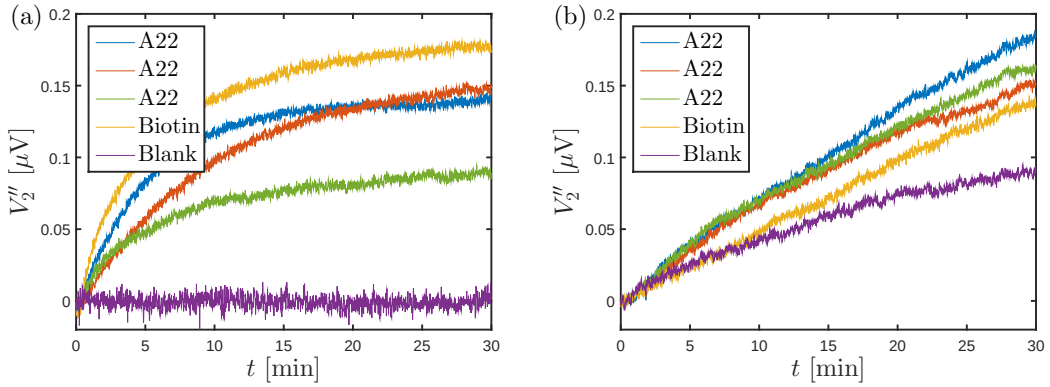

Figure 13.3: Hybridization signal between A22 and (a) 50 nm and (b) 100 nm beads coated with the complementary DNA sequence.

13.3.2 Aptamer binding to inactivated virus

Figure 13.4 shows the sandwich assay result where A22 coated magnetic beads could bind to inactivated virus. Three sensors have been used, a positive reference biotinylated sensor and two sensors coated with A22. The two sensors with A22 show no signal while the positive reference has a significant signal.

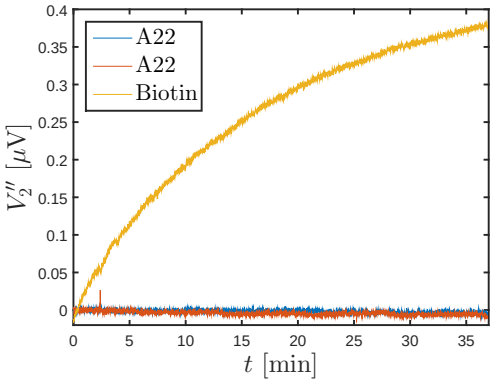

Figure 13.4: Sandwich assay signal for an assay with immobilized A22 aptamer, inactivated virus and magnetic beads coated with A22.

13.3.3 Aptamer binding to artificial virus

Figure 13.5 shows hybridization signals between (a) 50 nm beads and (b) 100 nm beads, both coated with H1N1 protein. In Fig. 13.5a, all four sensors (two with A22 aptamer, one with biotin, one with unspecific aptamer) show no significant signal. As the biotinylated sensor shows no signal, all streptavidin on the

beads must have hybridized to biotin-X-NTA. In Fig. 13.5b, the hybridization is done with 100 nm beads, again all four sensors show signals of similar magnitude, and more noise is observed.

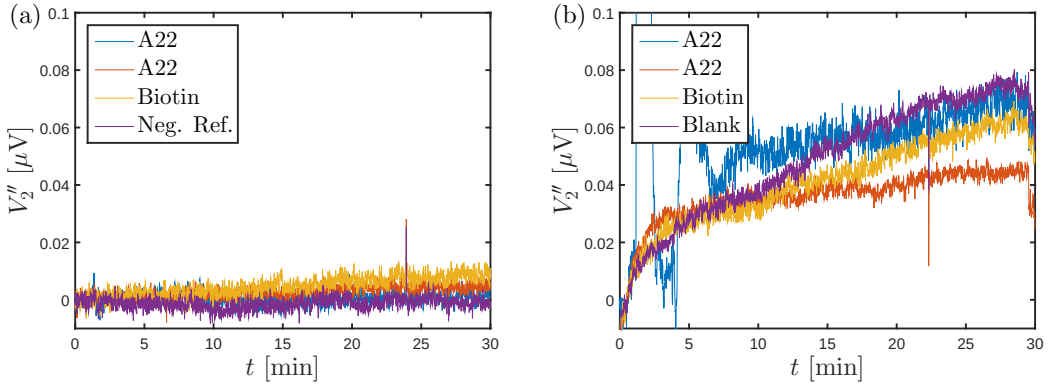

Figure 13.5: Hybridization signal between immobilized A22 aptamer and (a) 50 nm and (b) 100 nm beads coated with H1N1 protein.

Figure 13.6 shows four experiments where magnetic beads coated with H5N1-protein can bind to immobilized RHA0006. The RHA0006 aptamer was immobilized on two sensors, and the three other sensors were immobilized with A22, an unspecific aptamer (Neg. Ref. in legend) and biotinylated probes, respectively. Figure 13.6a shows the response from 50 nm beads in SB, all sensors show no significant response. Figure 13.6b shows the response from 80 nm beads in SB, all sensors give a signal of the same magnitude presumably due to sedimentation. Figure 13.6c shows the response from 50 nm beads in PBS, again all sensors show no significant response. Last, Fig. 13.6d shows the response from 50 nm beads in SB but where the concentration of artificial virus has been increased tenfold. Again, all sensors, except the biotinylated, show no significant signal. For the experiment in Fig. 13.6d, uncoated streptavidin beads were added to the artificial virus suspension to enable the positive reference to give a signal.

13.3.4 AFM measurements

Figure 13.7 shows the result of AFM (atomic force microscopy) measurements. The bead binding scheme was similar to Fig. 13.6d, with H5N1 coated 50 nm Miltenyi beads binding to the four probes: A22, RHA0006, Biotinylated DNA and an unspecific aptamer (Neg. Ref.). Note, that uncoated beads were added to the artificial virus suspension. For each AFM picture in Fig. 13.7, the surface coverage was estimated by doing a simple thresholding. All pixels with a height value above 80 % of the maximum measured height were assumed to be part of a bead. The biotinylated surface had a coverage of 15 % followed by a coverage of 12-11 % for the negative reference and RHA0006 coated surface, last the A22 surface only had s coverage of 6 %. The binding of artificial virus to both A22 and RHA0006 aptamer was comparable to the unspecific binding of the negative reference.

13.4 Discussion

13.4.1 Different beads sizes

Figures 13.3, 13.5 and 13.6 all show a significant signal from the negative reference or blank sensor when the bead size is above 50 nm. This signal, most likely, arises from beads sedimenting towards the sensor. As the dPHEB sensor measures differentially, between the top and bottom arm, this should not give a signal. The presence of the signal thus indicates that the dPHEB sensors are not perfectly balanced, which was also observed in Chapter 7. While the dPHEB sensor is not perfectly balanced, 50 nm beads are the better choice to prevent an unspecific signal, which can dominate the bead signal.

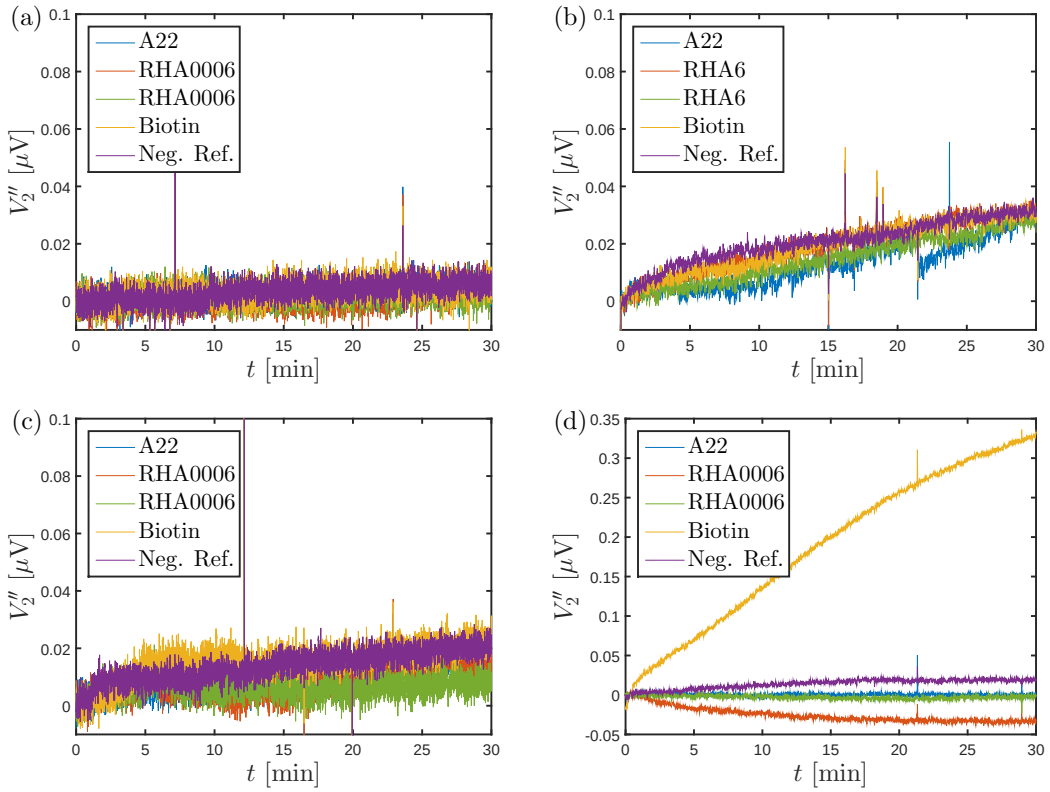

Figure 13.6: Hybridization signal between immobilized RHA0006 aptamer and (a,c,d) 50 nm and (b) 80 nm beads coated with H5N1 protein. Measurements were made in (a,b,d) SB or (c) PBS, and bead concentration was (a,b,c) 10× diluted or (d) stock concentration.

13.4.2 Positive reference sensor

The positive reference biotinylated sensors showed a significant signal when the magnetic beads were coated with A22 complementary DNA or aptamers (cf. Fig. 13.3, Fig. 13.4). Further, when the beads were coated with biotin-X-NTA and influenza proteins, no significant signal was observed for the biotinylated sensor (cf. Fig. 13.5, Fig. 13.6), unless uncoated beads were added to the bead suspension (cf. Fig. 13.6d). These results indicate that the biotinylated sensor functions as a positive reference, and that the biotin-X-NTA molecules saturates the available streptavidin. Thus, when saturating the streptavidin it is recommended to add new streptavidin beads.

13.4.3 Bead hybridization

Figure 13.3 shows that the A22 aptamers hybridized to beads with complementary DNA. This, along with the positive reference, indicate that the aptamers were spotted successfully on the chips and likely had the correct sequence. Contrary, when hybridizing to beads coated with both H1N1 and H5N1 proteins, (cf. Fig. 13.5, Fig. 13.6), none of the aptamer coated sensors showed a significant signal. Simlarly, the inactivated virus - A22 sandwich assay showed no significant signal. For the RHA0006 aptamer and H5N1 coated beads in Fig. 13.6, the exact same DNA sequence and virus strain was used as described by Shiratori *et al.* [2]. This was strongly expected to work and thus the hybridization was tested under the four different conditions described in Fig. 13.6, but none of them showed any signal.

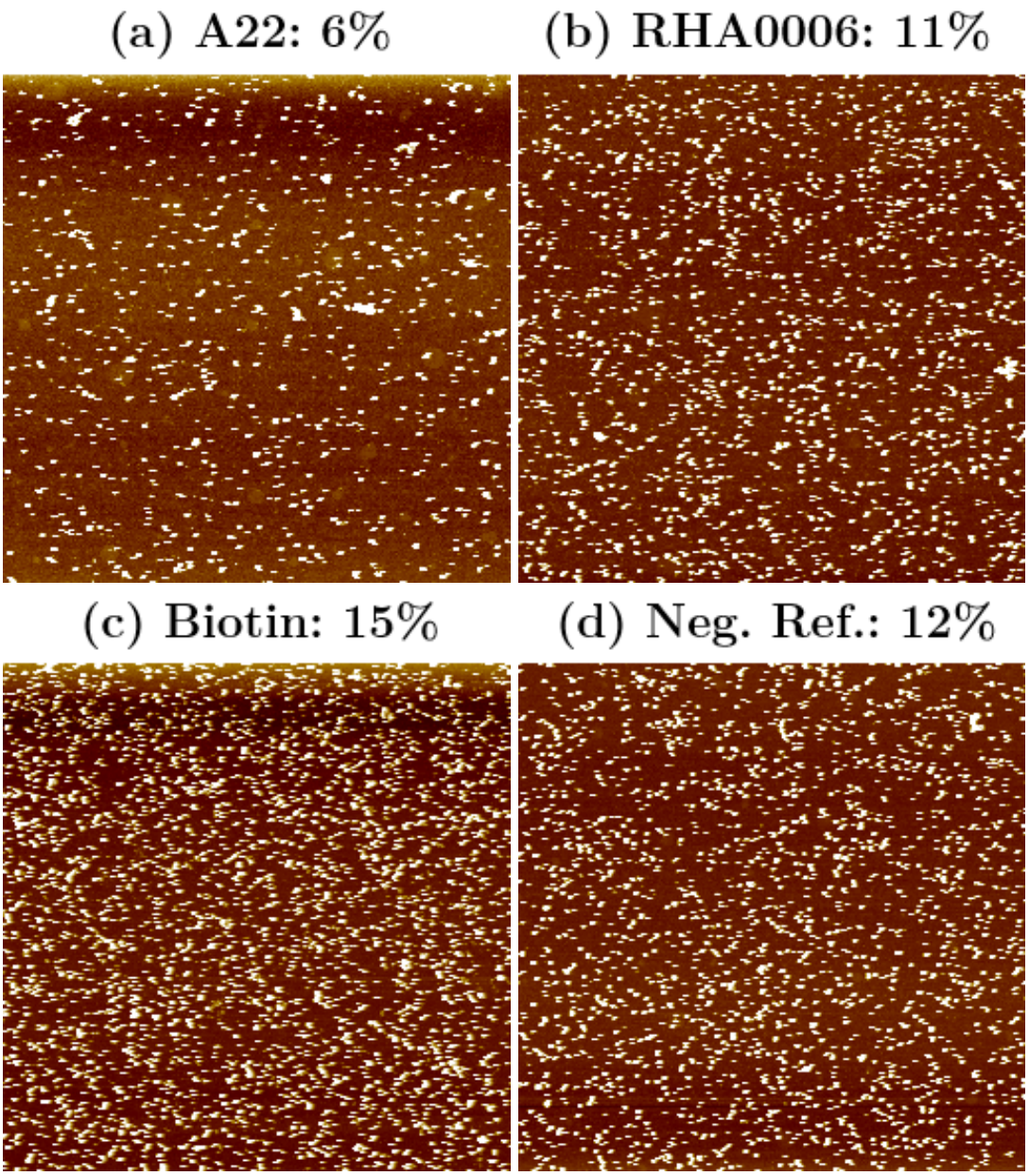

Figure 13.7: AFM picture of magnetic beads hybridizing to coated surface. The title of each plot states the sensor coating and bead surface coverage. All pictures have dimensions 10 µm × 10 µm.

13.4.4 AFM and magnetic measurements comparison

The AFM measurements of Fig. 13.7 agree with the magnetic measurements of Fig. 13.6. For both methods, bead hybridization is significantly higher on the biotinylated surface, when non coated beads are added. Similarly for both the A22 and RHA0006 aptamer, no significant hybridization is detected, as the bead signal and coverage is not above the negative reference levels. The AFM measurements were made with a bead suspension at the Miltenyi stock concentration, which resulted in a high background of 12 % for the negative reference. For future measurements, it could be advantageous to reduce this background by lowering the bead concentration.

13.4.5 Issues and improvements

The data in Section 13.3 indicate that the magnetic beads are coated with biotin-X-NTA, as there is no longer a signal from the positive reference sensor. Further, the aptamers are correctly immobilized on the sensors, as they can hybridize with complementary DNA. This leaves two places where the hybridization could have gone wrong, the protein coating and the aptamer protein bond.

To test the protein coating, it was speculated if the protein absorption could be measured by optical density measurements, but a simple calculation deemed any absorption signal to be below the limit of detection. However, instead of coating the beads with biotin-X-NTA and loading the NTA with nickel ions, beads preloaded with NTA and nickel ions can be bought commercial and used as an alternative to test this step. As an example, Ocean nanotech (San Diego, USA) sells 50 nm NTA-Ni conjugated magnetic beads, designed for affinity purification with His-tagged proteins.

Similarly, the aptamer-protein hybridization should be tested to pinpoint the problem. The data in Fig. 13.3 indicate that the aptamer is correctly immobilized and likely has the correct sequence. However, the conditions including the pre-experiment denature procedure, the selection buffer and its pH could prevent hybridization. To test this, the widely used aptamer-thrombin hybridization could be used as a test case. Immobilizing the thrombin aptamer on the chip and coating the beads with thrombin would allow testing the used conditions for general aptamer hybridization.

13.5 Conclusion

Chapter 13 investigated using aptamers to detect inactivated virus and artificial virus, i.e. magnetic beads coated with virus protein. This, in combination with the real-time measurement procedure used to measure DNA melting curve, could be a robust tool for determining the conditions under which the aptamer bounded to the virus, and under which an aptamer based assay would function. However, while the A22 aptamer could hybridized to beads coated with complementary DNA, both the A22 and RHA0006 aptamer never showed indications of binding to inactivated virus or beads coated with virus proteins. Suggestions for pinpointing the issues include using magnetic bead designed for affinity purification of His-tagged proteins and trying with the aptamer-thrombin hybridization as a test-case. More on this in Section 15.2.5.

Part IV

The statistics of measuring a bead surface coverage

14

Expected signal and its statistical fluctuation for bead measurements

Chapter 14 present a general approach for calculating the expected signal and the statistical fluctuation for beads detected by magnetoresistive (MR) sensor. The most common setup for bead detection is a stripe magnetoresistive sensor, usually with a spin-vale magnetic stack, that detects the presence of magnetic beads magnetized by a homogeneous external field [45, 48, 56]. The beads are usually attach to the surface through a sandwich assay with DNA-probes or antibodies functionalized on some biological active area (BAA) on top of the MR-sensor. As the MR sensors are in the micro-regime, the BAA often exceeds the sensor surface and magnetic beads will be uniformly present on both the sensor surface and its surroundings. This would be fine for fluorescence detection, where a uniform and dense layer of fluorescent labels is optimal. However, the dipole field from a magnetic bead rotated around the bead, and thus the added fields from a bead placed on top of the sensor and a bead outside the sensor partially cancels each-other. In the case of a bead monolayer, the MR sensor would experience no bead field. The origin of the bead field has thus never been clarified in the literature. Usually when calculating the signal per bead, beads outside the sensor surface are assumed to not contribute, and beads on the sensor are approximated as a dipole at the center of the sensor [42, 46, 113, 114, 115]. Chapter 14, based on Paper VIII, shows that these assumptions are widely inaccurate, and that the bead signal is actually provided by the beads *outside* the sensor, as these are at a lower height above the sensor plane, compared to the beads on top of the sensor. Paper VIII proposes a shift of paradigm to maximize the signal from the beads outside the sensor, either through the sensor design choices described, or through selectively not coating the sensor surface to prevent bead hybridization here [32].

Having clarified the origin of the bead signal, Chapter 14 then describes a theoretical framework for calculating the expected bead signal and its statistical fluctuations from the stochastic bead hybridization inside the BAA. These fluctuations of the signal, due to statistical sampling of the bead distribution, is another problem that has generally not been considered in the literature on magnetic biosensors. Chapter 14, based on Paper IX, shows in what cases the statistical fluctuations limit the lowest detectable bead coverage and the sensor dynamic range, and how to improve these.

Finally, Chapter 14 analyzes some sensors designs from the literature, that claim femto- and atto-molar limits of a detection, as examples of how to use the provided framework to analyze the sensor designs. Chapter 14 is based on Paper VIII and IX and more details can be found there.

14.1 Theory

14.1.1 Magnetoresistive sensors

Chapter 14 investigates the common magnetoresistive (MR) sensor, which consists of a magnetic stack in a stripe geometry with a resistance and output that depend linearly on the average field-component

$$V = G \times \frac{1}{A} \int_A H_y(\mathbf{r}) \mathrm{d}\mathbf{r} = G\langle H_y \rangle \tag{14.1}$$

where V is the sensor output, G is the sensitivity, A is the sensor area and $\langle H_y \rangle$ is the average magnetic field. Both geometries of a single stripe [45] or an array of stripes [56] are investigated, but the results

generally apply for both geometries. For most of the analysis, the sensor stripe is assumed infinitely long and oriented along the x-direction. Figure 14.1 shows the stripe and stripe-array geometries along with definitions of the coordinate origins, which is always at the sensor centroid, and the biological active area (BAA). Usually the BAA is bigger than the sensor, and beads are present both on top of and outside of the sensor, and in the case of a monolayer (without any height difference) the bead signal cancels out and the sensor signal is zero.

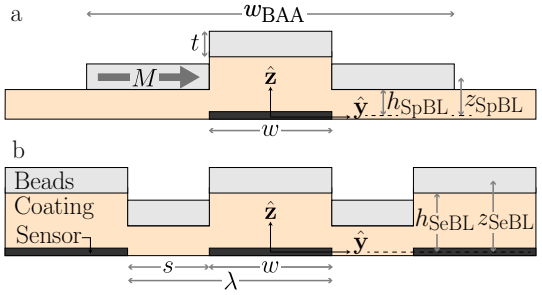

Figure 14.1: Cross-sections of (a) the single stripe geometry, and (b) the periodic stripe array geometry. Geometrical parameters and the coordinate system is also defined. The figure is adapted from Paper VIII.

14.1.2 Magnetic beads

The magnetic beads are assumed spherical with radius R, superparamagentic and magnetized by a homogeneous field H_{ext}, which gives a dipole moment of $m\hat{\mathbf{y}} = \frac{4\pi}{3}R^3\chi\mathbf{H}_{\mathrm{ext}}$. Assuming no magnetic interaction, the y-component of the magnetic dipole field at $\mathbf{r}$ is given by

$$H_{y,1}(\mathbf{r},\mathbf{r}_0) = \frac{m}{4\pi}\left(\frac{3(y-y_0)^2}{|\mathbf{r}-\mathbf{r}_0|^5} - \frac{1}{|\mathbf{r}-\mathbf{r}_0|^3}\right) \tag{14.2}$$

where $\mathbf{r}_0$ is the bead position. The dipole field, Eq. (14.2), averaged over the singles stripe sensor area, $A = l \times w$ is given by

$$\langle H_{y,1}\rangle(\mathbf{r}_0) = I(x_0+\tfrac{l}{2},y_0+\tfrac{w}{2}) - I(x_0+\tfrac{l}{2},y_0-\tfrac{w}{2}) - I(x_0-\tfrac{l}{2},y_0+\tfrac{w}{2}) + I(x_0-\tfrac{l}{2},y_0-\tfrac{w}{2}) \tag{14.3}$$

with

$$I(x_0,y_0) = \frac{-mx_0y_0}{4\pi A(y_0^2+z_0^2)|r_0|} \tag{14.4}$$

or from an infinite stripe in the x-direction

$$\langle H_{y,1}\rangle(\mathbf{r}_0) = \frac{m}{2\pi A}\left(\frac{y_0-w/2}{(y_0-w/2)^2+z_0^2} - \frac{y_0+w/2}{(y_0+w/2)^2+z_0^2}\right). \tag{14.5}$$

14.1.3 Signal position dependence

Figure 14.2 shows the total field in an infinite stripe sensor (cf. Eq. (14.5)) vs. the bead position. As seen from Fig. 14.2 both the magnitude and sign of the bead signal varies with bead position. As a good approximation, beads outside the sensor give rise to a positive field while beads on top of the sensor surface give rise to a negative field. Further, beads with a low z_0 value provide a stronger field, due to a stronger bead signal near the sensor edges ($y = \pm w/2$), which also leads to higher signal fluctuations.

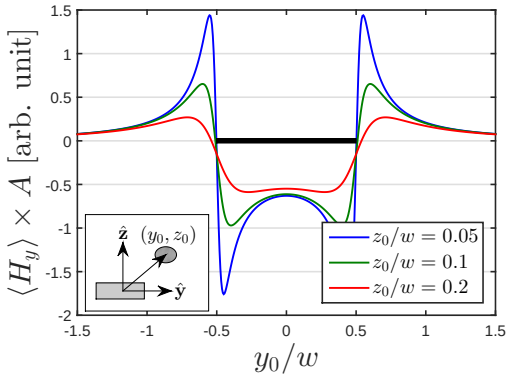

Figure 14.2: The total magnetic field detected by the infinite sensor from a single magnetic bead as a function of the bead position. The bead has magnetic moment, $m\hat{\mathbf{y}}$, and is positioned at (y_p, z_p) with respect to the sensor centroid (see inset). The figure is adapted from Paper VIII.

14.1.4 Expected signal and configurational fluctuation

If the Biological active area is limited to the sensor surface, all beads give rise to a negative field (cf. Fig. 14.2). However, when $w_{\mathrm{BAA}} > w$ the sensor signal from a magnetic bead distribution can be either positive or negative depending on where the beads hybridize. Due to the stochastic coverage, the sensor signal thus vary between experiments and these variations are referred to as configurational statistical fluctuations.

To estimate if the configurational fluctuations in the bead signal are significant, the expectation value of the sensor response as well as the standard deviation of the sensor response, need to be calculating, when the statistical sampling of the bead distribution is taken into account. Assuming equal probability for bead hybridization inside the BAA, the configurational expectation value of a function $f(\mathbf{r}_0)$ is

$$E[f] \equiv \frac{1}{A_{\mathrm{BAA}}} \int_{A_{\mathrm{BAA}}} f(\mathbf{r}_0)\, \mathrm{d}\mathbf{r}_0. \tag{14.6}$$

where A_{BAA} is the biological active area. The expectation values of the magnetic field, S_1, and its variance σ_1^2 for a single bead placed randomly on, A_{BAA}, are

$$S_1 = E[\langle H_{y,1} \rangle] \tag{14.7}$$

$$\sigma_1^2 = E[\langle H_{y,1} \rangle^2] - E[\langle H_{y,1} \rangle]^2. \tag{14.8}$$

Note, that S_1 and σ_1 depend on A, A_{BAA}, z_{SeBL} and z_{SpBL}. Assuming negligible magnetic and steric interactions (exclusion effects) between the beads, each bead signal is independent and identically distributed, *iid*, and the signal and its variance scales with the number of beads N. Usually, the exact number of beads is not known; instead the corresponding surface coverage can be estimated. The surface coverage is given by the ratio of the projected bead area to the BAA: $\phi(N) = N\pi R^2/A_{\mathrm{BAA}}$. Note, that ϕ has a limited range between a single bead and the coverage for a close-packed monolayer

$$\tfrac{\pi R^2}{A_{\mathrm{BAA}}} = \phi_1 \leq \phi \leq \phi_{\max} = \tfrac{\pi}{2\sqrt{3}} \approx 0.91, \tag{14.9}$$

The expectation value and variance for N beads or for the corresponding surface coverage, $\phi(N)$, is then

$$S_N = E[\sum_{i=1}^{N} \langle H_{y,i} \rangle] = NS_1 \qquad S_\phi = \frac{\phi A_{\mathrm{BAA}}}{\pi R^2} S_1 \tag{14.10}$$

$$\sigma_N^2 = \sigma^2[\sum_{i=1}^{N} \langle H_{y,i} \rangle] = N\sigma_1^2 \qquad \sigma_\phi^2 = \frac{\phi A_{\mathrm{BAA}}}{\pi R^2} \sigma_1^2 \tag{14.11}$$

If $\sigma_\phi > S_\phi$, the sensor signal variations between experiments are bigger than the sensor signal, and the signal cannot be trusted. The signal-to-standard deviation ratio (SDR) is defined as the ratio of the expected value to its fluctuation

$$SDR = \frac{|S_N|}{\sigma_N} = \frac{|S_1|}{\sigma_1}\sqrt{N} = \frac{|S_1|}{\sigma_1}\sqrt{\frac{\phi A_{\mathrm{BAA}}}{\pi R^2}}. \tag{14.12}$$

Note, that $SDR \propto \sqrt{N}$ in accordance with the central limit theorem. Likewise, the minimum surface coverage, ϕ_{stat}, that ensures the signal is higher than its configurational fluctuations, i.e. $SDR = 1$, is defined from Eq. (14.12) as

$$\phi_{\mathrm{stat}} = \frac{\pi R^2}{A_{\mathrm{BAA}}}\left(\frac{\sigma_1}{S_1}\right)^2. \tag{14.13}$$

Every sensor experiences some output voltage noise, V_{noise}. The magnetic bead coverage, ϕ_{noise}, that gives rise to a signal of the same magnitude as V_{noise} can be calculated from Eq. (14.1) and Eq. (14.10)

$$\phi_{\mathrm{noise}} = \frac{\pi R^2 V_{\mathrm{noise}}}{G A_{\mathrm{BAA}} S_1} = \frac{3V_{\mathrm{noise}}}{4R\chi H_{\mathrm{ext}} G A_{\mathrm{BAA}}(S_1/m)} \tag{14.14}$$

where in the last equation S_1 has been normalized with the magnetic bead moment to explicit state the dependence of ϕ_{noise} on the bead parameters R, χ. The parameters ϕ_1, ϕ_{stat} and ϕ_{noise} all limits the lowest bead coverages that can be resolved. For practical applications, it is assumed that one of them dominates and the resolution in surface coverage, ϕ_{res}, and the corresponding dynamic range (DR) is

$$\phi_{\mathrm{res}} = \max\{\phi_1, \phi_{\mathrm{stat}}, \phi_{\mathrm{noise}}\} \qquad DR = \frac{\phi_{\max}}{\phi_{\mathrm{res}}} = \frac{0.91}{\max\{\phi_1, \phi_{\mathrm{stat}}, \phi_{\mathrm{noise}}\}}. \tag{14.15}$$

The DR takes into account that the detectable bead coverage can be limited by the discrete nature of magnetic beads, by the statistical sampling fluctuations and by the electrical noise. Equation (14.15) should be evaluated on a case-to-case basis to estimate where the sensor design needs optimization.

14.1.5 Effect of bead distribution area

Figure 14.3 shows example calculations of (a) the sensor signal, (b) the configurational fluctuation and (c) signal-to-standard deviation ratio, all for a constant surface coverage, a square sensor and as function of the side length of the square BAA. For a small BAA $w_{\mathrm{BAA}} \ll w$, every bead placement gives equal signal, and S_1 is constant and the S_ϕ scales with A_{BAA}. Further, σ_ϕ and SDR are very low and high, respectively. As w_{BAA} increases the signal, $|S_\phi|$, increases to its maximum value at $w_{\mathrm{BAA}} = w$, where the sensor surface is covered. Likewise σ_ϕ increases rapidly due to more beads and higher fluctuations (cf. Fig. 14.2). As σ_ϕ increases faster than $|S_\phi|$, the SDR decreases. In general, if $z_{\mathrm{SeBL}} = z_{\mathrm{SpBL}}$, SDR decreases as w_{BAA}^{-1} but with a drop when the bead area is increased beyond the sensor surface. In general, beads with a low z-distance have a higher $|S_\phi|$ but a lower SDR.

Figure 14.3 clearly shows that the signal is optimized by limiting the BAA to only cover the sensor surface, and in this case it is generally found that $SDR \gg 1$. However, if the beads outside the sensor area are at a lower height ($z_{\mathrm{SpBL}} < z_{\mathrm{SeBL}}$, red dashed line in Fig. 14.3), the sensor signal changes sign and remains non-zero as $w_{\mathrm{BAA}} \gg w$. Usually magnetic beads are bound both inside and outside the sensor area, and at lower height outside the sensor are, thus the usual sensor response is dominated by the positive field from bead outside the sensor surface. If the BAA cannot be limited to the sensor surface and $z_{\mathrm{SpBL}} < z_{\mathrm{SeBL}}$, the BAA should be big enough to give a strong field from the outside beads as both the S_ϕ and SDR increases after S_ϕ changes sign.

14.2 The importance of height variations

Section 14.2 investigates how to increase the sensor signal S_1. The analysis focuses on an infinite array of stripes, cf. Fig. 14.1b, but arrays of only 10 stripes show the same behavior, cf. Paper VIII, and

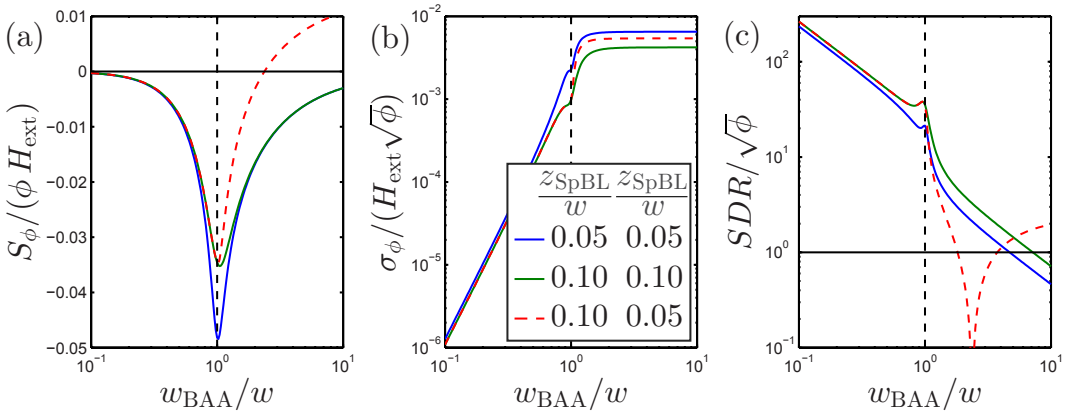

Figure 14.3: (a) The expected bead field, (b) the statistical fluctuations, (c) the signal to fluctuation ratio as a function of w_{BAA} for a constant surface coverage. The calculations were done for a square sensor $l = w = 1$ µm, for a square BAA $A_{\text{BAA}} = w_{\text{BAA}} \times w_{\text{BAA}}$, and for magnetic beads with $R = 50$ nm and $\chi = 1$.

the results are qualitatively correct for a single sensor. Each sensor stripe is assumed infinite in the x-direction which limits the problem to a 2D periodic geometry. For this geometry it is natural to normalize the geometrical parameters with the stripe period, λ, the normalized parameters are denoted by a tilde, i.e. $\tilde{z} = \frac{z}{\lambda}, \tilde{w} = \frac{w}{\lambda}, \tilde{s} = 1 - \tilde{w}$, and $\tilde{t} = \frac{t}{\lambda}$. Further, Section 14.2 distinguishes between the Sensor Bead Layers (SeBL) and the in-between bead layer i.e. the Space Bead Layers (SpBL). Section 14.2 summarizes selected results from Paper VIII, which can be read for more details.

14.2.1 Plate approximation

The expectation value of Eq. (14.7) is found by integrating the signal from all possible bead positions in the BAA. Equivalently valid, S_1 can be calculated by substituting the bead with an infinitely thin sheet of magnetic material for all bead positions. Alternatively, the dipole approximation can be abandon, and instead the bead distribution can be approximated by a plate with a finite thickness identical to the magnetic bead diameter, $t = 2R$. The plates have a constant magnetization, $\mathbf{M} = M\hat{\mathbf{y}} = \int_{\mathcal{V}_{\text{plate}}} m \mathrm{d}\mathcal{V}\hat{\mathbf{y}}$, which depends on the bead surface coverage and their magnetic moment. All results are given in terms of the average magnetic field in the sensor normalized to the plate magnetization $\langle \tilde{H}_y \rangle = \langle H_y \rangle / M$.

Figure 14.4 compares the approximation of a finite thickness plate as the thickness decreases towards 0 (i.e. towards the dipole approximation). The plot is calculated for the beads between the sensors, i.e. the SpBL, and shows $\langle \tilde{H}_y \rangle$ vs. $\tilde{z}_{\text{SpBL}}$. Further, as the magnetic moment changes for varying thickness, $\langle \tilde{H}_y \rangle$ has been further normalized with $\tilde{t}$. As seen in Fig. 14.4, the curves for different $\tilde{t}$ approach the universal curve for $\tilde{t} \to 0$ i.e. the dipole sheet curve. The inset of Fig. 14.4 shows the relative deviation from the dipole sheet curve as function of $\tilde{z}_{\text{SpBL}}/\tilde{t}$. The absolute relative deviation is observed to be below $\sim 15\%$ for $\tilde{z}_{\text{SpBL}} > \tilde{t}/2$ and below 5% for $\tilde{z}_{\text{SpBL}} > \tilde{t}$. When $\tilde{z}_{\text{SpBL}} \geq \tilde{t}/2$ (indicated by the dashed vertical lines in Fig. 14.4) the signal from a finite thickness and dipole sheet are approximately equal. However, when $\tilde{z}_{\text{SpBL}} \to 0$ the dipole sheet signal diverges. This divergence comes the model allowing the bead center to be touching the sensor, cf. $(y_0 = w/2, z_0 = 0)$ in Eq. (14.5). In practice, the bead center is always at least one radius away from the sensor. For the plate approximation, the magnetic moment is smeared out across the finite thickness, and thus plates are less sensitive to this issue, and thus a better approximation for $\tilde{z}_{\text{SpBL}} < \tilde{t}/2$. The plate approximation is used in the rest of Section 14.2, and the approximation is also numerically easier to calculate compared to any integral, as a closed-form solution exist as shown in Appendix A.

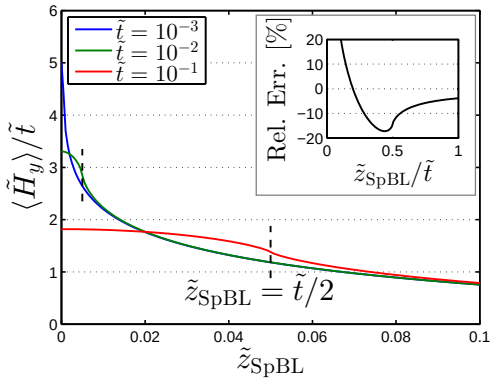

Figure 14.4: The sensor magnetic field, normalized to constant plate moment, vs. the height distance between the SpBL and the sensor. The dashed lines indicate when the edge of a SpBL passes the sensor-plane. The inset shows the relative error when comparing the dipole sheet to a plate of thickness $\tilde{t} = 0.1$. All calculations were done for $\tilde{w} = 0.5$. The figure is adapted from Paper VIII.

14.2.2 Effect of the sensor bead layer distance

As seen from Fig. 14.3 or Fig. 14.2, the field experienced by the sensor, $\langle \tilde{H}_y \rangle$, decreases with decreasing bead height, $\tilde{z}$. In Fig. 14.5a, $\langle \tilde{H}_y \rangle$ is calculated for the SpBL and as a function of $\tilde{z}_{\mathrm{SpBL}}$ and for different sensor widths. When the bead layer is in line with the sensor layer, $\tilde{z}_{\mathrm{SpBL}} \leq \tilde{t}/2$, the field decreases slowly with increasing $\tilde{z}_{\mathrm{SpBL}}$, cf. Fig. 14.4. As the bead passes the sensor layer, $\tilde{z}_{\mathrm{SpBL}} > \tilde{t}/2$, $\langle \tilde{H}_y \rangle$ decreases rapidly before then decreasing exponentially as $\langle \tilde{H}_y \rangle \propto \exp(-2\pi \tilde{z}_{\mathrm{SpBL}})$.

As a thought experiment, consider a SeBL which give rise to a field. Now one can superimpose a monolayer with magnetization $-M$. As a monolayer gives no signal this will not change the sensor signal. However, the added monolayer cancels the SeBL and a creates a SpBL with magnetization $-M$. As the signal has not changed, one can conclude that the SeBL give rise to a signal of same magnitude but opposite sign as a SpBL at the same height, and vice versa. This is shown in the inset of Fig. 14.5a where the average field from the SpBL (solid line), and from the SeBL (dashed line), are plotted. The SpBL height can be smaller, i.e. pass the sensor plane, but otherwise the fields only differ by their signs.

As the SpBL and SeBL partially cancel each other for all geometries, see the inset of Fig. 14.5b, the sensor signal is maximized by having one layer with a low height distance and one layer with a high height distance. Writing, $\tilde{z}_{\mathrm{SeBL}} = \tilde{z}_0 + \Delta\tilde{z}/2$ and $\tilde{z}_{\mathrm{SpBL}} = \tilde{z}_0 - \Delta\tilde{z}/2$, where $\tilde{z}_0$ is the average layer height and $\Delta\tilde{z}$ is the layer separation, Fig. 14.5b shows the sensor field vs. the layer separation, $\Delta\tilde{z}$. Figure 14.5b shows the importance of the height difference, as the signal scales approximately linearly with $\Delta\tilde{z}$, with a slope that increases with decreasing $\tilde{z}_0$. As the SpBL is usually at lower height, it dominates the signal contribution and the SeBL actually lowers the signal by partially canceling the SpBL field. This leads to the paradigm shift that SpBL should be optimized. For example, the sensor signal can be enhanced by selectively coating, e.g. by limiting the BAA to be only outside the sensor surfaces.

14.2.3 Effect of the sensor width and spacing

Of the different widths investigated in Fig. 14.5a, the signal is strongest for $\tilde{w} = 1/3$. When $\tilde{w}$ is reduced the distance between the magnetic poles of the SpBL decreases. This increases the field in the sensor, if the sensor is close to the SpBL, i.e. $z_{\mathrm{SpBL}} \approx 0$, but decreases the field if there is large height difference. The optimal width, $\tilde{w}_{\mathrm{opt}}$, that produces the highest signal depends on $\tilde{z}$ and $\tilde{t}$. Figure 14.6a shows $\tilde{w}_{\mathrm{opt}}$ vs. $\tilde{z}_{\mathrm{SpBL}}$ along with the curves of $\tilde{w}$ that give 90% and 95% of the signal obtained for $\tilde{w}_{\mathrm{opt}}$. When beads are close to the sensor ($|\tilde{z}| < \tilde{t}$), the sensor signal increases with decreasing $\tilde{w}$. And as shown in

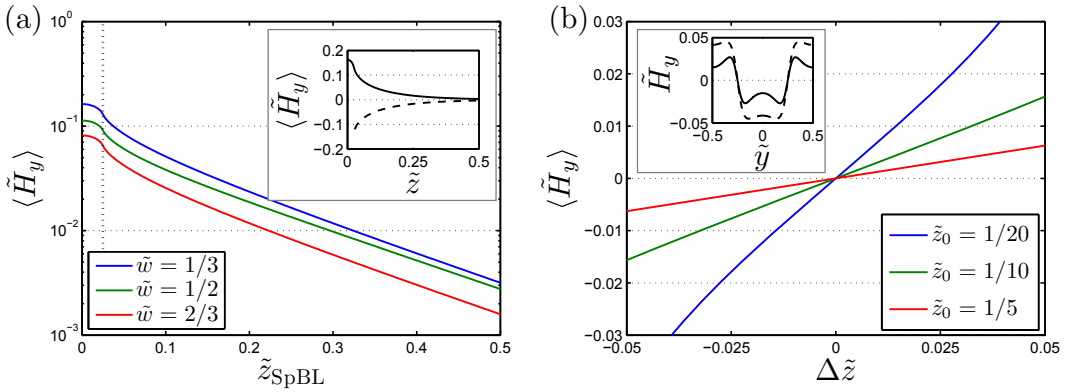

Figure 14.5: (a) $\langle \tilde{H}_y \rangle$ vs. $\tilde{z}_{\mathrm{SpBL}}$, i.e. only a SpBL, for three values of $\tilde{w}$. The inset shows $\langle \tilde{H}_y \rangle$ on a linear scale vs. $\tilde{z}$ for both a SpBL (solid line) and SeBL (dashed line), calculated for a geometry with $\tilde{w} = 1/3$ and $\tilde{w} = 0.5$. (b) $\langle \tilde{H}_y \rangle$ for both a SeBL and SpBL as a function of the separation distance between the SeBL and SpBL. The inset shows the magnetic field from only the SpBL (dashed line) and from both layers (solid line). Calculations were done for $\tilde{t} = 0.05$ and $\tilde{w} = 0.5$, and for the inset $\tilde{z}_{\mathrm{SpBL}} = 0.1$ and $\tilde{z}_{\mathrm{SeBL}} = 0.2$. The figure is adapted from Paper VIII.

Fig. 14.6b if $\tilde{w}$ is reduced from $\tilde{w} = 0.5$ to $\tilde{w} = 0.25$ the average magnetic field is increased by 80% for $\tilde{z} \leq 0.05$.

In practice, the sensor width is often fixed by the sensor design or fabrication limitations. And decreasing $\tilde{w}$ is only viable by increasing s. However, increasing s results in a decrease of $\tilde{t}$ (bad), $\tilde{z}$ (good) and $\tilde{w}$ (good). For this analysis it is easier to normalize each geometrical parameters to w. Figure 14.6c shows $\langle \tilde{H}_y \rangle$ as a function of s/w. Generally, $\langle \tilde{H}_y \rangle$ increases rapidly with s when $s \leq w$, then flattens out and becomes essentially independent when $s/w > 2$. As the SeBL and SpBL gives opposite fields the combined SpBL and SeBL field can be obtained by subtracting the curves, in Fig. 14.6c, for their corresponding z-values. However, the difference between curves at different heights (different colors in Fig. 14.6c) is mostly unchanged for $s \geq w$. If both the SpBL and SeBL are present, the signal is not significantly optimized by increasing s beyond w. Likewise, if both the SpBL and SeBL are present, and if w is reduced, s can also be reduced until $s = w$ without decreasing the sensitivity.

14.2.4 Summary of signal optimization

Section 14.2 showed that the SpBL contribute a higher signal than the SeBL and that the sensor signal can be increased by: (1) Reducing the average height $\tilde{z}_0$ of the SeBL and SpBL; (2) increasing the separation $\Delta\tilde{z}$ between the SeBL and SpBL; (3) decreasing the sensor width $\tilde{w}$ or period; (4) using magnetic beads with a higher magnetization or a larger size, which is discussed in Section 14.3. Further, the signal can usually be greatly improved, if the sensor can be selectively coated for beads to only bind on top of or outside the sensor surface. This knowledge presents a shift of paradigm as the literature has focused on optimizing the signal from the SeBL instead of the SpBL.

14.3 Configurational statics of magnetic beads

Section 14.2.1 shows that bigger beads yield a bigger sensor signal per bead. However, for the same surface coverage a few but big beads have a higher statistical fluctuation than more but smaller beads. Section 14.3 investigates the influence of the bead size on the sensor signal, on its fluctuation and on the corresponding ϕ_{res}. Figure 14.7a shows the normalized sensor signal $V/(G\chi H_{\mathrm{ext}}) = \tilde{R}^3 S_\phi$ for $\phi = \phi_{\max}$ and $\phi = \phi_1$, as function of R/w when $z/w = 0.05 + R/w$. The measurements were done for a square sensor $l = w$, and for a square BAA with side lengths w (left column) or $2w$ (right column). The blue

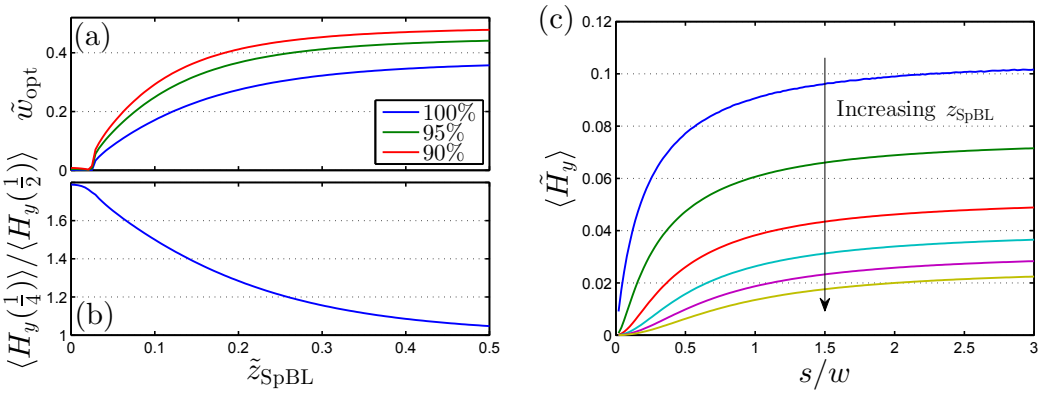

Figure 14.6: (a) The optimal sensor width $\tilde{w}_{\mathrm{opt}}$ (blue line) as a function of $\tilde{z}_{\mathrm{SpBL}}$. Also plotted are the sensor widths that give 95% and 90% of the improvement of $\tilde{w}_{\mathrm{opt}}$. (b) The gain from using a reduced width, $\tilde{w} = 0.25$, instead of $\tilde{w} = 0.5$. Calculations were done for $\tilde{t} = 0.05$. (c) $\langle \tilde{H}_y \rangle$ as function of s/w for $z_{\mathrm{SpBL}}/w = 0.05, 0.1, 0.2, 0.3, 0.4$ and 0.5. Calculations were done for $t/w = 0.1$. The figure is adapted from Paper VIII.

lines correspond to an arbitrary noise level of $V_{\mathrm{noise}}/(G\chi H_{\mathrm{ext}}) = 3 \times 10^{-4}$. As expected S_1 and $S_{\phi_{\max}}$ (solid lines in Fig 14.7a) and σ_1 and $\sigma_{\phi_{\max}}$ (dashed lines in Fig 14.7a) all generally increases with R due to higher magnetic moment. Note, that when $2R \approx w$, S_1 saturates due to the decreasing sensitivity with increasing z_0.

When the BAA can be limited to the sensor surface ($w_{\mathrm{BAA}} = w$), the configuration fluctuations are low and the detectable surface coverage is only limited by the sensor noise or the discrete nature of beads, i.e. single bead detection is possible as $\sigma_1 < S_1$. In this case the beads should be big enough for the signal to overcome the electrical noise, but not bigger as this would limit the dynamic range. Similarly, when $w_{\mathrm{BAA}} = 2w$, $\sigma_1 > S_1$ and equivalently $\phi_{\mathrm{stat}} > \phi_1$ and the detectable surface coverage is limited by the configuration fluctuations if big beads are used, or by the sensor noise for small beads.

Figure 14.7b shows the ϕ-values corresponding to the data in Fig 14.7a. As expected ϕ_1 and ϕ_{stat} increase with increasing bead size R/w, while bead coverage, needed to overcome the sensor noise, decreases. As mentioned, the statistical sampling fluctuation is important for $w_{\mathrm{BAA}} = 2w$ where $\phi_{\mathrm{stat}} > \phi_1$, and here it reduces the dynamic range. In all cases, if too small beads are used the dynamic range is limited by sensor noise, and if too big beads are used the dynamic range is limited by configurational fluctuations. Thus the optimize bead size (the size resulting in the largest dynamic range) can be found from the noise level and an analysis like this. For the cases in Fig. 14.7, the optimal bead sizes are $R/w \approx 0.05$ ($w_{\mathrm{BAA}} = w$) and $R/w \approx 0.03$ ($w_{\mathrm{BAA}} = 2w$) corresponding to dynamic ranges of 2.0 and 1.5 orders of magnitude.

14.4 Case studies

Section 14.4 uses the framework of Section 14.1 to analyze examples from the literature; three sensors designs, which can be seen in Fig. 14.8, by Graham *et al.* [45], Martins *et al.* [48], and Gaster *et al.* [56], respectively. Below, the three sensors are described. In the stack compositions, all thicknesses are given in nanometer and the free layer of the stack is underlined.

14.4.1 Sensor descriptions

Graham et al. *description.* Graham *et al.* [45], Fig. 14.8I, used a $w \times l = 2$ µm $\times$ 6 µm stripe sensor to detect hybridization of Nanomag®-D $2R = 250$ nm magnetic beads. The spin valve sensor stripe had a nominal magnetic stack of Ta(2)/NiFe(3)/CoFe(2.5)/Cu(2.6)/CoFe(2.5)/MnIr(6)/

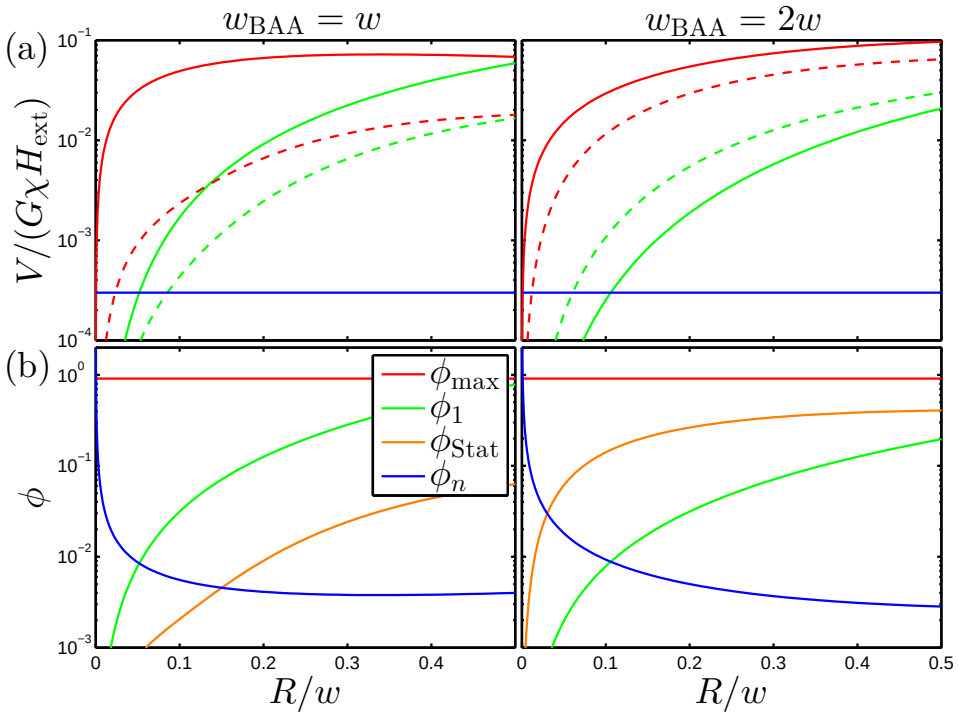

Figure 14.7: (a) Normalized sensor signal (solid lines) and its configurational fluctuations (dashed lines) for the maximum surface coverage (red lines) and for one bead (green lines) and the arbitrary sensor noise (blue line). (b) The corresponding surface coverages ($\phi_{\mathrm{max}}, \phi_1, \phi_{\mathrm{stat}}, \phi_{\mathrm{noise}}$). The calculations were performed for a square sensors ($l = w$), a square BAA $A_{\mathrm{BAA}} = w_{\mathrm{BAA}} \times w_{\mathrm{BAA}}$, and $z/w = R/w + 0.05$. The figure is adapted from Paper IX.

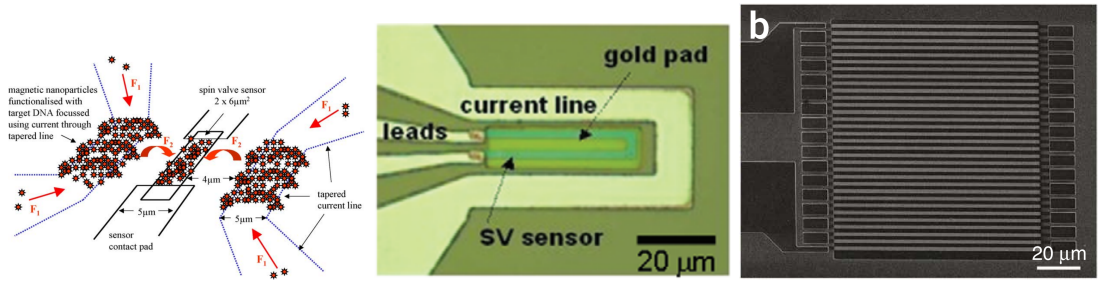

I II III

Figure 14.8: Three sensors from the literature analyzed using Section 14.1. I is from Graham *et al.* [45], II is from Martins *et al.* [48], III is from Gaster *et al.* [56].

Ta(3)/TiW(N)(15) and the sensor and its surroundings were coated with a 200 nm thick SiO_2 layer. During ion milling fabrication the sensor surroundings were overetched 5 nm. Graham *et al.* used current lines to attract the magnetic beads (cf. Fig. 14.8a) to the sensor region, and it is assumed that beads bind uniformly between these two current lines, which is a square BAA with side length $w_{\mathrm{BAA}} = 16$ μm.

Martins et al. *description.* Martins *et al.* [48], Fig. 14.8II, (same group as Graham *et al.*) used a U-shaped sensor strip with total length of 80 μm and width of 2.5 μm to detect Nanomag®-D

$2R = 250$ nm magnetic beads. The spin valve sensor stripes had a nominal magnetic stack of Ta(1.5)/NiFe(3)/CoFe(2.5)/Cu(2.1)/CoFe(2.5)/MnIr(8)/Ta(2)/TiW(N)(15) and the sensor and its surroundings were coated with a double oxide layer of Al_2O_3 (100 nm)/SiO_2 (200 nm). During ion milling fabrication the sensor surroundings were overetched 5 nm. Further, a 43 µm $\times$ 13 µm Ti(5 nm)/Au(20 nm) pad centered on top of the sensor U-branch was used for selective functionalization and defined the BAA. Further, a U-shaped current line structure was used to attract and focus the beads to the sensor stripe.

Gaster et al. *description.* Gaster *et al.* [56], Fig. 14.8III, used a meandering sensor array with 32 series-connected stripes, each of $w \times l = 0.75$ µm $\times$ 100 µm, to detect hybridization of Miltenyi Biotech $2R = 50$ nm magnetic beads. The spin valve sensor stripes had a nominal magnetic stack of Ta(5)/Seed layer(4)/MnIr(8)/CoFe(2)/Ru(0.8)/CoFe(2)/Cu(2.3)/CoFe(1.5)/Ta(3) and the sensor and its surroundings were coated with SiO_2(10)/Si_3Ni_4(20)/SiO_2(10) [13]. Again ion milling with overetching was used and the height difference between the stack and its surroundings was measured after deposition using an atomic force microscope to be 60 nm. As the BAA is unknown but significantly larger than the sensor, it is assumed to be infinite.

Descriptions summary The z_{SeBL} and z_{SpBL} were calculating as the vertical distances from the bead-center to the free sensor layer (underlined in descriptions). This along with the other geometrical parameters for the three sensors in Fig. 14.8 are summarized in Table 14.1.

Table 14.1: Geometrical parameters for the sensors in sensors in Fig. 14.8. A_{bead} is the estimated bead hybridization area of each sensor. The table is adapted from Paper IX.

	w [µm]	l [µm]	z_{SeBL} [nm]	z_{SpBL} [nm]	$\frac{z_{\mathrm{SeBL}}-z_{\mathrm{SpBL}}}{(z_{\mathrm{SeBL}}+z_{\mathrm{SpBL}})/2}$ [%]	R [nm]	A_{bead} [(µm)^2]
Graham *et al.* [45]	2	6	357	315	13	125	256
Martins *et al.* [48]	2.5	80	482	430	11	125	559
Gaster *et al.* [56]	0.75	32 $\times$ 100	69	9	154	25	∞

14.4.2 Results

Using Table 14.1, S_1 and σ_1 were calculated for all three sensors in Fig. 14.8. From the S_1 and σ_1 quantities, the values in Table 14.2 of ϕ_1, ϕ_{stat}, $\log_{10}(\mathrm{DR})$ and $S_{\phi_{\mathrm{max}}}$ were calculated. The top row of each geometry in Table 14.2 is calculated for $A_{\mathrm{BAA}} = A$ while the bottom row uses the real BAA $A_{\mathrm{BAA}} = A_{\mathrm{bead}}$ from Table 14.1.

When $A_{\mathrm{BAA}} = A$, all sensors are not limited by statistical fluctuations, i.e. $\phi_1 > \phi_{\mathrm{stat}}$, and all sensors have $DR > 2$. This is similar to the examples in Fig. 14.7. However, for $A_{\mathrm{BAA}} = A_{\mathrm{bead}}$, $\phi_{\mathrm{stat}} > \phi_1$, for all sensors. The signal at a given surface coverage is proportional to $S_{\phi_{\mathrm{max}}}$, as $S_\phi = S_{\phi_{\mathrm{max}}}\phi/\phi_{\mathrm{max}}$. Because of the low height difference, $\frac{z_{\mathrm{SeBL}}-z_{\mathrm{SpBL}}}{(z_{\mathrm{SeBL}}+z_{\mathrm{SpBL}})/2}$, for the designs of Graham *et al.* and Martins *et al.*, their signal (at a constant surface coverage) decreases 105 times and 28 times, respectively, when A_{BAA} is increased from A to A_{bead}. Contrary, for Gaster *et al.*, whose sensor has a good height difference, the signal is slightly increases when $A_{\mathrm{BAA}} = \infty$.

Studying Table 14.2 in the case of $A_{\mathrm{BAA}} = A_{\mathrm{bead}}$ the following conclusions can be made.

- The sensor design by Graham *et al.* is by far the worst. $S_{\phi_{\mathrm{max}}}$ is low and correspondingly $\phi_{\mathrm{stat}} \gg \phi_{\mathrm{max}}$. From this analysis, any single sensor measurement will be unreliable, and the design is far from optimal. More information is properly needed here.

- The sensor design by Martins *et al.* is an improvement compared to Graham *et al.*, but $S_{\phi_{\mathrm{max}}}$ is still greatly reduced when $A_{\mathrm{BAA}} = A_{\mathrm{bead}}$ and as a result statistical fluctuations limits the detectable surface coverage to 7.5 %, which is rather high. Similarly, when $\phi = \phi_{\mathrm{max}}$, $SDR_{\phi_{\mathrm{max}}} = 3.5$ i.e. the

statistical fluctuation will still be 29 % of the average signal. These large statistical fluctuations are seen in Martins *et al.* [48], as large error bars on their reference curve. The design is also limited by statistical fluctuation, which could be improved by increasing the relative height difference or by decreasing the ratio of the bead size to the BAA.

- The sensor design by Gaster *et al.* has a large positive $S_{\phi_{\max}}$, for $A_{\mathrm{BAA}} = A_{\mathrm{bead}}$. Thus, the signal is dominated by the magnetic beads outside the sensor surface. The large $S_{\phi_{\max}}$, combined with the small ratio of bead-size to sensor-size, greatly reduces the statistical sampling fluctuations so $\phi_{\mathrm{stat}} \ll \phi_{\max}$. For this design statistical sampling is not a problem and bigger beads could be used if electrical noise, and not variations in experimental conditions, limits the resolution.

Table 14.2: Statistical sensor characteristics for the sensors in Fig. 14.8. The first row of each design is calculated for $A_{\mathrm{BAA}} = A$ and the second row is calculated using the $A_{\mathrm{BAA}} = A_{\mathrm{bead}}$ from Table 14.1. The table is adapted from Paper IX.

	ϕ_1 [%]	ϕ_{stat} [%]	$\log_{10}(\mathrm{DR})$	$S_{\phi_{\max}}$	$SDR_{\phi_{\max}}$
Graham *et al.* [45]	0.4	$2.3 \cdot 10^{-2}$	2.4	-147	62
	$1.2 \cdot 10^{-2}$	$2.3 \cdot 10^{3}$	-1.4	-2	0.2
Martins *et al.* [48]	$2.5 \cdot 10^{-2}$	$1.0 \cdot 10^{-3}$	3.6	-253	301
	$8.8 \cdot 10^{-3}$	7.5	1.1	9	3.5
Gaster *et al.* [56]	$8.2 \cdot 10^{-5}$	$5.6 \cdot 10^{-6}$	6.1	-686	4020
	0	$7.2 \cdot 10^{-4}$	5.1	705	355

14.5 Conclusion

Chapter 14 analyzed the statistics of the most common bead detection technique, where the beads are magnetized by homogeneous field and detected by a stripe magnetic sensor. The sensor output is assumed proportional to the average field. The expected signal is found to be from the beads outside the sensor surface, as the biological active area usually extends past the sensor surface and as the beads located outside the sensor are usually at a lower height compared to beads on top of the sensor. This height difference, even if it is only a few nanometers, is the reason why the expected sensor signal is not zero. This gives rise to a paradigm shift where the signal from beads outside the sensor should be optimized for example by selectively preventing the sensor surface to be biologically coated. Further, it was found that the statistical sampling fluctuations may significantly reduce the sensitivity and obtainable dynamic range of a sensor. This becomes increasingly important as the bead size compared to the sensor size increases. Hence, it is essential to include statistical sampling considerations in the evaluation of the sensor design and used appropriately sized beads.

14.6 Perspective for self-field detection

The analysis in Chapter 14 has focused on detection beads magnetized by a homogeneous external field, as the origin of the bead field was not covered in the literature. However, Part II and Part III of this thesis focused on detected magnetic beads magnetized by the sensor self-field from the powering current. When the beads are magnetized by the sensor self-field their magnetic moments vary around the sensor. Thus, they provide a positive signal at any point. Though always positive, this signal is still position dependent. Assuming the sensor to be infinite, Fig. 14.9 shows the bead signal calculated for different bead positions and as expected, cf. Fig. 6.7, the signal is strongest for bead close to the sensor edges.

For $|y_p| > w/2$ the bead field in Fig. 14.9 decreases towards zero. For high values of w_{BAA}, the bead signal and its standard deviation show the following behaviors $S_1 \propto w_{\mathrm{BAA}}^{-1}$ and $\sigma_1 \propto w_{\mathrm{BAA}}^{-1/2}$. For $w_{\mathrm{BAA}} > w$, this results in ϕ_{stat} decreasing with w towards its asymptotic value. In other words, the surface coverage needed for the signal to be bigger than its statistical fluctuations decreases with the

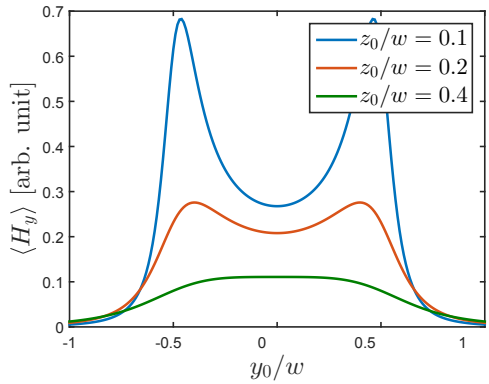

Figure 14.9: The average magnetic field in the sensor vs. the position of the magnetic bead when magnetized by the sensor self-field. The sensor is infinite in the x-direction.

BAA, and a bigger BAA always increases S_ϕ and the SDR. This was not the case for beads magnetized by a homogeneous field, cf. Fig. 14.3. Further, Fig. 14.9 shows the statistical fluctuations increase with decreasing height as the sensor is most sensitive close to its edges.

For the infinitely long sensor without a height difference, the BAA will be assumed to cover the sensor surface $w_{\text{BAA}} = w$, which is the worst case scenario for $w_{\text{BAA}} \geq w$. The statistical fluctuations then only depend on the bead size and the spacer layer, h. Figure 14.10a shows ϕ_{stat} for different bead sizes and spacers. ϕ_{stat} decreases with the spacer layer thickness, as this decreases the bead height, and increases with R, as this decreases N. For the values in Fig. 14.10a, ϕ_{stat} varies from 10^{-3} % to 0.5 %. Figure 14.10b shows the corresponding number of beads on a PHEB sensor, calculated for ϕ_{stat} in Fig. 14.10a and a sensor with four resistors with $l \times w = 250$ µm $\times$ 25 µm. The number of beads decreases with bead size or spacer thicknesses as this increases the bead height. For most of the experiments in Part II and Part III, $2R = 50$ nm beads were used along with a one micron Ormocomp spacer, which corresponds to $R/w = 10^{-3}$ and $h/w = 0.04$. For these values one finds $\phi_{\text{stat}} = 5 \cdot 10^{-4}$ %, corresponding to 65 beads. Statistical fluctuations are not a problem for our setup, and generally not a problem when beads are magnetized by the self-field.

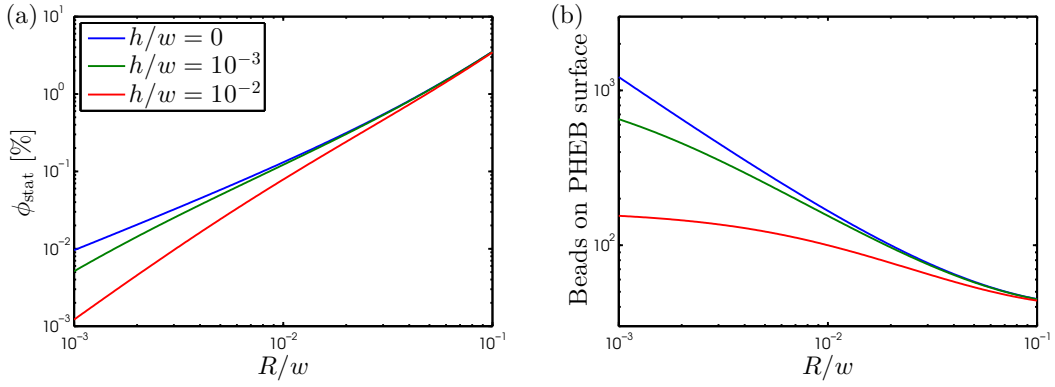

Figure 14.10: (a) ϕ_{stat} and (b) corresponding number of beads on a PHEB sensor as a function of R and h. The values was calculated for an infinitely long sensor and for $w_{\text{BAA}} = w$, (b) was further calculated for a sensor with area $4 \times 10w \times w$.

15

Conclusion and outlook

15.1 Conclusion

The uses of magnetic beads in magnetophoresis and as magnetic labels have been investigated. An experimental setup for bead transportation using a stripe based magnetophoresis chip was built, and the transportation properties of different stripe systems were measured. Similarly, planar Hall effect bridge (PHEB) sensors were used to detect magnetic beads, magnetized by the sensor self-field, arising from the sensor bias current. The magnetic stack and sensor geometries of the PHEB sensors were systematically optimized to increase the bead sensitivity and detection limit. Last, theoretical calculations of the bead signal and its configurational variation were used to generally investigate and optimize how to detect magnetic beads that are magnetized by a homogeneous external field.

The thesis was motivated by three aims, cf. Section 1.4.2. *(1)* A general goal of improving the fundamental understanding of how to best use magnetic beads. *(2)* A practical goal of enhancing the existing sensor system for better bead detection. *(3)* A forward-looking goal of adapting the system to work with aptamers for new possibilities in biodetection.

For magnetic transportation, stripe based magnetophoresis systems were investigated both theoretically and experimentally. It was found that a symmetric stripe geometry was optimal for bead transportation, and that the stripe period should aim to be approximately thrice the height difference between the bead center and stripe layer. While the stripe systems are very easy to fabricate using a single UV-lithography step, the minimum feature size of UV-lithography limits the beads to be approximately micron sized or bigger. This knowledge was published in Paper I and part of *Aim 1*.

Magnetic bead detection using planar Hall effect sensors, and magnetized by the sensor current, was investigated theoretically and experimentally. New sensor designs were introduced with the differential PHEB sensor being optimal for detection of small bead amounts and with the parallel PHEB being optimal for volume-based biodetection. In terms of magnetic sensor designs, a thorough comparison was done between ring and diamond shaped sensors, both design which have been argued to be optimal. The diamond sensor was found to be better when shape anisotropy was negligible, and having magnetic stack around the sensor was shown to reduce shape anisotropy. Further, optimization of the magnetic stack by introducing a copper spacer layer was investigated. The copper layer was found to increase the sensitivity of magnetic stack, but the layer needed to be sub-nanometer thin. Finally, the sensor heating from the bias current was investigated and the silicon dioxide layer was found to be the limiting factor for heat dissipation. This heat-flow could be easily theoretically modeled. This knowledge was published in Paper II, III, IV, V and VI and is primarily part of *Aim 2*.

Hybridization of magnetic bead to the sensor surface using DNA and aptamers was investigated experimentally. It was shown that by having a positive reference, where the biological bead tether was unaffected by temperature, here beads bound by biotin-streptavidin, any temperature dependence of the signal, except that from the bead binding biology, could be normalized out. This biotin-streptavidin positive reference improved on-chip measurements of DNA melting curves. Further, aptamers with high affinity to virus protein was spotted on chips and both real viruses and magnetic beads coated with virus protein were tried measured. However, the aptamer tests were ultimately unsuccessful for unknown reasons. This knowledge on DNA melting curves was published in Paper VII and the analyses are primarily part of *Aim 3*.

Last, a theoretical study of bead detection, when magnetic beads are magnetized by a homogeneous external field, was conducted. Generally, the signal from beads magnetized by a homogeneous field varies with position, and in the case of perfect monolayer, the beads give no signal. However, if the beads on the sensor surface are at a higher height than beads outside the sensor surface, the bead signal has a finite expected value. It is explained how this expected bead field and its standard deviation are calculated, and how to optimize the sensor performance. This is applied as case studies on state-of-the-art sensors from the literature. This knowledge was published in Paper VIII and IX and part of *Aim 1*.

15.2 Outlook

The work of this thesis was carried out over three years, but this finite time span still left several ideas that were conceived but never implemented or tested. Below are a list of such ideas yet to be carried out and developed, but which could all further fulfill the aims of the thesis.

15.2.1 Statistical calculation for measuring beads magnetized by the sensor self-field

A thorough analysis of the statistics on measuring magnetic beads was carried out. The analysis assumed the beads to be detected by a linear magnetoresistive sensor and to be magnetized by a homogeneous external field. However, the setup used for the practical work, cf. Chapter 8, detected bead magnetized by sensor self-field from the sensor bias current. When using the self-field statistical fluctuations are generally not a problem and a height difference is not as important, as in the case of homogeneous excitation field. However, a similar analysis like in "Part IV, The statistics of measuring a bead surface coverage" should be performed with focus on how the geometrical parameters influence the expected signal, especially varying the sensor width could be of interest. This would both optimize the setup and enhance the understanding of bead detection, which would fit into thesis *Aims 1* and *2*.

15.2.2 Magnetophoresis on a chip with varying width

In the magnetophoresis experiments the frequency was increased for each measurements and it was measured until which frequency beads stayed phase-locked. Instead of varying the frequency, the stripe period can by spatially increased across the chip. On such a chip, the beads would move until the stripe became too big to cross at the given frequency. After enough time, all beads would settle at their points of maximum stripe period, which depends on their magnetophoretic mobility and the frequency. For a suspension of mixed beads this would create stable bands of the different magnetic beads, which would be separated but not moving as time passed.

15.2.3 Improving the PHEB sensor setup

The PHEB sensors could be optimized in the following ways, which would fit into thesis *Aim 2*.

Reducing protective oxide thickness

The signal from beads magnetized by the sensor self-field rapidly decreases with the vertical separation from the protective coating (i.e. Ormocomp layer). This is due to both the self-field and dipole field decreasing with distance, cf. Fig. 14.9. Decreasing the protective coating would bring the beads closer to the sensor, which would improve the sensitivity and limit of detection but may decrease the sensor fabrication yield.

Reducing the insulating oxide thickness

It was shown that the bead signal scales with the Joule power, thus it is important that the thermal conditions of the sensor are as good as possible, to be able to use the highest power. As the electrically

insulating oxide on the wafer dominates heat transfer, the chip heat conductance could be improved by reducing the thickness of the insulating oxide, which is now one micron. It is hypothesized that the oxide thickness could be reduced by 50 % to 90 % without reducing the sensor yield, which would increase the possible sensor power by 65 % to 240 %, respectively.

Multiplexing

So far, chips with 5 PHEB sensors were used for all measurements. The number of sensors for each experiment was limited by each sensor needing its own preamplifier and lock-in amplifier. Instead of connecting each sensor separately, all sensors could be connected to a multiplexed printed circuit board and connected to a single preamplifier and lock-in amplifier. As each sensor can perform a differential measurement this would allow for many simultaneous measurements of mutations on DNA, which is of interest in for example cancer diagnostics. Note, that this would increase the measurement time.

15.2.4 Improving bio detection

Besides optimizing the PHEB sensor, the biology interactions on top of the sensor could also be optimized, which would fit into thesis *Aim 3*.

Kinetic studies

One of the big advantageous of magnetoresistive sensors, compared to e.g. ELISA, is the possibility of real-time measurements. Just like surface plasmon resonance, magnetoresistive sensors can thus be used for kinetic measurements, for example monitoring DNA hybridization rates as a function of temperature. As the binding molecules are detected through magnetic beads, advanced models are needed to make sure the beads, with e.g. slow diffusion times, do not influence the kinetics. Gaster *et al.* have shown an example how this can be done [13].

15.2.5 Step-by-step aptamer incorporation

By using aptamers spotted on the sensor surface, new biodetection possibilities was hypothesized. In practice, two different aptamers against virus protein were used, but neither hybridized to virus nor beads coated with virus protein. Instead of going directly to the specific case of virus detection, it could be advantageous to try with a more established aptamer target. The most used aptamer target and test case is thrombin, an important enzyme for blood coagulation. One should first make sure that beads coated with thrombin hybridized to aptamers against thrombin spotted on the sensor surface, and that the signal is not dominated by noise. If the aptamer-thrombin measurements are successful, the aptamer affinity could be measured and compared to the literature. After having succeeded with thrombin detection, one could move on to virus detection or other less tested aptamers. When using less tested aptamers that do not work, it could be beneficial to do a thorough analysis using a systematic variation of the binding buffer. Especially varying the salt concentration, the concentration of magnesium ions or the pH could be the key to getting a troublesome aptamer to bind.

When working, the setup would allow for characterizing the aptamer-virus bond. As real-time measurements are possible this characterization can be done for varying stringencies, to map out under which conditions the aptamer-virus bond is stable. As an example, Chapter 12 showed how the temperature can be varied, while only measuring the temperature dependence on the biological bond, such temperature variations are problematic for QCM (quartz crystal microbalance) and SPR (surface plasmon resonance). Similarly, the stringency can be increased by varying the buffer pH or salt concentration, which should not affect the magnetic detection scheme, but is problematic for electro chemical detections like impedance measurements. Bead based aptamer characterization has potential to be an important and versatile scientific tool for characterizing optimal working conditions and limitations.

Part V

Appendix

A

The magnetic field from periodic and infinite stripe array

A.1 Introduction

The following sections will analyze a periodic geometry consisting of magnetized stripe of infinite length and derive an analytic expression for the magnetic field.

A.2 Derivation approach

The magnetic field from an arbitrary periodic stripe geometry is derived using the following approach: First, the magnetized domain is converted to surface currents; then the field contributions from the different surface currents are split to focus on one of them. The field from one surface current is calculated by using a conformal mapping to the upper half plane, where a simple solution exists. Finally the solution is mapped back to the correct geometry.

A.3 General considerations

When dealing with periodic geometries, Maxwell's equations are best used in differential form, and the magnetic field can be found by solving the Ampère-Maxwell law for the magnetic vector potential ($\mathbf{A}$) [116, p. 417]

$$\nabla^2\mathbf{A} - \mu_0\epsilon_0\frac{\partial^2\mathbf{A}}{\partial t^2} - \nabla\left(\nabla\cdot\mathbf{A} + \mu_0\epsilon_0\frac{\partial V_\mathrm{E}}{\partial t}\right) = -\mu_0\mathbf{J} \tag{A.1}$$

where $\mathbf{A}$ is the magnetic vector potential related to the magnetic fields as $\mathbf{B} = \nabla\times\mathbf{A}$, $\mathbf{J}$ is the current density, ϵ_0 is the permittivity of free space, V_E is the electrical potential and t is the time.

Eq. (A.1) can be simplified by using the the Lorentz gauge [116, p. 421]

$$\nabla\cdot\mathbf{A} = -\mu_0\epsilon_0\frac{\partial V_\mathrm{E}}{\partial t} \tag{A.2}$$

and when working with magnetostatics ($\frac{\partial A}{\partial t} = 0$) the Ampère-Maxwell law simplifies into three Poisson equations

$$\nabla^2\mathbf{A} = -\mu_0\mathbf{J}. \tag{A.3}$$

A.4 Geometrical considerations

The geometry can be seen in Fig. A.1, and is formed by rectangular prisms (slabs) of homogeneously magnetized material of infinite length and arranged in a periodic array. In Fig. A.1, the coordinate system, geometrical parameters and magnetization are also defined. If more than one array are present the magnetic field can be summed by the principle of superposition.

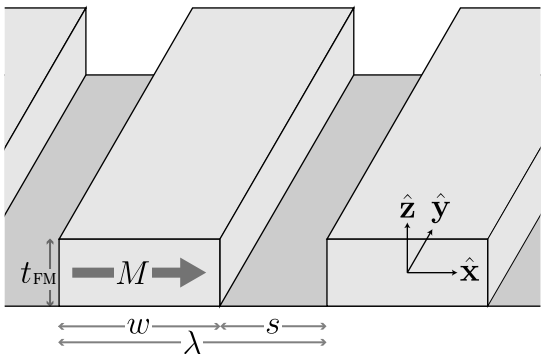

Figure A.1: The model used for the theoretical derivation of the stripe field

Any homogeneous magnetization is equivalent to a bound surface current ($\mathbf{K}$) given by [116, p. 264]

$$\mathbf{K} = \mathbf{M} \times \hat{\mathbf{n}} \tag{A.4}$$

where $\hat{\mathbf{n}}$ is the (outward-pointing) normal vector of the magnetized region. Converting the magnetization to two surface currents, the Poisson equations can be formulated as

$$\begin{aligned} \nabla^2 \mathbf{A} = -\mu_0 M \big(&- \delta(z - \tfrac{t_{\mathrm{FM}}}{2}) \left(\theta_{\mathrm{H}}(x + \tfrac{w}{2}) - \theta_{\mathrm{H}}(x - \tfrac{w}{2})\right) \\ &+ \delta(z + \tfrac{t_{\mathrm{FM}}}{2}) \left(\theta_{\mathrm{H}}(x + \tfrac{w}{2}) - \theta_{\mathrm{H}}(x - \tfrac{w}{2})\right) \big) \hat{\mathbf{y}} \end{aligned} \tag{A.5}$$

where $\delta(x)$ is the Dirac delta function and $\theta_{\mathrm{H}}(x)$ is Heaviside step function. Because the geometry is periodic in the $\hat{\mathbf{x}}$-direction the magnetic potential must also be periodic in the $\hat{\mathbf{x}}$-direction

$$\mathbf{A}\left(x = \frac{\lambda}{2}\right) = \mathbf{A}\left(x = \frac{-\lambda}{2}\right) \text{ and } \left.\frac{\partial \mathbf{A}}{\partial x}\right|_{x = \frac{\pm\lambda}{2}} = \mathbf{0}. \tag{A.6}$$

This forms the equivalent geometry, seen in Fig. A.2, to work with.

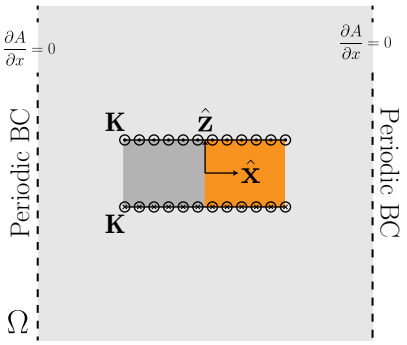

Figure A.2: Illustration of the problem when converted to surface currents in the periodic Ω domain. The gray and orange squares represent the magnetization with the orange being the north-pole; the circles represent the corresponding surface currents.

As all currents in Eq. (A.5) is in the $\hat{\mathbf{y}}$-direction, the only changing component of the magnetic potential

is the $\hat{\mathbf{y}}$-component, which varies in the xz-plane [116, p. 422]. This simplification leads to

$$\mathbf{A}(x,y,z) \equiv A_{\text{stripe}}(x,z)\hat{\mathbf{y}} \quad \text{and} \quad \mathbf{B} = \frac{\partial A_{\text{stripe}}}{\partial x}\hat{\mathbf{z}} - \frac{\partial A_{\text{stripe}}}{\partial z}\hat{\mathbf{x}}. \tag{A.7}$$

where A_{stripe} is the magnetic potential from the periodic geometry.

With the principle of superposition the magnetic potential from each surface current (A) in Eq. (A.5) can be derived individually and added as

$$A_{\text{stripe}}(x,z) = A(x, z - \tfrac{t_{\text{FM}}}{2}) - A(x, z + \tfrac{t_{\text{FM}}}{2}) \tag{A.8}$$

For deriving A the coordinate system has been translated to the center of each surface current. This translation makes the single current geometry symmetrical around the $\hat{\mathbf{x}}$-axis and thus one can restrict the domain to $z > 0$ knowing that $A(x,z) = A(x,-z)$. For $z > 0$ the Poisson equation simplifies to the Laplace's equation

$$\nabla^2 A = 0 \tag{A.9}$$

Further as $A(x,z) = A(x,-z)$ the $\hat{\mathbf{z}}$-derivative must change sign at $z = 0$ ($\frac{\partial A}{\partial z}\big|_{z=0+} = -\frac{\partial A}{\partial z}\big|_{z=0-}$). Knowing this, $\frac{\partial A}{\partial z}$ must be zero outside the surface current and for $|x| < \frac{w}{2}$ given by

$$\int_{0-}^{0+} \nabla^2 A \, \mathrm{d}z = \int_{0-}^{0+} \mu_0 M \delta(z) \, \mathrm{d}z \tag{A.10}$$

$$\left.\frac{\partial A}{\partial z}\right|_{z=0+} - \left.\frac{\partial A}{\partial z}\right|_{z=0-} = \mu_0 M \tag{A.11}$$

$$\left.\frac{\partial A}{\partial z}\right|_{z=0+} = \frac{\mu_0 M}{2} \tag{A.12}$$

This completes the Neumann boundary condition (BC) and the reduced geometry for a single sheet of current (Ω_{ss}) with its BCs can be seen in Fig. A.3.

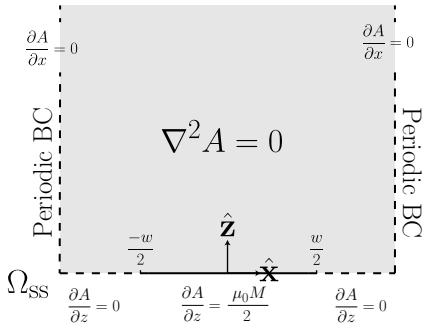

Figure A.3: The Ω_{ss} domain with governing Laplace's equation and BCs.

A.5 Conformal mapping

The Laplace's equation with Neumann BCs is solved using Neumann functions [117, p. 684] but before this can be done the domain is mapped to the upper-half plane ($Z > 0, -\infty < X < \infty$), which has a

simpler Neumann function. One can map the simple single sheet domain (Ω_{ss}) onto the upper-half plane (Ω_{uh}) by using the conformal mapping $f(\nu = x + iz) = \sin\left(\frac{\pi}{\lambda}\nu\right)$ where $i^2 = -1$. The mapping is given by

$$X(x,z) = \Re\left(\sin\left(\frac{\pi}{\lambda}(x+iz)\right)\right) = \sin\left(\frac{\pi}{\lambda}x\right)\cosh\left(\frac{\pi}{\lambda}z\right) \tag{A.13}$$

$$Z(x,z) = \Im\left(\sin\left(\frac{\pi}{\lambda}(x+iz)\right)\right) = \cos\left(\frac{\pi}{\lambda}x\right)\sinh\left(\frac{\pi}{\lambda}z\right). \tag{A.14}$$

This one-to-one mapping [117, p. 667] maps the boundary of Ω_{ss} onto the $\hat{\mathbf{X}}$-axis of Ω_{uh} as

$$z = 0\ ,\ \tfrac{-\lambda}{2} < x < \tfrac{\lambda}{2} \quad \overset{f(\nu)}{\rightarrow} \quad Z = 0\ ,\ -1 < X < 1 \tag{A.15}$$

$$0 < z < \infty\ ,\ x = \tfrac{-\lambda}{2} \quad \overset{f(\nu)}{\rightarrow} \quad Z = 0\ ,\ -\infty < X < -1 \tag{A.16}$$

$$0 < z < \infty\ ,\ x = \tfrac{\lambda}{2} \quad \overset{f(\nu)}{\rightarrow} \quad Z = 0\ ,\ 1 < X < \infty, \tag{A.17}$$

as illustrated in Fig. A.4 where the upper half plane domain and governing equation can also be seen.

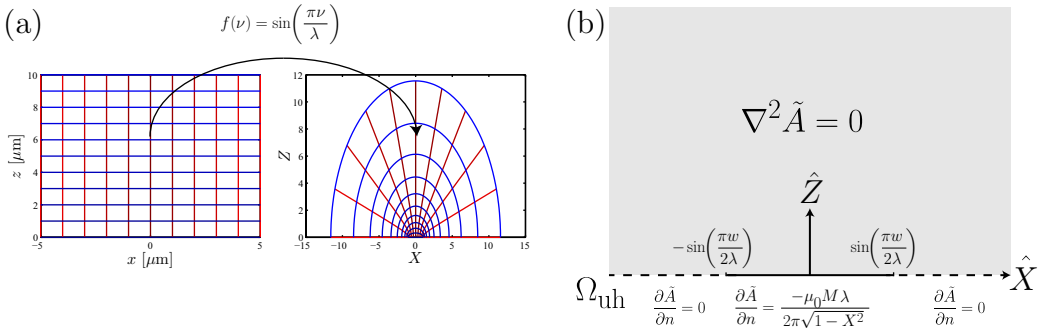

Figure A.4: (a) The mapping function f and how it transforms the domains. The lines in Ω_{ss} are transformed to the lines in Ω_{up} with the same color. (b) The Ω_{uh} domain with governing Laplace's equation and BCs.

It is known that any solution to Laplace's equation in a mapped domain ($\tilde{A}(X,Z)$), which is mapped back to the original domain (Ω_{ss}) is also a solution to Laplace's equation in the original domain [117, p. 664] i.e.

$$\tilde{A} \circ f = \tilde{A}(X(x,z), Z(x,z)) = A(x,z) \tag{A.18}$$

is a solution in Ω_{ss}, however the governing BCs change with the mapping as

$$\tilde{A}(X(x,z), Z(x,z)) = A(x,z) \tag{A.19}$$

$$\frac{\partial \tilde{A}}{\partial Z} = \frac{\partial A}{\partial z}\left(\frac{\partial Z}{\partial z}\right)^{-1} + \frac{\partial A}{\partial x}\left(\frac{\partial Z}{\partial x}\right)^{-1} \tag{A.20}$$

Inserting the mapping from Eqs. (A.13,A.14) along with the initial BC Eq. (A.12) and inverting the mapping to find $x(X,Z)$ and $z(X,Z)$ at the boundary yields the BC in Ω_{uh}

$$\frac{\partial \tilde{A}}{\partial Z} = \frac{M\mu_0\lambda}{2\pi\sqrt{1-X^2}} \quad \text{for } |X| < \sin\left(\frac{\pi w}{2\lambda}\right). \tag{A.21}$$

This is used in the solution to the Laplace's equation with known Neumann boundary conditions ($\frac{\partial \tilde{A}}{\partial n}$ known on a given boundary Γ) is [117, p. 685]

$$\tilde{A}(X,Z) = \frac{-1}{2\pi} \int_{\Gamma} N(X,Z,X_0,Z_0) \frac{\partial \tilde{A}(X_0,Z_0)}{\partial n} \, \mathrm{d}l \tag{A.22}$$

where (X_0, Z_0) is integrated along the boundary, Γ, and $N(X,Z,X_0,Z_0)$ is the Neumann function for the domain. For the upper-half plane the Neumann function is [117, p. 686]

$$N(X,Z,X_0,Z_0) = \frac{1}{2} \ln\left((X-X_0)^2 + (Z-Z_0)^2\right) + \frac{1}{2} \ln\left((X-X_0)^2 + (Z+Z_0)^2\right) \tag{A.23}$$

Inserting the Neumann function and noting that Γ is at $Z_0 = 0$, The solution in Ω_{uh}, Eq. (A.22), simplifies to

$$\tilde{A}(X,Z) = \frac{M\mu_0\lambda}{4\pi^2} \int_{-\sin(\frac{\pi w}{2\lambda})}^{\sin(\frac{\pi w}{2\lambda})} \frac{\ln\left((X-X_0)^2 + Z^2\right)}{\sqrt{1-X_0^2}} \, \mathrm{d}X_0 \tag{A.24}$$

A.6 Integration

While this integral in Eq. (A.24) cannot be evaluated its derivative, corresponding to physical magnetic field can, as the single sheet field is given by

$$B_{ss,x} = -\frac{\partial \tilde{A}}{\partial X}\frac{\partial X}{\partial z} - \frac{\partial \tilde{A}}{\partial Z}\frac{\partial Z}{\partial z} \tag{A.25}$$

$$B_{ss,z} = +\frac{\partial \tilde{A}}{\partial X}\frac{\partial X}{\partial x} + \frac{\partial \tilde{A}}{\partial Z}\frac{\partial Z}{\partial x}. \tag{A.26}$$

For simplifying the equations the following notation is used

$$B_{ss,x} = -\alpha_{x,1}\Theta_1 - \alpha_{x,2}\Theta_2 \tag{A.27}$$

$$B_{ss,z} = +\alpha_{z,1}\Theta_1 + \alpha_{z,2}\Theta_2 \tag{A.28}$$

$$\alpha_{x,1} = \frac{M\mu_0\lambda}{4\pi^2}\frac{\partial X}{\partial z} \tag{A.29}$$

$$\alpha_{x,2} = \frac{M\mu_0\lambda}{4\pi^2}\frac{\partial Z}{\partial z} \tag{A.30}$$

$$\alpha_{z,1} = \frac{M\mu_0\lambda}{4\pi^2}\frac{\partial X}{\partial x} \tag{A.31}$$

$$\alpha_{z,2} = \frac{M\mu_0\lambda}{4\pi^2}\frac{\partial Z}{\partial x} \tag{A.32}$$

$$\Theta_1 = \frac{\partial \tilde{A}}{\partial X} = \int_{-\beta}^{\beta} \frac{2(X_0 - X)}{((X-X_0)^2 + Z^2)\sqrt{1-X_0^2}} \, \mathrm{d}X_0 \tag{A.33}$$

$$\Theta_2 = \frac{\partial \tilde{A}}{\partial Z} = \int_{-\beta}^{\beta} \frac{2Z}{((X-X_0)^2 + Z^2)\sqrt{1-X_0^2}} \, \mathrm{d}X_0 \tag{A.34}$$

$$\beta = \sin\left(\frac{\pi w}{2\lambda}\right) \tag{A.35}$$

Note, that $\alpha_{x,1} = -\alpha_{z,2}$ and $\alpha_{x,2} = \alpha_{z,1}$

Starting with Θ_2, the integral can be rewritten by factoring $(X-X_0)^2 + Z^2$

$$\Theta_2 = \int_{-\beta}^{\beta} \frac{2Z}{(X_0 - r_1)(X_0 - r_2)\sqrt{1-X_0^2}} \, \mathrm{d}X_0 \tag{A.36}$$

$$r_1 = X + iZ \tag{A.37}$$

$$r_2 = \overline{r_1} = X - iZ \tag{A.38}$$

Using the identity $\frac{1}{(X_0-r_1)(X_0-r_2)} = \frac{1}{(X_0-r_1)(r_1-r_2)} - \frac{1}{(X_0-r_2)(r_1-r_2)}$, Θ_2 can be rewritten as

$$\Theta_2 = \frac{1}{i}\int_{-\beta}^{\beta} \frac{1}{(X_0-r_1)\sqrt{1-X_0^2}}\,\mathrm{d}X_0 - \frac{1}{i}\int_{-\beta}^{\beta} \frac{1}{(X_0-r_2)\sqrt{1-X_0^2}}\,\mathrm{d}X_0 \tag{A.39}$$

Defining these integrals as $I(r)$, Θ_2 can be written as

$$\Theta_2 = \frac{(I(r_1)-I(r_2))}{i} = 2\Im(I(r_1)) \tag{A.40}$$

And substituting $\chi = \arcsin(X)$ into I yields

$$I(r_1) = \int_{-2\tilde{w}}^{2\tilde{w}} \frac{1}{\sin(\chi)-r_1}\mathrm{d}\chi \tag{A.41}$$

$$= \frac{2}{\sqrt{r_1^2-1}}\left(\arctan\left(\frac{1-r_1\tan(\tilde{w})}{\sqrt{r_1^2-1}}\right) - \arctan\left(\frac{1+r_1\tan(\tilde{w})}{\sqrt{r_1^2-1}}\right)\right) \tag{A.42}$$

with $\tilde{w} = \frac{\pi w}{4\lambda}$. A similar procedure can be done for Θ_1 with the result

$$\Theta_1 = -I(r_1) - I(r_2) = -2\Re(I(r_1)) \tag{A.43}$$

A.7 Formula summary

One now have all the equations for describing the field from a periodic array of infinite magnetic material. All the derived results can summarized in the following formulas

$$\mathbf{B}(x,z) = (B_{ss,x}(x, z-\tfrac{t_{\mathrm{FM}}}{2}) - B_{ss,x}(x, z+\tfrac{t_{\mathrm{FM}}}{2}))\hat{\mathbf{x}} \tag{A.44}$$

$$+(B_{ss,z}(x, z-\tfrac{t_{\mathrm{FM}}}{2}) - B_{ss,z}(x, z+\tfrac{t_{\mathrm{FM}}}{2}))\hat{\mathbf{z}} \tag{A.45}$$

$$B_{ss,x} = +2\alpha_1\Re(I) - 2\alpha_2\Im(I) \tag{A.46}$$

$$B_{ss,z} = -2\alpha_2\Re(I) - 2\alpha_1\Im(I) \tag{A.47}$$

$$\alpha_1 = \frac{M\mu_0}{4\pi}\sin\left(\frac{\pi x}{\lambda}\right)\sinh\left(\frac{\pi z}{\lambda}\right) \tag{A.48}$$

$$\alpha_2 = \frac{M\mu_0}{4\pi}\cos\left(\frac{\pi x}{\lambda}\right)\cosh\left(\frac{\pi z}{\lambda}\right) \tag{A.49}$$

$$I = \frac{2}{\sqrt{r^2-1}}\left(\arctan\left(\frac{1-r\tan(\tilde{w})}{\sqrt{r^2-1}}\right) - \arctan\left(\frac{1+r\tan(\tilde{w})}{\sqrt{r^2-1}}\right)\right) \tag{A.50}$$

$$\tilde{w} = \frac{\pi w}{4\lambda} \tag{A.51}$$

$$r = \sin\left(\frac{\pi x}{\lambda}\right)\cosh\left(\frac{\pi z}{\lambda}\right) + i\cos\left(\frac{\pi x}{\lambda}\right)\sinh\left(\frac{\pi z}{\lambda}\right) \tag{A.52}$$

B

Stripe system fabrication process flow

Fabrication details for stripe systems in Part I: Magnetophoresis.

<table>
<tr><th>Step</th><th>Process:</th><th>Comment:</th></tr>
<tr><td>0a</td><td>Si wafers standard, p type</td><td></td></tr>
<tr><td>1.1</td><td>Wet oxidation
Boron Drive-in wet oxidation at 1100°C for 2 h (30 min ramp) to get 850 nm oxide.</td><td></td></tr>
<tr><td>1.2</td><td>Measure oxide thickness</td><td>Oxide thickness:</td></tr>
<tr><th colspan="3">2 - Definition of sensor stack – negative process (for liftoff)</th></tr>
<tr><td>2.1</td><td>HDMS</td><td>2 wafers</td></tr>
<tr><td>2.2</td><td>Resist spinning
apply 1.5 micrometer AZ5214e resist (SSE Spinner). (softbake). Use 1.5µm 4inch recipe</td><td></td></tr>
<tr><td>2.3</td><td>Exposure (Mask: Stack)
Use 6 inch aligner to make first print.
1.7 sec
Contact: Hard contact
prox: 30um
wec: 0.0
offset= +- 0
sep: 30um 10N
Print: first print
Light integration: ON.</td><td></td></tr>
<tr><td>2.4</td><td>Reversal bake
In SSE spinner or bake 2 min at 120C on hotplate.</td><td></td></tr>
<tr><td>2.5</td><td>Flood exposure
Flood exposure 30 sec in 6inch-aligner</td><td></td></tr>
<tr><td>2.6</td><td>Development
Development AZ351b 70s. Remember to check age and use of developer!</td><td></td></tr>
<tr><td>2.7</td><td>Microscope inspection
If you see rounded corners etc. you need to optimize the lithographic process. Also check if the resist is fully developed.</td><td></td></tr>
<tr><th colspan="3">3 - Sensor stack sputtering and Liftoff</th></tr>
<tr><td>3.1</td><td>Lesker System.</td><td>Single Layer sensor</td></tr>
<tr><td>3.2</td><td>Sputter
<table>
<tr><th>Mat.</th><th>Thick.</th><th>Press.</th><th>power</th><th>Substr. bias</th></tr>
<tr><td>Ta</td><td>3nm</td><td>3mTorr Ar</td><td>180W</td><td>3W</td></tr>
<tr><td>Ni80Fe20</td><td>5 nm</td><td>2.8mTorr</td><td>157W</td><td>3W</td></tr>
<tr><td>Mn74Ir26</td><td>10nm</td><td>3mTorr</td><td>157W</td><td>3W</td></tr>
<tr><td>Ni80Fe20</td><td>10 -20 nm</td><td>2.8mTorr</td><td>157W</td><td>3W</td></tr>
<tr><td>Mn74Ir26</td><td>10nm</td><td>3mTorr</td><td>157W</td><td>3W</td></tr>
<tr><td>Ta</td><td>3nm</td><td>3mTorr Ar</td><td>180W</td><td>3W</td></tr>
</table></td><td>DC Stack with RF Bias
Ta(3nm)/NiFe(5nm)/ MnIr(20nm) …
/NiFe(t_{FM})/MnIr(20nm)/Ta(5nm)
1. wafer: t_{FM} 10 nm
2. wafer: t_{FM} 20 nm</td></tr>
<tr><td>3.3</td><td>Lift off Acetone (rough). Wafer holder in one pyrex (1L) glass, 30 min in an ultrasonic bath.</td><td>Do not check during lift-off!</td></tr>
<tr><td>3.4</td><td>Wafer holder in pyrex glass with water(rough), 1min in ultrasonic bath</td><td></td></tr>
</table>

<table>
<tr><td>3.5</td><td>Lift-off in acetone (fine). Wafer holder in pyrex glass, 30 min ultrasonic bath.</td><td></td></tr>
<tr><td>3.6</td><td>Wafer holder in pyrex glass with water (fine). 1min ultrasonic bath</td><td></td></tr>
<tr><td>3.7</td><td>Spin dry</td><td></td></tr>
<tr><td>3.8</td><td>Microscope check of condition. Check if the resist is fully developed.</td><td></td></tr>
<tr><td colspan="3">4- SiO2 protective coating</td></tr>
<tr><td>4.1</td><td>Insert in Lesker System</td><td></td></tr>
<tr><td>4.2</td><td>Sputter:<table><tr><td>Mat.</td><td>Thick.</td><td>Press.</td><td>power</td><td>Substr. bias</td></tr><tr><td>Si</td><td>100nm</td><td>3mTorr (Ar+O2 10%)</td><td>90W</td><td>20W</td></tr></table></td><td></td></tr>
<tr><td colspan="3">5 – Dicing</td></tr>
<tr><td>5.1</td><td>Resist spinning
apply 1.5 micrometer AZ5214e resist (SSE Spinner). Check T=90_C (softbake). Use 1.5µm 4inch NB recipe</td><td></td></tr>
<tr><td>5.2</td><td>Dice with Si saw, work height 200-250 um</td><td></td></tr>
<tr><td>5.3</td><td>Carefully remove plastic</td><td></td></tr>
</table>

C

Sensor fabrication process flow

Fabrication details for planar Hall effect sensors in Part II: Planar Hall effect sensor for magnetic bead detection.

<table>
<tr><th>Step</th><th>Process:</th><th>Comment:</th></tr>
<tr><td>0a</td><td>Si wafers standard, p type</td><td></td></tr>
<tr><td>1.1</td><td>Wet oxidation
Boron Drive-in wet oxidation at 1100°C for 2 h (30 min ramp) to get 850 nm oxide.</td><td></td></tr>
<tr><td>1.2</td><td>Measure oxide thickness</td><td>Oxide thickness:</td></tr>
<tr><th colspan="3">2 - Definition of sensor stack – negative process (for liftoff)</th></tr>
<tr><td>2.1</td><td>HDMS</td><td></td></tr>
<tr><td>2.2</td><td>Resist spinning
Apply 1.5 micrometer AZ5214e resist (SSE Spinner). Check T=90_C (softbake). Use 1.5µm 4inch</td><td></td></tr>
<tr><td>2.3</td><td>Exposure (Mask: Stack)
Use KS aligner to make first print. Use, t = 3.4 s (check log for recent exposure times).
Contact: Hard contact
prox: 30um
wec: 0.0
offset= +- 0</td><td></td></tr>
<tr><td>2.4</td><td>Reversal bake
Bake 2 min at 120C on hotplate.</td><td></td></tr>
<tr><td>2.5</td><td>Flood exposure
Flood exposure 30 s in KS-aligner. Use Lamp test</td><td></td></tr>
<tr><td>2.6</td><td>Development
Development PRD-1 AZ351b 70s min. Remember to check age and use of developer!</td><td></td></tr>
<tr><td>2.7</td><td>Microscope inspection
If you see rounded corners etc. you need to optimize the lithographic process. Also check if the resist is fully developed.</td><td></td></tr>
<tr><th colspan="3">3 - Sensor stack sputtering, Liftoff and annealing</th></tr>
<tr><td>3.1</td><td>Lesker System.</td><td></td></tr>
<tr><td>3.2</td><td>Sputter
<table>
<tr><th>Mat.</th><th>Thick.</th><th>Press.</th><th>power</th><th>Substr. bias</th></tr>
<tr><td>Ta</td><td>3nm</td><td>3mTorr Ar</td><td>180W</td><td>3W</td></tr>
<tr><td>Ni80Fe20</td><td>30nm</td><td>2.8mTorr</td><td>157W</td><td>3W</td></tr>
<tr><td>Mn74Ir26</td><td>20nm</td><td>3mTorr</td><td>157W</td><td>3W</td></tr>
<tr><td>Ta</td><td>3nm</td><td>3mTorr Ar</td><td>180W</td><td>3W</td></tr>
</table></td><td></td></tr>
<tr><td>3.3</td><td>Lift off Acetone (rough). Wafer holder in one pyrex (1L) glass in an ultrasonic bath</td><td>Do not check during lift-off!</td></tr>
<tr><td>3.5</td><td>Wafer holder in pyrex glass with water(rough) in ultrasonic bath</td><td></td></tr>
<tr><td>3.6</td><td>Lift-off in acetone (fine). Wafer holder in pyrex glass, ultrasonic bath.</td><td></td></tr>
<tr><td>3.7</td><td>Wafer holder in pyrex glass with water (fine). 1min ultrasonic bath</td><td></td></tr>
<tr><td>3.9</td><td>Spin dry</td><td></td></tr>
<tr><td>3.10</td><td>Microscope check of condition</td><td></td></tr>
</table>

4 - Second resist layer (Negative process for gold)		
4.1	*Resist spinning* Apply 1.5 micrometer AZ5214e resist (SSE Spinner). Check T=90_C (softbake). Use 1.5µm 4inch	Comment: no HDMS is needed
4.2	*Exposure (Mask: **Contact**)* Use KS aligner to make first print. Use, t = 3.4 s (check log for recent exposure times). Contact: Hard contact prox: 30um wec: 0.0 offset= +- 0	
4.3	*Reversal bake* Bake 2 min at 120C on hotplate.	
4.4	*Flood exposure* Flood exposure 30 s in KS-aligner. Use Lamp test	
4.5	Development Development PRD-1 AZ351b 70s min. Remember to check age and use of developer!	
4.6	Microscope inspection If you see rounded corners etc. you need to optimize the lithographic process. Also check if the resist is fully developed.	
5 - Contact E-Beam evaporation		
5.1	Wordentech	
5.2	Sputter clean at 200W for 5 min	Extremely important
5.3	Apply: 10nm Ti 100nm Pt 100nm Au 10nm Ti	
5.4	Resist strip **Acetone** (Rough) Wafer holder in Pyrex glass in ultrasonic bath	
5.5	Wafer holder in pyrex glass with **water**. Ultrasound 1 min	
5.6	Resist strip **acetone** (fine). Wafer holder in pyrex glass in ultrasonic bath	
5.7	Wafer holder in pyrex glass with **water.** Ultrasound 1 min	
5.8	Spin dry	
5.9	Microscope check	
6 – Ormocomp		
6.1	Dehydration bake: 15min @ 120C Hot plate	
6.2	Spin coating: Ormocomp 1:2.5 ma-T 1050 thinner Manual spinner(Polymers) 3000rpm 60s Open lid	
6.3	Prebake: Hot plate 5min @ 100C Hot plate	
6.4	KS aligner: (Oxide coating - feb2011) Set Global WEC (F1) Chuck with hole	

	Program Proximity/globalWEC Substrate thickness 700um Mask: Exposure: 30s	
6.5	Post exposure bake: 3min @ 90C Hot plate	
6.6	Development Ormodev 120s	
6.7	Rinse with water and spin dry.	
6.8	Flood exposure: KS aligner 100s	
6.9	Hard bake: 3h @ 150C Hot plate or Lesker sputter system	
7 – Dicing		
7.1	Resist spinning Apply 1.5 micrometer AZ5214e resist (SSE Spinner). Check T=90_C (softbake). Use 1.5µm 4inch	
7.2	Dice with Si saw, work height 200-250 um	
7.3	Carefully remove plastic	

Bibliography

[1] H. J. Sung, B. Kayhan, T. Ben-Yedidia, and R. Arnon. A DNA aptamer prevents influenza infection by blocking the receptor binding region of the viral hemagglutinin. *J. Biol. Chem.*, 279(46):48410–48419, 2004.

[2] I. Shiratori, J. Akitomi, D. A. Boltz, K. Horii, M. Furuichi, and I. Waga. Selection of DNA aptamers that bind to influenza A viruses with high affinity and broad subtype specificity. *Biochem. Biophys. Res. Commun.*, 443(1):37–41, 2014.

[3] G. A. Posthuma-Trumpie, J. Korf, and A. van Amerongen. Lateral flow (immuno)assay: Its strengths, weaknesses, opportunities and threats. A literature survey. *Anal. Bioanal. Chem.*, 393(2):569–582, 2009.

[4] L. C. Clark and C. Lyons. Electrode systems for continuous monitoring in cardiovascular surgery. *Ann. N.Y. Acad. Sci.*, 102(1):29–45, 1962.

[5] L. Gold, D. Ayers, J. Bertino, C. Bock, A. Bock, E. N. Brody, J. Carter, A. B. Dalby, B. E. Eaton, T. Fitzwater, D. Flather, A. Forbes, T. Foreman, C. Fowler, B. Gawande, M. Goss, M. Gunn, S. Gupta, D. Halladay, J. Heil, J. Heilig, B. Hicke, G. Husar, N. Janjic, T. Jarvis, S. Jennings, E. Katilius, T. R. Keeney, N. Kim, T. H. Koch, S. Kraemer, L. Kroiss, N. Le, D. Levine, W. Lindsey, B. Lollo, W. Mayfield, M. Mehan, R. Mehler, S. K. Nelson, M. Nelson, D. Nieuwlandt, M. Nikrad, U. Ochsner, R. M. Ostroff, M. Otis, T. Parker, S. Pietrasiewicz, D. I. Resnicow, J. Rohloff, G. Sanders, S. Sattin, D. Schneider, B. Singer, M. Stanton, A. Sterkel, A. Stewart, S. Stratford, J. D. Vaught, M. Vrkljan, J. J. Walker, M. Watrobka, S. Waugh, A. Weiss, S. K. Wilcox, A. Wolfson, S. K. Wolk, C. Zhang, and D. Zichi. Aptamer-Based Multiplexed Proteomic Technology for Biomarker Discovery. *PLoS One*, 5(12):17, 2010.

[6] R. S. Gaster, D. A. Hall, and S. X. Wang. nanoLAB: an ultraportable, handheld diagnostic laboratory for global health. *Lab Chip*, 11(5):950–956, 2011.

[7] Q. A. Pankhurst, J. Connolly, S. K. Jones, and J. Dobson. Applications of magnetic nanoparticles in biomedicine. *J. Phys. D Appl. Phys.*, 36(13):R167–R181, 2003.

[8] M. A. M. Gijs, F. Lacharme, and U. Lehmann. Microfluidic applications of magnetic particles for biological analysis and catalysis. *Chem. Rev.*, 110(3):1518–1563, 2010.

[9] J. Llandro, J. J. Palfreyman, A. Ionescu, and C. H. W. Barnes. Magnetic biosensor technologies for medical applications: A review. *Med. Biol. Eng. Comput.*, 48(10):977–998, 2010.

[10] S. Mornet, S. Vasseur, F. Grasset, and E. Duguet. Magnetic nanoparticle design for medical diagnosis and therapy. *J. Mater. Chem.*, 14(14):2161–2175, 2004.

[11] A. H. Lu, E. L. Salabas, and F. Schüth. Magnetic nanoparticles: Synthesis, protection, functionalization, and application. *Angew. Chem. Int. Ed.*, 46(8):1222–1244, 2007.

[12] K. M. Krishnan. Biomedical nanomagnetics: A spin through possibilities in imaging, diagnostics, and therapy. *IEEE Trans. Magn.*, 46(7):2523–2558, 2010.

[13] R. S. Gaster, L. Xu, S.-J. Han, R. J. Wilson, D. A. Hall, S. J. Osterfeld, H. Yu, and S. X. Wang. Quantification of protein interactions and solution transport using high-density GMR sensor arrays. *Nat. Nanotechnol.*, 6:314–320, 2011.

[14] K. Landfester and L. P. Ramirez. Encapsulated magnetite particles for biomedical application. *J. Phys. Condens. Matter*, 15(15):S1345–S1361, 2003.

[15] G. Fonnum, C. Johansson, A. Molteberg, S. Mørup, and E. Aksnes. Characterisation of Dynabeads by magnetization measurements and Mössbauer spectroscopy. *J. Magn. Magn. Mater.*, 293(1):41–47, 2005.

[16] C. L. Sawyers. The cancer biomarker problem. *Nature*, 452(7187):548–552, 2008.

[17] C. R. Tamanaha, S. P. Mulvaney, J. C. Rife, and L. J. Whitman. Magnetic labeling, detection, and system integration. *Biosens. Bioelectron.*, 24(1):1–13, 2008.

[18] D. Issadore, Y. I. Park, H. Shao, C. Min, K. Lee, M. Liong, R. Weissleder, and H. Lee. Magnetic sensing technology for molecular analyses. *Lab Chip*, 14(14):2385–97, 2014.

[19] S. Tumanski. Induction coil sensors - A review. *Meas. Sci. Technol.*, 18(3):R31–R46, 2007.

[20] J. Richardson, P. Hawkins, and R. Luxton. The use of coated paramagnetic particles as a physical label in a magneto-immunoassay. *Biosens. Bioelectron.*, 16(9-12):989–993, 2001.

[21] M. Liong, A. N. Hoang, J. Chung, N. Gural, C. B. Ford, C. Min, R. R. Shah, R. Ahmad, M. Fernandez-Suarez, S. M. Fortune, M. Toner, H. Lee, and R. Weissleder. Magnetic barcode assay for genetic detection of pathogens. *Nat. Commun.*, 4:1752, 2013.

[22] H. J. Chung, C. M. Castro, H. Im, H. Lee, and R. Weissleder. A magneto-DNA nanoparticle system for rapid detection and phenotyping of bacteria. *Nat. Nanotechnol.*, 8(5):369–75, 2013.

[23] S. Bamrungsap, T. Chen, M. I. Shukoor, Z. Chen, K. Sefah, Y. Chen, and W. Tan. Pattern recognition of cancer cells using aptamer-conjugated magnetic nanoparticles. *ACS Nano*, 6(5):3974–3981, 2012.

[24] M. Megens and M. Prins. Magnetic biochips: A new option for sensitive diagnostics. *J. Magn. Magn. Mater.*, 293(1):702–708, 2005.

[25] P. P. Freitas, R. Ferreira, S. Cardoso, and F. Cardoso. Magnetoresistive sensors. *J. Phys. Condens. Matter*, 19(16):165221, 2007.

[26] S. X. Wang and G. Li. Advances in Giant Magnetoresistance Biosensors With Magnetic Nanoparticle Tags: Review and Outlook. *IEEE Trans. Magn.*, 44:1687–1702, 2008.

[27] N. T. Thanh, M. G. Chun, N. D. Ha, K. Y. Kim, C. O. Kim, and C. Kim. Thickness dependence of exchange anisotropy in NiFe/IrMn bilayers studied by Planar Hall Effect. *J. Magn. Magn. Mater.*, 305(2):432–435, 2006.

[28] N. T. Thanh, L. T. Tu, N. D. Ha, C. O. Kim, C. Kim, K. H. Shin, and B. P. Rao. Thickness dependence of parallel and perpendicular anisotropic resistivity in Ta/NiFe/IrMn/Ta multilayer studied by anisotropic magnetoresistance and planar Hall effect. *J. Appl. Phys.*, 101(5):053702, 2007.

[29] T. Q. Hung, S. Oh, S. Anandakumar, J. R. Jeong, D. Y. Kim, and C. Kim. Optimization of the multilayer structures for a high field-sensitivity biochip sensor based on the planar Hall effect. *IEEE Trans. Magn.*, 45(10):4518–4521, 2009.

[30] T. Q. Hung, S. Oh, B. Sinha, J.-R. Jeong, D.-Y. Kim, and C. Kim. High field-sensitivity planar Hall sensor based on NiFe/Cu/IrMn trilayer structure. *J. Appl. Phys.*, 107(9):09E715, 2010.

[31] B. Sinha, S. Oh, T. Sri Ramulu, J. Lim, D. Y. Kim, and C. G. Kim. Planar Hall Effect Ring Sensors for High Field-Sensitivity. *Adv. Mat. Res.*, 317:1136–1140, 2011.

[32] S. Oh, N. S. Baek, S.-D. Jung, M.-A. Chung, T. Q. Hung, S. Anandakumar, V. S. Rani, J.-R. Jeong, and C. Kim. Selective binding and detection of magnetic labels using PHR sensor via photoresist micro-wells. *J. Nanosci. Nanotechnol.*, 11(5):4452–4456, 2011.

[33] S. Oh, P. B. Patil, T. Q. Hung, B. Lim, M. Takahashi, D. Y. Kim, and C. Kim. Hybrid AMR/PHR ring sensor. *Solid State Commun.*, 151(18):1248–1251, 2011.

[34] B. Sinha, S. Anandakumar, S. Oh, and C. Kim. Micro-magnetometry for susceptibility measurement of superparamagnetic single bead. *Sens. Actuators, A*, 182:34–40, 2012.

[35] S. Oh, J.-S. Yu, J. Lim, M. Jadhav, T.-M. Lee, D. Kim, and C. Kim. Highly Flexible Magnetoelectronic Device Integrated With Embedded Ag Nanoparticle Electrode. *IEEE Sens. J.*, 13(10):3957—-3961, 2013.

[36] T. Q. Hung, F. Terki, S. Kamara, K. Kim, S. Charar, and C. Kim. Planar Hall ring sensor for ultra-low magnetic moment sensing. *J. Appl. Phys.*, 117(15):154505, 2015.

[37] L. Ejsing, M. F. Hansen, A. K. Menon, H. A. Ferreira, D. L. Graham, and P. P. Freitas. Planar Hall effect sensor for magnetic micro- and nanobead detection. *Appl. Phys. Lett.*, 84(23):4729, 2004.

[38] C. D. Damsgaard, S. C. Freitas, P. P. Freitas, and M. F. Hansen. Exchange-biased planar Hall effect sensor optimized for biosensor applications. *J. Appl. Phys.*, 103(7):07A302 – 07A302–3, 2008.

[39] F. W. Østerberg, B. T. Dalslet, C. D. Damsgaard, S. C. Freitas, P. P. Freitas, and M. F. Hansen. Bead Capture on Magnetic Sensors in a Microfluidic System. *IEEE Sens. J.*, 9(6), 2009.

[40] A. D. Henriksen, B. T. Dalslet, D. H. Skieller, K. H. Lee, F. Okkels, and M. F. Hansen. Planar Hall effect bridge magnetic field sensors. *Appl. Phys. Lett.*, 97(1):013507, 2010.

[41] F. W. Østerberg, G. Rizzi, M. Donolato, R. S. Bejhed, A. Mezger, M. Strömberg, M. Nilsson, M. Strømme, P. Svedlindh, and M. F. Hansen. On-Chip Detection of Rolling Circle Amplified DNA Molecules from Bacillus Globigii Spores and Vibrio Cholerae. *Small*, 10(14):2877–2882, 2014.

[42] D. A. Hall, R. S. Gaster, T. Lin, S. J. Osterfeld, S. Han, B. Murmann, and S. X. Wang. GMR biosensor arrays: a system perspective. *Biosens. Bioelectron.*, 25:2051–2057, 2010.

[43] S. J. Osterfeld, H. Yu, R. S. Gaster, S. Caramuta, L. Xu, S.-J. Han, D. A. Hall, R. J. Wilson, S. Sun, R. L. White, R. W. Davis, N. Pourmand, and S. X. Wang. Multiplex protein assays based on real-time magnetic nanotag sensing. *PNAS*, 105(52):20637–20640, 2008.

[44] G. Li, V. Joshi, R. L. White, S. X. Wang, J. T. Kemp, C. Webb, R. W. Davis, and S. Sun. Detection of single micron-sized magnetic bead and magnetic nanoparticles using spin valve sensors for biological applications. *J. Appl. Phys.*, 93(10):7557, 2003.

[45] D. L. Graham, H. A. Ferreira, N. Feliciano, P. P. Freitas, L. A. Clarke, and M. D. Amaral. Magnetic field-assisted DNA hybridisation and simultaneous detection using micron-sized spin-valve sensors and magnetic nanoparticles. *Sens. Actuators, B*, 107(2):936–944, 2005.

[46] H. A. Ferreira, N. Feliciano, D. L. Graham, and P. P. Freitas. Effect of spin-valve sensor magnetostatic fields on nanobead detection for biochip applications. *J. Appl. Phys.*, 97:10Q904–10Q904, 2005.

[47] A. Guedes, J. M. Almeida, S. Cardoso, R. Ferreira, and P. P. Freitas. Improving magnetic field detection limits of spin valve sensors using magnetic flux guide concentrators. *IEEE Trans. Magn.*, 43(6):2376–2378, 2007.

[48] V. C. Martins, F. A. Cardoso, J. Germano, S. Cardoso, L. Sousa, M. Piedade, P. P. Freitas, and L. P. Fonseca. Femtomolar limit of detection with a magnetoresistive biochip. *Biosens. Bioelectron.*, 24(8):2690–2695, 2009.

[49] J. Loureiro, P. Z. Andrade, S. Cardoso, C. L. Da Silva, J. M. Cabral, and P. P. Freitas. Spintronic chip cytometer. *J. Appl. Phys.*, 109(7):07B311, 2011.

[50] B. Srinivasan, Y. Li, Y. Jing, Y. Xu, X. Yao, C. Xing, and J.-P. Wang. A detection system based on giant magnetoresistive sensors and high-moment magnetic nanoparticles demonstrates zeptomole sensitivity: Potential for personalized medicine. *Angew. Chem. Int. Ed.*, 48(15):2764–2767, 2009.

[51] W. Wang, Y. Wang, L. Tu, Y. Feng, T. Klein, and J.-P. Wang. Magnetoresistive performance and comparison of supermagnetic nanoparticles on giant magnetoresistive sensor-based detection system. *Sci. Rep.*, 4:5716, 2014.

[52] Y. Wang, W. Wang, L. Yu, L. Tu, Y. Feng, T. Klein, and J.-P. Wang. Giant magnetoresistive-based biosensing probe station system for multiplex protein assays. *Biosens. Bioelectron.*, 70:61–68, 2015.

[53] G. Rizzi, F. W. Østerberg, M. Dufva, and M. F. Hansen. Magnetoresistive sensor for real-time single nucleotide polymorphism genotyping. *Biosens. Bioelectron.*, 52:445–451, 2014.

[54] B. M. de Boer, J. A. H. M. Kahlman, T. P. G. H. Jansen, H. Duric, and J. Veen. An integrated and sensitive detection platform for magneto-resistive biosensors. *Biosens. Bioelectron.*, 22(9-10):2366–2370, 2007.

[55] A. Sandhu, Y. Kumagai, A. Lapicki, S. Sakamoto, M. Abe, and H. Handa. High efficiency Hall effect micro-biosensor platform for detection of magnetically labeled biomolecules. *Biosens. Bioelectron.*, 22(9-10):2115–2120, 2007.

[56] R. S. Gaster, D. A. Hall, C. H. Nielsen, S. J. Osterfeld, H. Yu, K. E. Mach, R. J. Wilson, B. Murmann, J. C. Liao, S. S. Gambhir, and S. X. Wang. Matrix-insensitive protein assays push the limits of biosensors in medicine. *Nat. Med.*, 15:1327–1332, 2009.

[57] P. A. Belter, E. L. Cussler, and W.-S. Hu. *Bioseparations: Downstream Processing for Biotechnology.* Wiley-Interscience, 1st edition, 1988.

[58] A. Tiselius. A new apparatus for electrophoretic analysis of colloidal mixtures. *Trans. Faraday Soc.*, 33:524–531, 1937.

[59] A. Tiselius, K. O. Pedersen, and T. Svedberg. Analytical Measurements of Ultracentrifugal Sedimentation. *Nature*, 140(3550):848–849, 1937.

[60] S. Sieben, C. Bergemann, A. Lübbe, B. Brockmann, and D. Rescheleit. Comparison of different particles and methods for magnetic isolation of circulating tumor cells. *J. Magn. Magn. Mater.*, 225(1-2):175–179, 2001.

[61] M. Zborowski and J. J. Chalmers. Rare cell separation and analysis by magnetic sorting. *Anal. Chem.*, 83(21):8050–8056, 2011.

[62] J. J. Chalmers, M. Zborowski, L. Sun, and L. Moore. Flow Through , Immunomagnetic Cell Separation. *Biotechnol. Progr.*, 14(1):141–148, 1998.

[63] K.-H. Han and A. B. Frazier. Paramagnetic capture mode magnetophoretic microseparator for high efficiency blood cell separations. *Lab Chip*, 6(2):265–273, 2006.

[64] N. Pamme and A. Manz. On-chip free-flow magnetophoresis: Continuous flow separation of magnetic particles and agglomerates. *Anal. Chem.*, 76(24):7250–7256, 2004.

[65] S. Miltenyi, W. Müller, W. Weichel, and A. Radbruch. High gradient magnetic cell separation with MACS. *Cytometry*, 11(2):231–238, 1990.

[66] T. Deng, M. Prentiss, and G. M. Whitesides. Fabrication of magnetic microfiltration systems using soft lithography. *Appl. Phys. Lett.*, 80(3):461, 2002.

[67] L. Gao, N. J. Gottron, L. N. Virgin, and B. B. Yellen. The synchronization of superparamagnetic beads driven by a micro-magnetic ratchet. *Lab Chip*, 10(16):2108–14, 2010.

[68] B. Lim, V. Reddy, X. Hu, K. Kim, M. Jadhav, R. Abedini-Nassab, Y.-W. Noh, Y. T. Lim, B. B. Yellen, and C. Kim. Magnetophoretic circuits for digital control of single particles and cells. *Nat. Commun.*, 5:3846, 2014.

[69] J. Darabi and C. Guo. On-chip magnetophoretic isolation of CD4 + T cells from blood. *Biomicrofluidics*, 7(5):054106, 2013.

[70] J. Qian, X. Lou, Y. Zhang, Y. Xiao, and H. T. Soh. Generation of highly specific aptamers via micromagnetic selection. *Anal. Chem.*, 81(13):5490–5495, 2009.

[71] A. Csordas, A. E. Gerdon, J. D. Adams, J. Qian, S. S. Oh, Y. Xiao, and H. T. Soh. Detection of proteins in serum by micromagnetic aptamer PCR (MAP) technology. *Angew. Chem. Int. Ed.*, 49(2):355–358, 2010.

[72] B. S. Ferguson, S. F. Buchsbaum, T.-T. Wu, K. Hsieh, Y. Xiao, R. Sun, and H. T. Soh. Genetic analysis of H1N1 influenza virus from throat swab samples in a microfluidic system for point-of-care diagnostics. *J. Am. Chem. Soc.*, 133(23):9129–9135, 2011.

[73] J. D. Adams, U. Kim, and H. T. Soh. Multitarget magnetic activated cell sorter. *PNAS*, 105(47):18165–18170, 2008.

[74] B. B. Yellen, R. M. Erb, H. S. Son, R. Hewlin, H. Shang, and G. U. Lee. Traveling wave magnetophoresis for high resolution chip based separations. *Lab Chip*, 7(12):1681–1688, 2007.

[75] B. B. Yellen and L. N. Virgin. Nonlinear dynamics of superparamagnetic beads in a traveling magnetic-field wave. *Phys. Rev. E Stat. Nonlinear Soft Matter Phys.*, 80(1):011402, 2009.

[76] P. Li, A. Mahmood, and G. U. Lee. Flow-Enhanced Nonlinear Magnetophoresis for High-Resolution Bioseparation. *Langmuir*, 27(10):6496–6503, 2011.

[77] L. Johansson, K. Gunnarsson, S. Bijelovic, K. Eriksson, A. Surpi, E. Göthelid, P. Svedlindh, and S. Oscarsson. A magnetic microchip for controlled transport of attomole levels of proteins. *Lab Chip*, 10(5):654–661, 2010.

[78] M. Donolato, P. Vavassori, M. Gobbi, M. Deryabina, M. F. Hansen, V. Metlushko, B. Ilic, M. Cantoni, D. Petti, S. Brivio, and R. Bertacco. On-chip manipulation of protein-coated magnetic beads via domain-wall conduits. *Adv. Mater.*, 22(24):2706–2710, 2010.

[79] A. Ehresmann, D. Lengemann, T. Weis, A. Albrecht, J. Langfahl-Klabes, F. Göllner, and D. Engel. Asymmetric magnetization reversal of stripe-patterned exchange bias layer systems for controlled magnetic particle transport. *Adv. Mater.*, 23(46):5568–5573, 2011.

[80] X. Lou, J. Qian, Y. Xiao, L. Viel, A. E. Gerdon, E. T. Lagally, P. Atzberger, T. M. Tarasow, A. J. Heeger, and H. T. Soh. Micromagnetic selection of aptamers in microfluidic channels. *PNAS*, 106(9):2989–2994, 2009.

[81] J. Petersen, L. Poulsen, S. Petronis, H. Birgens, and M. Dufva. Use of a multi-thermal washer for DNA microarrays simplifies probe design and gives robust genotyping assays. *Nucleic Acids Res.*, 36(2):e10, 2008.

[82] A. D. Henriksen. *Selective magnetic bead transportation using magnetic microstripes.* M.Sc. report, DTU Nanotech, 2012.

[83] C. D. Damsgaard, B. T. Dalslet, S. C. Freitas, P. P. Freitas, and M. F. Hansen. Temperature effects in exchange-biased planar hall sensors for bioapplications. *Sens. Actuators, A*, 156(1):103–108, 2009.

[84] G. Rizzi. *Planar Hall Effect Sensors for Biodetection.* M.Sc. report, DTU Nanotech, 2014.

[85] G. Rizzi, N. C. Lundtoft, F. W. Østerberg, and M. F. Hansen. Reversible and Irreversible Temperature-induced Changes in Exchange-biased Planar Hall Effect Bridge (PHEB) Magnetic Field Sensors. *Sensors & Transducers*, 15:22–34, 2012.

[86] F. W. Østerberg. *On-Chip Magnetorelaxometry Using Planar Hall Effect Magnetic Field Sensors.* M.Sc. report, DTU Nanotech, 2013.

[87] F. W. Østerberg, G. Rizzi, T. Zardán Gómez de la Torre, M. Strömberg, M. Strø mme, P. Svedlindh, and M. F. Hansen. Measurements of Brownian relaxation of magnetic nanobeads using planar Hall effect bridge sensors. *Biosens. Bioelectron.*, 40(1):147–152, 2013.

[88] A. B. Iliuk, L. Hu, and W. A. Tao. Aptamer in bioanalytical applications. *Anal. Chem.*, 83(12):4440–4452, 2011.

[89] A. D. Keefe, S. Pai, and A. Ellington. Aptamers as therapeutics. *Nat. Rev. Drug Discov.*, 9(7):537–550, 2010.

[90] E. Levy-Nissenbaum, A. F. Radovic-Moreno, A. Z. Wang, R. Langer, and O. C. Farokhzad. Nanotechnology and aptamers: applications in drug delivery. *Trends Biotechnol.*, 26(8):442–449, 2008.

[91] K. Kiilerich-Pedersen, J. Daprà, S. Cherré, and N. Rozlosnik. High sensitivity point-of-care device for direct virus diagnostics. *Biosens. Bioelectron.*, 49:374–379, 2013.

[92] C. D. Damsgaard and M. F. Hansen. Theoretical study of in-plane response of magnetic field sensor to magnetic beads in an in-plane homogeneous field. *J. Appl. Phys.*, 103(6), 2008.

[93] A. Engel and R. Friedrichs. On the electromagnetic force on a polarizable body. *Am. J. Phys*, 70(4):8, 2001.

[94] H. Bruus. *Theoretical microfluidics.* Oxford Master Series in Condensed Matter Physics. Oxford University Press, 2008.

[95] R. Wirix-Speetjens, W. Fyen, K. Xu, J. De Boeck, and G. Borghs. A force study of on-chip magnetic particle transport based on tapered conductors. *IEEE Trans. Magn.*, 41(10):4128–4133, 2005.

[96] M. Donolato, B. T. Dalslet, and M. F. Hansen. Microstripes for transport and separation of magnetic particles. *Biomicrofluidics*, 6(2):024110, 2012.

[97] V. Gehanno, P. P. Freitas, A. Veloso, J. Ferrira, B. Almeida, J. B. Soasa, A. Kling, J. C. Soares, and M. F. da Silva. Ion beam deposition of Mn-Ir spin valves. *IEEE Trans. Magn.*, 35(5):4361–4367, 1999.

[98] A. D. Henriksen. *Planar Hall effect bridge magnetic field sensors.* B.Sc. report, DTU Nanotech, 2010.

[99] E. C. Stoner and E. P. Wohlfarth. A mechanism of magnetic hysteresis in heterogeneous alloys. *Philos. Trans. R. Soc. London, Ser. A*, 240(826):599—-642, 1948.

[100] M. Beleggia, M. D. Graef, and Y. T. Millev. The equivalent ellipsoid of a magnetized body. *J. Phys. D Appl. Phys.*, 39(5):891–899, 2006.

[101] T. B. G. Hansen, C. D. Damsgaard, B. T. Dalslet, and M. F. Hansen. Theoretical study of in-plane response of magnetic field sensor to magnetic beads magnetized by the sensor self-field. *J. Appl. Phys.*, 107(12):124511, 2010.

[102] W. F. Brown. Thermal fluctuations of a single-domain particle. *J. Appl. Phys.*, 130(5):1677–1686, 1963.

[103] M. L. Néel. Théorie Du Trainage Magnétique des Ferromagnétiques en Grains Fins avec Applications aux Terres Cuites. *Ann. Géophysique*, 5(2):99–136, 1949.

[104] P. Debye. *Polar molecules*. Chemical Catalogue Co, 1929.

[105] B. T. Dalslet. *Practical Lock-in Detection on Planar Hall Sensors*. Internal note, DTU Nanotech, 2010.

[106] B. Sinha, T. Quang Hung, T. Sri Ramulu, S. Oh, K. Kim, D.-Y. Kim, F. Terki, and C. Kim. Planar Hall resistance ring sensor based on NiFe/Cu/IrMn trilayer structure. *J. Appl. Phys.*, 113(6):063903, 2013.

[107] F. W. Østerberg, A. D. Henriksen, G. Rizzi, and M. F. Hansen. Comment on 'Planar Hall resistance ring sensor based on NiFe/Cu/IrMn trilayer structure' [J. Appl. Phys. 113, 063903 (2013)]. *J. Appl. Phys.*, 114(10):106101, 2013.

[108] N. Gökemeijer, T. Ambrose, and C. Chien. Long-Range Exchange Bias across a Spacer Layer. *Phys. Rev. Lett.*, 79(21):4270–4273, 1997.

[109] W. F. Brown. Single-Domain Particles : New Uses of Old Theorems. *Am. J. Phys*, 28(6):542, 1960.

[110] W. James. Aptamers. *Encycl. Anal. Chem.*, pages 4848–4871, 2000.

[111] R. Stoltenburg, C. Reinemann, and B. Strehlitz. SELEX–a (r)evolutionary method to generate high-affinity nucleic acid ligands. *Biomol. Eng.*, 24(4):381–403, 2007.

[112] C. Tuerk and L. Gold. Systematic evolution of ligands by exponential enrichment: RNA ligands to bacteriophage T4 DNA polymerase. *Science*, 249(4968):505–510, 1990.

[113] M. Tondra, M. Porter, and R. J. Lipert. Model for detection of immobilized superparamagnetic nanosphere assay labels using giant magnetoresistive sensors. *J. Vac. Sci. Technol., A*, 18:1125–1129, 2000.

[114] G. Li and S. X. Wang. Analytical and micromagnetic modeling for detection of a single magnetic microbead or nanobead by spin valve sensors. *IEEE Trans. Magn.*, 39:3313–3315, 2003.

[115] G. Li, S. X. Wang, and S. Sun. Model and experiment of detecting multiple magnetic nanoparticles as biomolecular labels by spin valve sensors. *IEEE Trans. Magn.*, 40:3000–3002, 2004.

[116] D. J. Griffiths. *Introduction to Electrodynamics*. Benjamin Cummings, 3rd edition, 1999.

[117] N. H. Asmar. *Partial differential equations with Fourier series and boundary value problems*. Pearson Prentice Hall, 2nd edition, 2005.

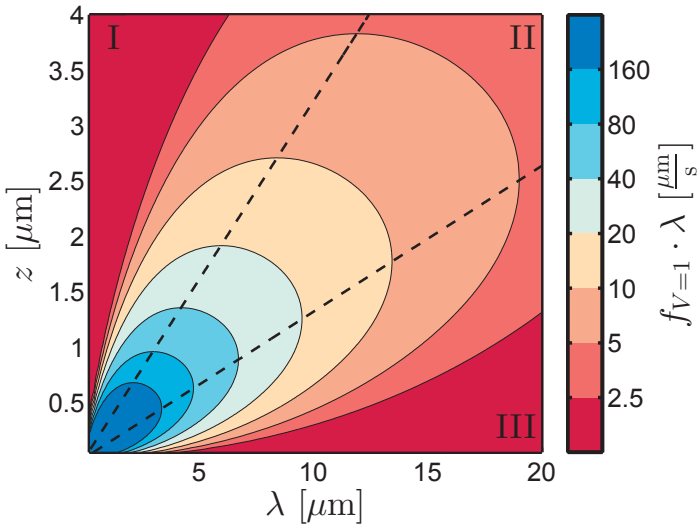

Copyright: Anders Dahl Henriksen
All rights reserved

Published by:
DTU Nanotech
Department of Micro- and Nanotechnology
Technical University of Denmark
Ørsteds Plads, building 345B
DK-2800 Kgs. Lyngby